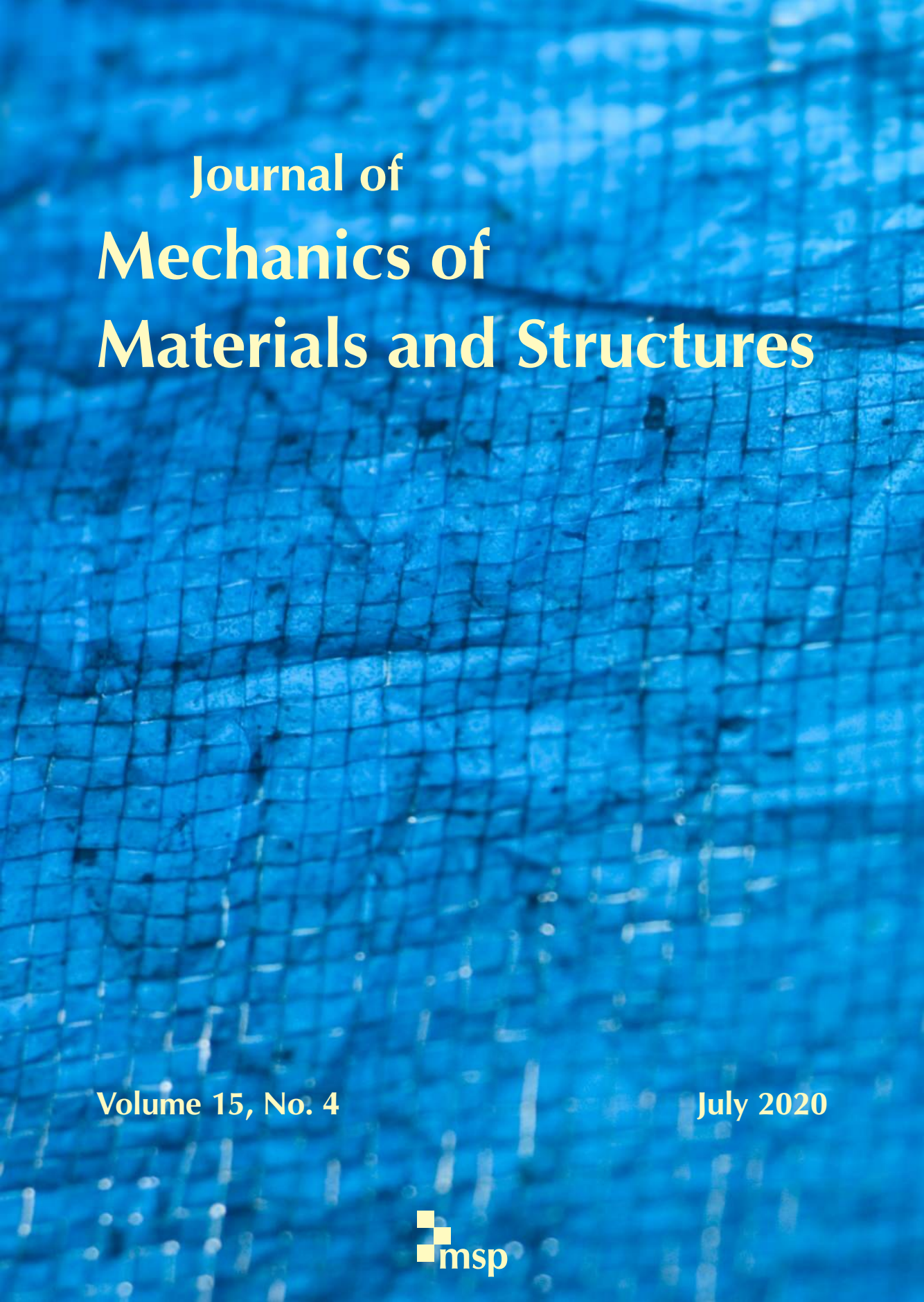

Volume 15, No. 4 July 2020

msp

JOURNAL OF MECHANICS OF MATERIALS AND STRUCTURES

msp.org/jomms

Founded by Charles R. Steele and Marie-Louise Steele

Cover photo: Mando Gomez, www.mandolux.com

See msp.org/jomms for submission guidelines.

JoMMS (ISSN 1559-3959) at Mathematical Sciences Publishers, 798 Evans Hall #6840, c/o University of California, Berkeley, CA 94720-3840, is published in 10 issues a year. The subscription price for 2020 is US $660/year for the electronic version, and $830/year (+$60, if shipping outside the US) for print and electronic. Subscriptions, requests for back issues, and changes of address should be sent to MSP.

JoMMS peer-review and production is managed by EditFLOW® from Mathematical Sciences Publishers.

PUBLISHED BY

mathematical sciences publishers

nonprofit scientific publishing

http://msp.org/

JOURNAL OF MECHANICS OF MATERIALS AND STRUCTURES
Vol. 15, No. 4, 2020
https://doi.org/10.2140/jomms.2020.15.435

WAVE PROPAGATION IN THREE-DIMENSIONAL GRAPHENE AEROGEL CYLINDRICAL SHELLS RESTING ON WINKLER–PASTERNAK ELASTIC FOUNDATION

CHEN LIANG AND YAN QING WANG

The objective of this work is to investigate the wave propagation characteristics of circular cylindrical shells made of three-dimensional graphene aerogel (3D-GA). Different distributions of 3D-GA inside the shells are taken into account. The first-order shear deformation (FSD) shell theory is utilized to model the present shells. Hamilton's principle is employed to drive the equations of motion, which governs the wave propagation behavior of 3D-GA cylindrical shells. The analytical wave dispersion relations with longitudinal and circumferential wave numbers are obtained. In addition, detailed parametric studies are conducted to emphasize the influences of the porosity distribution, the porosity coefficient, the radius-to-thickness ratio, the applied forces and the elastic foundation on wave propagation characteristics of 3D-GA cylindrical shells.

1. Introduction

Since the isolation of graphene films was first achieved by Novoselov et al. [2004], this type of carbon materials has been one of the most interesting materials owing to its extraordinary fracture strength, superior Young's modulus, extreme thermal conductivity and so on [Lee et al. 2008; Geim and Novoselov 2009; Chatterjee et al. 2012; Wang et al. 2012; Geim 2009]. Recently, based on several physical and chemical methods, the macroscopic architecture of three-dimensional graphene aerogel (3D-GA) was successfully fabricated by using the controlled micro/nano-scale graphene sheets as building blocks [Vickery et al. 2009; Xu et al. 2010; Chen et al. 2011; Huang et al. 2012; Kuang et al. 2013; Jiang and Fan 2014; Li et al. 2014; Sha et al. 2016; 2017; Strek et al. 2017]. Such creative design make 3D-GA possess many exciting properties, such as high compressibility, super elasticity, extremely low density and electrochemical stability [Chen et al. 2014; Wu et al. 2015; Xu et al. 2016; Qin et al. 2017; Qiu et al. 2017].

As one of the most novel developments in advanced porous structures, 3D-GA structures exhibit tremendous potentials and applications in biological, environmental, electric and chemical engineering. For instance, using 3D-GA structures as the conductive and biocompatible scaffold, it can support neural stem cells (NSCs) growth and keep NSCs at the positive proliferation state [Li et al. 2013]. With the abilities of reversible absorption and discharge of liquids and strong hydrophobicity, 3D-GA structures can be applied for the liquid transfer and environmental cleanup [Wu et al. 2015]. Owing to their high

Wang is the corresponding author.
Keywords: three-dimensional graphene aerogel, cylindrical shell, wave propagation, Winkler–Pasternak elastic foundation, first-order shear deformation theory.

specific surface area, 3D-GA structures were proposed as recyclable and versatile sorbent with the efficient absorption of not only toxic solvents, but also fats and petroleum products [Bi et al. 2012]. It is worth mentioning that the porous structures could be analyzed by using the gradient elasticity [Xu et al. 2008; 2014; Askes and Aifantis 2009; Sun and Aifantis 2014; Aifantis 2016; Lurie et al. 2018].

Investigation of wave propagation characteristics in structures is of significance in practical engineering applications [Wang 2010; Zeighampour et al. 2017; 2018; Zhen 2017]. Zeighampour and Beni [2017] carried out the wave propagation analysis of functionally graded (FG) cylindrical shells reinforced by CNTs. Hu et al. [2008] investigated the transverse and torsional wave propagation in double- and single-walled CNTs. Ma et al. [2018] utilized the classical and FSD shell theories to study wave propagation in magneto-electro-elastic nanoshells. Based on the fast Fourier transform (FFT), Shakeri et al. [2006] investigated wave propagation characteristics in FG thick cylindrical shells subjected to dynamic load. Aminipour et al. [2018] utilized Reddy's higher-order shear deformation theory to study the wave propagation of FG anisotropic doubly-curved shells. Thorp et al. [2005] analyzed the attenuation of wave propagation in fluid-loaded cylindrical shells with periodic shunted piezoelectric rings. Using the three-dimensional theory of anisotropic elasticity, Talebitooti and Choudari Khameneh [2017] analyzed the wave propagation across double-walled laminated composite cylindrical shells along with air-gap. Sorokin and Ershova [2004] studied the plane wave propagation in periodic cylindrical shells with and without fluid loads. The wave propagation analysis in spherically symmetric shells made of laminated piezoelectric materials was carried out in [Dai and Wang 2005]. Here the electric excitation and the thermal shock loads were taken into account. By using the reverberation ray matrix method and the generalized ray method, Liu et al. [2011] investigated the transient elastic wave propagation in laminated composite circular cylindrical shells. The Flügge shell theory was utilized to investigate wave propagation of CNTs in [Wang and Varadan 2007]. Using the Cooper–Naghdi thick shell theory and Love's thin shell theory, Liew and Wang [2007] studied wave propagation in single- and double-walled CNTs.

In this study, wave propagation analysis of circular cylindrical shells made of 3D-GA is carried out for the first time. Different distributions of 3D-GA inside the shells are taken into account. The FSD shell theory and Hamilton's principle are employed to obtain the governing equations. The analytical wave dispersion relations for 3D-GA cylindrical shells are derived. In addition, the influences of several parameters are investigated on the wave propagation in 3D-GA cylindrical shells resting on the Winkler–Pasternak elastic foundation.

2. Material properties of 3D-GA cylindrical shells

A 3D-GA cylindrical shell with the middle-surface radius r and thickness h, subjected to applied axial and circumferential distributed forces N_{px} and $N_{p\theta}$, is shown in Figure 1. Suppose that the shell is resting on the Winkler–Pasternak elastic foundation with spring constant k_w and shear constant k_p. A cylindrical coordinate system (x, θ, z) is set on the middle surface of the shell.

As illustrated in Figure 2, four types of porosity distribution across the shell thickness, namely, porosity-1, porosity-2, porosity-3 and porosity-4, are taken into account.

In the porosity-1 shell, the mass density and elastic moduli have the maxima on the inner and outer surfaces which are equal to corresponding material parameters of solid graphene without internal foams,

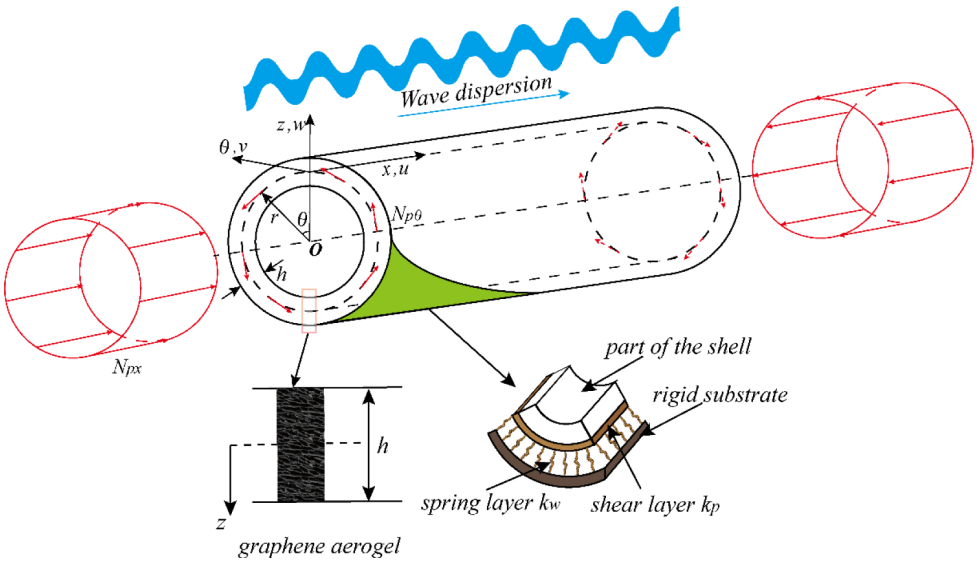

Figure 1. Schematic diagram of 3D-GA cylindrical shell.

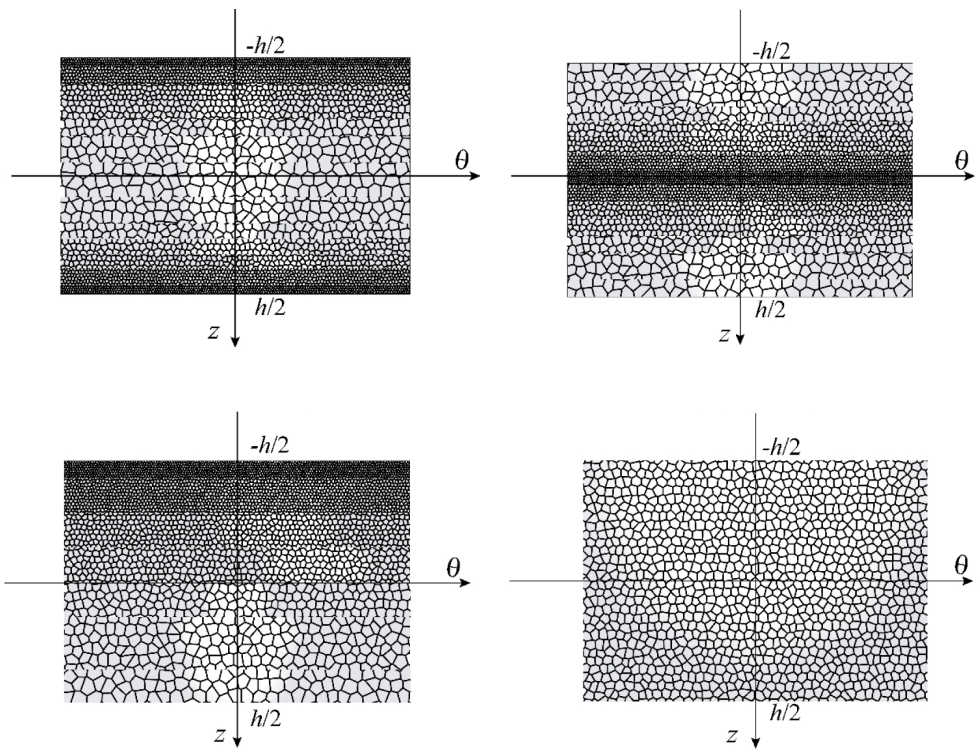

Figure 2. Different types of porosity distribution: porosity-1 (top left), porosity-2 (top right), porosity-3 (bottom left) and porosity-4 (bottom right).

while the mass density and elastic moduli reach the minimum values on the middle-surface owing to the largest size of internal pores. In the porosity-2 shell, the mass density and elastic moduli are the minima on the inner and outer surfaces, while the maxima of mass density and elastic moduli are on the middle-surface. In the porosity-3 shell, mass density and elastic moduli are the minima on the outer surface and increase gradually to the maxima on the inner surface. In the porosity-4 shell, the mass density and elastic moduli remain constant.

Young's modules $E(z)$, shear modules $G(z)$ and mass density $\rho(z)$ for porosity-1, porosity-2, porosity-3 and porosity-4 shells are expressed below [Magnucki and Stasiewicz 2004; Jabbari et al. 2014; Chen et al. 2015; Yang et al. 2018; Wang et al. 2019].

Porosity-1 shell:

$$E(z) = E_g\left[1 - e_1 \cos\frac{\pi z}{h}\right], \tag{1a}$$

$$G(z) = G_g\left[1 - e_1 \cos\frac{\pi z}{h}\right], \tag{1b}$$

$$\rho(z) = \rho_g\left[1 - e_1^* \cos\frac{\pi z}{h}\right]. \tag{1c}$$

Porosity-2 shell:

$$E(z) = E_g\left\{1 - e_2\left[1 - \cos\frac{\pi z}{h}\right]\right\}, \tag{2a}$$

$$G(z) = G_g\left\{1 - e_2\left[1 - \cos\frac{\pi z}{h}\right]\right\}, \tag{2b}$$

$$\rho(z) = \rho_g\left\{1 - e_2^*\left[1 - \cos\frac{\pi z}{h}\right]\right\}. \tag{2c}$$

Porosity-3 shell:

$$E(z) = E_g\left[1 - e_3 \cos\left(\frac{\pi z}{2h} + \frac{\pi}{4}\right)\right], \tag{3a}$$

$$G(z) = G_g\left[1 - e_3 \cos\left(\frac{\pi z}{2h} + \frac{\pi}{4}\right)\right], \tag{3b}$$

$$\rho(z) = \rho_g\left[1 - e_3^* \cos\left(\frac{\pi z}{2h} + \frac{\pi}{4}\right)\right]. \tag{3c}$$

Porosity-4 shell:

$$E(z) = E_g\,\zeta, \tag{4a}$$

$$G(z) = G_g\,\zeta, \tag{4b}$$

$$\rho(z) = \rho_g\,\zeta^*, \tag{4c}$$

where the maximum value of Young's modules, shear modules and mass density are E_g, G_g and ρ_g, respectively; e_1, e_2 and e_3 $(0 \le e_1,\ e_2,\ e_3 < 1)$ are porosity coefficients for the porosity-1, porosity-2 and porosity-3 shells, respectively; and the corresponding coefficients of mass density are e_1^*, e_2^* and e_3^*; ζ and ζ^* are corresponding coefficients for the porosity-4 shell. The shear modulus is given by

$$G(z) = \frac{E(z)}{2(1+\mu)}, \tag{5}$$

where Poisson's ratio μ is a constant.

For the graphene aerogel with open-cell foams, the relationship of the material properties is provided as [Qin et al. 2017]

$$\frac{E(z)}{E_g} = \left[\frac{\rho(z)}{\rho_g}\right]^{2.73}. \tag{6}$$

Therefore, the relationships between porosity coefficients and mass density coefficients can be expressed as

$$1 - e_1^* \cos\frac{\pi z}{h} = \sqrt[2.73]{1 - e_1 \cos\frac{\pi z}{h}}, \tag{7}$$

$$1 - e_2^*\left[1 - \cos\frac{\pi z}{h}\right] = \sqrt[2.73]{1 - e_2\left[1 - \cos\frac{\pi z}{h}\right]}, \tag{8}$$

$$1 - e_3^* \cos\left(\frac{\pi z}{2h} + \frac{\pi}{4}\right) = \sqrt[2.73]{1 - e_3 \cos\left(\frac{\pi z}{2h} + \frac{\pi}{4}\right)}, \tag{9}$$

$$\zeta^* = \sqrt[2.73]{\zeta}. \tag{10}$$

Without the loss of generality, let the masses of 3D-GA cylindrical shells with different porosity distributions keep equal to each other. Hence, we obtain [Yang et al. 2018]

$$\int_{-h/2}^{h/2} \sqrt[2.73]{1 - e_1 \cos\frac{\pi z}{h}}\, \mathrm{d}z = \int_{-h/2}^{h/2} \sqrt[2.73]{1 - e_2\left[1 - \cos\frac{\pi z}{h}\right]}\, \mathrm{d}z, \tag{11}$$

$$\int_{-h/2}^{h/2} \sqrt[2.73]{1 - e_1 \cos\frac{\pi z}{h}}\, \mathrm{d}z = \int_{-h/2}^{h/2} \sqrt[2.73]{1 - e_3 \cos\left(\frac{\pi z}{2h} + \frac{\pi}{4}\right)}\, \mathrm{d}z, \tag{12}$$

$$\int_{-h/2}^{h/2} \sqrt[2.73]{1 - e_1 \cos\frac{\pi z}{h}}\, \mathrm{d}z = \int_{-h/2}^{h/2} \sqrt[2.73]{\zeta}\, \mathrm{d}z, \tag{13}$$

which means that the values of e_2, e_3 and ζ can be calculated by a given e_1. As observed in Figure 3, the increase of e_1 leads to the increase of e_2 and e_3 and the decrease of ζ. When $e_1 = 0.6$, e_2 approaches the upper limit. Therefore, the range of e_1 $(0 \le e_1 \le 0.6)$ is selected in the following calculations.

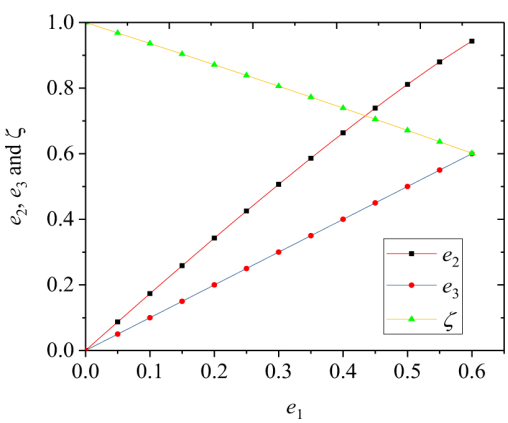

Figure 3. Variations of porosity coefficients for different porosity distributions.

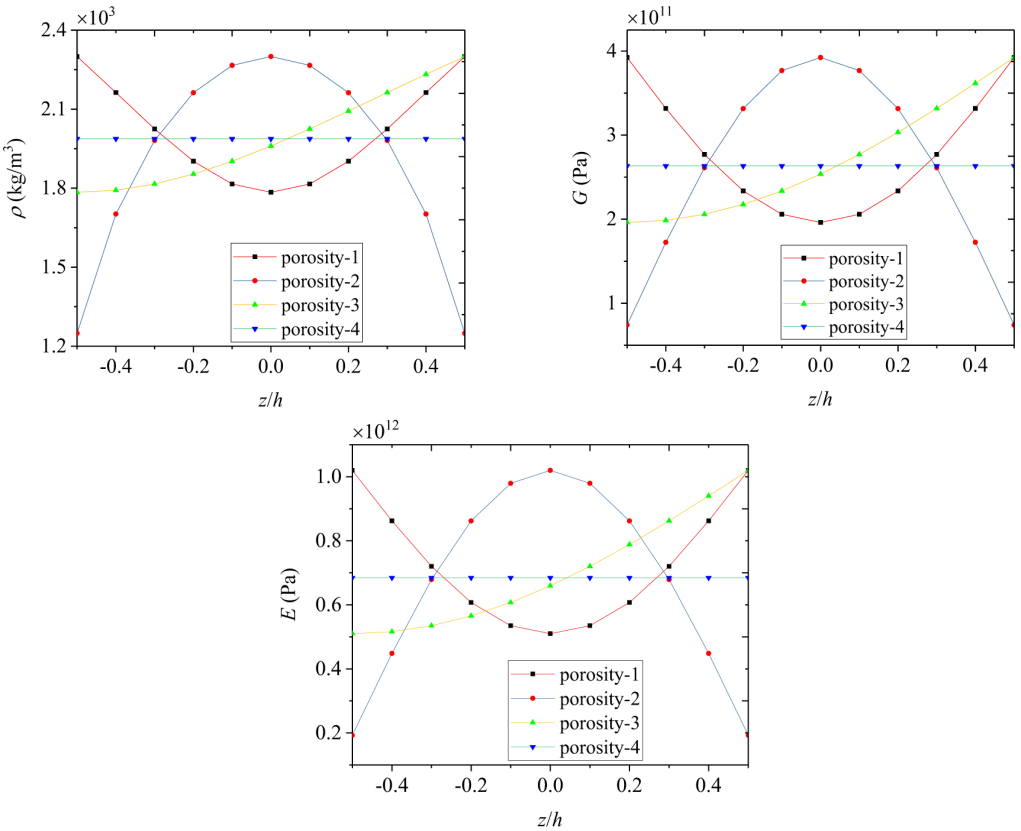

Figure 4. Variations of material properties along the radial direction: mass density (top left), shear modulus (top right) and Young's modulus (bottom).

In Figure 4, the changing curves of mass density, shear modulus and Young's modulus along the radial direction are depicted for porosity-1, porosity-2, porosity-3 and porosity-4 shells, respectively. Herein the following parameters are utilized: $E_g = 1.02\,\text{TPa},\ \mu = 0.3,\ \rho_g = 2300\,\text{kg/m}^3,\ e_0 = 0.5,\ h = 0.1\,\text{m},\ r = 0.3\,\text{m}$.

3. Wave propagation via FSD shell theory

On the basis of the FSD shell theory [Reddy 2004], the displacement field of an arbitrary point in the shell along the x-, θ- and z-axes, denoted by $u_x(x,\theta,z,t),\ v_\theta(x,\theta,z,t)$ and $w_z(x,\theta,z,t)$ are

$$u_x(x,\theta,z,t) = u(x,\theta,t) + z\phi_x(x,\theta,t), \tag{14}$$

$$v_\theta(x,\theta,z,t) = v(x,\theta,t) + z\phi_\theta(x,\theta,t), \tag{15}$$

$$w_z(x,\theta,z,t) = w(x,\theta,t), \tag{16}$$

where $u(x,\theta,t),\ v(x,\theta,t)$ and $w(x,\theta,t)$ are the displacements of a point at the midplane; t is time; $\phi_x(x,\theta,t)$ and $\phi_\theta(x,\theta,t)$ denote the rotations of a transverse normal about the θ- and x-axes, respectively.

The relations between strains and displacements can be written as

$$\varepsilon_x = \frac{\partial u}{\partial x} + z\frac{\partial \phi_x}{\partial x}, \tag{17}$$

$$\varepsilon_\theta = \frac{1}{r}\left(\frac{\partial v}{\partial \theta} + w\right) + \frac{z}{r}\frac{\partial \phi_\theta}{\partial \theta}, \tag{18}$$

$$\gamma_{x\theta} = \frac{\partial v}{\partial x} + \frac{1}{r}\frac{\partial u}{\partial \theta} + z\left(\frac{\partial \phi_\theta}{\partial x} + \frac{1}{r}\frac{\partial \phi_x}{\partial \theta}\right), \tag{19}$$

$$\gamma_{xz} = \phi_x + \frac{\partial w}{\partial x}, \tag{20}$$

$$\gamma_{\theta z} = \phi_\theta + \frac{1}{r}\frac{\partial w}{\partial \theta} - \frac{v}{r}. \tag{21}$$

The relations between stresses and strains can be given by [Reddy 2004]

$$\sigma_x = \frac{E(z)}{1-\mu^2}(\varepsilon_x + \mu\varepsilon_\theta), \tag{22}$$

$$\sigma_\theta = \frac{E(z)}{1-\mu^2}(\varepsilon_\theta + \mu\varepsilon_x), \tag{23}$$

$$\tau_{x\theta} = G(z)\,\gamma_{x\theta}, \tag{24}$$

$$\tau_{xz} = G(z)\,\gamma_{xz}, \tag{25}$$

$$\tau_{\theta z} = G(z)\,\gamma_{\theta z}. \tag{26}$$

The resultant moments and forces are expressed as

$$\begin{Bmatrix} N_x \\ N_\theta \\ N_{x\theta} \end{Bmatrix} = \int_{-h/2}^{h/2} \begin{Bmatrix} \sigma_x \\ \sigma_\theta \\ \tau_{x\theta} \end{Bmatrix} \mathrm{d}z, \tag{27}$$

$$\begin{Bmatrix} M_x \\ M_\theta \\ M_{x\theta} \end{Bmatrix} = \int_{-h/2}^{h/2} \begin{Bmatrix} \sigma_x \\ \sigma_\theta \\ \tau_{x\theta} \end{Bmatrix} z\,\mathrm{d}z, \tag{28}$$

$$\begin{Bmatrix} Q_{\theta z} \\ Q_{xz} \end{Bmatrix} = \kappa_s \int_{-h/2}^{h/2} \begin{Bmatrix} \tau_{\theta z} \\ \tau_{xz} \end{Bmatrix} \mathrm{d}z, \tag{29}$$

where the shear correction coefficient is $\kappa_s = 5/6$ [Reddy 2004].

From (17)–(29), we obtain

$$N_x = A_{11}\frac{\partial u}{\partial x} + A_{12}\frac{\partial \phi_x}{\partial x} + A_{13}\frac{1}{r}\left(\frac{\partial v}{\partial \theta} + w\right) + A_{14}\frac{1}{r}\frac{\partial \phi_\theta}{\partial \theta}, \tag{30}$$

$$N_\theta = A_{11}\frac{1}{r}\left(\frac{\partial v}{\partial \theta} + w\right) + A_{12}\frac{1}{r}\frac{\partial \phi_\theta}{\partial \theta} + A_{13}\frac{\partial u}{\partial x} + A_{14}\frac{\partial \phi_x}{\partial x}, \tag{31}$$

$$N_{x\theta} = B_{11}\left(\frac{\partial v}{\partial x} + \frac{1}{r}\frac{\partial u}{\partial \theta}\right) + B_{12}\left(\frac{\partial \phi_\theta}{\partial x} + \frac{1}{r}\frac{\partial \phi_x}{\partial \theta}\right), \tag{32}$$

$$M_x = C_{11}\frac{\partial u}{\partial x} + C_{12}\frac{\partial \phi_x}{\partial x} + C_{13}\frac{1}{r}\left(\frac{\partial v}{\partial \theta} + w\right) + C_{14}\frac{1}{r}\frac{\partial \phi_\theta}{\partial \theta}, \tag{33}$$

$$M_\theta = C_{11}\frac{1}{r}\left(\frac{\partial v}{\partial \theta} + w\right) + C_{12}\frac{1}{r}\frac{\partial \phi_\theta}{\partial \theta} + C_{13}\frac{\partial u}{\partial x} + C_{14}\frac{\partial \phi_x}{\partial x}, \tag{34}$$

$$M_{x\theta} = D_{11}\left(\frac{\partial v}{\partial x} + \frac{1}{r}\frac{\partial u}{\partial \theta}\right) + D_{12}\left(\frac{\partial \phi_\theta}{\partial x} + \frac{1}{r}\frac{\partial \phi_x}{\partial \theta}\right), \tag{35}$$

$$Q_{xz} = \kappa_s B_{11}\left(\phi_x + \frac{\partial w}{\partial x}\right), \tag{36}$$

$$Q_{\theta z} = \kappa_s B_{11}\left(\phi_\theta + \frac{1}{r}\frac{\partial w}{\partial \theta} - \frac{v}{r}\right), \tag{37}$$

where the parameters A_{ij}, B_{ij}, C_{ij} and D_{ij} $(i, j = 1, 2, 3, 4)$ are given in Appendix A.

The strain energy of the 3D-GA shell is written as

$$S = \frac{1}{2}\int_0^L\int_0^{2\pi}\int_{-h/2}^{h/2}(\sigma_x\,\varepsilon_x + \sigma_\theta\,\varepsilon_\theta + \tau_{x\theta}\,\gamma_{x\theta} + \tau_{xz}\,\gamma_{xz} + \tau_{\theta z}\,\gamma_{\theta z})\,r\,\mathrm{d}z\,\mathrm{d}\theta\,\mathrm{d}x. \tag{38}$$

The kinetic energy is represented as

$$K = \frac{1}{2}\int_0^L\int_0^{2\pi}\int_{-h/2}^{h/2}\rho(z)\left[\left(\frac{\partial u}{\partial t} + z\frac{\partial \phi_x}{\partial t}\right)^2 + \left(\frac{\partial v}{\partial t} + z\frac{\partial \phi_\theta}{\partial t}\right)^2 + \left(\frac{\partial w}{\partial t}\right)^2\right] r\,\mathrm{d}z\,\mathrm{d}\theta\,\mathrm{d}x. \tag{39}$$

The work done by the applied forces can be expressed as

$$W_F = \frac{1}{2}\int_0^L\int_0^{2\pi}\left[N_{px}\left(\frac{\partial w}{\partial x}\right)^2 + N_{p\theta}\left(\frac{1}{r}\frac{\partial w}{\partial \theta}\right)^2\right] r\,\mathrm{d}\theta\,\mathrm{d}x, \tag{40}$$

where the applied axial and circumferential distributed forces are given by

$$N_{px} = N_{p\theta} = N_p. \tag{41}$$

The additional strain energy results from the Winkler–Pasternak elastic foundation is written as [Winkler 1867; Pasternak 1954]

$$W_G = \frac{1}{2}\int_0^L\int_0^{2\pi}\left\{k_w\,w^2 + k_p\left[\left(\frac{\partial w}{\partial x}\right)^2 + \left(\frac{1}{r}\frac{\partial w}{\partial \theta}\right)^2\right]\right\} r\,\mathrm{d}\theta\,\mathrm{d}x. \tag{42}$$

By employing Hamilton's principle

$$\int_0^t [\delta K - (\delta S + \delta W_F + \delta W_G)]\,\mathrm{d}t = 0, \tag{43}$$

the governing equations of the 3D-GA shell can be obtained as

$$\frac{\partial N_x}{\partial x}+\frac{1}{r}\frac{\partial N_{x\theta}}{\partial \theta}=I_1\frac{\partial^2 u}{\partial t^2}+I_2\frac{\partial^2 \phi_x}{\partial t^2}, \tag{44}$$

$$\frac{\partial N_{x\theta}}{\partial x}+\frac{1}{r}\frac{\partial N_{\theta}}{\partial \theta}+\frac{Q_{\theta z}}{r}=I_1\frac{\partial^2 v}{\partial t^2}+I_2\frac{\partial^2 \phi_\theta}{\partial t^2}, \tag{45}$$

$$\frac{\partial Q_{xz}}{\partial x}+\frac{1}{r}\frac{\partial Q_{\theta z}}{\partial \theta}-\frac{N_\theta}{r}+N_{px}\frac{\partial^2 w}{\partial x^2}+N_{p\theta}\frac{1}{r^2}\frac{\partial^2 w}{\partial \theta^2}-k_w w+k_p\left(\frac{\partial^2 w}{\partial x^2}+\frac{1}{r^2}\frac{\partial^2 w}{\partial \theta^2}\right)=I_1\frac{\partial^2 w}{\partial t^2}, \tag{46}$$

$$\frac{\partial M_x}{\partial x}+\frac{1}{r}\frac{\partial M_{x\theta}}{\partial \theta}-Q_{xz}=I_2\frac{\partial^2 u}{\partial t^2}+I_3\frac{\partial^2 \phi_x}{\partial t^2}, \tag{47}$$

$$\frac{\partial M_{x\theta}}{\partial x}+\frac{1}{r}\frac{\partial M_{\theta}}{\partial \theta}-Q_{\theta z}=I_2\frac{\partial^2 v}{\partial t^2}+I_3\frac{\partial^2 \phi_\theta}{\partial t^2}, \tag{48}$$

where the coefficients I_1, I_2 and I_3 take the form of

$$I_1=\int_{-h/2}^{h/2}\rho(z)\,\mathrm{d}z, \tag{49}$$

$$I_2=\int_{-h/2}^{h/2}\rho(z)\,z\,\mathrm{d}z, \tag{50}$$

$$I_3=\int_{-h/2}^{h/2}\rho(z)\,z^2\,\mathrm{d}z. \tag{51}$$

By substituting (30)–(37) into (44)–(48), it yields

$$A_{11}\frac{\partial^2 u}{\partial x^2}+A_{12}\frac{\partial^2 \phi_x}{\partial x^2}+\frac{A_{13}}{r}\left(\frac{\partial w}{\partial x}+\frac{\partial^2 v}{\partial x\,\partial \theta}\right)+\frac{A_{14}}{r}\frac{\partial^2 \phi_\theta}{\partial x\,\partial \theta}+B_{11}\left(\frac{1}{r^2}\frac{\partial^2 u}{\partial \theta^2}+\frac{1}{r}\frac{\partial^2 v}{\partial x\,\partial \theta}\right)$$
$$+B_{12}\left(\frac{1}{r^2}\frac{\partial^2 \phi_x}{\partial \theta^2}+\frac{1}{r}\frac{\partial^2 \phi_\theta}{\partial x\,\partial \theta}\right)=I_1\frac{\partial^2 u}{\partial t^2}+I_2\frac{\partial^2 \phi_x}{\partial t^2}, \tag{52}$$

$$\frac{A_{11}}{r^2}\left(\frac{\partial^2 v}{\partial \theta^2}+\frac{\partial w}{\partial \theta}\right)+\frac{A_{12}}{r^2}\frac{\partial^2 \phi_\theta}{\partial \theta^2}+\frac{A_{13}}{r}\frac{\partial^2 u}{\partial x\,\partial \theta}+\frac{A_{14}}{r}\frac{\partial^2 \phi_x}{\partial x\,\partial \theta}+B_{12}\left(\frac{1}{r}\frac{\partial^2 \phi_x}{\partial x\,\partial \theta}+\frac{\partial^2 \phi_\theta}{\partial x^2}\right)$$
$$+B_{11}\left(\frac{1}{r}\frac{\partial^2 u}{\partial x\,\partial \theta}+\frac{\partial^2 v}{\partial x^2}+\frac{\kappa_s}{r^2}\frac{\partial w}{\partial \theta}+\frac{\kappa_s}{r}\phi_\theta-\frac{\kappa_s}{r^2}v\right)=I_1\frac{\partial^2 v}{\partial t^2}+I_2\frac{\partial^2 \phi_\theta}{\partial t^2}, \tag{53}$$

$$A_{11}\frac{1}{r^2}\left(w+\frac{\partial v}{\partial \theta}\right)+A_{12}\frac{1}{r^2}\frac{\partial \phi_\theta}{\partial \theta}+A_{13}\frac{1}{r}\frac{\partial u}{\partial x}+A_{14}\frac{1}{r}\frac{\partial \phi_x}{\partial x}$$
$$+\kappa_s B_{11}\left(\frac{\partial \phi_x}{\partial x}+\frac{\partial^2 w}{\partial x^2}+\frac{1}{r^2}\frac{\partial^2 w}{\partial \theta^2}+\frac{1}{r}\frac{\partial \phi_\theta}{\partial \theta}-\frac{1}{r^2}\frac{\partial v}{\partial \theta}\right)+N_{px}\frac{\partial^2 w}{\partial x^2}+\frac{N_{p\theta}}{r^2}\frac{\partial^2 w}{\partial \theta^2}$$
$$-k_w w+k_p\left(\frac{\partial^2 w}{\partial x^2}+\frac{1}{r^2}\frac{\partial^2 w}{\partial \theta^2}\right)=I_1\frac{\partial^2 w}{\partial t^2} \tag{54}$$

$$-B_{11}\kappa_s\left(\phi_x+\frac{\partial w}{\partial x}\right)+C_{11}\frac{\partial^2 u}{\partial x^2}+C_{12}\frac{\partial^2\phi_x}{\partial x^2}+C_{13}\frac{1}{r}\left(\frac{\partial w}{\partial x}+\frac{\partial^2 v}{\partial x\,\partial\theta}\right)+C_{14}\frac{1}{r}\frac{\partial^2\phi_\theta}{\partial x\,\partial\theta}$$
$$+D_{11}\left(\frac{1}{r^2}\frac{\partial^2 u}{\partial\theta^2}+\frac{1}{r}\frac{\partial^2 v}{\partial x\,\partial\theta}\right)+D_{12}\left(\frac{1}{r^2}\frac{\partial^2\phi_x}{\partial\theta^2}+\frac{1}{r}\frac{\partial^2\phi_\theta}{\partial x\,\partial\theta}\right)=I_2\frac{\partial^2 u}{\partial t^2}+I_3\frac{\partial^2\phi_x}{\partial t^2},\quad(55)$$

$$\kappa_s B_{11}\left(\frac{v}{r}-\frac{1}{r}\frac{\partial w}{\partial\theta}-\phi_\theta\right)+\frac{C_{11}}{r^2}\left(\frac{\partial w}{\partial\theta}+\frac{\partial^2 v}{\partial\theta^2}\right)+\frac{C_{12}}{r^2}\frac{\partial^2\phi_\theta}{\partial\theta^2}+\frac{C_{13}}{r}\frac{\partial^2 u}{\partial x\,\partial\theta}+\frac{C_{14}}{r}\frac{\partial^2\phi_x}{\partial x\,\partial\theta}$$
$$+D_{11}\left(\frac{1}{r}\frac{\partial^2 u}{\partial x\,\partial\theta}+\frac{\partial^2 v}{\partial x^2}\right)+D_{12}\left(\frac{1}{r}\frac{\partial^2\phi_x}{\partial x\,\partial\theta}+\frac{\partial^2\phi_\theta}{\partial x^2}\right)=I_2\frac{\partial^2 v}{\partial t^2}+I_3\frac{\partial^2\phi_\theta}{\partial t^2}.\quad(56)$$

The wave propagation solutions of (52)–(56) are expressed as

$$u(x,\theta,t)=Ue^{\mathrm{i}(kx+n\theta-\omega t)},\quad(57)$$
$$v(x,\theta,t)=Ve^{\mathrm{i}(kx+n\theta-\omega t)},\quad(58)$$
$$w(x,\theta,t)=We^{\mathrm{i}(kx+n\theta-\omega t)},\quad(59)$$
$$\phi_x(x,\theta,t)=\Phi_x\,e^{\mathrm{i}(kx+n\theta-\omega t)},\quad(60)$$
$$\phi_\theta(x,\theta,t)=\Phi_\theta\,e^{\mathrm{i}(kx+n\theta-\omega t)},\quad(61)$$

where $\mathrm{i}=\sqrt{-1}$; k and n are the wave numbers in the longitudinal and circumferential directions, respectively; ω is the frequency of wave motion; U, V, W, Φ_x and Φ_θ are the amplitudes of wave motion.

Substituting (57)–(61) into (52)–(56) yields a generalized eigenvalue problem:

$$(L_{5\times5}-\omega^2 H_{5\times5})\begin{Bmatrix}U\\V\\W\\\Phi_x\\\Phi_\theta\end{Bmatrix}=\{0\},\quad(62)$$

where the elements L_{ij} and H_{ij} $(i,j=1,2,\ldots,5)$ in the matrix $L_{5\times5}$ and $H_{5\times5}$ can be found in Appendix B.

The dispersion relation derived from (62) takes the form of

$$\mathrm{Det}[L_{5\times5}-\omega^2 H_{5\times5}]=0.\quad(63)$$

The relation between the wave frequency ω and phase velocity v is [Wang and Varadan 2007]

$$v=\omega/k.\quad(64)$$

According to (63) and (64), five positive analytical solutions of wave phase velocity can be obtained. The first three low-value solutions which correspond to the coupled longitudinal, radial and circumferential (L-R-C) modes are discussed hereinbelow.

4. Results and discussion

For the purpose of demonstrating the effectiveness of the present analysis, Figure 5 presents a comparative study of the dispersion relation between phase velocity and circumferential wave number for a homogeneous cylindrical shell. The present 3D-GA cylindrical shell model can be simplified to a homogeneous cylindrical shell by setting $N_p = 0\,\mathrm{N}$, $k_w = 0\,\mathrm{N/m^3}$, $k_p = 0\,\mathrm{N/m}$ and $e_1 = 0$. The thickness, the middle-surface radius, Poisson's ratio and the mass density of the cylindrical shell are $h = 0.34\,\mathrm{nm}$, $r = 5\,\mathrm{nm}$, $\mu = 0.2$ and $\rho = 2.27\,\mathrm{g/cm^3}$, respectively. The bending rigidity is $D = 2\,\mathrm{eV}$ and the in-plane stiffness is $Eh = 360\,\mathrm{J/m^2}$. The results from the classical shell theory were given in [Wang and Varadan 2007]. The present results have good consistency with those in the literature, manifesting the effectiveness of the present analysis.

Hereinafter, the wave propagation analysis in 3D-GA cylindrical shells is conducted. If not specified, the following geometric and material parameters are utilized: $h = 0.1\,\mathrm{m}$, $r = 0.3\,\mathrm{m}$, $E_g = 1.02\,\mathrm{TPa}$, $\rho_g = 2300\,\mathrm{kg/m^3}$ and $\mu = 0.3$.

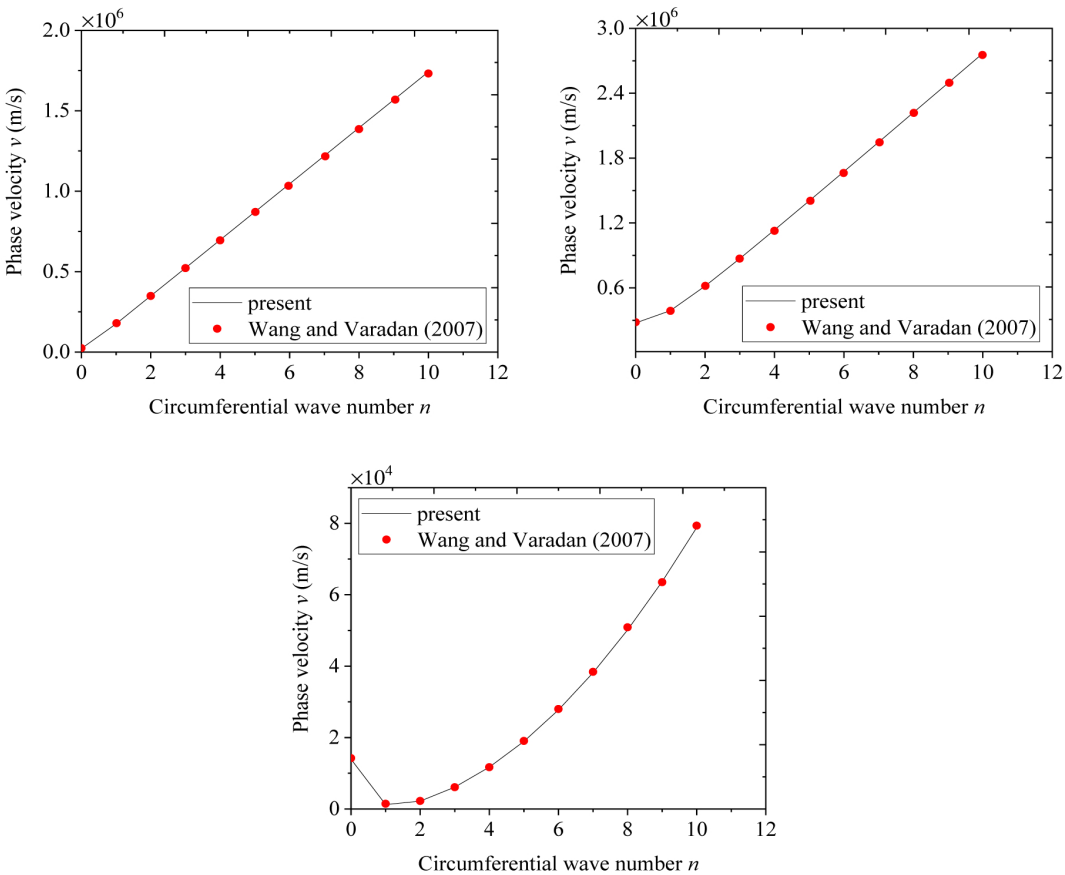

Figure 5. Comparisons of wave characteristics in a homogenous cylindrical shell ($k = 8 \times 10^6\,\mathrm{m^{-1}}$, $e_0 a = 0$): the first mode (top left), the second mode (top right) and the third mode (bottom).

Figure 6 demonstrates the curves of phase velocity versus longitudinal wave number k of 3D-GA shells for the L-R-C modes. Dispersion relations are investigated for porosity-1, porosity-2, porosity-3 and porosity-4 shells. For clearer discussion, we define the mode number by the numerical order of phase velocity in the following results, which is different from Figure 5. As can be observed, for all porosity distributions, the phase velocity for the first L-R-C mode fluctuates initially and then tends to be constant. As for the second and third L-R-C modes, the phase velocities initially exhibit a decreasing trend and then tend to be constant. The nonlinear variation of phase velocities is because the coupling exists among the longitudinal, radial and circumferential wave modes, which arises from the coupled displacement fields. It is worth mentioning that at the larger longitudinal wave number $k > 10^2\,\mathrm{m}^{-1}$, or at corresponding smaller longitudinal wavelength $\lambda = 1/k < 0.01$ m, all the phase velocities for the L-R-C modes are close to each other.

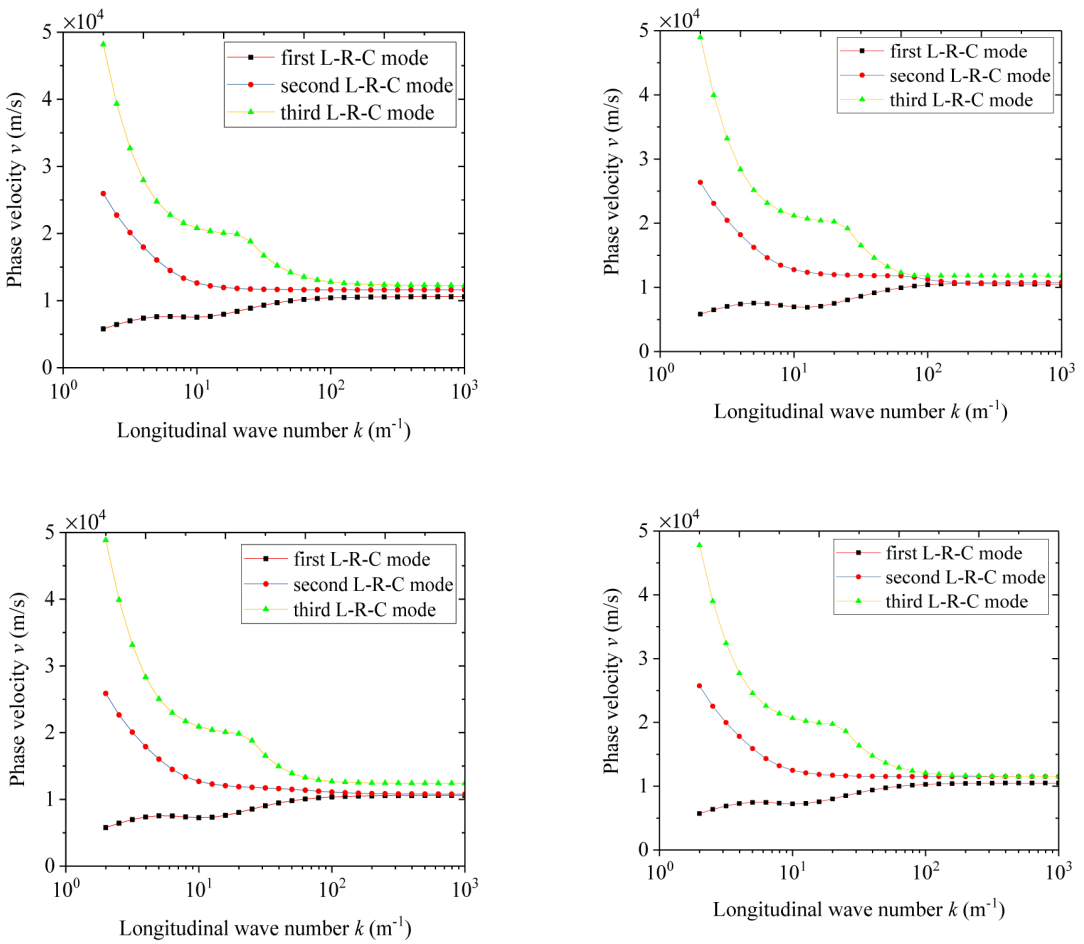

Figure 6. Phase velocity versus longitudinal wave number k of 3D-GA shell ($e_1 = 0.5$, $n = 1$, $N_p = 0\,\mathrm{N}$, $k_w = 0\,\mathrm{N/m^3}$, $k_p = 0\,\mathrm{N/m}$): porosity-1 (top left), porosity-2 (top right), porosity-3 (bottom left) and porosity-4 (bottom right).

In Figure 7, the dispersion relations between the phase velocity and circumferential wave number n for different porosity distributions are shown. It is found that for the first L-R-C mode, the phase velocity decreases initially and then increases with the circumferential wave number. Moreover, the lowest phase velocity occurs at $n = 2$. As for the second and third L-R-C modes, the phase velocities exhibit an increasing-trend variation with increasing circumferential wave number.

Figure 8 depicts the effect of porosity coefficient e_1 on the dispersion relations for different porosity distributions. One can find that the phase velocities in the 3D-GA shell decrease with the increasing porosity coefficient. Among all types of porosity distribution, the porosity-1 shell has the largest phase velocity and the porosity-2 shell has the smallest phase velocity. Moreover, the phase velocity in the porosity-4 shell is smaller than that in the porosity-3 shell.

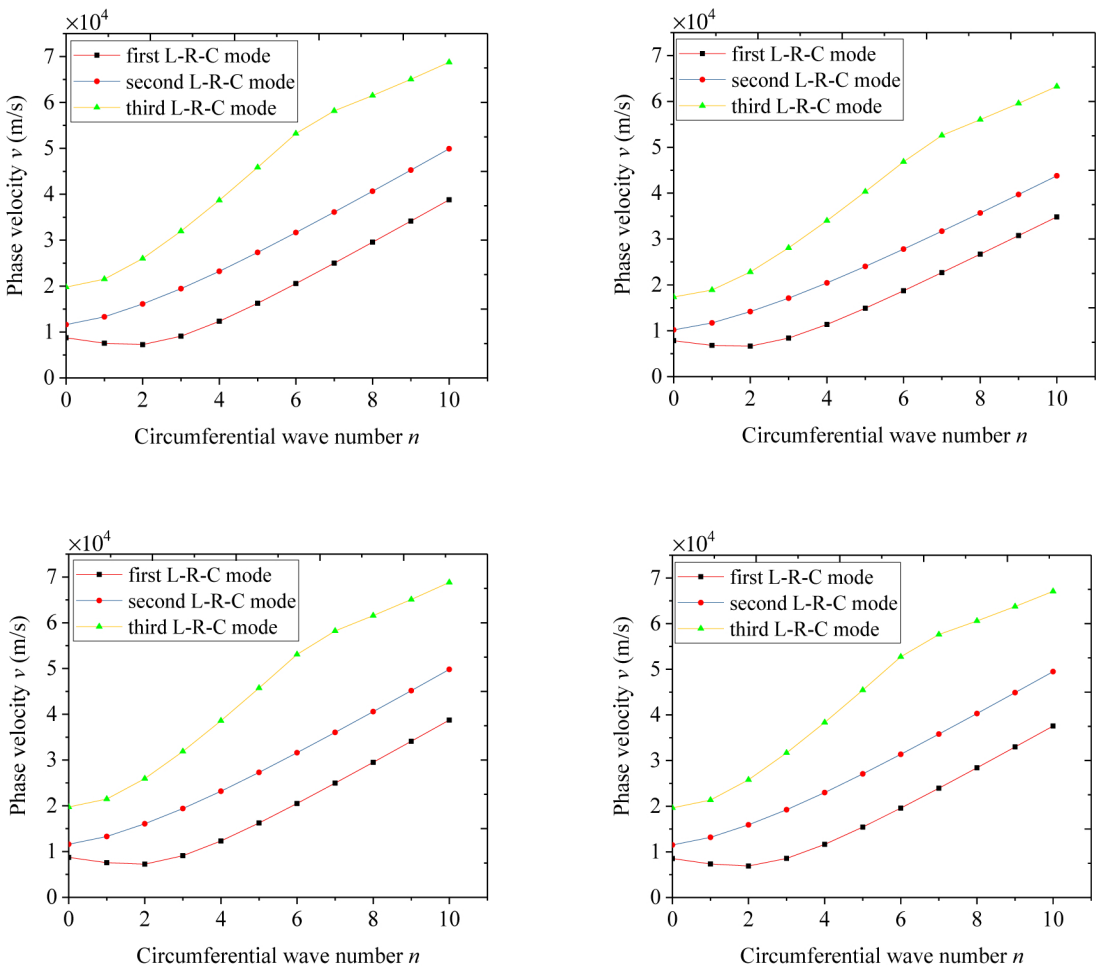

Figure 7. Phase velocity versus circumferential wave number n of 3D-GA shell ($e_1 = 0.5$, $k = 8\,\mathrm{m}^{-1}$, $N_p = 0\,\mathrm{N}$, $k_w = 0\,\mathrm{N/m^3}$, $k_p = 0\,\mathrm{N/m}$): porosity-1 (top left), porosity-2 (top right), porosity-3 (bottom left) and porosity-4 (bottom right).

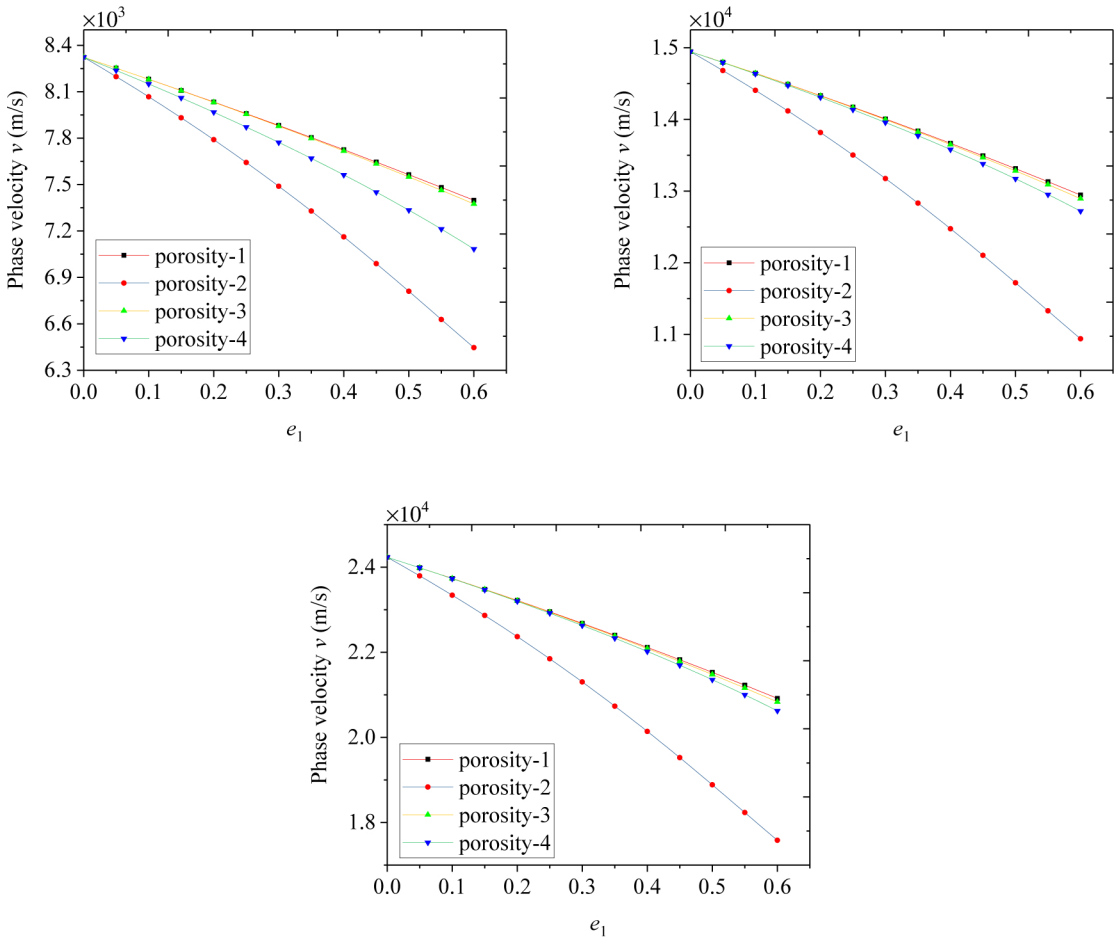

Figure 8. Phase velocity versus porosity coefficient e_1 of 3D-GA shell ($n = 1$, $k = 8\,\mathrm{m}^{-1}$, $N_p = 0\,\mathrm{N}$, $k_w = 0\,\mathrm{N/m^3}$, $k_p = 0\,\mathrm{N/m}$): the first L-R-C mode (top left), the second L-R-C mode (top right), and the third L-R-C mode (bottom).

The influence of applied force N_p on the dispersion relations of the 3D-GA shell is plotted in Figure 9. For all the porosity distributions, the phase velocities initially increase slightly, then increase rapidly, and finally approach to constant. This interesting phenomenon indicates that the applied force has significant effect on the dispersion relation in certain range; beyond this range, however, it affects slightly the dispersion relation.

Figure 10 illustrates the effect of spring constant k_w on the dispersion relations of 3D-GA shells with different porosity distributions. It is interesting that a similar variation tendency of phase velocity can be observed with the comparison of Figure 9. In certain range, spring constant has significant influence on the phase velocity but it is insignificant for phase velocity beyond this range. For example, the phase velocity for the first L-R-C mode changes rapidly when $10^{11}\,\mathrm{N/m^3} \le k_w \le 10^{13}\,\mathrm{N/m^3}$, while it almost remains constant if $k_w < 10^{11}\,\mathrm{N/m^3}$ or $k_w > 10^{13}\,\mathrm{N/m^3}$.

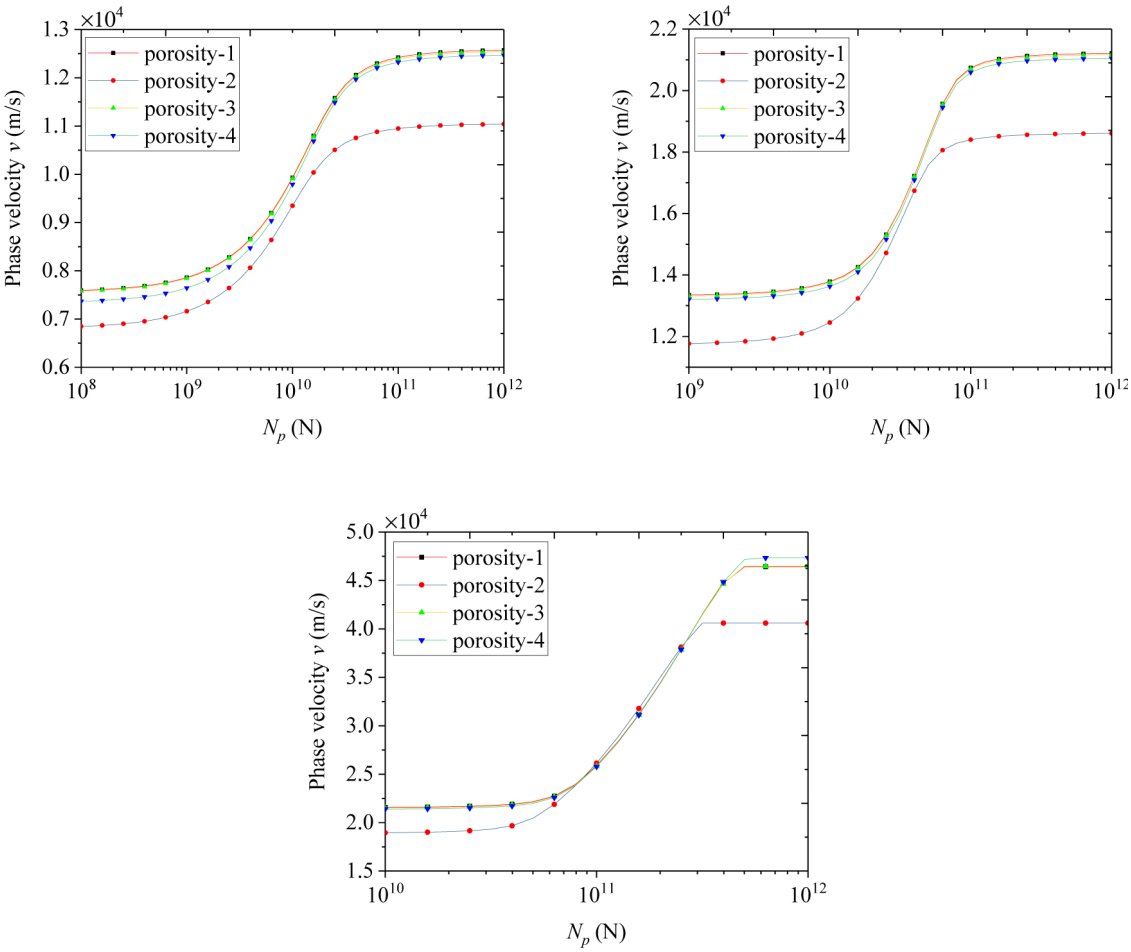

Figure 9. Phase velocity versus applied force N_p of 3D-GA shell ($e_1 = 0.5$, $n = 1$, $k = 8\,\mathrm{m}^{-1}$, $k_w = 0\,\mathrm{N/m}^3$, $k_p = 0\,\mathrm{N/m}$): the first L-R-C mode (top left), the second L-R-C mode (top right), and the third L-R-C mode (bottom).

Figure 11 examines the effect of shear constant k_p on the dispersion relations of the 3D-GA shell. When the shear constant is in the certain range, it has conspicuous effect on the phase velocity of the 3D-GA shell. From Figures 9–11, it is concluded that the applied force, spring constant and shear constant have similar influence on the phase velocity of 3D-GA shells. Such observations are significant for guiding the structural design of 3D-GA shells by adjusting the corresponding parameters.

In Figure 12, phase velocity versus radius-to-thickness ratio r/h of the 3D-GA shell is depicted. It is found that the phase velocities for the L-R-C modes initially decrease rapidly and then tend to be constant. In particular, the phase velocities for the second and third L-R-C modes decrease faster than that for the first L-R-C mode. Additionally, it is worth mentioning that when $r/h > 15$, the phase velocities are insensitive to the radius-to-thickness ratio.

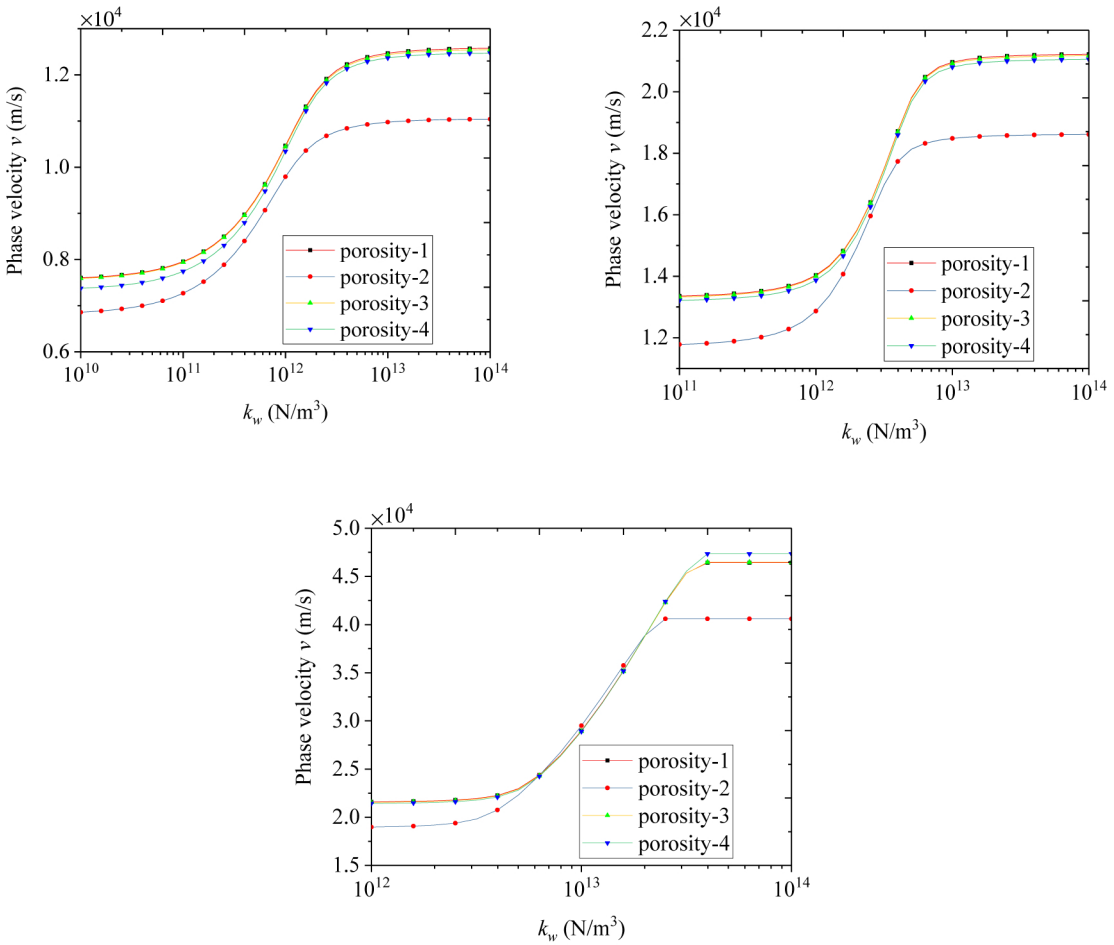

Figure 10. Phase velocity versus spring constant k_w of 3D-GA shell ($e_1 = 0.5$, $n = 1$, $k = 8\,\mathrm{m}^{-1}$, $N_p = 0\,\mathrm{N}$, $k_p = 0\,\mathrm{N/m}$): the first L-R-C mode (top left), the second L-R-C mode (top right), and the third L-R-C mode (bottom).

5. Concluding remarks

Wave propagation characteristics in 3D-GA cylindrical shells are studied in the framework of the FSD shell theory. Hamilton's principle is utilized to derive the governing equations. The effects of longitudinal and circumferential wave numbers, the porosity distribution, the porosity coefficient, the applied forces, the Winkler–Pasternak elastic foundation and the radius-to-thickness ratio on wave dispersion relations of 3D-GA shells are investigated. The main conclusions are summarized as follows:

(1) An increasing porosity coefficient leads to a decrease in the phase velocities of 3D-GA shells. Among different types of porosity distribution, the porosity-1 shell has the largest phase velocity whereas the porosity-2 shell has the smallest phase velocity.

(2) For the L-R-C modes of 3D-GA shells, the phase velocities show nonlinear variation with the change of longitudinal and circumferential wave numbers. It is found that phase velocities of the three L-R-C modes approach to constant and are close to each other when the longitudinal wave number is large.

(3) As the applied forces, the spring constant and the shear constant increase, the phase velocities of 3D-GA shells initially increase slightly, then increase rapidly, and finally approach to constant.

(4) With the increase in radius-to-thickness ratio, the phase velocities of 3D-GA shells initially decrease rapidly but finally are insensitive to the radius-to-thickness ratio.

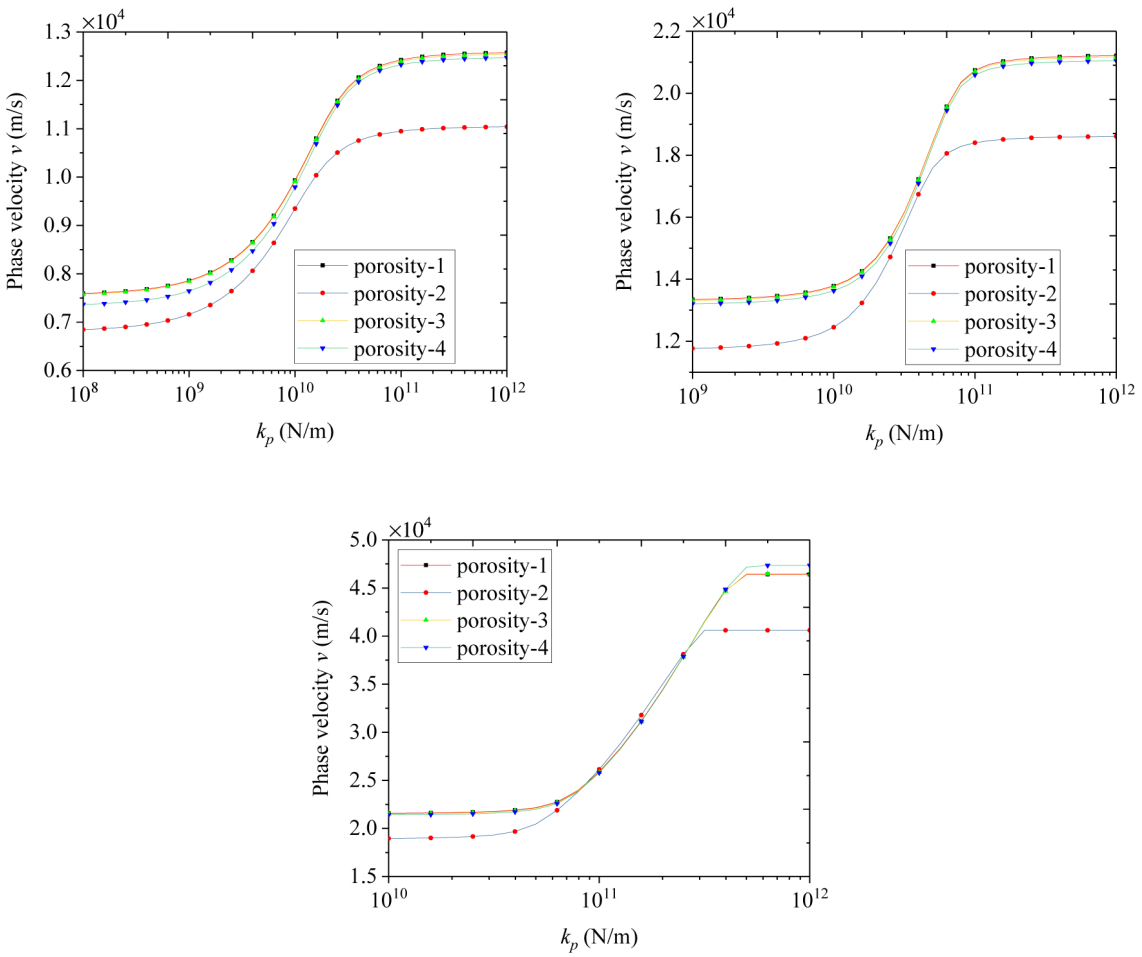

Figure 11. Phase velocity versus shear constant k_p of 3D-GA shell ($e_1 = 0.5$, $n = 1$, $k = 8\,\mathrm{m}^{-1}$, $N_p = 0\,\mathrm{N}$, $k_w = 0\,\mathrm{N/m}^3$): the first L-R-C mode (top left), the second L-R-C mode (top right), and the third L-R-C mode (bottom).

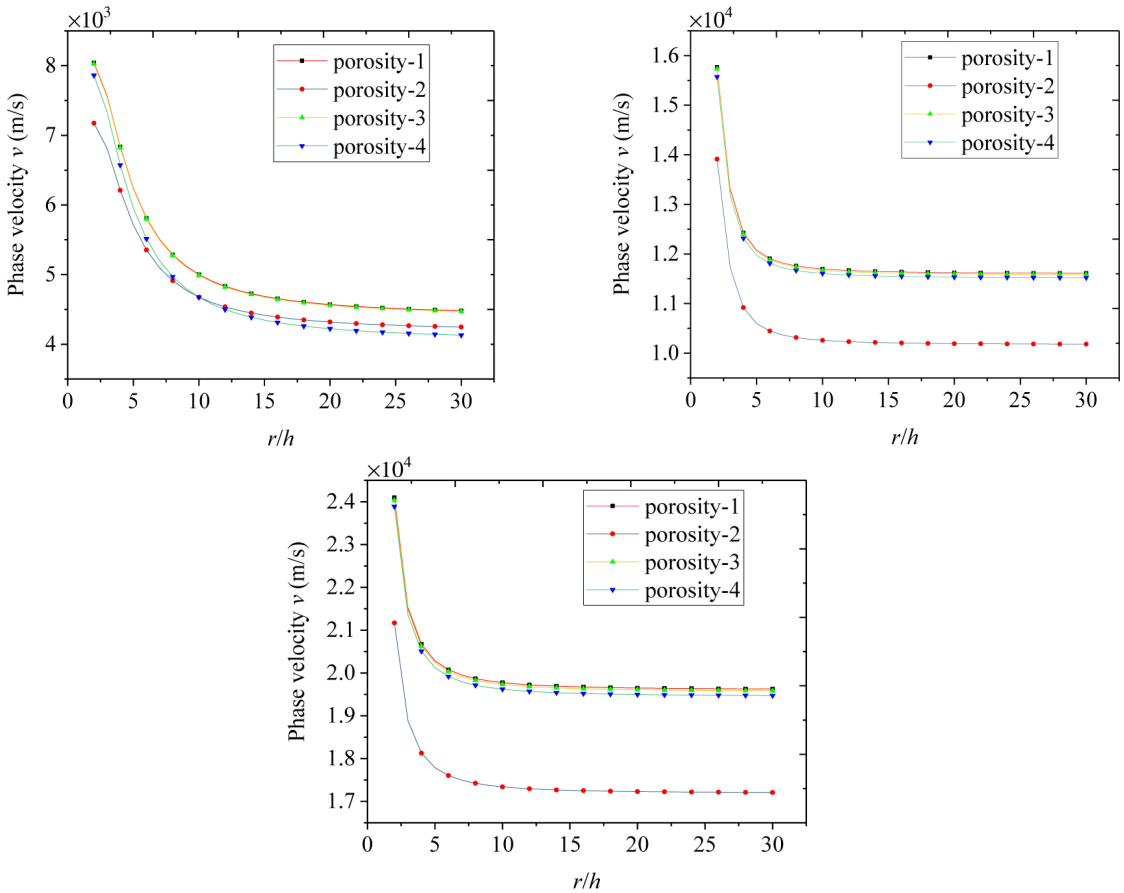

Figure 12. Phase velocity versus radius-to-thickness ratio r/h of 3D-GA shell ($e_1 = 0.5$, $n = 1$, $k = 8\,\mathrm{m}^{-1}$, $N_p = 0\,\mathrm{N}$, $k_w = 0\,\mathrm{N/m^3}$, $k_p = 0\,\mathrm{N/m}$): the first L-R-C mode (top left), the second L-R-C mode (top right), and the third L-R-C mode (bottom).

Appendix A

$$A_{11} = \int_{-h/2}^{h/2} \frac{E(z)}{1-\mu^2}\,\mathrm{d}z \qquad A_{12} = \int_{-h/2}^{h/2} \frac{E(z)}{1-\mu^2} z\,\mathrm{d}z \qquad A_{13} = \int_{-h/2}^{h/2} \frac{\mu E(z)}{1-\mu^2}\,\mathrm{d}z \qquad A_{14} = \int_{-h/2}^{h/2} \frac{\mu E(z)}{1-\mu^2} z\,\mathrm{d}z$$

$$B_{11} = \int_{-h/2}^{h/2} G(z)\,\mathrm{d}z \qquad B_{12} = \int_{-h/2}^{h/2} G(z) z\,\mathrm{d}z \qquad C_{11} = A_{12} \qquad C_{12} = \int_{-h/2}^{h/2} \frac{E(z)}{1-\mu^2} z^2\,\mathrm{d}z$$

$$C_{13} = A_{14} \qquad C_{14} = \int_{-h/2}^{h/2} \frac{\mu E(z)}{1-\mu^2} z^2\,\mathrm{d}z \qquad D_{11} = B_{12} \qquad D_{12} = \int_{-h/2}^{h/2} G(z) z^2\,\mathrm{d}z$$

Appendix B

$$L_{11} = A_{11}k^2r^2 + B_{11}n^2 \qquad L_{12} = (A_{13} + B_{11})\,knr \qquad L_{13} = -\mathrm{i}A_{13}kr$$

$$L_{14} = A_{12}k^2r^2 + B_{12}n^2 \qquad L_{15} = (A_{14} + B_{12})\,knr \qquad L_{21} = (A_{13} + B_{11})\,knr$$

$$L_{22} = A_{11}n^2 + B_{11}k^2r^2 + \kappa_s B_{11} \qquad L_{23} = -\mathrm{i}n(A_{11} + \kappa_s B_{11}) \qquad L_{24} = (A_{14} + B_{12})\,knr$$
$$L_{25} = A_{12}n^2 - \kappa_s B_{11}r + B_{12}k^2r^2 \qquad L_{31} = \mathrm{i}A_{13}\,kr \qquad L_{32} = \mathrm{i}n(A_{11} + \kappa_s B_{11})$$
$$L_{33} = A_{11} + \kappa_s B_{11}(n^2 + k^2r^2) + N_{px}k^2r^2 + N_{p\theta}n^2 + k_w r^2 + k_p(n^2 + k^2r^2)$$
$$L_{34} = \mathrm{i}(A_{14} - \kappa_s B_{11}r)\,kr \qquad L_{35} = \mathrm{i}n(A_{12} - \kappa_s B_{11}r) \qquad L_{41} = C_{11}k^2r^2 + D_{11}n^2$$
$$L_{42} = (C_{13} + D_{11})\,knr \qquad L_{43} = \mathrm{i}(\kappa_s B_{11}r - C_{13})\,kr \qquad L_{44} = \kappa_s B_{11}r^2 + C_{12}k^2r^2 + D_{12}n^2$$
$$L_{45} = (C_{14} + D_{12})\,knr \qquad L_{51} = (C_{13} + D_{11})\,knr \qquad L_{52} = -\kappa_s B_{11}r + C_{11}n^2 + D_{11}k^2r^2$$
$$L_{53} = \mathrm{i}n(\kappa_s B_{11}r - C_{11}) \qquad L_{54} = (C_{14} + D_{12})\,knr \qquad L_{55} = \kappa_s B_{11}r^2 + C_{12}n^2 + D_{12}k^2r^2$$

$$H_{11} = I_1r^2 \quad H_{14} = I_2r^2 \quad H_{12} = H_{13} = H_{15} = 0 \qquad H_{21} = H_{23} = H_{24} = 0$$
$$H_{22} = I_1r^2 \quad H_{25} = I_2r^2 \quad H_{31} = H_{32} = H_{34} = H_{35} = 0 \quad H_{33} = I_1r^2$$
$$H_{41} = I_2r^2 \quad H_{44} = I_3r^2 \quad H_{42} = H_{43} = H_{45} = 0 \qquad H_{51} = H_{53} = H_{54} = 0$$
$$H_{52} = I_2r^2 \quad H_{55} = I_3r^2$$

Acknowledgements

This research was supported by the National Natural Science Foundation of China (Grant nos. 11922205 and 11672071), LiaoNing Revitalization Talents Program (Grant no. XLYC1807026), and the Fundamental Research Funds for the Central Universities (Grant no. N2005019).

References

[Aifantis 2016] E. C. Aifantis, "Internal length gradient (ILG) material mechanics across scales and disciplines", pp. 1–110 in *Advances in applied mechanics*, 1st ed., vol. 49, Elsevier, 2016.

[Aminipour et al. 2018] H. Aminipour, M. Janghorban, and L. Li, "A new model for wave propagation in functionally graded anisotropic doubly-curved shells", *Compos. Struct.* **190** (2018), 91–111.

[Askes and Aifantis 2009] H. Askes and E. C. Aifantis, "Gradient elasticity and flexural wave dispersion in carbon nanotubes", *Phys. Rev. B* **80**:19 (2009), 195412.

[Bi et al. 2012] H. Bi et al., "Spongy graphene as a highly efficient and recyclable sorbent for oils and organic solvents", *Adv. Funct. Mater.* **22**:21 (2012), 4421–4425.

[Chatterjee et al. 2012] S. Chatterjee et al., "Mechanical reinforcement and thermal conductivity in expanded graphene nanoplatelets reinforced epoxy composites", *Chem. Phys. Lett.* **531** (2012), 6–10.

[Chen et al. 2011] Z. Chen et al., "Three-dimensional flexible and conductive interconnected graphene networks grown by chemical vapour deposition", *Nat. Mater.* **10**:6 (2011), 424–428.

[Chen et al. 2014] S. Chen et al., "Hierarchical 3D mesoporous silicon@graphene nanoarchitectures for lithium ion batteries with superior performance", *Nano Res.* **7**:1 (2014), 85–94.

[Chen et al. 2015] D. Chen, J. Yang, and S. Kitipornchai, "Elastic buckling and static bending of shear deformable functionally graded porous beam", *Compos. Struct.* **133** (2015), 54–61.

[Dai and Wang 2005] H. L. Dai and X. Wang, "Stress wave propagation in laminated piezoelectric spherical shells under thermal shock and electric excitation", *Struct. Eng. Mech.* **24**:2 (2005), 263–276.

[Geim 2009] A. K. Geim, "Graphene: status and prospects", *Science* **324**:5934 (2009), 1530–1534.

[Geim and Novoselov 2009] A. K. Geim and K. S. Novoselov, "The rise of graphene", pp. 11–19 in *Nanoscience and technology: a collection of reviews from Nature journals*, 2009.

[Hu et al. 2008] Y.-G. Hu et al., "Nonlocal shell model for elastic wave propagation in single- and double-walled carbon nanotubes", *J. Mech. Phys. Solids* **56**:12 (2008), 3475–3485.

[Huang et al. 2012] X. Huang et al., "Functional nanoporous graphene foams with controlled pore sizes", *Adv. Mater.* **24**:32 (2012), 4419–4423.

[Jabbari et al. 2014] M. Jabbari, A. Mojahedin, A. R. Khorshidvand, and M. R. Eslami, "Buckling analysis of a functionally graded thin circular plate made of saturated porous materials", *J. Eng. Mech.* (*ASCE*) **140**:2 (2014), 287–295.

[Jiang and Fan 2014] L. Jiang and Z. Fan, "Design of advanced porous graphene materials: from graphene nanomesh to 3D architectures", *Nanoscale* **6**:4 (2014), 1922–1945.

[Kuang et al. 2013] J. Kuang et al., "A hierarchically structured graphene foam and its potential as a large-scale strain-gauge sensor", *Nanoscale* **5**:24 (2013), 12171.

[Lee et al. 2008] C. Lee, X. Wei, J. W. Kysar, and J. Hone, "Measurement of the elastic properties and intrinsic strength of monolayer graphene", *Science* **321**:5887 (2008), 385–388.

[Li et al. 2013] N. Li et al., "Three-dimensional graphene foam as a biocompatible and conductive scaffold for neural stem cells", *Sci. Rep.* **3** (2013), 1604.

[Li et al. 2014] Y. Li et al., "Highly compressible macroporous graphene monoliths via an improved hydrothermal process", *Adv. Mater.* **26**:28 (2014), 4789–4793.

[Liew and Wang 2007] K. M. Liew and Q. Wang, "Analysis of wave propagation in carbon nanotubes via elastic shell theories", *Int. J. Eng. Sci.* **45**:2-8 (2007), 227–241.

[Liu et al. 2011] C.-C. Liu, F.-M. Li, and W.-H. Huang, "Transient wave propagation and early short time transient responses of laminated composite cylindrical shells", *Compos. Struct.* **93**:10 (2011), 2587–2597.

[Lurie et al. 2018] S. A. Lurie et al., "Modeling the effective mechanical properties of "fuzzy fiber" composites across scales length", *Compos. B Eng.* **142** (2018), 24–35.

[Ma et al. 2018] L. H. Ma et al., "Wave propagation characteristics in magneto-electro-elastic nanoshells using nonlocal strain gradient theory", *Compos. Struct.* **199** (2018), 10–23.

[Magnucki and Stasiewicz 2004] K. Magnucki and P. Stasiewicz, "Elastic buckling of a porous beam", *J. Theor. Appl. Mech.* (*Warsaw*) **42**:4 (2004), 859–868.

[Novoselov et al. 2004] K. S. Novoselov et al., "Electric field effect in atomically thin carbon films", *Science* **306**:5696 (2004), 666–669.

[Pasternak 1954] P. L. Pasternak, *On a new method of analysis of an elastic foundation by means of two foundation constants*, Gosudarstvennoe Izdatelstvo Literaturi po Stroitelstvu I Arkhitekture, Moscow, 1954. in Russian.

[Qin et al. 2017] Z. Qin, G. S. Jung, M. J. Kang, and M. J. Buehler, "The mechanics and design of a lightweight three-dimensional graphene assembly", *Sci. Adv.* **3**:1 (2017), e160153.

[Qiu et al. 2017] L. Qiu et al., "Extremely low density and super-compressible graphene cellular materials", *Adv. Mater.* **29**:36 (2017), 1701553.

[Reddy 2004] J. N. Reddy, *Mechanics of laminated composite plates and shells: theory and analysis*, CRC press, 2004.

[Sha et al. 2016] J. Sha et al., "Preparation of three-dimensional graphene foams using powder metallurgy templates", *ACS Nano* **10**:1 (2016), 1411–1416.

[Sha et al. 2017] J. Sha et al., "Three-dimensional printed graphene foams", *ACS Nano* **11**:7 (2017), 6860–6867.

[Shakeri et al. 2006] M. Shakeri, M. Akhlaghi, and S. M. Hoseini, "Vibration and radial wave propagation velocity in functionally graded thick hollow cylinder", *Compos. Struct.* **76**:1-2 (2006), 174–181.

[Sorokin and Ershova 2004] S. V. Sorokin and O. A. Ershova, "Plane wave propagation and frequency band gaps in periodic plates and cylindrical shells with and without heavy fluid loading", *J. Sound Vib.* **278**:3 (2004), 501–526.

[Strek et al. 2017] W. Strek et al., "Laser induced white lighting of graphene foam", *Sci. Rep.* **7**:1 (2017), 41281.

[Sun and Aifantis 2014] B. Sun and E. C. Aifantis, "Gradient elasticity formulations for micro/nanoshells", *J. Nanomater.* **2014** (2014), 846370.

[Talebitooti and Choudari Khameneh 2017] R. Talebitooti and A. M. Choudari Khameneh, "Wave propagation across double-walled laminated composite cylindrical shells along with air-gap using three-dimensional theory", *Compos. Struct.* **165** (2017), 44–64.

[Thorp et al. 2005] O. Thorp, M. Ruzzene, and A. Baz, "Attenuation of wave propagation in fluid-loaded shells with periodic shunted piezoelectric rings", *Smart Mater. Struct.* **14**:4 (2005), 594–604.

[Vickery et al. 2009] J. L. Vickery, A. J. Patil, and S. Mann, "Fabrication of graphene-polymer nanocomposites with higher-order three-dimensional architectures", *Adv. Mater.* **21**:21 (2009), 2180–2184.

[Wang 2010] L. Wang, "Wave propagation of fluid-conveying single-walled carbon nanotubes via gradient elasticity theory", *Comput. Mater. Sci.* **49**:4 (2010), 761–766.

[Wang and Varadan 2007] Q. Wang and V. K. Varadan, "Application of nonlocal elastic shell theory in wave propagation analysis of carbon nanotubes", *Smart Mater. Struct.* **16**:1 (2007), 178–190.

[Wang et al. 2012] J. Wang et al., "Reinforcement with graphene nanosheets in aluminum matrix composites", *Scr. Mater.* **66**:8 (2012), 594–597.

[Wang et al. 2019] Y. Q. Wang, C. Ye, and J. W. Zu, "Nonlinear vibration of metal foam cylindrical shells reinforced with graphene platelets", *Aerosp. Sci. Technol.* **85** (2019), 359–370.

[Winkler 1867] E. Winkler, *Die lehre von der elastizität und festigkeit (The theory of elasticity and stiffness)*, H. Dominius, Prague, 1867.

[Wu et al. 2015] Y. Wu et al., "Three-dimensionally bonded spongy graphene material with super compressive elasticity and near-zero Poisson's ratio", *Nat. Commun.* **6**:1 (2015), 6141.

[Xu et al. 2008] K. Y. Xu, E. C. Aifantis, and Y. H. Yan, "Vibrations of double-walled carbon nanotubes with different boundary conditions between inner and outer tubes", *J. Appl. Mech.* (*ASME*) **75**:2 (2008), 021013.

[Xu et al. 2010] Y. Xu, K. Sheng, C. Li, and G. Shi, "Self-assembled graphene hydrogel *via* a one-step hydrothermal process", *ACS Nano* **4**:7 (2010), 4324–4330.

[Xu et al. 2014] K. Y. Xu et al., "Free transverse vibrations of a double-walled carbon nanotube: gradient and internal inertia effects", *Acta Mech. Solida Sin.* **27**:4 (2014), 345–352.

[Xu et al. 2016] X. Xu et al., "Naturally dried graphene aerogels with superelasticity and tunable Poisson's ratio", *Adv. Mater.* **28**:41 (2016), 9223–9230.

[Yang et al. 2018] J. Yang, D. Chen, and S. Kitipornchai, "Buckling and free vibration analyses of functionally graded graphene reinforced porous nanocomposite plates based on Chebyshev–Ritz method", *Compos. Struct.* **193** (February 2018), 281–294.

[Zeighampour and Beni 2017] H. Zeighampour and Y. T. Beni, "Size dependent analysis of wave propagation in functionally graded composite cylindrical microshell reinforced by carbon nanotube", *Compos. Struct.* **179** (2017), 124–131.

[Zeighampour et al. 2017] H. Zeighampour, Y. T. Beni, and I. Karimipour, "Wave propagation in double-walled carbon nanotube conveying fluid considering slip boundary condition and shell model based on nonlocal strain gradient theory", *Microfluid. Nanofluid.* **21**:5 (2017), 85.

[Zeighampour et al. 2018] H. Zeighampour, Y. Tadi Beni, and M. Botshekanan Dehkordi, "Wave propagation in viscoelastic thin cylindrical nanoshell resting on a visco-Pasternak foundation based on nonlocal strain gradient theory", *Thin-Walled Struct.* **122** (2018), 378–386.

[Zhen 2017] Y. X. Zhen, "Wave propagation in fluid-conveying viscoelastic single-walled carbon nanotubes with surface and nonlocal effects", *Physica E* **86** (2017), 275–279.

Received 24 Jun 2019. Revised 14 May 2020. Accepted 30 May 2020.

CHEN LIANG: neuliangchen@gmail.com
Department of Mechanics, Northeastern University, Shenyang 110819, China

YAN QING WANG: wangyanqing@mail.neu.edu.cn
Department of Mechanics, Northeastern University, Shenyang 110819, China

and

Key Laboratory of Ministry of Education on Safe Mining of Deep Metal Mines, Northeastern University, Shenyang 110819, China

JOURNAL OF MECHANICS OF MATERIALS AND STRUCTURES
Vol. 15, No. 4, 2020
https://doi.org/10.2140/jomms.2020.15.457

SEMIINFINITE MOVING CRACK IN A SHEAR-FREE ORTHOTROPIC STRIP

SANATAN JANA, PRASANTA BASAK AND SUBHAS MANDAL

We have considered a semiinfinite crack moving with constant velocity in an orthotropic strip with shear-free boundaries. The crack is propagating subjected to constant normal displacements applied at the boundaries of the strip. The Fourier transformation is applied to convert the boundary value problem into the standard Wiener–Hopf equation. This equation has been solved to find out the analytical expressions for the stress intensity factor and crack-opening displacement. The graphs of stress intensity factor and crack-opening displacement have been plotted against various parameters such as crack velocity, strip width etc. to show the effects of these parameters and material orthotropy on stress intensity factor and crack-opening displacement.

1. Introduction

In recent times the study of the nature of elastic waves in the presence of cracks has gained momentum in many engineering applications like designing metal and polymer-forming processes, machining, etc. These types of research problems have great importance and versatility in potential applications in the fields of seismology and geophysics. The analytical study of cracks and inclusion is very important in civil, aerospace, nuclear and mechanical engineering, especially in civil and mechanical engineering where designing of load-bearing components of vehicles, power generation, reduction of cracks are important and challenging issues. The foremost motive in civil structure is to elude the progress of a crack initiated originally. Researchers found that the stress has a square root singularity at the tip of the crack. A nondimensional quantity called the stress intensity factor has been calculated to show the nature of stress at the tip of the crack. Many researchers did their work in this field to find the stress intensity factor and other expressions related to fracture. Initially researchers considered the problems involving static cracks only.

The moving Griffith crack model was introduced in [Yoffe 1951]. She considered that the crack propagates with a constant speed and without a change in length along the crack propagation axis. Knauss [1966] studied the problem of stresses in an infinitely long isotropic strip of finite width containing a straight semiinfinite crack for the case of displaced clamped boundaries normal to the crack. He applied the Wiener–Hopf technique to find the stress intensity factor and stresses. The correction to this work was made in [Rice 1967]. Nilsson [1972; 1973] explored a method to find the analytical expression for the stress intensity factor by the Wiener–Hopf technique. The same technique was later used in [Atkinson and Popelar 1979; Kousiounelos and Williams Jr. 1982; Georgiadis 1986]. Georgiadis and Papadopoulos [1987] analyzed the steady state solution for the stress intensity factor in a cracked plane orthotropic strip by the Wiener–Hopf technique. De and Patra [1990] considered the problem of a moving Griffith crack

Keywords: semiinfinite crack, orthotropic strip, Wiener–Hopf equation, Rayleigh wave velocity, stress intensity factor, crack-opening displacement.

in a stressed orthotropic strip. The problem of four coplanar Griffith cracks moving in an infinitely long elastic strip under antiplane shear stress was solved in [Sarkar et al. 1996]. Lee [2000] obtained stress and displacement fields for the propagating crack along the interface of dissimilar orthotropic materials under dynamic mode I and mode II load. Wang et al. [2001] analyzed the problem of the dynamic stress intensity factor for a semiinfinite crack in orthotropic materials with concentrated shear impact loads. They found out the dynamic stress intensity factor by the Wiener–Hopf technique for orthotropic as well as isotropic media. The problem of the stress intensity factor around a moving Griffith crack in an infinite elastic layer between two elastic half-planes was studied in [Itou 2004]. Ma et al. [2005] considered the problem of the moving Griffith crack in the functionally graded orthotropic strip under plane loading. Bagheri et al. [2015] investigated the analytical solution of multiple moving cracks in functionally graded piezoelectric strip. Nourazar and Ayatollahi [2016] studied the problem of multiple moving interfacial cracks between two dissimilar piezoelectric layers under electromechanical loading.

This paper is a generalization of investigations done in [Nilsson 1972; 1973; Georgiadis and Papadopoulos 1987]. Nilsson obtained the expression for the stress intensity factor for an isotropic strip weakened by a semiinfinite moving crack. He considered both shear-free and clamped strip boundaries. Later, Georgiadis and Papadopoulos investigated the problems of an orthotropic strip weakened by a semiinfinite static crack. They first (1987) considered the problem where shear-free boundaries were considered and later (1988) they solved another problem where clamped boundaries were considered. The dynamical problem of the work of Georgiadis and Papadopoulos [1988] had been done in [Basak and Mandal 2017]. We have considered the dynamical problem of the work done in [Georgiadis and Papadopoulos 1987]. Here we have considered an orthotropic strip which contains a semiinfinite crack moving along the mid-plane of the strip with constant velocity. The crack surfaces and the strip boundaries have been assumed traction-free. The crack is subjected to constant normal displacements applied at the boundaries of the strip. In order to reduce the boundary value problem to the standard Wiener–Hopf equation, we have applied the Fourier transform technique. One can solve the Wiener–Hopf equation to obtain the necessary expression for the stresses and the displacements. Due to mathematical complexities, the explicit solution of the Wiener–Hopf equation has not been found; instead, asymptotic expressions for the stresses and displacements have been obtained for limited cases only. However, this asymptotic solution is sufficient to obtain the analytical expressions for the stress intensity factor and crack-opening displacement, which are the quantities of physical interest. One thing here to note that many of the earlier problems involving the Wiener–Hopf technique solved by many authors, did not follow the correct analysis of the method as pointed in [Nilsson 1973]. We have applied the analysis of the Wiener–Hopf method as revised and corrected in [Nilsson 1973]. Finally, the deductions of the solution have been made for isotropic and statical cases to compare and ensure the accuracy of the solution.

2. Formulation of the problem

Let us consider the problem of interaction of a semiinfinite crack situated at the interior of an orthotropic strip of width $2h$ moving along the plane with constant velocity c. The crack is propagating due to the actions of the constant normal displacements applied at the boundaries of the strip. Let X, Y, Z be the fixed cartesian coordinates which are the axes of symmetry of the orthotropic material. The strip is defined by $-\infty < X < \infty,\ -h < Y < h,\ -\infty < Z < \infty$. At any time t, position of the crack is assumed

as $-\infty < X \le ct,\ Y = 0$, which is propagating along the positive X-axis with a constant velocity c. Due to symmetry we shall consider the two dimensional (X, Y) problem.

The nonvanishing displacements $U(X, Y, t)$ and $V(X, Y, t)$ along the X- and Y-axes satisfy the following Navier's equations:

$$C_{11}\frac{\partial^2 U}{\partial X^2} + C_{66}\frac{\partial^2 U}{\partial Y^2} + (C_{12} + C_{66})\frac{\partial^2 V}{\partial X\,\partial Y} = \rho\frac{\partial^2 U}{\partial t^2}, \tag{1}$$

$$C_{66}\frac{\partial^2 V}{\partial X^2} + C_{22}\frac{\partial^2 V}{\partial Y^2} + (C_{12} + C_{66})\frac{\partial^2 U}{\partial X\,\partial Y} = \rho\frac{\partial^2 V}{\partial t^2}, \tag{2}$$

where C_{66} is the shear modulus, ρ is the material density and C_{11}, C_{22}, C_{12} are material constants related to orthotropic elastic constants by

$$C_{11} = E_1/\left(1 - (E_2/E_1)\,\nu_{12}^2\right), \quad C_{22} = (E_2/E_1)\,C_{11}, \quad C_{12} = \nu_{12}C_{22} = \nu_{21}C_{11}$$

for generalized plane stress problems. Moreover E_1, E_2 are Young's Moduli and ν_{12}, ν_{21} are Poisson's ratios of the medium.

To make the crack stationary, the Galilean transformation $x = X - ct,\ y = Y,\ t = t$ is introduced so that the above displacement equations (1) and (2) reduce to

$$(C_{11} - \rho c^2)\frac{\partial^2 u}{\partial x^2} + C_{66}\frac{\partial^2 u}{\partial y^2} + (C_{12} + C_{66})\frac{\partial^2 v}{\partial x\,\partial y} = 0, \tag{3}$$

$$(C_{66} - \rho c^2)\frac{\partial^2 v}{\partial x^2} + C_{22}\frac{\partial^2 v}{\partial y^2} + (C_{12} + C_{66})\frac{\partial^2 u}{\partial x\,\partial y} = 0, \tag{4}$$

where $u(x, y) = U(X, Y, t)$ and $v(x, y) = V(X, Y, t)$ are the displacements in the moving coordinate system.

The required stresses can be obtained from the well-known relations

$$\tau_{xx} = C_{11}\frac{\partial u}{\partial x} + C_{12}\frac{\partial v}{\partial y}, \tag{5}$$

$$\tau_{yy} = C_{12}\frac{\partial u}{\partial x} + C_{22}\frac{\partial v}{\partial y}, \tag{6}$$

$$\tau_{xy} = C_{66}\left(\frac{\partial u}{\partial y} + \frac{\partial v}{\partial x}\right). \tag{7}$$

The crack surfaces are assumed to be traction-free, so we consider the following boundary conditions (see Figure 1):

$$\tau_{yy}(x, 0) = 0, \qquad x < 0, \tag{8}$$

$$\tau_{xy}(x, 0) = 0, \qquad -\infty < x < \infty, \tag{9}$$

$$v(x, 0) = 0, \qquad x > 0, \tag{10}$$

$$\tau_{xy}(x, \pm h) = 0, \qquad -\infty < x < \infty, \tag{11}$$

$$v(x, \pm h) = \pm v_0, \qquad -\infty < x < \infty, \tag{12}$$

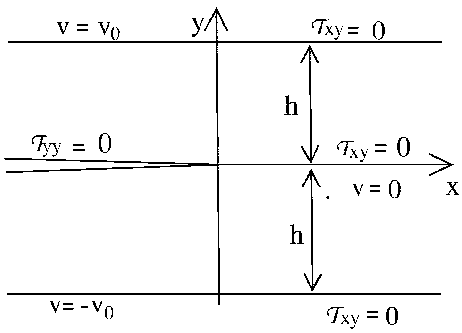

Figure 1. Geometry of the original problem.

where v_0 is a known constant.

We wish to solve the problem by using the Wiener–Hopf technique, but the above boundary conditions are not eligible for applying that technique. It can be shown that [Georgiadis and Papadopoulos 1987] the above set of boundary conditions can be converted to a more suitable form (see Figure 2):

$$\tau_{yy}(x, 0) = \tau_0 \qquad x < 0, \tag{13}$$

$$v(x, 0) = 0, \qquad x > 0, \tag{14}$$

$$\tau_{xy}(x, 0) = 0, \quad -\infty < x < \infty, \tag{15}$$

$$\tau_{xy}(x, \pm h) = 0, \quad -\infty < x < \infty, \tag{16}$$

$$v(x, \pm h) = 0, \quad -\infty < x < \infty \tag{17}$$

by introducing a constant homogeneous load $\tau_{yy} = \tau_0$ in the system. Although the selection of the constant load τ_0 is not arbitrary, it satisfies the relation $\tau_0 = -(C_{22}/h)v_0$ for the given problem.

Now we slightly change the boundary condition (13) as discussed in [Nilsson 1973] introducing a slightly variable load

$$\tau_{yy}(x, 0) = \tau_0 e^{\epsilon x}, \quad x < 0, \tag{13$'$}$$

where ϵ is a very small positive quantity which can be assumed as tending to zero. Since the problem is symmetric with respect to the x-axis, it is sufficient to consider the half-strip $0 \le y \le h$ only.

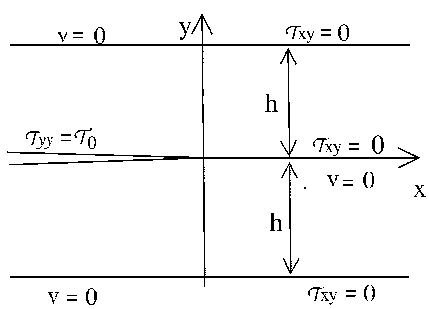

Figure 2. Geometry of the transformed problem.

The well-known Fourier transform is defined by

$$\bar{f}(\omega,\ y) = \frac{1}{\sqrt{2\pi}} \int_{-\infty}^{\infty} f(x, y)\, e^{i\omega x}\, dx \tag{18}$$

with the inverse

$$f(x, y) = \frac{1}{\sqrt{2\pi}} \int_{-\infty}^{\infty} \bar{f}(\omega, y)\, e^{-i\omega x}\, d\omega, \tag{19}$$

where $\omega = \sigma + i\tau$ is the complex variable in the Fourier transform plane.

Now introducing the Fourier transform on (3) and (4), the solutions can be assumed as

$$\bar{u}(\omega, y) = P(\omega)\, e^{\gamma_1 \omega y} + Q(\omega)\, e^{-\gamma_1 \omega y} + R(\omega)\, e^{\gamma_2 \omega y} + S(\omega)\, e^{-\gamma_2 \omega y}, \tag{20}$$

$$\bar{v}(\omega, y) = i[\alpha_1 P(\omega)\, e^{\gamma_1 \omega y} - \alpha_1 Q(\omega)\, e^{-\gamma_1 \omega y} + \alpha_2 R(\omega)\, e^{\gamma_2 \omega y} - \alpha_2 S(\omega)\, e^{-\gamma_2 \omega y}], \tag{21}$$

where $\bar{u}(\omega, y)$ and $\bar{v}(\omega, y)$ are Fourier transforms of $u(x, y)$ and $v(x, y)$, respectively; $\alpha_j,\ (j = 1, 2)$ are given by

$$\alpha_j = \frac{C_{11} - \rho c^2 - C_{66}\, \gamma_j^2}{(C_{12} + C_{66})\, \gamma_j}, \quad j = 1, 2, \tag{22}$$

where $i = \sqrt{-1}$ and γ_1^2, γ_2^2 are the positive roots of the equation

$$C_{22}\, C_{66}\, \gamma^4 + \{C_{12}^2 + 2C_{12}\, C_{66} - C_{11} C_{22} + (C_{66} + C_{22})\, \rho c^2\}\, \gamma^2 + (C_{11} - \rho c^2)(C_{66} - \rho c^2) = 0. \tag{23}$$

Moreover, $P(\omega)$, $Q(\omega)$, $R(\omega)$ and $S(\omega)$ are unknown functions of ω.

The expressions for the stresses can be obtained as

$$\frac{1}{C_{66}} \bar{\tau}_{xy}(\omega, y) = \omega(\gamma_1 + \alpha_1)\left(e^{\gamma_1 \omega y} P(\omega) - e^{-\gamma_1 \omega y} Q(\omega)\right) + \omega(\gamma_2 + \alpha_2)\left(e^{\gamma_2 \omega y} R(\omega) - e^{-\gamma_2 \omega y} S(\omega)\right), \tag{24}$$

$$\begin{aligned} \bar{\tau}_{yy}(\omega, y) = {} & i\omega(C_{22}\, \alpha_1 \gamma_1 - C_{12})\left(e^{\gamma_1 \omega y} P(\omega) + e^{-\gamma_1 \omega y} Q(\omega)\right) \\ & + i\omega(C_{22}\, \alpha_2 \gamma_2 - C_{12})\left(e^{\gamma_2 \omega y} R(\omega) + e^{-\gamma_2 \omega y} S(\omega)\right), \end{aligned} \tag{25}$$

where $\bar{\tau}_{xy}(\omega, y)$ and $\bar{\tau}_{yy}(\omega, y)$ are the Fourier transforms of $\tau_{xy}(x, y)$ and $\tau_{yy}(x, y)$.

3. Method of solution

The normal stress $\tau_{yy}(x, 0)$ and displacement $v(x, 0)$ are unknown for $x > 0$ and $x < 0$. Hence we consider

$$\tau_{yy}(x, 0) = f(x), \quad x > 0, \tag{26}$$

$$v(x, 0) = g(x), \quad x < 0. \tag{27}$$

The objective of the method is to obtain the expression of the stress $f(x)$ at the tip of the crack. We define half-range Fourier transforms of the above functions as

$$\bar{f}_+(\omega) = \frac{1}{\sqrt{2\pi}} \int_0^\infty f(x)\, e^{i\omega x}\, dx, \tag{28}$$

$$\bar{g}_-(\omega) = \frac{1}{\sqrt{2\pi}} \int_{-\infty}^0 g(x)\, e^{i\omega x}\, dx, \tag{29}$$

where the existence of the above transforms are still unclear but can be proved by the following assumptions that the stresses and displacements are bounded at the infinity, so the functions $f(x)$ and $g(x)$ should be bounded there. Therefore, without any loss of generality we may assume that

$$|f(x)| < Fx^{-l_f}, \qquad \text{as } x \to \infty, \tag{30}$$

$$|g(x)| < G|x|^{-l_g}, \quad \text{as } x \to -\infty \tag{31}$$

for some $l_f > 0$, $l_g > 0$ with F and G being finite positive numbers. The conditions (30) and (31) ensure the existence of the transforms (28) and (29); in fact the functions $\bar{f}_+(\omega)$ and $\bar{g}_-(\omega)$ are now analytic for $\tau \geq 0$ and $\tau \leq 0$.

Introducing Fourier transforms on the boundary conditions (15), (16) and (17) with the help of (21) and (24), the unknown functions $Q(\omega)$, $R(\omega)$ and $S(\omega)$ can be expressed in terms of $P(\omega)$ as

$$Q(\omega) = \frac{\Delta_1}{\Delta} P(\omega), \quad R(\omega) = \frac{\Delta_2}{\Delta} P(\omega), \quad S(\omega) = \frac{\Delta_3}{\Delta} P(\omega), \tag{32}$$

where

$$\Delta_1 = 2(\gamma_2 + \alpha_2)\, e^{\gamma_1 \omega h} \sinh(\gamma_2 \omega h)(\alpha_2\gamma_1 - \alpha_1\gamma_2), \tag{33}$$

$$\Delta_2 = 2(\gamma_1 + \alpha_1)\, e^{-\gamma_2 \omega h} \sinh(\gamma_1 \omega h)(\alpha_1\gamma_2 - \alpha_2\gamma_1), \tag{34}$$

$$\Delta_3 = 2(\gamma_1 + \alpha_1)\, e^{\gamma_2 \omega h} \sinh(\gamma_1 \omega h)(\alpha_1\gamma_2 - \alpha_2\gamma_1), \tag{35}$$

$$\Delta = 2(\gamma_2 + \alpha_2)\, e^{-\gamma_1 \omega h} \sinh(\gamma_2 \omega h)(\alpha_2\gamma_1 - \alpha_1\gamma_2). \tag{36}$$

Next, using the conditions (13′), (14) with the help of (28), (29) we get a pair of equations involving $\bar{f}_+(\omega)$ and $\bar{g}_-(\omega)$ as

$$\bar{\tau}_{yy}(\omega, 0) = \bar{f}_+(\omega) + \frac{\tau_0}{\sqrt{2\pi}(\epsilon + i\omega)}, \tag{37}$$

$$\bar{v}(\omega, 0) = \bar{g}_-(\omega). \tag{38}$$

Replacing the values of the stress and displacement from (21), (25) and after some manipulation using (32)–(36) we get the following equation of two unknown functions:

$$\bar{f}_+(\omega) = K(\omega)\, \bar{g}_-(\omega) - \frac{\tau_0}{\sqrt{2\pi}(\epsilon + i\omega)}, \tag{39}$$

where the kernel $K(\omega)$ is given by

$$K(\omega) = \omega K_1(\omega)/K_2(\omega), \tag{40}$$

with

$$K_1(\omega) = (C_{22}\,\alpha_1\,\gamma_1 - C_{12})(1 + e^{2\gamma_1\omega h})\,\Delta + (C_{22}\,\alpha_2\,\gamma_2 - C_{12})(1 + e^{2\gamma_2\omega h})\,\Delta_2, \tag{41}$$

$$K_2(\omega) = (\alpha_1 - \alpha_1\,e^{2\gamma_1\omega h})\,\Delta + (\alpha_2 - \alpha_2\,e^{2\gamma_2\omega h})\,\Delta_2. \tag{42}$$

Equation (39) is the standard Wiener–Hopf equation with the kernel given by (40).

The first and most important step of the Wiener–Hopf technique is the factorization of the kernel $K(\omega)$ in the following form:

$$K(\omega) = K_+(\omega)\,K_-(\omega) \tag{43}$$

such that the function $K_+(\omega)$ is analytic and nonzero in some upper half plane $\tau > \tau_1$ $(\tau_1 < 0)$ and $K_-(\omega)$ is analytic and nonzero in some lower half plane $\tau < \tau_2$ $(\tau_2 > 0)$.

Once the factorization (43) is done, (39) can be written as

$$\frac{\bar{f}_+(\omega)}{K_+(\omega)} = K_-(\omega)\,\bar{g}_-(\omega) - \frac{\tau_0}{\sqrt{2\pi}\,(\epsilon + i\omega)\,K_+(\omega)}. \tag{44}$$

The next task is the decomposition of the last part of (44) as

$$\frac{\tau_0}{\sqrt{2\pi}\,(\epsilon + i\omega)\,K_+(\omega)} = L(\omega) = L_+(\omega) + L_-(\omega), \tag{45}$$

where

$$L_+(\omega) = \frac{\tau_0}{\sqrt{2\pi}\,(\epsilon + i\omega)}\left[\frac{1}{K_+(\omega)} - \frac{1}{K_+(i\epsilon)}\right], \tag{46}$$

$$L_-(\omega) = \frac{\tau_0}{\sqrt{2\pi}\,(\epsilon + i\omega)\,K_+(i\epsilon)}. \tag{47}$$

It can be shown [Noble 1958] that $L_+(\omega)$ and $L_-(\omega)$ are analytic and nonzero in the regions $\tau > \tau_1$ and $\tau < \epsilon$.

Now utilizing (45), equation (44) can be written as

$$\frac{\bar{f}_+(\omega)}{K_+(\omega)} + L_+(\omega) = K_-(\omega)\,\bar{g}_-(\omega) - L_-(\omega), \tag{48}$$

It may be noted that the regions of analyticity of the functions $\bar{f}_+(\omega)$, $\bar{g}_-(\omega)$, $K_+(\omega)$, $K_-(\omega)$, $L_+(\omega)$ and $L_-(\omega)$ are $\tau \geq 0$, $\tau \leq 0$, $\tau > \tau_1(\tau_1 < 0)$, $\tau < \tau_2(\tau_2 > 0)$, $\tau > \tau_1(\tau_1 < 0)$ and $\tau < \epsilon$, respectively. Therefore, the left-hand side of (48) is analytic in the upper half plane $\tau \geq 0$ and the right-hand side is analytic in the lower half plane $\tau \leq 0$ for any arbitrary small positive values of ϵ. Since the regions of analyticity overlap and the line $\tau = 0$ is the common line of analyticity, hence by a well-known theorem on the analytic continuation the whole equation (48) is analytic and single valued throughout the complex ω-plane. We may now assume that both sides of (48) is equal to an entire function, say $J(\omega)$.

It may be easily verified that both $K_+(\omega)$ and $K_-(\omega)$ tend to $\omega^{1/2}$ for large ω. Furthermore, $\bar{f}_+(\omega)$ and $\bar{g}_-(\omega)$ are bounded for large ω. Therefore, the left-hand side of (48) and consequently $J(\omega)$ tends to $\omega^{-1/2}$ for large value of ω in the upper half plane $\tau \geq 0$; similarly, the right-hand side of (48) and consequently $J(\omega)$ tends to $\omega^{1/2}$ for large ω in the lower half plane $\tau \leq 0$. Hence, by the extended Liouville theorem it can be concluded that $J(\omega)$ is a constant, more specifically zero.

Therefore, from (46)–(48) we find

$$\bar{f}_+(\omega) = \frac{\tau_0}{\sqrt{2\pi}(\epsilon + i\omega)}\left[\frac{K_+(\omega)}{K_+(i\epsilon)} - 1\right], \quad \bar{g}_-(\omega) = \frac{\tau_0}{\sqrt{2\pi}(\epsilon + i\omega)}\frac{1}{K_+(i\epsilon)K_-(\omega)}.$$

Now for constant loading we may take $\epsilon \to 0$; consequently the above equations become

$$\bar{f}_+(\omega) = \frac{\tau_0}{\sqrt{2\pi}\, i\omega}\left[\frac{K_+(\omega)}{K_+(0)} - 1\right], \tag{49}$$

$$\bar{g}_-(\omega) = \frac{\tau_0}{\sqrt{2\pi}\, i\omega}\frac{1}{K_+(0)K_-(\omega)}. \tag{50}$$

The main difficulty in the Wiener–Hopf technique is the decomposition of the kernel $K(\omega)$. Due to mathematical complexities, factorization of the kernel $K(\omega)$ is not easy. Nilsson [1972] introduced a technique where behavior of normal stress at the crack-tip can be obtained by only knowing the values of $K(\omega)$ for very large ω and also for very small ω.

It can be easily verified that

$$\lim_{\omega\to\infty}\frac{K(\omega)}{\omega} = \theta, \tag{51}$$

where

$$\theta = \frac{(C_{22}\alpha_2\gamma_2 - C_{12})(\gamma_1 + \alpha_1) - (C_{22}\alpha_1\gamma_1 - C_{12})(\gamma_2 + \alpha_2)}{\alpha_1\gamma_2 - \alpha_2\gamma_1} \tag{52}$$

and

$$\lim_{\omega\to 0} K(\omega) = -\frac{C_{22}}{h} - \frac{C_{12}(\gamma_1^2 - \gamma_2^2 + \alpha_1\gamma_1 - \alpha_2\gamma_2)}{h\gamma_1\gamma_2(\alpha_1\gamma_2 - \alpha_2\gamma_1)} = \theta_0, \text{ say.} \tag{53}$$

Now for very large values of ω, equations (49) and (50) can be written as

$$\lim_{\omega\to\infty}\bar{f}_+(\omega) = \lim_{\omega\to\infty}\frac{\tau_0}{\sqrt{2\pi}\, i K_+(0)\,\omega^{1/2}}\frac{K_+(\omega)}{\omega^{1/2}} - \lim_{\omega\to\infty}\frac{\tau_0}{\sqrt{2\pi}\, i\omega} \tag{54}$$

and

$$\lim_{\omega\to\infty}\bar{g}_-(\omega) = \lim_{\omega\to\infty}\frac{\tau_0}{\sqrt{2\pi}\, i K_+(\omega)\,\omega^{3/2}}\frac{\omega^{1/2}}{K_-(\omega)}, \tag{55}$$

Taking Inverse Fourier transform on (54) and (55) and using asymptotic property with the help of equations (51)–(53) we get

$$\lim_{x\to 0^+} f(x) = -\tau_0\sqrt{\frac{2\theta}{\pi\theta_0}}\, x^{-1/2}, \tag{56}$$

and

$$\lim_{x\to 0^-} g(x) = -\tau_0\sqrt{\frac{1}{\pi\theta\theta_0}}\,(-x)^{1/2}. \tag{57}$$

Equation (56) shows the normal stress τ_{yy} just outside the crack-tip. It is found that the normal stress component τ_{yy} has a square root singularity at the tip of the crack which was expected. Moreover, equation (57) represents the displacement v just inside the crack-tip.

4. Quantities of physical interest

The stress intensity factor (SIF) that denotes the state of stress at the crack-tip is defined as

$$\mathrm{SIF} = \lim_{x\to 0^+} \sqrt{2\pi x}\,\tau_{yy}(x,0) \tag{58}$$

and found to be

$$\mathrm{SIF} = -\tau_0\sqrt{2\theta/\theta_0}, \tag{59}$$

where θ is given by (52). Therefore, the stress intensity factor of the original problem is given by

$$K_I = \sqrt{\frac{2\theta}{\theta_0}}\frac{C_{22}\,v_0}{h}. \tag{60}$$

Another quantity of physical interest is the crack-opening displacement (COD):

$$\mathrm{COD} = v(x,0^+) - v(x,0^-). \tag{61}$$

Since the problem is symmetric with respect to the x-axis, we can write

$$\mathrm{COD} = -2\tau_0\sqrt{\frac{1}{\pi\theta\theta_0}}\,(-x)^{1/2}. \tag{62}$$

Therefore, COD of the original problem normalized with respect to v_0 is

$$\mathrm{COD} = 2\sqrt{\frac{-x}{\pi\theta\theta_0}}\,\frac{C_{22}}{h}. \tag{63}$$

Comparison of results. For isotropic media we write $C_{11} = C_{22} = \lambda + 2\mu$, $C_{12} = \lambda$ and $C_{66} = \mu$, where λ and μ are Lamé constants; so we get

$$\gamma_1^2 = 1 - c^2/c_1^2, \tag{64}$$

$$\gamma_2^2 = 1 - c^2/c_2^2, \tag{65}$$

$$\alpha_1 = \gamma_1^{-1}, \tag{66}$$

$$\alpha_2 = \gamma_2, \tag{67}$$

$$\theta = \frac{\mu\{(1+\gamma_1^2)^2 - 4\gamma_1\gamma_2\}}{\gamma_2(1-\gamma_1^2)}, \tag{68}$$

$$\theta_0 = \frac{\mu}{h}.\frac{(1+\gamma_1^2)^2 - 4\gamma_2^2}{\gamma_2^2(1-\gamma_1^2)}, \tag{69}$$

where $c_1 = \sqrt{\mu/\rho}$ and $c_2 = \sqrt{\lambda+2\mu/\rho}$ are the velocities of shear waves and dilatational waves, respectively. Therefore, using (64)–(69), the expression (59) of the stress intensity factor becomes

$$\mathrm{SIF}_{\mathrm{ISO}} = -\tau_0\sqrt{2h\gamma_2\frac{(1+\gamma_1^2)^2 - 4\gamma_1\gamma_2}{(1+\gamma_1^2)^2 - 4\gamma_2^2}}, \tag{70}$$

which is exactly the expression Nilsson [1972] obtained for isotropic strip.

For statical problem ($c = 0$) the expression for the stress intensity factor after some algebraic manipulation has been obtained as

$$K_I^{\text{stat}} = C_{22}\, v_0 \sqrt{\frac{2\bar{\gamma}_1\bar{\gamma}_2}{(\bar{\gamma}_1+\bar{\gamma}_2)h}}, \tag{71}$$

where $\bar{\gamma}_1^2$, $\bar{\gamma}_2^2$ are positive roots of the equation

$$C_{22}C_{66}\,\gamma^4 + (C_{12}^2 + 2C_{12}C_{66} - C_{11}C_{22})\,\gamma^2 + C_{11}C_{66} = 0. \tag{72}$$

Georgiadis and Papadopoulos [1987] obtained the same expression as that of (71) for statical problem of semiinfinite crack at the interior of orthotropic strip.

The above two results show the correctness of the solution of our problem.

5. Numerical results and discussions

In elasticity, two well-known wave velocities — velocities of shear waves and dilatational waves — are given by

$$c_1 = c_s = \sqrt{\mu_{12}/\rho} \quad \text{and} \quad c_2 = c_L = \sqrt{C_{11}/\rho}. \tag{73}$$

Moreover, the velocity of the Rayleigh surface waves is denoted by c_R. It is known that the value of c_R is slightly less than that of the shear waves. Also, Rayleigh surface wave velocity is the theoretical upper limit [Broberg 1999] of the crack propagation velocity, although practically the maximum crack propagation velocity is much less than the Rayleigh surface wave velocity. Hence, in this problem we assume that velocity of the crack $c < c_R < \min\{c_1, c_2\}$.

From the expressions of the stress intensity factor (SIF) and crack-opening displacement (COD) the numerical values of the SIF and COD have been plotted against various parameters. Material constants (in GPa) and densities (in g/cm^3) of some orthotropic materials are given [Rubio-Gonzalez and Lira-Vergara 2011] in Table 1.

The values of the stress intensity factor (SIF) normalized with respect to v_0 have been plotted against the velocity (cm/μs) of the crack for each of the two types of materials.

For type I material, velocity of Rayleigh surface wave is $c_R = 0.2138\,\text{cm}/\mu\text{s}$. From Figure 3, it is clear that the SIF depends on the crack propagation velocity c. For fixed crack width, the SIF decreases with the increasing value of c and tends to zero as c approaches c_R. Consequently, $K_I = 0$ when $c = c_R$. Practically our concern is for $c < c_R$, hence the case $K_I = 0$ is of no interest. The graph is not valid for super Rayleigh velocities ($c > c_R$) as c_R is the theoretical upper limit of the crack velocity. Moreover, for fixed crack propagation velocity the value of the SIF decreases as the width of the strip h increases which is obvious from the expression of the SIF in (60). This is also justified with the fact that as the strip becomes wider, the impact of the displacement v_0 on the crack surface is less. Similarly, for

		C_{11}	C_{22}	C_{12}	μ_{12}	ρ
type I	graphite epoxy	155.36	16.31	3.67	7.48	1.6
type II	E-glass epoxy	46.09	12.60	2.86	5.50	2.1

Table 1. Engineering elastic constants.

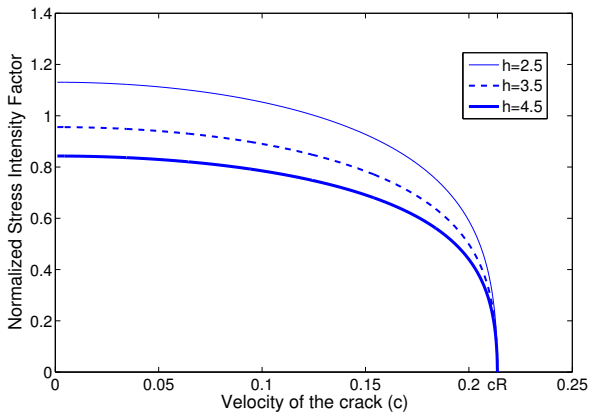

Figure 3. SIF against the crack velocity c for type I material.

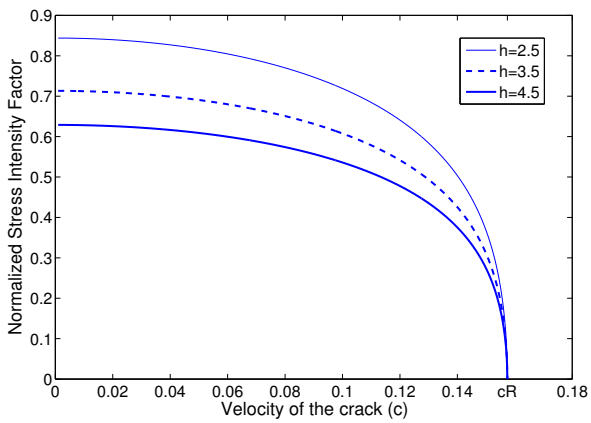

Figure 4. SIF against the crack velocity c for type II material.

type II materials the velocity of the Rayleigh waves is $0.1574\,\mathrm{cm}/\mu\mathrm{s}$ and the graph (Figure 4) is very much similar to Figure 3. These results agree with the results obtained in [Nilsson 1972] for isotropic materials.

Values of the COD has been plotted against negative x-axis for different parameters viz. crack velocity and strip width. From all the figures of the COD (Figures 5–8) it is clear that the values of the COD normalized with respect to v_0 decreases as we approach the crack-tip along the negative x-axis and finally vanishes at the crack-tip. This result is very much expected and agrees with the physical nature of the crack. Figures 5 and 7 show the effect of strip width h on the COD for fixed value of the crack velocity c and it shows that the COD decreases with the increasing value of h for fixed c. Again, Figures 6 and 8 show the effect of crack velocity c on the COD for fixed value of crack width h. It is clear that for subsonic propagation the value of the COD increases with the increasing value of the crack velocity subjected to same crack width.

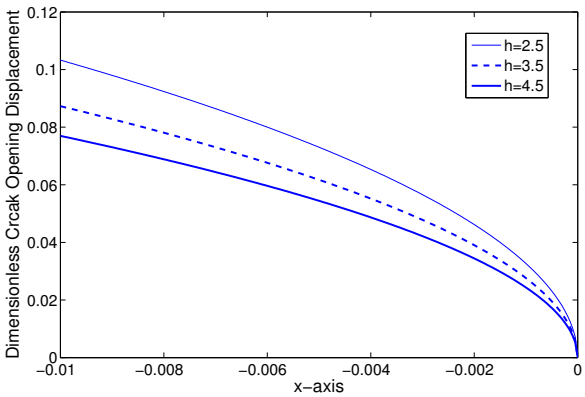

Figure 5. Crack-opening displacement against x for type I material and $c = 0.12$.

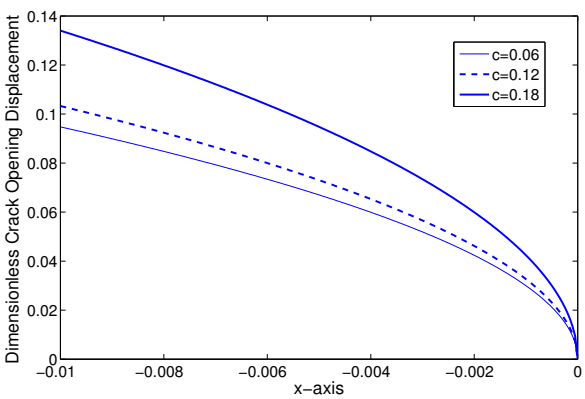

Figure 6. Crack-opening displacement against x for type I material and $h = 2.5$.

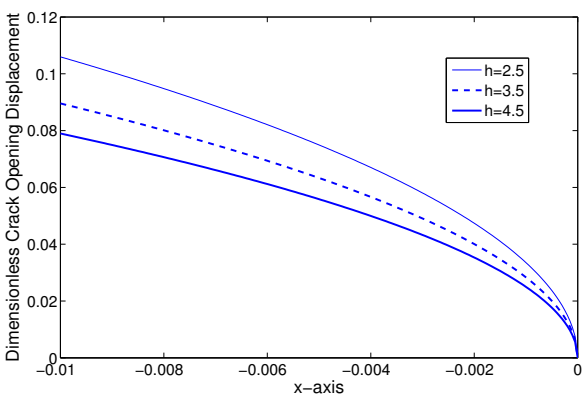

Figure 7. Crack-opening displacement against x for type II material and $c = 0.08$.

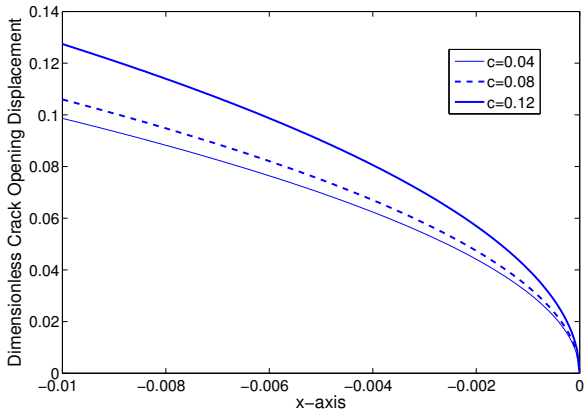

Figure 8. Crack-opening displacement against x for type II material and $h = 2.5$.

6. Conclusions

The diffraction problem of a semiinfinite moving crack in an orthotropic strip due to shear-free boundaries has been investigated. At first, the problem has been converted to the problem of a semiinfinite moving crack subjected to uniform normal stresses at the crack surfaces to make the boundary conditions suitable for the Wiener–Hopf technique. Then Fourier transform has been used to reduce the boundary value problem to the standard Wiener–Hopf equation which has been solved for asymptotic cases to obtain the expressions of the stress intensity factor and crack-opening displacement. The dependence of the stress intensity factor on the material constants, velocity and strip width have been shown with graphs. As the target of this work is to find an idea regarding how to arrest the propagation of the crack, it is necessary to keep the values of the stress intensity factor and crack-opening displacement within a certain limit. Propagation of crack depends on the SIF at the tip of the crack. From graphs it is observed that by controlling stress on the crack i.e., displacement on the surface of the strip, crack velocity and consequently propagation of crack can be made insignificant. The results given by (60) and (63) are applicable in fabrication process of large construction.

Acknowledgement

This research work has been supported by RUSA 2.0, Jadavpur University.

References

[Atkinson and Popelar 1979] C. Atkinson and C. H. Popelar, "Antiplane dynamic crack propagation in a viscoelastic strip", *J. Mech. Phys. Solids* **27**:5-6 (1979), 431–439.

[Bagheri et al. 2015] R. Bagheri, M. Ayatollahi, and S. M. Mousavi, "Analytical solution of multiple moving cracks in functionally graded piezoelectric strip", *Appl. Math. Mech.* **36**:6 (2015), 777–792.

[Basak and Mandal 2017] P. Basak and S. C. Mandal, "Semi-infinite moving crack in an orthotropic strip", *Int. J. Solids Struct.* **128** (2017), 221–230.

[Broberg 1999] K. B. Broberg, *Cracks and fracture*, Academic Press, 1999.

[De and Patra 1990] J. De and B. Patra, "Moving Griffith crack in an orthotropic strip", *Int. J. Eng. Sci.* **28**:8 (1990), 809–819.

[Georgiadis 1986] H. G. Georgiadis, "Complex-variable and integral-transform methods for elastodynamic solutions of cracked orthotropic strips", *Eng. Fract. Mech.* **24**:5 (1986), 727–735.

[Georgiadis and Papadopoulos 1987] H. G. Georgiadis and G. A. Papadopoulos, "Determination of SIF in a cracked plane orthotropic strip by the Wiener–Hopf technique", *Int. J. Fract.* **34** (1987), 57–64.

[Georgiadis and Papadopoulos 1988] H. G. Georgiadis and G. A. Papadopoulos, "Cracked orthotropic strip with clamped boundaries", *J. Appl. Math. Phys.* **39** (1988), 573–578.

[Itou 2004] S. Itou, "Stress intensity factors around a moving Griffith crack in a non-homogeneous layer between two dissimilar elastic half-planes", *Acta Mech.* **167**:3 (2004), 213–232.

[Knauss 1966] W. H. Knauss, "Stresses in an infinite strip containing a semi-infinite crack", *J. Appl. Mech.* (*ASME*) **33**:2 (1966), 356–362.

[Kousiounelos and Williams Jr. 1982] P. N. Kousiounelos and J. H. Williams Jr., "Dynamic fracture of unidirectional graphite fiber composite strips", *Int. J. Fract.* **20** (1982), 47–63.

[Lee 2000] K. H. Lee, "Stress and displacement fields for propagating the crack along the interface of dissimilar orthotropic materials under dynamic mode I and II load", *J. Appl. Mech.* (*ASME*) **67**:1 (2000), 223–228.

[Ma et al. 2005] L. Ma, L. Wu, and L. Guo, "On the moving Griffith crack in a nonhomogeneous orthotropic strip", *Int. J. Fract.* **136**:1 (2005), 187–205.

[Nilsson 1972] F. Nilsson, "Dynamic stress-intensity factors for finite strip problems", *Int. J. Fract. Mech.* **8**:4 (1972), 403–411.

[Nilsson 1973] F. Nilsson, "Erratum to Dynamic stress-intensity factors for finite strip problems", *Int. J. Fract.* **9**:4 (1973), 477.

[Noble 1958] B. Noble, *Methods based on the Wiener–Hopf technique*, Pergamon Press, New York, 1958.

[Nourazar and Ayatollahi 2016] M. Nourazar and M. Ayatollahi, "Multiple moving interfacial cracks between two dissimilar piezoelectric layers under electromechanical loading", *Smart Mater. Struct.* **25**:7 (2016), 075011.

[Rice 1967] J. R. Rice, "Discussion: "Stresses in an infinite strip containing a semi-infinite crack" (Knauss, W. G., 1966, ASME J. Appl. Mech., 33, pp. 356–362)", *J. Appl. Mech.* (*ASME*) **34**:1 (1967), 248–249.

[Rubio-Gonzalez and Lira-Vergara 2011] C. Rubio-Gonzalez and E. Lira-Vergara, "Dynamic response of interfacial finite cracks in orthotropic materials subjected to concentrated loads", *Int. J. Fract.* **169**:2 (2011), 145–158.

[Sarkar et al. 1996] J. Sarkar, M. L. Ghosh, and S. C. Mandal, "Four coplanar Griffith cracks moving in an infinitely long elastic strip under antiplane shear stress", *Proc. Indian Acad. Sci.* (*Math. Sci.*) **106**:1 (1996), 91–103.

[Wang et al. 2001] C. Y. Wang, C. Rubio-Gonzalez, and J. Mason, "The dynamic stress intensity factor for a semi-infinite crack in orthotropic materials with concentrated shear impact loads", *Int. J. Solids Struct.* **38**:8 (2001), 1265–1280.

[Yoffe 1951] E. H. Yoffe, "The moving Griffith crack", *Philos. Mag.* **42**:330 (1951), 739–750.

Received 20 Nov 2019. Revised 23 Apr 2020. Accepted 8 May 2020.

SANATAN JANA: sanatanmath@gmail.com
Department of Mathematics, Jadavpur University, Kolkata 700032, India

PRASANTA BASAK: pbasak.kgec@gmail.com
Department of Mathematics, Kalyani Government Engineering College, Kalyani 741235, India

SUBHAS MANDAL: scmandal.ju@gmail.com
Department of Mathematics, Jadavpur University, Kolkata 700032, India

JOURNAL OF MECHANICS OF MATERIALS AND STRUCTURES
Vol. 15, No. 4, 2020
https://doi.org/10.2140/jomms.2020.15.471

A BERNOULLI–EULER BEAM MODEL BASED ON THE LOCAL GRADIENT THEORY OF ELASTICITY

OLHA HRYTSYNA

Using the total energy balance equation and principle of the frame indifference, a fundamental set of relations of the local gradient continuum model of elastic solids is formulated. The model is based on taking account of non-convective and non-diffusive mass flux related to the changes in the material microstructure. Linear stationary governing equations of the local gradient theory and corresponding boundary conditions are also derived by variational principle. In order to investigate the size-dependent behavior of nano-scale structures, this model is combined with the Bernoulli–Euler beam theory. Deflection of the cantilever beam subjected to the end-point loading under the plane stress conditions is evaluated and compared to the corresponding ones provided by the classical theory and by the strain gradient theory. It is shown that the beam deflection within the local gradient theory is smaller than that predicted by the classical Bernoulli–Euler beam theory. This work may be of special interest for designing the devices utilizing the micro/nano-beam elements.

1. Introduction

It is known that surface and size phenomena play an important role in determining mechanical behaviors of small-scale structures. Laboratory investigations showed that thin films, nanowires, and nanobeams exhibit different physical properties compared with macro-sized structures of the same material [Espinosa et al. 2003; Greer and Nix 2005; Hardwick 1987; Kakunai et al. 1985; Ma and Clarke 1995; Weihs et al. 1988]. Since the classical theory of elasticity cannot explain a specific mechanical behavior of micro/nano-scale structures, various modified mathematical models of elastic continua were developed in the last six decades. Among them there are the couple stress theory [Mindlin and Tiersten 1962; Toupin 1962], strain gradient theories of elasticity [Mindlin 1965], theory of elastic micromorphic materials [Eringen 1999; Eringen and Suhubi 1964; Mindlin 1964], micropolar theory [Eringen 1966; Kafadar and Eringen 1971], microstrech theory [Eringen 1999], nonlocal theory of elasticity with integral-type constitutive relations [Edelen 1969; Eringen 1972], etc. In recent years, modified theories of the elastic continua were effectively adapted in order to investigate the mechanical behavior of elastic micro/nanoscale beams, plates, rods, rings, and shells (see, for example, [Akgöz and Civalek 2011; Lazopoulos and Lazopoulos 2010; Liebold and Müller 2015; Lurie and Solyaev 2019; Repka et al. 2018; Shokrieh and Zibaei 2015; Tahaei Yaghoubi et al. 2018], etc). The papers studied the size-dependent mechanical behaviour of micro-/nano-beams using modified continuum models are reviewed in [Niiranen et al. 2019]. The applications of the surface elasticity theory, pure nonlocal elastic models and nonlocal strain gradient elasticity theories in static and dynamic analysis of nanobeams, nanotubes and nanoplates are presented in [Wang et al.

Keywords: gradient-type theory, continuum mechanics modeling, local gradient elasticity, Bernoulli–Euler beam, micro/nano-beams, size effect.

2016; Farajpour et al. 2018]. Trends in the development of the nonlocal and gradient-type theories of elastic beams are highlighted in reviews [Reddy 2007; Eltaher et al. 2016; Thai et al. 2017; Spagnuolo and Andreaus 2019], etc.

In 1987, Burak proposed a new continuum-thermodynamic approach to the construction of gradient-type continuum theory of elastic solids. The mentioned approach is based on taking account of non-diffusive and non-convective mass flux $\mathbf{J}_{ms}$ associated with the changes in the material microstructure. Such changes in the material microstructure can be observed, for instance, in the vicinity of the newly-created surfaces. Burak related the mentioned non-diffusive and non-convective mass flux to the process referred to as the local mass displacement. [Marchenko et al. 2009] observed this kind of mass flux within the near-surface regions of thin films during their formation. Making use the total energy balance equation and assuming that the mass flux $\mathbf{J}_{ms}$ causes an energy flux $\mu\,\mathbf{J}_{ms}$, where μ is the chemical potential, [Burak 1987] received gradient-type constitutive equations. The additional pair of conjugate variables $(\nabla\mu,\,\mathbf{\Pi}_m)$ related to the local mass displacement was obtained within this theory. Here, $\mathbf{\Pi}_m$ is the vector of local mass displacement related to the vector of mass flux $\mathbf{J}_{ms}$ by the formula [Burak 1987]

$$\mathbf{\Pi}_m(\mathbf{r},\,t)=\int_0^t \mathbf{J}_{ms}(\mathbf{r},\,t')dt' \Rightarrow \mathbf{J}_{ms}=\frac{\partial\mathbf{\Pi}_m}{\partial t}, \tag{1}$$

where $\mathbf{r}$ is the position vector and t denotes the time variable.

This is called the local gradient theory of elasticity. The relations of that theory were applied to describe surface and size effects not covered by the classical theory (see the review article [Hrytsyna et al. 2006] and references therein). In the cited papers, specific studies were carried out in linear approximation with the assumption that convective term in the material time derivative can be neglected.

Two decades later, [Burak et al. 2007] proposed a modified local gradient theory of thermoelasticity in which two additional constitutive parameters related to the local mass displacement were introduced. The mentioned theory contains a new balance-type differential equation that governs the behavior of thermoelastic media in addition to the classical momentum balance equation and entropy balance equation. The local gradient theory was successfully used to describe a near-surface inhomogeneity of mechanical fields [Burak et al. 2008], high-frequency dispersion of longitudinal elastic waves [Kondrat and Hrytsyna 2010], the propagation of antiplane horizontally polarized surface shear waves (SH waves) in homogeneous solids [Hrytsyna 2017], etc.

The objectives of the present paper are (*i*) to derive stationary balance equations and boundary conditions of the local gradient elasticity from the variational principle, (*ii*) to establish a local gradient Bernoulli–Euler linear beam model to incorporate the surface and size effects, and (*iii*) to test the obtained relations on simple problem of a cantilevered beam under the end-point loading.

The paper is organized as follows. In Section 2, the nonlinear local gradient mathematical model of elastic solids is developed based on the total energy balance equation and on the principle of the frame indifference. In Section 3, the stationary balance equations and constitutive relations are formulated for linear approximation. In Section 4, the linear governing equations of local gradient elasticity and corresponding boundary conditions are derived from the variational principle. Based on these relations, the Bernoulli–Euler local gradient beam model is developed in Section 5. The deflection of the cantilever beam loaded by a point force is obtained in this section. The numerical results are discussed in Section 6. Conclusions are drawn in the final Section 7.

2. Basic equations of nonlinear local gradient elasticity

In the classical elasticity, the position of a small body element (body particle) is identified with the position of its center of mass. In such a theory, the change of position of the mass center of the small body element can be caused only by the convective displacement of this element (Figure 1a). The local gradient theory takes into account that a change in the center of mass of the body particle may be induced not only by its convective displacement as a rigid entity (i.e., translational displacement of the particle geometric center) but by the changes of the relative positions of microparticles within this element as well, i. e., the change of its microstructure (Figure 1b). Within the local gradient theory mentioned changes in microstructure are described by non-convective and non-diffusive mass flux $\mathbf{J}_{ms}$. This mass flux was linked with the process of the local mass displacement.

To describe the local mass displacement, new physical quantities associated with this process should be introduced. Following [Burak 1987], alongside with the mass flux $\mathbf{J}_{ms}$, we introduce vector of the local mass displacement $\mathbf{\Pi}_m$. Let us assume that above vectors are related by Eq. (1). Note that the vector $\mathbf{\Pi}_m$ of the local mass displacement has a dimension of the density of a dipole mass moment ($\mathrm{kg}\cdot\mathrm{m}/\mathrm{m}^3$) while its specific quantity $\boldsymbol{\pi}_m = \mathbf{\Pi}_m/\rho$ has the length dimension (m) (here, ρ is the mass density).

For an arbitrary body of finite size (domain (V)), using the relation [Burak et al. 2008]

$$\int_{(V)} \mathbf{\Pi}_m dV = \int_{(V)} \rho_{m\pi}\, \mathbf{r}\, dV, \tag{2}$$

we introduce a new scalar physical quantity $\rho_{m\pi}$ that has the dimension of mass density. Here, $\mathbf{r}$ is the position vector of the material point. From integral relation (2), formula

$$\rho_{m\pi} = -\nabla \cdot \mathbf{\Pi}_m \tag{3}$$

can be obtained [Hrytsyna and Kondrat 2019]. Here, $\nabla = (\partial/\partial\xi_1, \partial/\partial\xi_2, \partial/\partial\xi_3)$ is the nabla operator, where ξ_i, $i = \overline{1,3}$, are the space coordinates.

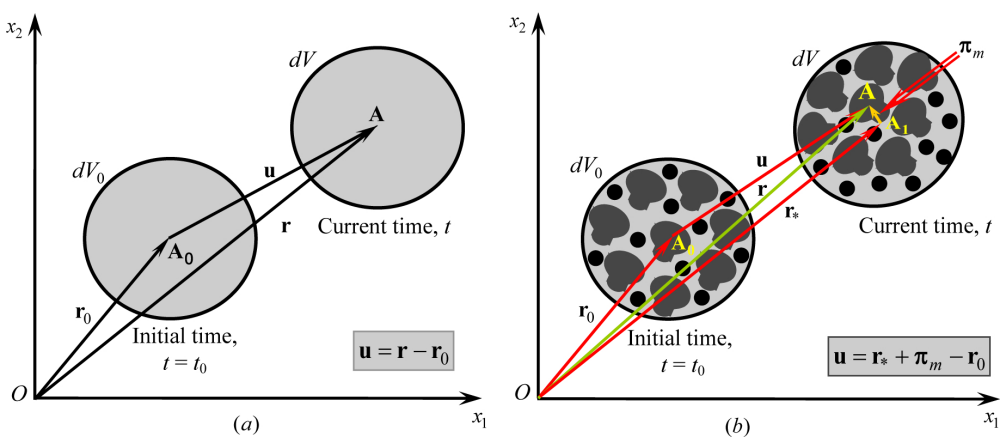

Figure 1. Mass-center displacement of a small volume element due to action of external load: (a) the classical theory of elasticity, $\mathbf{u} = \mathbf{r} - \mathbf{r}_0$; ($b$) the local gradient theory of elasticity, $\mathbf{u} = \mathbf{r}_* + \boldsymbol{\pi}_m - \mathbf{r}_0$ where $\boldsymbol{\pi}_m = \mathbf{\Pi}_m \rho$.

Note that in electrodynamics by similar formula $\rho_{e\pi} = -\nabla \cdot \mathbf{\Pi}_e$, the density of an induced charge $\rho_{e\pi}$ was introduced into consideration (here, $\mathbf{\Pi}_e$ is the polarization vector, i.e., the vector of the local displacement of electric charges) [Bredov et al. 1985]. Thus, by analogy with the electrodynamics, we refer to $\rho_{m\pi}$ as the density of an induced mass [Hrytsyna and Kondrat 2019].

By differentiating expression (3) with respect to time and taking formula (1) into account, one can obtain the balance-type differential equation

$$\frac{\partial \rho_{m\pi}}{\partial t} + \nabla \cdot \mathbf{J}_{ms} = 0, \tag{4}$$

for quantities $\rho_{m\pi}$ and $\mathbf{J}_{ms}$ introduced for a description of the local mass displacement.

Within this subsection, we derive the constitutive and balance equations, using the energy conservation law and the principle of frame indifference. We consider an elastic body that occupies the region (V) and is bounded by a smooth surface (Σ). Let us separate from the body a fixed small volume (V') bounded by closed surface (Σ'). We represent the total energy of this volume as the sum of internal ρu and kinetic $\rho \mathbf{v}^2/2$ energies. Here, u denotes the specific internal energy and $\mathbf{v}$ is the velocity of continuum of centre mass. The change in the total energy is caused (*i*) by the convective energy transport $\rho\big(u + \mathbf{v}^2/2\big)\mathbf{v}$ through the body surface, (*ii*) by the energy flux $\hat{\boldsymbol{\sigma}} \cdot \mathbf{v}$ due to the mechanical work of the surface forces, (*iii*) by the energy flux $\mu \mathbf{J}_m$ linked with the mass transport relative to the mass-centre of the small body particle, (*iv*) by the energy flux $\mu_{\boldsymbol{\pi}} \mathbf{J}_{ms}$ related to the material microstructure ordering (i. e., the local mass displacement) as well as (*v*) by the action of mechanical mass forces $\mathbf{F}$. Thus, for the fixed volume (V'), the energy balance equation can be written as follows:

$$\frac{d}{dt}\int_{(V')} \big(\rho u + \tfrac{1}{2}\rho \mathbf{v}^2\big)\, dV = -\oint_{(\Sigma')} \big[\rho\big(u + \tfrac{1}{2}\mathbf{v}^2\big)\mathbf{v} - \hat{\boldsymbol{\sigma}} \cdot \mathbf{v} + \mu \mathbf{J}_m + \mu_\pi\, \mathbf{J}_{ms}\big] \cdot \mathbf{n}\, d\Sigma + \int_{(V')} \rho \mathbf{F} \cdot \mathbf{v}\, dV. \tag{5}$$

Here, $\hat{\boldsymbol{\sigma}}$ represents the classical Cauchy stress tensor; μ_π is the energy measure of the effect of the local mass displacement on the internal energy; $\mathbf{J}_m = \rho(\mathbf{v}_* - \mathbf{v})$; $\mathbf{v}_*$ is the velocity of convective displacement of the small body element; $\mathbf{n}$ is the unit vector normal to the material surface (Σ'), and the dot denotes the scalar product. Note that vectors $\mathbf{v}_*$ and $\mathbf{v}$ are related through the following expression (see Figure 1):

$$\mathbf{v} = \mathbf{v}_* + \frac{1}{\rho}\frac{\partial \mathbf{\Pi}_m}{\partial t}. \tag{6}$$

Note also that by virtue of Eqs. (1) and (6), the mass flux $\mathbf{J}_m$ can be written down as follows:

$$\mathbf{J}_m = -\frac{\partial \mathbf{\Pi}_m}{\partial t}. \tag{7}$$

Making use of the divergence theorem as well as of the expressions (1) and (7), from integral equation (5), in view of the arbitrary of the volume (V') one obtains the local form of the energy conservation law for the elastic continuum

$$\frac{\partial}{\partial t}\big(\rho u + \tfrac{1}{2}\rho \mathbf{v}^2\big) = -\nabla \cdot \big[\rho \mathbf{v}\big(u + \tfrac{1}{2}\mathbf{v}^2\big)\big] + \nabla \cdot (\hat{\boldsymbol{\sigma}} \cdot \mathbf{v}) + \rho \mathbf{F} \cdot \mathbf{v} - \nabla \mu'_\pi \cdot \frac{\partial \mathbf{\Pi}_m}{\partial t} + \mu'_\pi \frac{\partial(-\nabla \cdot \mathbf{\Pi}_m)}{\partial t}. \tag{8}$$

Here, $\mu'_\pi = \mu_\pi - \mu$ is the modified chemical potential.

After some algebra, expression (8) can be written as follows:

$$\rho\frac{du}{dt}+\left(u+\tfrac{1}{2}\mathbf{v}^2\right)\left[\frac{\partial\rho}{\partial t}+(\nabla\cdot\rho\mathbf{v})\right] = \mathbf{v}\cdot\left(-\rho\frac{d\mathbf{v}}{dt}+\nabla\cdot\hat{\boldsymbol{\sigma}}+\rho\mathbf{F}\right)+\hat{\boldsymbol{\sigma}}:(\nabla\otimes\mathbf{v})-\nabla\mu'_\pi\cdot\frac{\partial\boldsymbol{\Pi}_m}{\partial t}+\mu'_\pi\frac{\partial\rho_{m\pi}}{\partial t}. \quad (9)$$

Here, $d/dt=\partial/\partial t+\mathbf{v}\cdot\nabla$ denotes the substantive derivative, and $\otimes$ is the tensor product.

Let us introduce specific quantities $\boldsymbol{\pi}_m=\boldsymbol{\Pi}_m/\rho$ and $\rho_m=\rho_{m\pi}/\rho$. Substituting these two relations into the energy balance equation (9) after some transformations, we obtain

$$\rho\frac{du}{dt}+\rho\nabla\mu'_\pi\cdot\frac{d\boldsymbol{\pi}_m}{dt}-\rho\mu'_\pi\frac{d\rho_m}{dt}-\hat{\boldsymbol{\sigma}}_*:(\nabla\otimes\mathbf{v})=\mathbf{v}\cdot\left(-\rho\frac{d\mathbf{v}}{dt}+\nabla\cdot\hat{\boldsymbol{\sigma}}_*+\rho\mathbf{F}_*\right) -\left(\frac{\partial\rho}{\partial t}+\nabla\cdot(\rho\mathbf{v})\right)\left(u+\frac{1}{2}\mathbf{v}^2-\rho_m\mu'_\pi+\nabla\mu'_\pi\cdot\boldsymbol{\pi}_m\right), \quad (10)$$

where

$$\hat{\boldsymbol{\sigma}}_*=\hat{\boldsymbol{\sigma}}-\rho(\rho_m\mu'_\pi-\boldsymbol{\pi}_m\cdot\nabla\mu'_\pi)\hat{\mathbf{I}}, \quad (11)$$

$$\mathbf{F}_*=\mathbf{F}+\rho_m\nabla\mu'_\pi-\boldsymbol{\pi}_m\cdot\nabla\otimes\nabla\mu'_\pi, \quad (12)$$

where $\hat{\mathbf{I}}$ represents the unit tensor.

Following [Green and Rivlin 1964], assume that the energy balance equation (10) remains valid under superimposed rigid body translation. As a result from (10), we get the equation of motion and the mass balance equation, namely [Hrytsyna and Kondrat 2019]:

$$\nabla\cdot\hat{\boldsymbol{\sigma}}_*+\rho\mathbf{F}_*=\rho\frac{d\mathbf{v}}{dt}, \quad (13)$$

$$\frac{\partial\rho}{\partial t}+\nabla\cdot(\rho\mathbf{v})=0. \quad (14)$$

From formulae (11)–(13), it follows that the local mass displacement being taken into consideration leads to the modification of the stress tensor $\hat{\boldsymbol{\sigma}}_*$ and to the appearance of an additional nonlinear mass force $\mathbf{F}'_*=\rho_m\nabla\mu'_\pi-\boldsymbol{\pi}_m\cdot\nabla\otimes\nabla\mu'_\pi$ in equation of motion (13).

Since the energy balance equation (10) should be invariant under superimposed rigid body rotation with a constant angular rate, it follows that $\hat{\boldsymbol{\sigma}}_*$ is a symmetric tensor [Hrytsyna and Kondrat 2019].

In view of Eqs. (13) and (14), the balance equation (10) for the internal energy simplifies and can be written as follows:

$$\rho\frac{du}{dt}=\hat{\boldsymbol{\sigma}}_*:\frac{d\hat{\boldsymbol{e}}}{dt}-\rho\nabla\mu'_\pi\cdot\frac{d\boldsymbol{\pi}_m}{dt}+\rho\mu'_\pi\frac{d\rho_m}{dt}. \quad (15)$$

Here, $\hat{\boldsymbol{e}}$ is the strain tensor related to the mechanical displacement vector $\mathbf{u}$ by the formula

$$\hat{\boldsymbol{e}}=\tfrac{1}{2}\left(\nabla\otimes\mathbf{u}+(\nabla\otimes\mathbf{u})^{\mathrm{T}}\right), \quad (16)$$

where superscript T stands for transpose.

Let us introduce a new energy density function $H=H(\hat{\boldsymbol{e}},\ \mu'_\pi,\ \nabla\mu'_\pi)$ through the Legendre transformation $H=u+\rho_m\mu'_\pi+\nabla\mu'_\pi\cdot\boldsymbol{\pi}_m$. Based on (15) we can write the following generalized Gibbs relation:

$$dH = \frac{1}{\rho}\hat{\boldsymbol{\sigma}}_* : d\hat{\boldsymbol{e}} - \rho_m d\mu'_\pi + \boldsymbol{\pi}_m \cdot d\nabla\mu'_\pi. \tag{17}$$

Since H is the function of scalar μ'_π, vector $\nabla\mu'_\pi$, and tensor $\hat{\boldsymbol{e}}$ arguments, its full differential looks as follows:

$$dH = \frac{\partial H}{\partial \hat{\boldsymbol{e}}} d\hat{\boldsymbol{e}} + \frac{\partial H}{\partial \mu'_\pi} d\mu'_\pi + \frac{\partial H}{\partial(\nabla\mu'_\pi)} \cdot d(\nabla\mu'_\pi). \tag{18}$$

Subtracting formulae (17) and (18), we get

$$\left(\frac{\partial H}{\partial \hat{\boldsymbol{e}}} - \frac{1}{\rho}\hat{\boldsymbol{\sigma}}_*\right) d\hat{\boldsymbol{e}} + + \left(\frac{\partial H}{\partial \mu'_\pi} + \rho_m\right) d\mu'_\pi + \left(\frac{\partial H}{\partial(\nabla\mu'_\pi)} - \boldsymbol{\pi}_m\right) \cdot d(\nabla\mu'_\pi) = 0. \tag{19}$$

Equation (19) must hold for arbitrary $d\hat{\boldsymbol{e}}$, $d\mu'_\pi$, and $d(\nabla\mu'_\pi)$. Thus, (19) yields the following gradient-type constitutive equations:

$$\hat{\boldsymbol{\sigma}}_* = \rho \frac{\partial H}{\partial \hat{\boldsymbol{e}}}\bigg|_{\mu'_\pi, \nabla\mu'_\pi}, \; \rho_m = -\frac{\partial H}{\partial \mu'_\pi}\bigg|_{\hat{\boldsymbol{e}}, \nabla\mu'_\pi}, \; \boldsymbol{\pi}_m = \frac{\partial H}{\partial(\nabla\mu'_\pi)}\bigg|_{\hat{\boldsymbol{e}}, \mu'_\pi}, \tag{20}$$

where the subscripts to the right from the vertical lines indicate the variables that are held constant during the differentiation. Note that within the framework of this higher-order theory of elastic media, the set of conjugate variables is complemented by two additional pairs of variables (ρ_m, μ'_π) and ($\boldsymbol{\pi}_m$, $\nabla\mu'_\pi$) related to the local mass displacement.

3. Linear set of equations for stationary approximation

Let us represent the constitutive relations (20) in an explicit form. To this end, we expand the potential H in the vicinity of the natural state ($\hat{\boldsymbol{e}} = 0$, $\hat{\boldsymbol{\sigma}}_* = 0$, $\mu'_\pi = \mu'_{\pi 0}$, $\nabla\mu'_\pi = 0$, $\boldsymbol{\pi}_m = 0$, and $\rho_m = 0$) into a Taylor series. We retain quadratic terms in this decomposition which enables us to get linear constitutive equations. Let $e_{ij} \ll 1$, $\tilde{\mu}'_\pi \ll 1$, and $\nabla\tilde{\mu}'_\pi \ll 1$, where $\tilde{\mu}'_\pi = \mu'_\pi - \mu'_{\pi 0}$. For anisotropic media, we can write:

$$H = H_0 + \frac{1}{2\rho_0}\hat{\mathbf{C}}^{(4)} :: (\hat{\boldsymbol{e}} \otimes \hat{\boldsymbol{e}}) - \frac{1}{2} d_\mu \tilde{\mu}'^2_\pi - \frac{1}{2}\hat{\boldsymbol{\chi}}^m : (\nabla\tilde{\mu}'_\pi \otimes \nabla\tilde{\mu}'_\pi) - \frac{1}{\rho_0}\hat{\boldsymbol{\alpha}}^\mu \; : \hat{\boldsymbol{e}} \; \tilde{\mu}'_\pi$$
$$- \frac{1}{\rho_0}\hat{\mathbf{g}}^{(3)} \vdots (\hat{\boldsymbol{e}} \otimes \nabla\tilde{\mu}'_\pi) - (\boldsymbol{\gamma}^\mu \cdot \nabla\tilde{\mu}'_\pi)\tilde{\mu}'_\pi. \tag{21}$$

Here, ρ_0 is the reference mass density, $\hat{\mathbf{C}}^{(4)}$ is the fourth-order tensor of the elastic constants, $\hat{\boldsymbol{\alpha}}^\mu$ denotes the tensor of volumetric expansion caused by the local mass displacement, $\hat{\mathbf{g}}^{(3)}$ is the third-order tensor of piezomass constants, d_μ is the isochoric coefficient of the dependency of specific density of the induced mass on perturbation of modified chemical potential $\tilde{\mu}'_\pi$, $\hat{\boldsymbol{\chi}}^m$ denote the tensor characterizing the dependence of vectors of the local mass displacement on $\nabla\tilde{\mu}'_\pi$, $\hat{\boldsymbol{\gamma}}^\mu$ is the vector characterizing the dependence of the induced mass density on $\nabla\tilde{\mu}'_\pi$.

Note that for the linear approximation, tensor $\hat{\boldsymbol{\sigma}}_*$ can be replaced by the ordinary Cauchy stress tensor $\hat{\boldsymbol{\sigma}}$. Therefore, using relations (20) and (21), we obtain the following state equations:

$$\hat{\boldsymbol{\sigma}} = \hat{\mathbf{C}}^{(4)} : \hat{\boldsymbol{e}} - \hat{\boldsymbol{\alpha}}^{\mu}\, \tilde{\mu}'_{\pi} - \boldsymbol{\nabla}\tilde{\mu}'_{\pi} \cdot \hat{\mathbf{g}}^{(3)}, \tag{22a}$$

$$\rho_m = d_{\mu}\tilde{\mu}'_{\pi} + \frac{1}{\rho_0}\hat{\boldsymbol{\alpha}}^{\mu} : \hat{\boldsymbol{e}} + \boldsymbol{\gamma}^{\mu} \cdot \boldsymbol{\nabla}\tilde{\mu}'_{\pi}, \tag{22b}$$

$$\boldsymbol{\pi}_m = -\hat{\boldsymbol{\chi}}^{m} \cdot \boldsymbol{\nabla}\tilde{\mu}'_{\pi} - \boldsymbol{\gamma}^{\mu}\, \tilde{\mu}'_{\pi} - \frac{1}{\rho_0}\hat{\mathbf{g}}^{(3)} : \hat{\boldsymbol{e}}. \tag{22c}$$

Due to the accounting for the local mass displacement, the constitutive equations (22) contain new material constants d_{μ}, $\boldsymbol{\gamma}^{\mu}$, $\hat{\boldsymbol{\alpha}}^{\mu}$, $\hat{\boldsymbol{\chi}}^{m}$, and $\hat{\mathbf{g}}^{(3)}$, characterizing the physical properties of material. The tensors of the second order $\hat{\boldsymbol{\alpha}}^{\mu}$ and $\hat{\boldsymbol{\chi}}^{m}$ have 6 components and vector $\boldsymbol{\gamma}^{\mu}$ has 3 components. The third-order tensor of the piezomass coefficients $\hat{\mathbf{g}}^{(3)}$ contains 18 independent components (they are symmetric about the permutation of the second and third subscripts).

The number of material constants is decreased for isotropic media. For such media, constitutive relations are as follows:

$$\hat{\boldsymbol{\sigma}} = 2G\hat{\boldsymbol{e}} + \left[\left(K - \tfrac{2}{3}G\right)e - K\alpha_{\mu}\tilde{\mu}'_{\pi}\right]\hat{\mathbf{I}}, \tag{23a}$$

$$\rho_m = d_{\mu}\tilde{\mu}'_{\pi} + \frac{K\alpha_{\mu}}{\rho_0}e, \tag{23b}$$

$$\boldsymbol{\pi}_m = -\chi_m \boldsymbol{\nabla}\tilde{\mu}'_{\pi}. \tag{23c}$$

The local gradient theory yields five coefficients for isotropic materials, two of which are classical elastic moduli (i. e., K and G), and α_{μ}, d_{μ}, and χ_m are new material coefficients.

It is worth to note that the stress for isotropic materials is related not only to the strain, as in classical elasticity, but also to the modified chemical potential $\tilde{\mu}'_{\pi}$. Therefore, in general, the local mass displacement can influence the stress-strain state of an isotropic solid body.

For linear stationary approximation, Eqs. (4) and (13) can be written as:

$$\rho_m = -\boldsymbol{\nabla} \cdot \boldsymbol{\pi}_m, \tag{24}$$

$$\boldsymbol{\nabla} \cdot \hat{\boldsymbol{\sigma}} + \rho_0 \mathbf{F} = 0. \tag{25}$$

For static fields, the complete linear system of field equations consists of Eqs. (24) and (25), the constitutive relations (22) (or ((23))), and the strain-displacement relation (16).

4. Variational approach

In this section, the variational principle is used to derive the governing equations and corresponding boundary conditions of the linear local gradient elasticity.

Assume that energy density potential H exists for the elastic continuum introduced in Section 2. To take the changes in the material microstructure into account, we assume the potential H to be a C^2-continuous function of the strain tensor $\hat{\boldsymbol{e}}$, modified chemical potential $\tilde{\mu}'_{\pi}$ as well as on its space gradient $\boldsymbol{\nabla}\tilde{\mu}'_{\pi}$, that is: $H(\hat{\boldsymbol{e}}, \tilde{\mu}'_{\pi}, \boldsymbol{\nabla}\tilde{\mu}'_{\pi})$. Let us also assume that constitutive relations are defined by the formulae (20). For elastic solids that occupy the region (V) bounded by a smooth surface (Σ), the

variational principle can be expressed by formula

$$\delta\Big(-\int_{(V)} H(\hat{\boldsymbol{e}},\tilde{\mu}'_{\pi},\nabla\tilde{\mu}'_{\pi})\,dV+\int_{(V)} W_V\,dV+\int_{(\Sigma)} W_s\,d\Sigma\Big)=0. \tag{26}$$

The second and third integrals in (26) correspond to the virtual work done by the external body force and surface loading, respectively.

In view of the constitutive equations (20), the first integral in the above relation can be represented as

$$\begin{aligned}\delta\int_{(V)} H(\hat{\boldsymbol{e}},\tilde{\mu}'_{\pi},\nabla\tilde{\mu}'_{\pi})\,dV&=\int_{(V)}\Big(\frac{\partial H}{\partial\hat{\boldsymbol{e}}}\delta\hat{\boldsymbol{e}}+\frac{\partial H}{\partial\tilde{\mu}'_{\pi}}\delta\tilde{\mu}'_{\pi}+\frac{\partial H}{\partial\nabla\tilde{\mu}'_{\pi}}\delta\nabla\tilde{\mu}'_{\pi}\Big)\,dV\\&=\int_{(V)}\Big(\frac{1}{\rho_0}\hat{\boldsymbol{\sigma}}:\delta\hat{\boldsymbol{e}}-\rho_m\delta\tilde{\mu}'_{\pi}+\boldsymbol{\pi}_m\cdot\delta\nabla\tilde{\mu}'_{\pi}\Big)\,dV.\end{aligned}$$

Since $\hat{\boldsymbol{\sigma}}$ is a symmetric tensor, and taking strain-displacement relation (16) and equations

$$\begin{aligned}\boldsymbol{\pi}_m\cdot\delta\nabla\tilde{\mu}'_{\pi}&=\nabla\cdot(\boldsymbol{\pi}_m\delta\tilde{\mu}'_{\pi})-(\nabla\cdot\boldsymbol{\pi}_m)\delta\tilde{\mu}'_{\pi},\\\hat{\boldsymbol{\sigma}}:\delta(\nabla\otimes\mathbf{u})&=\nabla\cdot(\hat{\boldsymbol{\sigma}}\cdot\delta\mathbf{u})-(\nabla\cdot\hat{\boldsymbol{\sigma}})\cdot\delta\mathbf{u}\end{aligned}$$

into account, the variation of the potential H can be expressed as follows:

$$\delta\int_{(V)} H\,dV=\int_{(V)}\Big(\frac{1}{\rho_0}\nabla\cdot(\hat{\boldsymbol{\sigma}}\cdot\delta\mathbf{u})-\frac{1}{\rho_0}(\nabla\cdot\hat{\boldsymbol{\sigma}})\cdot\delta\mathbf{u}-(\rho_m+\nabla\cdot\boldsymbol{\pi}_m)\delta\tilde{\mu}'_{\pi}+\nabla\cdot(\boldsymbol{\pi}_m\delta\tilde{\mu}'_{\pi})\Big)\,dV.$$

The variation of the external mass force is

$$\delta\int_{(V)} W_V\,dV=\int_{(V)}\mathbf{F}\cdot\delta\mathbf{u}\,dV.$$

Thus, by the divergence theorem for smooth surface (Σ), we can rewrite the expression (26) as

$$\int_{(V)}\Big(\frac{1}{\rho_0}(\nabla\cdot\hat{\boldsymbol{\sigma}}+\rho_0\mathbf{F})\cdot\delta\mathbf{u}+(\rho_m+\nabla\cdot\boldsymbol{\pi}_m)\delta\tilde{\mu}'_{\pi}\Big)\,dV-\int_{(\Sigma)}\Big(\frac{1}{\rho_0}\boldsymbol{\sigma}_n\cdot\delta\mathbf{u}+\pi_{mn}\delta\tilde{\mu}'_{\pi}-\delta W_s\Big)d\Sigma=0, \tag{27}$$

where $\boldsymbol{\sigma}_n=\mathbf{n}\cdot\hat{\boldsymbol{\sigma}}$, and $\pi_{mn}=\mathbf{n}\cdot\boldsymbol{\pi}_m$. From variational relation (27), the stationary equations (24) and (25) as well as the following boundary conditions ensue:

$$(\boldsymbol{\sigma}_n-\boldsymbol{\sigma}_{ns})\cdot\delta\mathbf{u}=0,\quad\forall\mathbf{r}\in(\Sigma), \tag{28}$$

$$(\pi_{mn}-\pi_{ms})\delta\tilde{\mu}'_{\pi}=0,\quad\forall\mathbf{r}\in(\Sigma). \tag{29}$$

Here, $\boldsymbol{\sigma}_{ns}$ and π_{ms} are the surface values of the corresponding quantities.

The equations set (16), (22), (24), and (25), along with the boundary conditions (28) and (29) constitute the stationary boundary-value problem for linear local gradient elasticity.

5. Bernoulli–Euler local gradient beam model; cantilever beam bending problem

In this section, based on relations of local gradient elasticity, the bending problem of elastic cantilever nanobeam is studied. The length of the cantilever beam is L, thickness is h and width is b. The beam

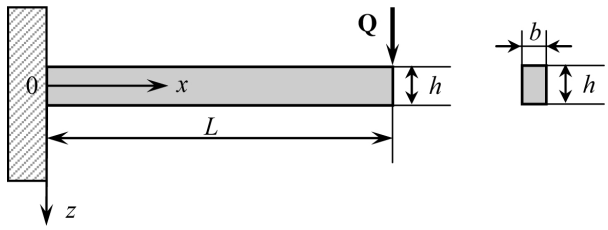

Figure 2. The cantilever beam with rectangular cross section subjected to a tip-point load.

thickness and width are assumed to be much less than the cantilever length, i. e., $L >> h$ and $L >> b$. Assume that beam is fixed at one end and concentrated load $\mathbf{Q}$ is applied at the free end of the cantilever beam (Figure 2). Let the x-axis be along the beam length, the y-axis be along the width of the beam, and the z-axis be along the thickness of the beam. The applied load and the beam geometry are treated in such a way that the plane stress conditions are realized in the body. For this case, the displacement vector and the modified chemical potential are functions of x and z space coordinates only.

For the sake of simplicity, we neglect the effect of the gradient of modified chemical potential on stress distribution $\hat{\boldsymbol{\sigma}}$ as well as on the density of the induced mass ρ_m. In this case, the constitutive equations (22) read as:

$$\hat{\boldsymbol{\sigma}} = \hat{\mathbf{C}}^{(4)} : \hat{\boldsymbol{e}} - \hat{\boldsymbol{\alpha}}^{\mu}\, \tilde{\mu}'_{\pi}, \quad \rho_m = d_{\mu}\tilde{\mu}'_{\pi} + \frac{1}{\rho_0}\hat{\boldsymbol{\alpha}}^{\mu} : \hat{\boldsymbol{e}}, \quad \boldsymbol{\pi}_m = -\hat{\boldsymbol{\chi}}^{m} \cdot \nabla\tilde{\mu}'_{\pi}. \tag{30}$$

In order to derive the relations of local gradient beam theory, we introduce the Bernoulli–Euler hypotheses. Thus, the displacement components are expressed as follows:

$$u_1 = -zw_{,x}\,, \quad u_2 = 0, \quad u_3 = w(x). \tag{31}$$

Here, $w(x)$ is the beam deflection, and the comma indicates differentiation with respect to the spatial variables. For this case, there is only one nonzero strain component e_{11}, that is

$$e_{11} = -zw_{,xx}\,. \tag{32}$$

Similarly to formulae (31), we represent the modified chemical potential as the linear function of z-coordinate, namely:

$$\tilde{\mu}'_{\pi}(x, z) = zm(x), \tag{33}$$

where $m(x)$ is unknown function of x-coordinate.

Let us consider the following material property matrices:

$$\begin{bmatrix} C_{11} & C_{13} & 0 \\ C_{13} & C_{33} & 0 \\ 0 & 0 & C_{55} \end{bmatrix}, \begin{bmatrix} \alpha_1^{\mu} \\ \alpha_3^{\mu} \\ 0 \end{bmatrix}, \begin{bmatrix} -\chi_1^{m} & 0 \\ 0 & -\chi_3^{m} \end{bmatrix}, \tag{34}$$

where the Voigt notation (i.e., $11 \to 1$, $22 \to 2$, $33 \to 3$, $23 \to 4$, $13 \to 5$, $12 \to 6$) are employed.

In view of relations (32)–(34), constitutive equations (30) may be rewritten as follows:

$$\sigma_{11}(x,z) = -z(C_{11}w_{,xx} + \alpha_1^{\mu} m) = z\sigma_1'(x), \tag{35a}$$

$$\sigma_{33}(x,z) = -z(C_{13}w_{,xx} + \alpha_3^{\mu} m) = z\sigma_3'(x), \tag{35b}$$

$$\sigma_{13} = 0, \tag{35c}$$

$$\rho_m(x,z) = z(d_{\mu}m - \alpha_1^{\mu}\rho_0^{-1}w_{,xx}) = z\rho_m'(x), \tag{35d}$$

$$\pi_m^1(x,z) = -\chi_1^m z m_{,x} = z\pi_1'(x), \tag{35e}$$

$$\pi_m^3(x) = -\chi_3^m m(x). \tag{35f}$$

To obtain the equations of local gradient beam model, let us consider the variation of the potential H. In view of (21) and (35), we have the following form for this energy:

$$H - H_0 = \frac{1}{\rho_0}\sigma_{11}e_{11} - \rho_m\tilde{\mu}_{\pi}' + \pi_m^1\,\tilde{\mu}_{\pi}'_{,x} + \pi_m^3\,d\tilde{\mu}_{\pi}'_{,z}\,. \tag{36}$$

By means of the variation of the relation (36), we obtain

$$\begin{aligned}
&\delta\int_{(V)} H\,dV \\
&= \int_{(V)}\left(\frac{1}{\rho_0}\sigma_{11}\delta e_{11} - \rho_m\,\delta\tilde{\mu}_{\pi}' + \pi_m^1\,\delta\tilde{\mu}_{\pi}'_{,x} + \pi_m^3\,\delta\tilde{\mu}_{\pi}'_{,z}\right)dV \\
&= \int_0^L\int_{-h/2}^{h/2}\int_0^b\left(-\frac{1}{\rho_0}\sigma_{11}z\,\delta w_{,xx} - (\rho_m + \pi_{m,x}^1 + \pi_{m,z}^3)\delta\tilde{\mu}_{\pi}' + (\pi_m^1\,\delta\tilde{\mu}_{\pi}')_{,x} + (\pi_m^3\,\delta\tilde{\mu}_{\pi}')_{,z}\right)dx\,dy\,dz.
\end{aligned}$$

The above relation may be expressed as

$$\begin{aligned}
\delta\int_{(V)} H\,dV = -b\int_0^L\int_{-h/2}^{h/2}\left[\frac{1}{\rho_0}\sigma_{11}z\,\delta w_{,xx} + (\rho_m + \pi_{m,x}^1)\delta\tilde{\mu}_{\pi}'\right]dx\,dz \\
+ b\int_0^L\left(\pi_m^3\,\delta\tilde{\mu}_{\pi}'\right)\Big|_{z=-\frac{h}{2}}^{z=\frac{h}{2}}dx + b\int_{-h/2}^{h/2}\left(\pi_m^1\,\delta\tilde{\mu}_{\pi}'\right)\Big|_{x=0}^{x=L}dz.
\end{aligned}$$

Taking (35) and the relation

$$\sigma_{11}\delta w_{,xx} = (\sigma_{11}\delta w_{,x} - \sigma_{11,x}\,\delta w)_{,x} + \sigma_{11,xx}\,\delta w$$

into account and integrating by parts in the space coordinates, yields

$$\begin{aligned}
\delta\int_{(V)} H\,dV = -\int_0^L\left\{\frac{I}{\rho_0}\sigma_{1,xx}'\,\delta w + \left(I(\rho_m' + \pi_{1,x}') - S\pi_m^3\right)\delta m\right\}dx \\
+ I\left(\pi_1'\delta m\right)\Big|_{x=0}^{x=L} - \frac{I}{\rho_0}\left(\sigma_1'\,\delta w_{,x} - \sigma_{1,x}'\,\delta w\right)\Big|_{x=0}^{x=L}.
\end{aligned} \tag{37}$$

Here, $S = bh$ is the cross-section area and $I = bh^3/12$ is the second moment of cross-section area.

Due to the arbitrariness of δw and δm, based on the variational relation (37), we obtain the governing equations

$$M_{,xx} = 0, \quad I(\rho_m' + \pi_{1,x}') - S\pi_m^3 = 0, \tag{38}$$

with boundary conditions that are defined at the ends $x = 0$ and $x = L$ of the cantilever beam the following quantities:

$$M \text{ or } w_{,x}\,, \quad M_{,x} \text{ or } w, \quad I\pi_1^{'} \text{ or } m.$$

Here, $M = -I(C_{11}w_{,xx} + \alpha_1^{\mu} m)$ is the bending moment.

Substituting (35) into (38) yields the equations to determine the unknown functions $w(x)$ and $m(x)$:

$$C_{11}w_{,xxxx} + \alpha_1^{\mu} m_{,xx} = 0, \tag{39}$$

$$m_{,xx} - \lambda_0^2(1 + \mathsf{M}_h)m + \frac{\alpha_1^{\mu}}{\rho_0 \chi_1^m} w_{,xx} = 0, \tag{40}$$

where $\mathsf{M}_h = S\chi_3^m / I d_{\mu}$, and $\lambda_0 = \sqrt{d_{\mu}/\chi_1^m}$. Note that $l_* = \lambda_0^{-1}$ is the internal material length scale parameter. This kind of parameter appears within the gradient-type theories of elasticity while it is absent in the classical theory.

For cantilever beam, the boundary conditions can be written as:

$$x = 0: \quad w = 0, \quad w_{,x} = 0, \quad m = 0, \tag{41}$$

$$x = L: \quad M = 0, \quad M_{,x} = Q, \quad m = 0. \tag{42}$$

Finally, from Eqs. (39) and (40), we get the sixth-order ordinary differential equation for beam deflection

$$(w_{,xx} - \lambda^2 w)_{,xxxx} = 0 \tag{43}$$

in contrast to the fourth-order equation of the classical Euler–Bernoulli beam model. Here, $\lambda^2 = \lambda_0^2(1 + \mathsf{M} + \mathsf{M}_h)$, and $\mathsf{M} = (\alpha_1^{\mu})^2/\rho_0 d_{\mu} C_{11}$.

The solution to the formulated boundary-value problems (40)–(43) is as follows:

$$\begin{aligned} w(X) &= \frac{6QL^3}{C_{11}bh^3(1+\Omega)} \left\{ X^2 - \frac{X^3}{3} \right. \\ &\left. + \frac{2\Omega[\exp(\xi)(\exp(-\xi X) - 1 + \xi X) - \exp(-\xi)(\exp(\xi X) - 1 - \xi X)]}{\xi^2[\exp(\xi) - \exp(-\xi)]} \right\}, \\ m(X) &= \frac{12QL\Omega}{\alpha_1^{\mu} bh^3(1+\Omega)} \left[1 - X - \frac{\exp(\xi(1-X)) - \exp(-\xi(1-X))}{\exp(\xi) - \exp(-\xi)} \right]. \end{aligned} \tag{44}$$

Here, $\xi = L\lambda$, $\Omega = \mathsf{M}/(1 + \mathsf{M}_h)$, and $X = x/L$ is the dimensionless space coordinate.

If the local mass displacement effect is neglected ($1/\lambda \to 0$), the governing equation (43) can be reduced to a known fourth order differential equation of the classical Bernoulli–Euler beam theory, namely, $w_{,xxxx} = 0$ [Shokrieh and Zibaei 2015]. The analytical solution for classical theory is as follows:

$$w_{cl}(X) = \frac{6QL^3}{C_{11}bh^3} \left(X^2 - \frac{X^3}{3} \right). \tag{45}$$

6. Numerical calculations and discussions

We now discuss the effect of local mass displacement on mechanical response of nanobeam. To illustrate this effect, the deflection of cantilever beam under the end-point load was plotted in Figures 3–6 for

material PZT-5H. The concentrated force is Q = 1 nN and the geometry of the nanobeam is $L = 500\,\text{nm}$, $h = 20\,\text{nm}$, and $b = 10\,\text{nm}$. The elastic material constants for PZT-5H are $C_{11} = 12.6 \times 10^{10}\,\text{Pa}$, $C_{13} = 5.3 \times 10^{10}\,\text{Pa}$, and $C_{33} = 11.7 \times 10^{10}\,\text{Pa}$. Unfortunately, the relevant parameters d_μ, α_i^μ, and χ_i^m for PZT-5H are not available in the literature. Hence, the material properties related to the local mass displacement (i. e., internal material length scale parameters) adopted here are: $l_* = \sqrt{\chi_1^m/d_\mu} = 3\,\text{nm}$, and $l_{*3} = \sqrt{\chi_3^m/d_\mu} = 1\,\text{nm}$.

Note that based on the Bernoulli–Euler strain-gradient theory [Lurie and Solyaev 2019], the deflection can be calculated as

$$w_{st}(X) = \frac{6QL^5}{c_{11}bh^3\zeta^2 l^2} \times \left(X^2 - \frac{X^3}{3} - \frac{2X}{\zeta^2} + 2\frac{(\exp(\zeta X)-1)(1-\exp(-\zeta))+(\exp(-\zeta X)-1)(1-\exp(\zeta))}{\zeta^3(\exp(\zeta)-\exp(-\zeta))} \right), \quad (46)$$

where l is the material characteristic length scale parameter, and $\zeta = Ll^{-1}\sqrt{1+12l^2/h^2}$.

Solution (46) satisfies the following boundary conditions:

$$x = 0: \quad w = 0, \quad w_{,x} = 0, \quad M^H = 0,$$
$$x = L: \quad M^H = 0, \quad M + P - M^H_{,x} = 0, \quad (M + P - M^H_{,x})_{,x} = Q,$$

where M is the bending moment,

$$M(x) = \int_0^b \int_{-h/2}^{h/2} z\sigma_{11}(x,z)\,dy\,dz, \quad \sigma_{11}(x,z) = -C_{11}z\frac{d^2w(x)}{dx^2},$$

M^H is the higher-order bending moment,

$$M^H(x) = \int_0^b \int_{-h/2}^{h/2} z\tau_{111}(x,z)\,dy\,dz, \quad \tau_{111}(x,z) = -l^2C_{11}z\frac{d^3w(x)}{dx^3},$$

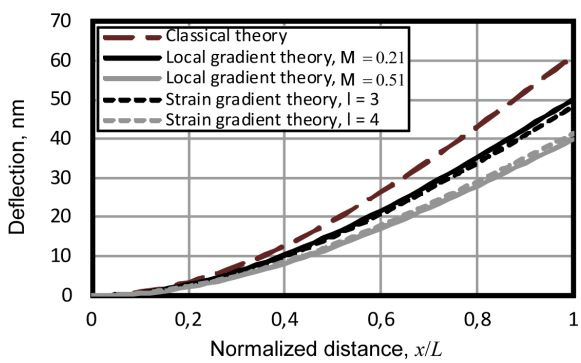

Figure 3. The deflections predicted by the classical theory, local gradient theory and strain gradient theory of the elastic beams.

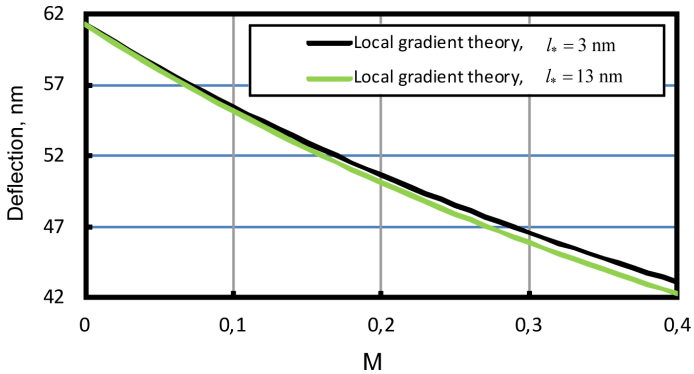

Figure 4. The end-point deflection $w(L)$ versus the coupling factor M for different length scale parameters.

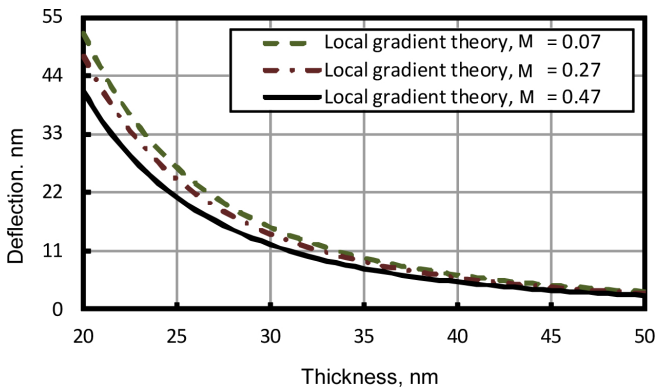

Figure 5. Variation of the end-point deflection $w(L)$ with the beam thickness h.

and P is the higher-order shear forces:

$$P(x) = \int_0^b \int_{-h/2}^{h/2} \tau_{113}(x, z)\, dy\, dz, \quad \tau_{113} = -l^2 C_{11} \frac{d^2 w(x)}{dx^2}.$$

A comparison of the deflection between the analytical solution (45) for classical theory, solution (46) for strain-gradient theory, and solution (44) for local gradient theory is presented in Figure 3. The deflection predicted by the local gradient beam theory is smaller than that by the classical elastic Bernoulli–Euler beam theory. Such a result describes the experimental data reported in the literature and agrees well with the results obtained within the strain-gradient theory of beam. The graphs in Figure 4 show that the beam deflection essentially depends on the coupling factor M. An increased parameter M the beam deflection decreases.

The deflection of the end-point of cantilever beam versus the different beam thickness and length are shown in Figures 5 and 6, respectively. As it follows from Figure 5, the deflection in the local gradient beam theory increases if the beam thickness decreases. This effect became more significant when the thickness of the nanobeam became comparable to the internal material length scale parameter.

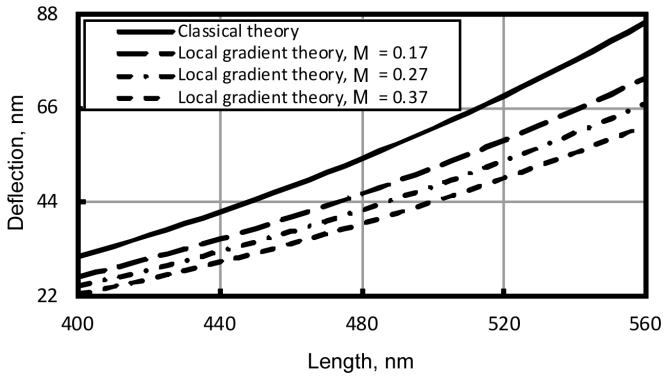

Figure 6. Variation of the end-point deflection $w(L)$ with the beam length L.

Note that the beam stiffness is directly related to the deflection. Therefore, the stiffness based on the relations of local gradient elasticity is higher than that of predicted by classical theory, i. e., the local mass displacement being taken into account stiffens the elastic cantilever nanobeam.

Note that the analytical solution (44) can be used to evaluate material constants pertinent to the local mass displacement. Indeed, based on formula (44), we get

$$\Omega = \frac{QL^3/3 - w(L)C_{11}I}{QL^3 g(\zeta) + w(L)C_{11}I}, \tag{47}$$

where $\zeta = L/l_* >> 1$ and $g(\zeta) = (\text{th}\zeta - \zeta^{-1})/\zeta \approx \zeta^{-1}$. The mechanical deflection $w(L)$ of nanocantilever beam subjected to the end-point loading can be defined from force-displacement measurements with the help of atomic force microscopy or other techniques of mechanical property measurement [Hardwick 1987; Weihs et al. 1988; Liebold and Müller 2015]. The length scale parameter l_* can be evaluated using the methods of molecular dynamics or lattice theory [Askar et al. 1970]. Then, based on formula (47), the material constant Ω can be evaluated using the known values of the concentrated force Q, beam geometric properties (i.e., b, h and L), elastic module C_{11}, beam deflection $w(L)$ and length scale parameter l_*.

7. Conclusion

In the present study, the classical theory of elasticity is extended by taking account of non-diffusive and non-convective mass flux associated with the possible changes in the material microstructure. This flux is related to the process of local mass displacement. New physical quantities associated with this process are introduced and an additional balance equation for these quantities is formulated. Based on the total energy balance equation and on the principle of frame-indifference, a fundamental system of coupled nonlinear equations of local gradient theory of elastic solids is derived. Within the framework of this theory, the set of conjugate variables is complemented by two additional pairs of variables (μ'_π, ρ_m) and $(\boldsymbol{\pi}_m, \nabla\mu'_\pi)$, related to the local mass displacement. The local mass displacement being taken into consideration leads to the appearance of an additional nonlinear mass force in the equation of motion and to the redefinition of the stress tensor $\hat{\boldsymbol{\sigma}}_*$. It is shown that the linear relations of the local gradient elasticity can be also formulated within a framework of the variational principle.

A simple cantilever problem with Bernoulli–Euler kinematics is investigated to illustrate the efficiency of the theory. The governing equations of local gradient Bernoulli–Euler nanobeam model and corresponding boundary conditions are derived from a variational principle. An analytical solution to the resultant differential equation of the sixth order is derived and the effect of the local mass displacement on beam behavior under the end-point load is discussed. It is shown that the deflection within the local gradient theory is smaller than that in the classical Bernoulli–Euler nanobeam model. This indicates that the local mass displacement being taken into account stiffens the nanocantilever beam. The obtained result agrees well with the strain gradient theory as well as with the data of experimental investigations available in the scientific literature. The possibility of the evaluation of new material constants associated with the local gradient elasticity is pointed out. It is shown that the developed local gradient Bernoulli–Euler micro-beam model recovers the classical Bernoulli–Euler beam theory for vanishing length scale parameters.

Acknowledgements

Financial support from the Slovak Science and Technology Assistance Agency registered under number SK-CN-RD-18-0005 and the National Academy of Sciences of Ukraine (grant number 0117U004156) is gratefully acknowledged. The author also thanks Prof. Jan Sladek for helpful discussions.

References

[Akgöz and Civalek 2011] B. Akgöz and Ö. Civalek, "Strain gradient elasticity and modified couple stress models for buckling analysis of axially loaded micro-scaled beams", *Int. J. Eng. Sci.* **49**:11 (2011), 1268–1280.

[Askar et al. 1970] A. Askar, P. C. Y. Lee, and A. S. Cakmak, "Lattice dynamics approach to the theory of elastic dielectrics with polarization gradient", *Phys. Rev. B* **1**:8 (1970), 3525–3537.

[Bredov et al. 1985] M. M. Bredov, V. V. Rumyantsev, and I. N. Toptygin, Классическая электродинамика, Nauka, Moscow, 1985.

[Burak 1987] Y. Burak, "Constitutive equations of locally gradient thermomechanics", *Proc. Acad. Sci. USSR* **12** (1987), 19–23. In Ukranian.

[Burak et al. 2007] Y. Burak, Y. Chaplia, V. Kondrat, and O. Hrytsyna, "Mathematical modeling of thermomechanical processes in elastic solids taking the local mass displacement into account", *Proc. Acad. Sci. USSR* **4**:6 (2007), 45–49. In Ukranian.

[Burak et al. 2008] Y. Burak, V. Kondrat, and O. Hrytsyna, "An introduction of the local displacements of mass and electric charge phenomena into the model of the mechanics of polarized electromagnetic solids", *J. Mech. Mater. Struct.* **3**:6 (2008), 1037–1046.

[Edelen 1969] D. G. B. Edelen, "Protoelastic bodies with large deformation", *Arch. Ration. Mech. Anal.* **34**:4 (1969), 283–300.

[Eltaher et al. 2016] M. A. Eltaher, M. E. Khater, and S. A. Emam, "A review on nonlocal elastic models for bending, buckling, vibrations, and wave propagation of nanoscale beams", *Appl. Math. Model.* **40**:5-6 (2016), 4109–4128.

[Eringen 1966] A. C. Eringen, "Linear theory of micropolar elasticity", *J. Math. Mech.* **15**:6 (1966), 909–923.

[Eringen 1972] A. C. Eringen, "Linear theory of nonlocal elasticity and dispersion of plane waves", *Int. J. Eng. Sci.* **10**:5 (1972), 425–435.

[Eringen 1999] A. C. Eringen, *Microcontinuum field theories, I: Foundations and solids*, Springer, 1999.

[Eringen and Suhubi 1964] A. C. Eringen and E. S. Suhubi, "Nonlinear theory of simple micro-elastic solids, I", *Int. J. Eng. Sci.* **2**:2 (1964), 189–203.

[Espinosa et al. 2003] H. D. Espinosa, B. C. Prorok, and M. Fischer, "A methodology for determining mechanical properties of freestanding thin films and MEMS materials", *J. Mech. Phys. Solids* **51**:1 (2003), 47–67.

[Farajpour et al. 2018] A. Farajpour, M. H. Ghayesh, and H. Farokhi, "A review on the mechanics of nanostructures", *Int. J. Eng. Sci.* **133** (2018), 231–263.

[Green and Rivlin 1964] A. E. Green and R. S. Rivlin, "On Cauchy's equations of motion", *Z. Angew. Math. Phys.* **15** (1964), 290–292.

[Greer and Nix 2005] J. R. Greer and W. D. Nix, "Size dependence of mechanical properties of gold at the sub-micron scale", *Appl. Phys. A Mater. Sci. Process.* **80**:8 (2005), 1625–1629.

[Hardwick 1987] D. A. Hardwick, "The mechanical properties of thin films: a review", *Thin Solid Films* **154**:1-2 (1987), 109–124.

[Hrytsyna 2017] O. R. Hrytsyna, "Influence of subsurface inhomogeneity on the propagation of SH waves in isotropic materials", *Mater. Sci.* (*Russia*) **53**:2 (2017), 273–281.

[Hrytsyna and Kondrat 2019] O. Hrytsyna and V. Kondrat, *Local gradient theory for dielectrics: fundamentals and applications*, Stanford, Singapore, 2019.

[Hrytsyna et al. 2006] O. Hrytsyna, T. Nahirnyy, and K. Tchervinka, "Local gradient approach in thermomechanics", *Phys.-Math. Model. Inf. Technol.* **3** (2006), 72–83. In Ukranian.

[Kafadar and Eringen 1971] C. B. Kafadar and A. C. Eringen, "Micropolar media, I: The classical theory", *Int. J. Eng. Sci.* **9**:3 (1971), 271–305.

[Kakunai et al. 1985] S. Kakunai, J. Masaki, R. Kuroda, K. Iwata, and R. Nagata, "Measurement of apparent Young's modulus in the bending of cantilever beam by heterodyne holographic interferometry", *Exp. Mech.* **25**:4 (1985), 408–412.

[Kondrat and Hrytsyna 2010] V. F. Kondrat and O. R. Hrytsyna, "Mechanoelectromagnetic interaction in isotropic dielectrics with regard for the local displacement of mass", *J. Math. Sci.* (*NY*) **168**:5 (2010), 688–698.

[Lazopoulos and Lazopoulos 2010] K. A. Lazopoulos and A. K. Lazopoulos, "Bending and buckling of thin strain gradient elastic beams", *Eur. J. Mech. A Solids* **29**:5 (2010), 837–843.

[Liebold and Müller 2015] C. Liebold and W. H. Müller, "Applications of strain gradient theories to the size effect in submicro-structures incl. experimental analysis of elastic material parameters", *Bull. TICMI* **19**:1 (2015), 45–55.

[Lurie and Solyaev 2019] S. Lurie and Y. Solyaev, "On the formulation of elastic and electroelastic gradient beam theories", *Contin. Mech. Therm.* **31**:6 (2019), 1601–1613.

[Ma and Clarke 1995] Q. Ma and D. R. Clarke, "Size dependent hardness of silver single crystals", *J. Mater. Res.* **10**:4 (1995), 853–863.

[Marchenko et al. 2009] I. G. Marchenko, I. M. Neklyudov, and I. I. Marchenko, "Collective atomic ordering processes during the low-temperature film deposition", *Proc. Nat. Acad. Sci. Ukraine* **10** (2009), 97–103. In Russian.

[Mindlin 1964] R. D. Mindlin, "Micro-structure in linear elasticity", *Arch. Ration. Mech. Anal.* **16** (1964), 51–78.

[Mindlin 1965] R. D. Mindlin, "Second gradient of strain and surface-tension in linear elasticity", *Int. J. Solids Struct.* **1**:4 (1965), 417–438.

[Mindlin and Tiersten 1962] R. D. Mindlin and H. F. Tiersten, "Effects of couple-stresses in linear elasticity", *Arch. Ration. Mech. Anal.* **11** (1962), 415–448.

[Niiranen et al. 2019] J. Niiranen, V. Balobanov, J. Kiendl, and S. B. Hosseini, "Variational formulations, model comparisons and numerical methods for Euler–Bernoulli micro- and nano-beam models", *Math. Mech. Solids* **24**:1 (2019), 312–335.

[Reddy 2007] J. N. Reddy, "Nonlocal theories for bending, buckling and vibration of beams", *Int. J. Eng. Sci.* **45**:2-8 (2007), 288–307.

[Repka et al. 2018] M. Repka, V. Sladek, and J. Sladek, "Gradient elasticity theory enrichment of plate bending theories", *Compos. Struct.* **202** (2018), 447–457.

[Shokrieh and Zibaei 2015] M. M. Shokrieh and I. Zibaei, "Determination of the appropriate gradient elasticity theory for bending analysis of nano-beams by considering boundary conditions effect", *Lat. Amer. J. Solids Struct.* **12**:12 (2015), 2208–2230.

[Spagnuolo and Andreaus 2019] M. Spagnuolo and U. Andreaus, "A targeted review on large deformations of planar elastic beams: extensibility, distributed loads, buckling and post-buckling", *Math. Mech. Solids* **24**:1 (2019), 258–280.

[Tahaei Yaghoubi et al. 2018] S. Tahaei Yaghoubi, V. Balobanov, S. M. Mousavi, and J. Niiranen, "Variational formulations and isogeometric analysis for the dynamics of anisotropic gradient-elastic Euler–Bernoulli and shear-deformable beams", *Eur. J. Mech. A Solids* **69** (2018), 113–123.

[Thai et al. 2017] H.-T. Thai, T. P. Vo, T.-K. Nguyen, and S.-E. Kim, "A review of continuum mechanics models for size-dependent analysis of beams and plates", *Compos. Struct.* **177** (2017), 196–219.

[Toupin 1962] R. A. Toupin, "Elastic materials with couple-stresses", *Arch. Ration. Mech. Anal.* **11** (1962), 385–414.

[Wang et al. 2016] K. F. Wang, B. L. Wang, and T. Kitamura, "A review on the application of modified continuum models in modeling and simulation of nanostructures", *Acta Mech. Sinica* **32**:1 (2016), 83–100.

[Weihs et al. 1988] T. P. Weihs, S. Hong, J. C. Bravman, and W. D. Nix, "Mechanical deflection of cantilever microbeams: a new technique for testing the mechanical properties of thin films", *J. Mater. Res.* **3**:5 (1988), 931–942.

Received 10 Jan 2020. Revised 13 May 2020. Accepted 27 Jun 2020.

OLHA HRYTSYNA: hrytsyna.olha@gmail.com
Institute of Construction and Architecture, Slovak Academy of Sciences, 84503 Bratislava 45, Slovakia

and

Center of Mathematical Modeling, Pidstryhach Institute for Applied Problems of Mechanics and Mathematics, National Academy of Sciences of Ukraine, 79005 Lviv, Ukraine

JOURNAL OF MECHANICS OF MATERIALS AND STRUCTURES
Vol. 15, No. 4, 2020
https://doi.org/10.2140/jomms.2020.15.489

NONLINEAR DEFLECTION EXPERIMENTS: WRINKLING OF PLATES PRESSED ONTO FOUNDATIONS

NICHOLAS J. SALAMON AND PEGGY B. SALAMON

Experiments are done on elastic plates set unilaterally on foundations or substrates and driven into large deflections by a centrally located load. Previous and related work that report wrinkling in such problems, especially in thin layers on substrates, is reviewed. Deflection contours and tabulated data are given for one wrinkled state. Photographs of others illustrate wrinkling in plates of various geometry. It is found that for certain plate-foundation relative stiffnesses, a characteristic, periodic wrinkling shape evolves, but on the brink of instability that presents a challenge for both analytical solution and numerical simulation.

1. Introduction

The Problem is that of an elastic plate, set unilaterally on a foundation or elastic substrate, undergoing large deflections under a centrally located load. The issue is that such plates may naturally tend to wrinkle. To illustrate transitions from linear to nonlinear behavior, we presented in [Salamon 1984] photographs of The Problem's response for both thick and thin plates, the former deflect into smooth shapes, the latter wrinkle, Figure 1. To relate such intriguing behavior with beam contact problems, Pawlak et al. [1985] drew upon the work of [Dundurs and Stippes 1970; Dundurs 1975], especially the counter-intuitive phenomena that in linear receding contact situations, beams maintain a constant contact length independent of nonzero load. Concurrently, Yu and Stronge [1985] applied an energy method to solve for large deformations in a plate fixed vertically to a circumferential ring yet free to move radially when pressed by a rigid, spherical punch; the plate wrinkled in regions of compressive circumferential stress and they found criteria for its occurrence.

Research on related problems inspired renewed interest in The Problem: wrinkles appear in thin surface layers attached to elastic substrates that undergo compression; for examples, see [Sun et al. 2012; Cerda and Mahadevan 2003; Huang et al. 2005]. Terminology varies (buckling, folding, blistering) as in [Dong et al. 2016; Chen and Hutchinson 2004; Ortiz and Gioia 1994]; "snapping" appears in [Holmes 2009] and "bifurcation" in [Masters and Salamon 1994].

Applications of The Problem further fire interest: examples include [Trejo et al. 2013] on bacteria, [DUMAIS 2007] on plant leaves, [Srinivasa and Ross 2005] on designing shapes, [Wang et al. 2019] on Van der Waals materials, [Semler et al. 2014] on nanotube-polymer bilayers. Pertinent applications involve the mechanics of exoskeletons on soft substrates; e.g., [Martini and Barthelat 2016] on hard plates both bonded and not bonded to soft substrates.

Several works employ experiments to address The Problem, but do not report wrinkling: [Kaiser 1936] measures large deflections in a thin square plate, simply supported, but "free-standing", and does finite

Keywords: plate, nonlinear, deflection, foundation, unilateral, contact, wrinkling.

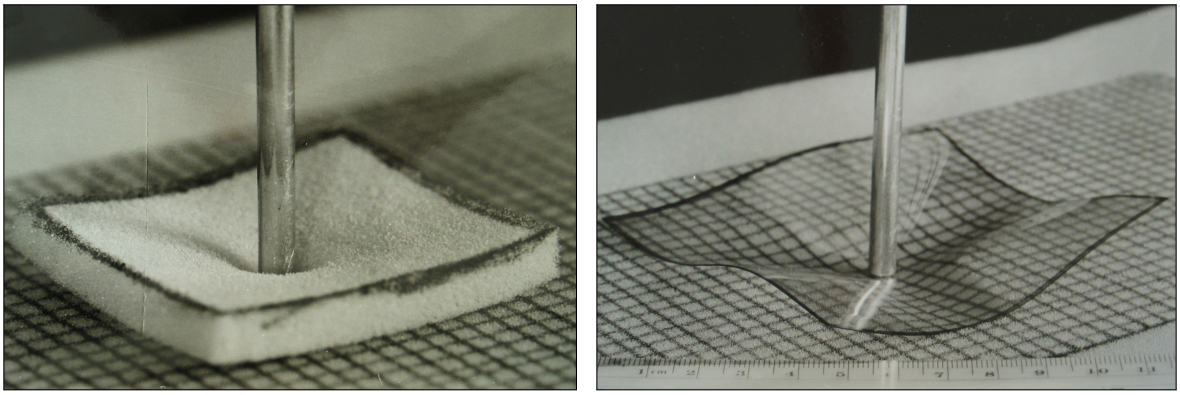

Figure 1. Plate deflection: linear smooth (left) and nonlinear wrinkled (right). From [Salamon 1984].

difference calculations over a declared "symmetric" triangular region that disagree with experiments only where, notably, the in-plane forces go compressive; [Laermann 1981a] combines photoelasticity and moiré methods with difference analysis to solve nonlinear differential equations for centrally loaded plates resting on elastomeric substrates; [Laermann 1981b] extends experiments to include strain gage methods; [Klučka et al. 2014] employs a proprietary apparatus to measure deflection in an edge-loaded circular plate resting on an elastic foundation; the plate may be too stiff or insufficiently loaded to wrinkle. The role of in-plane compression is paramount: indeed it is seen in [Timoshenko 1940, p. 332] and [Timoshenko and Woinowsky-Krieger 1959, p. 399] that nonlinear bending of plates generates in-plane compressive forces.

But in what may be the first report of wrinkling behavior, Biot [1959] finds surface wrinkling in an analytical solution of a semi-infinite viscoelastic medium under compression. Although a half-space deviates from The Problem, visco-effects are very much of interest.

This work presents both laboratory and desktop experiments. One deflection state is graphically shown and quantitatively tabulated. Observations of similar experiments are described. Photographs of desktop experiments are presented for plates of various geometry resting on flat soft foundations and on a stiff ring. Stability of and bifurcation in plate response and behavior of the foam foundation material are discussed.

2. Laboratory experiments

The objective of the laboratory experiments is to observe the response of a plate as it develops and measure a developed deflection state while holding it constant on laboratory models of The Problem. The experiments are done using a Tinius Olsen Universal Testing Machine to apply downward load through a 25.4 mm diameter, flat-bottomed rod centered on a model, each of which comprise a flat plate freely resting upon a foam foundation that sets on the tabletop of the machine; see Figure 2. Observations were made as the load on the model was increased until a desired end-state was reached, then the position of the machine crosshead was held constant while measurements of this deflection state were taken. These were obtained by traversing, magnetically clamping and reading an analog dial indicator, 0 to 25.4 mm

Figure 2. Plate on foam under load.

range (± 0.01 mm accuracy), attached through extension rods to a magnetic base, at all grid intersections that could be reached; five to six grid points near the loading rod that could not be reached and several at two corners that lifted out of range of the instruments were determined by a two-dimensional quadratic curve fit using surrounding data; the measured descent of the loading rod provided a center point datum. Experiments were run on several rectangular plates. It should be noted that the Tinius Olsen machine, over-sized by far for these experiments, maintained crosshead position, although load read-out oscillated.

2.1. ***Properties of a square plate.*** The plate, of titanium stock, 305 mm square, nominally flat, 0.289 mm average thickness (maximum deviations: $+0.019$ mm, -0.022 mm) has a Young's modulus of 111 GPa as measured by an uniaxial tensile test run on a MTS 810 Material Test System. Poisson's ratio was not measured, nominally it's 0.34.

2.2. ***Properties of the foam foundation.*** The foundation material, polyurethane packing foam, density $27.9\,kg/m^3$, dimensions 305 mm square, 48.6 mm thick, is used in all testing machine experiments. Properties of the foam, complicated by its cellular structure, were determined through five compression tests run on the MTS 810 machine using two samples, each 108 mm diameter, 48.6 mm thick. In order to closely conform with conditions in the plate deflection experiments, test samples were oriented exactly the same as in the experiments and compressed between nonporous steel platens (hence deviating from the strict ASTM D3574 procedure) at an average load rate of 0.5 N/s. Both Stress and Poisson's ratio versus strain were slightly nonlinear over the full range of strain $[0, -64)\%$, but (1) for the strain range $(-0.2\%, -12.7\%)$, where 12.7% is the maximum strain in the plate bending experiments, the Young's modulus, averaged over four of the tests (one outlier dropped), is 35.3 kPa (maximum deviations $+2.7$, -1.7 kPa); (2) over the full strain range in one test, six measurements of circumference were made and converted for calculation of transverse strain; after dropping an outlier at low load, a curve fit to the remaining data gives Poisson's ratio as $0.1602 \times \text{strain} + 0.0988$. Single measurements in three other tests corroborate this equation. At large compressive strains the ratio goes negative as reported in the literature, overall this result tallies with [Pierron 2010, Figures 19 and 25] and with [Widdle et al. 2008]. It should

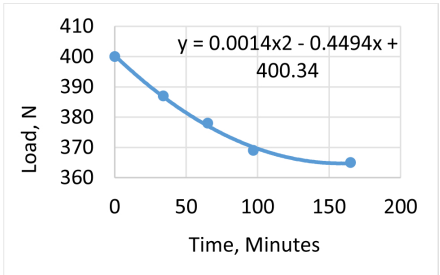

Figure 3. Load decrease with time while holding center deflection constant. Deflection contours in millimeters for the model in Section 2 show a trilobate shape.

be noted that all foam samples visually displayed full recovery after loading, hence the material appears to be elastic or, as indicated Figure 3, viscoelastic which shows the load decrease while the machine crosshead holds the center deflection of the square titanium plate constant.

2.3. ***The square plate deflections.*** Deflections, measured at points on a 12×12 grid drawn onto the top surface of the plate, required 2.75 hours to complete each of two passes. The first pass measured flatness of the model while it was held just snug by the loading rod; either model or plate could be slid horizontally by hand and the Tinius Olsen displayed an oscillating load too small to be reliable. Out-of-flatness ranged from -0.12 mm to $+0.56$ mm at one corner. The machine crosshead was then lowered slowly until the plate wrinkled into an end-state, Figure 2, center deflection 6.15 mm, load 400 N. As the load passed through 267 N, one quadrant, say, snapped into a lobate shape. (A shape characterized by radial valleys between radial ridges that resemble lobes.) The second pass measured deflections at points on the 12×12 grid while this center deflection was held constant. As readings were taken, the load to hold the center deflection constant decreased quadratically, Figure 3, over the 2.75 hours to 365 N, indicating time-dependent viscoelastic behavior of the foam. After unloading, both plate and foam fully recovered with no permanent set visible. Deflection readings minus out-of-flatness readings were processed using Mathematica 12.0 to obtain the plate deflection state shown in Figure 2 and as contours in Figure 4 with respective numerical values in Table 1, where values in red were obtained by a curve fit through neighboring values and those in blue are measured, but lie between grid points. These special values result from loading rod interference with the instruments.

3. Other model experiments

For tests run on several rectangular plates resting upon the same foam material, observations confirm the above deformation state and show an effect of aspect ratio, level of load and foundation to plate relative stiffness.

Two sister plates, same dimensions and material as in Section 2, evolved under load into trilobate shapes, similar in magnitude and pattern: one smoothly; the other snapped into position as did the plate in Section 2.3. The loading rod left a slightly visible permanent set in one plate. The foam recovered completely to the eye.

Two plates, much thinner, cut from 0.089 mm thick stainless steel roll stock, generated mixed results, perhaps in part due to their curvature. One, 305 mm square, lifted-off the foundation at all corners,

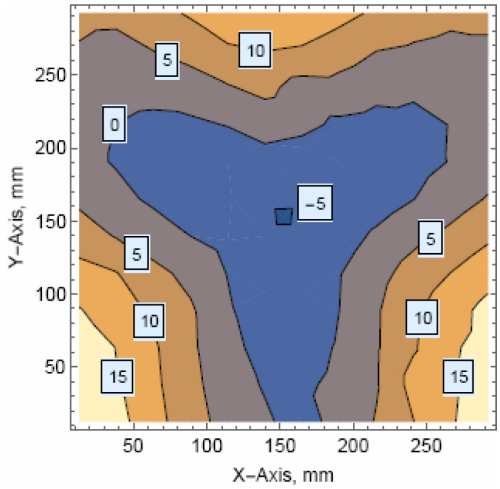

Figure 4. Deflection contours in millimeters for the model in Section 2 show a trilobate shape.

22.40	22.81	25.88	15.32	11.76	7.44	4.01	1.35	1.32	2.54	4.19	7.39
16.81	15.77	14.53	12.17	10.16	4.67	1.35	–0.38	–0.05	1.83	2.08	7.16
11.71	11.05	10.67	9.22	6.38	2.31	–0.81	–1.88	–1.09	1.60	5.05	8.26
7.06	6.30	5.79	5.64	3.61	–0.03	–2.92	–3.35	–0.89	2.72	6.71	10.57
3.12	2.36	1.55	0.66	–0.20	–1.52	–4.32	–3.63	0.20	4.60	9.22	13.46
0.76	–0.46	–1.88	–3.18	–3.94	–3.07	–3.63	0.05	2.11	6.32	10.08	14.35
–2.21	–0.86	–2.24	–3.53	–4.17	–3.18	–3.73	–1.40	1.30	2.97	9.45	13.61
1.96	1.14	0.51	–0.03	–0.25	–2.43	–4.75	–3.94	–0.94	3.28	7.42	11.53
5.28	4.62	4.50	4.47	3.30	0.89	–2.51	–3.78	–1.63	1.55	5.05	9.19
9.91	11.89	9.47	9.04	7.01	3.68	–0.10	–1.75	–1.30	0.84	4.29	7.49
14.76	14.58	14.35	12.90	10.06	6.22	2.59	0.20	0.13	1.24	3.51	6.32
16.51	17.05	16.68	16.51	13.13	9.12	5.33	2.64	1.83	2.06	4.04	6.32

Table 1. Deflection values in millimeters for the model in Section 2. Curve-fit values are in red, those measured between grids are blue. The center deflection (drop of machine crosshead) is −6.15 mm.

one diagonally opposite pair significantly higher than the other, denoting twist. The second plate, 178×305 mm, deformed into a near-trilobate shape, then upon subsequent reload, into a clear trilobate shape. Afterward, permanent set under the loading rod was evident in both plates.

An aluminum plate, 305 mm square, 0.946 mm thick, deformed smoothly into an unsymmetric bending mode, lifting off along two opposite edges and at all corners under central loads up to 800 N that left a permanent set under the loading rod.

Another aluminum plate, $254 \times 305 \times 1.52$ mm, deformed into a slightly unsymmetric, beam-like bending mode about the short dimension with slight liftoff on one end of the long dimension, the remainder in contact.

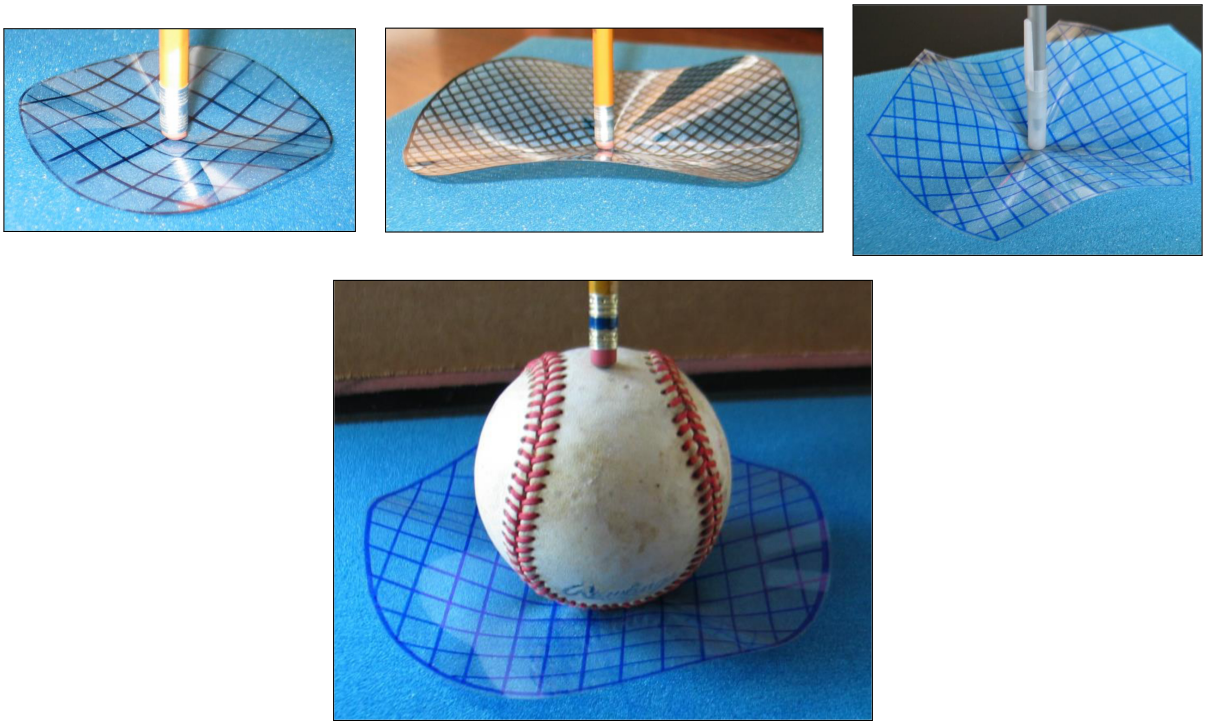

Figure 5. Top row: circular (left), elliptic (middle) and hexagonal (right) plates on foam, showing trilobate wrinkles. Below: Circular plate on foam, small punch, four lobes.

4. Desktop experiments

The desktop experiments are done with plastic plates set on two types of foundations, flat cushioning foam, as in Figures 5, and a stiff plastic jar lid (diameter 11.3 cm), as in Figures 6. On the foam, a concentrated force in the form of a pencil or pen is applied to circular, elliptical, and hexagonal plates (Figure 5, top row), and a punch-like load, a small ball, is applied to a circular plate (Figure 5, bottom). Similarly, on the jar lid, a circular plate is depressed by a punch-like load, a large ball (Figure 6, left) and a concentrated force (Figure 6, right). The plates are cut from 3M transparency film, PP2200, consisting

Figure 6. Circular plate on lid. Left: large punch, five lobes. Right: concentrated load, trilobate wrinkles.

of polyethylene terephthalate plastic, 0.1 mm thick. In Figures 5 and 6, the maximum number of wrinkles each model is capable of generating is displayed: three lobes under a concentrated load, four under the small-sized ball, five under the large one. It is noted that the jar lid limited the depth of deflection at the center to approximately 1.5 cm enabling that point to be held steady at maximum depression.

5. Discussion of results

When driven into large deflections, thin plates unilaterally set on foundations may wrinkle, forming a characteristic shape described herein as lobate. In the present experiments, under a central, concentrated increasing load, this shape terminates as trilobate. Under an increasing punch-like load, wrinkling may progress through more than three lobes. Experience with the experiments demonstrates that this behavior may not be smooth, indeed, for stiff plates on soft foundations, wrinkling may not occur at all, as witnessed in pressing the aluminum plates into the foam foundation. In general, with increasing load, in-plane compression develops, plates become inherently unstable and their response may bifurcate along different paths. Yet when unloaded, all plates studied (as well as foam foundations) fully recovered their flatness, the exception being some metal plates that yielded under the loading rod. Hence, to the eye, wrinkling in plates and compression of the foam foundation appears to be reversibly elastic.

5.1. ***Instability under concentrated load.*** For the metal plates machine loaded at a slow rate, of those that wrinkled, only one plate smoothly formed a trilobate shape; for all others, the third lobe would snap to complete the trilobate shape. This behavior may be subtle, neither visibly obvious, nor distinctly audible.

For the plastic plates, hand loading provided freedom to play. Under a rapid concentrated load, sometimes plates on the foam foundation developed a trilobate end-state directly. Most times, particularly under light load or a slow load rate, lobes tend to form stepwise: first one or two smoothly, then for the third and final lobe, perturbation might be required, i.e., in the form of flicking the plate with a finger.

5.2. ***Bifurcation under concentrated load.*** Sometimes a plate, metal or plastic, will develop one or two lobes that monotonically grow with increasing load to reach a stable end-state without launching additional lobes. At that point, perturbation has no effect. One example is the hexagonal plastic plate under a slowly increasing concentrated load: (1) sometimes an edge lifts off smoothly followed by a second opposite edge, both now proceed to a stable end-state — flicking does not trigger the third lobe; (2) other times, one corner lifts off smoothly followed by the snap of an opposite edge, then under increasing load, a second corner lifts off to form a stable trilobate shape. These two different responses denote bifurcation.

5.3. ***Response under punch-like loads.*** Intrigued by Yu and Stronge's problem [Yu and Stronge 1985], circular plastic plates were set on the jar lid. When subjected to punch-like loads, they wrinkled, but in a manner different from the analytical predictions in [Yu and Stronge 1985]. In Figure 6, wrinkles emanate from the center and extend radially, reaching an apex at a plate's periphery whereas in their analysis, wrinkles terminate there because of the imposition of zero vertical displacement around the plate edge. Furthermore, they report criterion for as many as eight wrinkles; the jar-lid experiments reveal a maximum of five wrinkles. (Not shown: a circular plastic plate set upon the open glass jar itself, which allows a deeper center depression, generates up to seven wrinkles with perturbation.) Hence the

problems differ: their boundary conditions constrain the response, apparently enabling solution of a stable, well-posed problem; the unilateral conditions herein allow freedoms that permit instability.

Under increasing punch-like loads applied by either ball to circular, hexagonal and rectangular plastic plates set on the foam foundation, as in Figure 5, bottom, wrinkles beyond the first snapped into place, but did not require perturbation. The maximum number of wrinkles generated were five for the circular and hexagonal plates under the large ball, four for all others (not shown).

5.4. ***Relative stiffness ratio.*** In an attempt to predict wrinkling, a plate-to-foundation stiffness ratio for rectangular plates, $\mathrm{SR} = k_p/k_f$, is defined where $k_p = E_p t^3/L^2$ is the plate stiffness derived from plate flexure [Timoshenko and Woinowsky-Krieger 1959] and its associated rigidity modulus and where $k_f = E_f wL/d$ is the foundation stiffness derived from uniaxial deformation. For the plate, $w < L$ are its width and length, respectively, t is its thickness and E_p is the elastic modulus. For the foundation, d is the actual or a characteristic depth of the foundation (the foam in this case) and E_f is an elastic modulus in compression. To orders of magnitude, for the four metal plates above that wrinkled, $\mathrm{SR} \le 10^{-4}$, for four that did not wrinkle, $\mathrm{SR} \ge 10^{-3}$.

But a contradiction arose: $\mathrm{SR} = 2.16 \cdot 10^{-05}$ for the square stainless steel plate, yet it did not wrinkle in a lobular fashion, it bent into a twist; ironically, the rectangular stainless steel plate with $\mathrm{SR} = 3.71 \cdot 10^{-05}$, did wrinkle. Could these two very thin, rather flimsy sheets lack sufficient structural integrity to act as plates? ...Making their behavior a toss-up? With more certainty, the three titanium plates, $\mathrm{SR} = 4.26 \cdot 10^{-04}$, did wrinkle, and the two aluminum plates, $\mathrm{SR} = 4.76 \cdot 10^{-02}$ and $9.38 \cdot 10^{-03}$, did not wrinkle. Hence, stiffness ratio, while an indicator of wrinkling, is clearly not absolute. For nonrectangular plates, one would have to seek characteristic dimensions.

6. Conclusion

Plates have been well studied — Naruoka [1981] lists 12,717 references, yet deflection-induced wrinkling shown herein does not appear there. The Problem, fundamental in the class of problems dealing with plates on foundations, has come to the fore through a manifold of applications dealing with films or coatings on substrates, particularly in situations where bonding is weak. It is shown that the wrinkling of plates provides important lessons in mechanics. In analysis, such wrinkling demonstrates that the assumption of symmetry, common in linear mechanics, does not carry over to nonlinear mechanics: indeed, the misapplication of symmetry was done by one reference cited herein. In education, this seemingly simple problem vividly illustrates that the transition from linear to nonlinear behavior concomitant with the onset of instability and bifurcation in response, escalates its complexity and presents a challenge to both analytical solution and numerical simulation. The wrinkling of plates into such a characteristic shape denotes protean behavior (after Proteus, the shape-shifting Greek God); however, students bestowed upon it a more memorable description: “the flying carpet problem”.

Acknowledgements

We thank C. Bakis for advice and use of his laboratories; A. Brown and W. Dyer for laboratory assistance; R. P. McNitt for the purchase of gages; N. Carrier, E. Dunkelberger and B. Genet for machining help; D. Fura and D. Faulds for Civil Engineering laboratory time; M. LaCorte, MTS Systems for advice; and F. Schlegel, Harkness Industries, for materials.

References

[Biot 1959] M. A. Biot, "Folding of a layered viscoelastic medium derived from an exact stability theory of a continuum under initial stress", *Quart. Appl. Math.* **17** (1959), 185–204.

[Cerda and Mahadevan 2003] E. Cerda and L. Mahadevan, "Geometry and Physics of Wrinkling", *Phys. Rev. Lett.* **90**:7 (2003), art. id. 074302.

[Chen and Hutchinson 2004] X. Chen and J. W. Hutchinson, "Herringbone Buckling Patterns of Compressed Thin Films on Compliant Substrates", *J. Appl. Mech.* (*ASME*) **71**:5 (2004), 597–603.

[Dong et al. 2016] J. H. Dong, X. Ma, J. E. Mills, and Z. G. Yan, "A Review of Skin Buckling Theory in Composite Members", *Appl. Mech. Mat.* **846** (2016), 312–317.

[DUMAIS 2007] J. DUMAIS, "Can mechanics control pattern formation in plants?", *Current Opinion in Plant Biology* **10**:1 (2007), 58–62.

[Dundurs 1975] J. Dundurs, "Properties of elastic bodies in contact", pp. 54–66 in *The mechanics of the contact between deformable bodies* (IUTAM Symposium, Enschede, Netherlands, 1974), edited by A. D. de Pater and J. J. Kalker, Delft University Press, 1975.

[Dundurs and Stippes 1970] J. Dundurs and M. Stippes, "Role of elastic constants in certain contact problems", *J. Appl. Mech.* (*ASME*) **37**:4 (1970), 965–970.

[Holmes 2009] D. P. Holmes, *Wrinkling, folding, and snapping instabilities in polymer films*, DS Dissertation, University of Massachusetts Amherst, 2009.

[Huang et al. 2005] Z. Y. Huang, W. Hong, and Z. Suo, "Nonlinear analyses of wrinkles in a film bonded to a compliant substrate", *J. Mech. Phys. Solids* **53**:9 (2005), 2101–2118.

[Kaiser 1936] R. Kaiser, "Rechnerische und experimentelle Ermittlung der Durchbiegungen und Spannungen von quadratischen Platten bei freier Auflagerung an den Rändern, gleichmäßig verteilter Last und großen Ausbiegungen", *Z. Angew. Math. Mech.* **16**:2 (1936), 73–98.

[Klučka et al. 2014] R. Klučka, K. Frydrýšek, and M. Mahdal, "Measuring the deflection of a circular plate on an elastic foundation and comparison with analytical and FE approaches", *Appl. Mech. Mat.* **684** (2014), 407–412.

[Laermann 1981a] K.-H. Laermann, "Hybrid analysis of plate problems", *Experiment. Mech.* **21**:10 (1981), 386–388.

[Laermann 1981b] K.-H. Laermann, "Advanced theoretical and experimental analysis of plates and plates in contact", pp. 135–198 in *New physical trends in experimental mechanics*, Springer, 1981.

[Martini and Barthelat 2016] R. Martini and F. Barthelat, "Stability of hard plates on soft substrates and application to the design of bioinspired segmented armor", *Journal of the Mechanics and Physics of Solids* **92** (2016), 195–209.

[Masters and Salamon 1994] C. B. Masters and N. J. Salamon, "Geometrically nonlinear stress-deflection relations for thin film/substrate systems with a finite element comparison", *J. Appl. Mech.* (*ASME*) **61**:4 (1994), 872–878.

[Naruoka 1981] M. Naruoka, *Bibliography on theory of plates*, Gihodo, Tokyo, 1981.

[Ortiz and Gioia 1994] M. Ortiz and G. Gioia, "The morphology and folding patterns of buckling-driven thin-film blisters", *J. Mech. Phys. Solids* **42**:3 (1994), 531–559.

[Pawlak et al. 1985] T. P. Pawlak, N. J. Salamon, and F. F. Mahmoud, "Beams in receding/advancing contact: Dundurs problems", *J. Appl. Mech.* (*ASME*) **52**:4 (1985), 933–936.

[Pierron 2010] F. Pierron, "Identification of Poisson's ratios of standard and auxetic low-density polymeric foams from full-field measurements", *J. Strain Anal. Engin. Design* **45**:4 (2010), 233–253.

[Salamon 1984] N. J. Salamon, "Visualization of curious phenomena in solid mechanics", pp. 134–137 in *Engineering education: preparation for life: Proc. ASEE 1984 Annual meeting* (Salt Lake City, UT, 1984), 1984.

[Semler et al. 2014] M. R. Semler, J. M. Harris, and E. K. Hobbie, "Wrinkling and folding of nanotube-polymer bilayers", *The Journal of Chemical Physics* **141**:4 (2014), art. id. 044901.

[Srinivasa and Ross 2005] N. Srinivasa and R. Ross, "An automated approach to design shape morphing strategies for reconfigurable surfaces", pp. 164–171 Proceedings of the SPIE - The International Society for Optical Engineering **5757**, 2005.

[Sun et al. 2012] J.-Y. Sun, S. Xia, M.-W. Moon, K. H. Oh, and K.-S. Kim, "Folding wrinkles of a thin stiff layer on a soft substrate", *Proc. R. Soc. A.* **468**:2140 (2012), 932–953.

[Timoshenko 1940] S. P. Timoshenko, *Theory of plates and shells*, McGraw-Hill, New York, 1940.

[Timoshenko and Woinowsky-Krieger 1959] S. Timoshenko and S. Woinowsky-Krieger, *Theory of plates and shells*, 2nd ed., McGraw-Hill, New York, 1959.

[Trejo et al. 2013] M. Trejo, C. Douarche, V. Bailleux, C. Poulard, S. Mariot, C. Regeard, and E. Raspaud, "Elasticity and wrinkled morphology of Bacillus subtilis pellicles", *Proc. Nat. Acad. Sci. USA* **110**:6 (2013), 2011–2016.

[Wang et al. 2019] G. Wang, Z. Dai, J. Xiao, S. Feng, C. Weng, L. Liu, Z. Xu, R. Huang, and Z. Zhang, "Bending of Multilayer van der Waals Materials", *Phys. Rev. Lett.* **123**:11 (2019), art. id116101.

[Widdle et al. 2008] R. Widdle, Jr., A. Bajaj, and P. Davies, "Measurement of the Poisson's ratio of flexible polyurethane foam and its influence on a uniaxial compression model", *Int. J. Engin. Sci.* **46**:1 (2008), 31–49.

[Yu and Stronge 1985] T. Yu and W. Stronge, "Wrinkling of a circular elastic plate stamped by a spherical punch", *Int. J. Solids Struct.* **21**:10 (1985), 995–1003.

Received 28 Feb 2020. Accepted 6 May 2020.

NICHOLAS J. SALAMON: ns1@psu.edu
Engineering Science and Mechanics, The Pennsylvania State University, University Park, PA 16802, United States

PEGGY B. SALAMON: plbsalamon@gmail.com

JOURNAL OF MECHANICS OF MATERIALS AND STRUCTURES
Vol. 15, No. 4, 2020
https://doi.org/10.2140/jomms.2020.15.499

BUCKLING OF CIRCULAR CFDST SLENDER COLUMNS WITH COMPLIANT INTERFACES: EXACT SOLUTION

SIMON SCHNABL AND BOJAN ČAS

The paper presents a new mathematical model and its exact solution for the buckling analysis of circular CFDST slender columns with compliant interfaces between the steel tubes and sandwiched concrete. The exact critical buckling loads are calculated for the first time. The results are compared to the experimental results and good agreement is obtained. A parametric study is also performed to investigate the effects of different parameters on buckling loads. It is shown that buckling loads can be significantly affected by the finite interface compliance.

1. Introduction

Concrete-filled double-skin steel tubular (CFDST) columns are structural members that are increasingly being used worldwide in new building developments. Owning to their good mechanical properties, fire, corrosion, blast and impact resistance and light weight cross-sections they are used as tall piers for bridges, electric transmission towers, underwater pressure vessels, columns in high-rise building, and so on. Nonetheless, when subjected to compressive loading, slender CFDST columns can be prone to buckling.

In the past, several series of test have been performed on short CFDST columns [Han et al. 2004; Tao et al. 2004; Hassanein et al. 2013; Hassanein and Kharoob 2014b; Huang et al. 2010; Li et al. 2012; Yang et al. 2012] and only a few studies exist on slender CFDST columns [Romero et al. 2015; Essopjee and Dundu 2015; Romero et al. 2017; Hassanein and Kharoob 2014a]. Romero et al. [2015; 2017] investigated slender double-tube ultra-high strength concrete-filled tubular columns under ambient temperature and fire. Similarly, Hassanein and Kharoob [2014a] investigated CFDST columns with external stainless steel tubes and Essopjee and Dundu [2015] experimentally and numerically analyzed circular CFDST columns in compression. However, as far as the authors' knowledge is concerned all these studies assumed perfect contact between the components of CFDST columns. In practice, full bonding of steel tubes and sandwiched concrete is impossible to obtain. As a result, always an incomplete or partial connection exists between the steel tubes and concrete core which can have a considerable effect on buckling behaviour of CFDST columns.

The present paper derives a mathematical model and its *exact* solution for investigation of slender CFDST columns with interface compliance between the steel tubes and sandwiched concrete. The theoretical basis used in the derivation of this new mathematical model is partially taken from [Schnabl et al. 2007; Kryžanowski et al. 2009], and from [Schnabl et al. 2015], where the concrete-filled steel tubular columns with compliant interfaces was analyzed analytically. The proposed mathematical model is validated to the test and adjusted code (see [Eurocode 2004; SANS 2011]) results obtained in [Essopjee and Dundu 2015]. After the validation, a parametric study is performed by which the effects of different

Keywords: buckling, double-skin, debonding, column, exact.

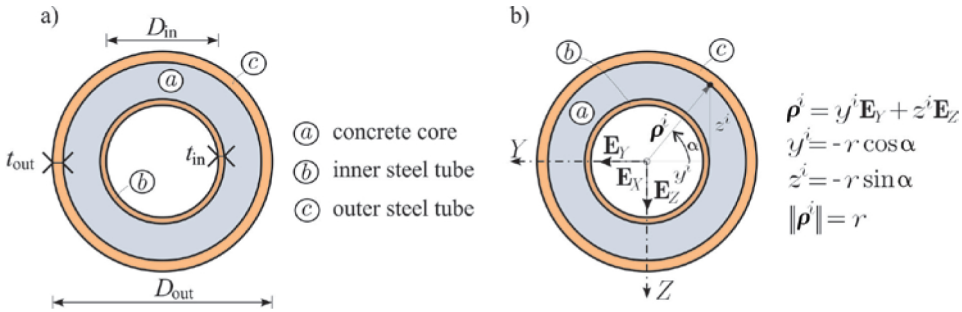

Figure 1. Cross-section of a circular CFDST slender column: details and dimensions (left) and coordinate system (right).

parameters like column slenderness, hollow and thickness ratio, and concrete elastic modulus on the buckling load of CFDST columns is investigated in detail.

2. Problem formulation

2.1. ***Preliminaries.*** We consider a straight, planar, geometrically perfect CFDST slender column shown in Figure 1. The CFDST slender column has an undeformed length L. It consists of sandwiched concrete core, a, concentric inner, b, and outer, c, steel tubes. All these three components are joined together by an interface adhesive layer of negligible thickness and finite stiffness.

The CFDST slender column is placed in the (X, Z) plane of a global Cartesian coordinate system with coordinates (X, Y, Z) and unit base vectors $\boldsymbol{E}_X$, $\boldsymbol{E}_Y$, and $\boldsymbol{E}_Z$. The reference axis of the CFDST slender column is common to all three components. It is parameterized by the undeformed arc-length x. The material particles of the sandwiched concrete core and inner and outer steel tubes are identified by material coordinates (x^i, y^i, z^i), $(i = a, b, c)$ in local coordinate system with coordinates (x, y, z). It is assumed that initially the local coordinate system coincides with the global coordinate system, and then follows the deformation of the CFDST slender column. The CFDST slender column is subjected axially to a conservative compressive load P in such a way, that homogeneous stress-strain state is achieved in the primary configuration of the column.

2.2. ***Preliminaries.*** The formulation of the governing equations of the mathematical model of a CFDST slender column is based on the following basic assumptions as well:

- The sandwiched concrete core, inner and outer steel tubes are prismatic, homogeneous, isotropic and linear elastic.
- A linearized Reissner planar shear-stiff beam theory [Reissner 1972] is used for each component.
- The components are continuously connected and contact stiffness is finite and constant.
- The components can deform relative to each other, i.e. generalized slips in axial, radial and circumferential direction can occur.
- Only the global type of instability can occur.
- The generalized slips are small.

2.3. ***Algebraic-differential equations of a CFDST column.*** The linearized Reissner algebraic-differential equations of the CFDST column are kinematic, equilibrium, constitutive and constraining equations along with the boundary conditions. In this paper, a compact comma notation $(\cdot)^i$ will be used, where superscript $i = (a,\ b,\ c)$ indicates to which components the quantity $(\cdot)$ belongs to. Hence, the governing equations of a CFDST column constitute a system of 34 algebraic and first order differential equations with constant coefficients for 34 unknown functions u^i, w^i, φ^i, ε^i, κ^i, R_X^i, R_Z^i, M_Y^i, $\Delta_{X,\text{in}}$, $\Delta_{X,\text{out}}$, $\Delta_{Z,\text{in}}$, $\Delta_{Z,\text{out}}$, $p_{X,\text{in}}$, $p_{X,\text{out}}$:

Kinematic equations

$$\frac{\mathrm{d}u^i}{\mathrm{d}x} - \varepsilon^i = 0, \tag{1}$$

$$\frac{\mathrm{d}w^i}{\mathrm{d}x} + \left(1 - \frac{P}{\sum\limits_i E^i A^i}\right)\varphi^i = 0, \tag{2}$$

$$\frac{\mathrm{d}\varphi^i}{\mathrm{d}x} - \kappa^i = 0, \tag{3}$$

Equilibrium equations

$$\frac{\mathrm{d}R_X^a}{\mathrm{d}x} - p_{X,\text{out}} + p_{X,\text{in}} = 0, \tag{4}$$

$$\frac{\mathrm{d}R_X^b}{\mathrm{d}x} - p_{X,\text{in}} = 0, \tag{5}$$

$$\frac{\mathrm{d}R_X^c}{\mathrm{d}x} + p_{X,\text{out}} = 0, \tag{6}$$

$$\frac{\mathrm{d}R_Z^a}{\mathrm{d}x} - p_{Z,\text{out}} + p_{Z,\text{in}} = 0, \tag{7}$$

$$\frac{\mathrm{d}R_Z^b}{\mathrm{d}x} - p_{Z,\text{in}} = 0, \tag{8}$$

$$\frac{\mathrm{d}R_Z^c}{\mathrm{d}x} + p_{Z,\text{out}} = 0, \tag{9}$$

$$\frac{\mathrm{d}R_Z^a}{\mathrm{d}x} - p_{Z,\text{out}} + p_{Z,\text{in}} = 0, \tag{11}$$

$$\frac{\mathrm{d}R_Z^b}{\mathrm{d}x} - p_{Z,\text{in}} = 0, \tag{12}$$

$$\frac{\mathrm{d}M_Y^i}{\mathrm{d}x} - \left(\frac{E^i A^i}{\sum\limits_i E^i A^i} P\right)\frac{\mathrm{d}w^i}{\mathrm{d}x} - \left(1 - \frac{P}{\sum\limits_i E^i A^i}\right)R_Z^i = 0, \tag{13}$$

Constitutive equations

$$R_X^i - E^i A^i \varepsilon^i = 0, \tag{14}$$

$$M_Y^i - E^i J^i \kappa^i = 0, \tag{15}$$

Constraining equations

$$\Delta_{X,\text{in}} - u^b + u^a = 0, \tag{16}$$
$$\Delta_{X,\text{out}} - u^a + u^c = 0, \tag{17}$$
$$\Delta_{Z,\text{in}} - w^b + w^a = 0, \tag{18}$$
$$\Delta_{Z,\text{out}} - w^a + w^c = 0, \tag{19}$$
$$p_{X,\text{in}} - K_{\text{in}}\Delta_{X,\text{in}} = 0, \tag{20}$$
$$p_{X,\text{out}} - K_{\text{out}}\Delta_{X,\text{out}} = 0, \tag{21}$$
$$p_{Z,\text{in}} - C_{\text{in}}\Delta_{Z,\text{in}} = 0, \tag{22}$$
$$p_{Z,\text{out}} - C_{\text{out}}\Delta_{Z,\text{out}} = 0, \tag{23}$$

Boundary conditions
$x = 0$:

$$S_1^i + R_X^i(0) = 0 \quad \text{or} \quad u_1^i - u^i(0) = 0, \tag{24}$$
$$S_2^i + R_Z^i(0) = 0 \quad \text{or} \quad u_1^i - w^i(0) = 0, \tag{25}$$
$$S_3^i + M_Y^i(0) = 0 \quad \text{or} \quad u_3^i - \varphi^i(0) = 0. \tag{26}$$

$x = L$:

$$S_4^i - R_X^i(L) = 0 \quad \text{or} u_4^i - u^i(L) = 0, \tag{27}$$
$$S_5^i - R_Z^i(L) = 0 \quad \text{or} \quad u_5^i - w^i(L) = 0, \tag{28}$$
$$S_6^i - M_Y^i(L) = 0 \quad \text{or} \quad u_6^i - \varphi^i(L) = 0, \tag{29}$$

where u_k^i and S_k^i (k = 1-6) are the generalized boundary displacements and their complementary generalized forces at the edges of the components of the CFDST column.

2.4. ***Exact solution of buckling equations.*** In order to obtain the exact solution of the system of governing algebraic-differential equations (1)–(23) it is suitable to write the equations (1)–(23) and boundary conditions (24)–(29) in a compact form as a homogeneous system of 18 first order linear differential equations:

$$\frac{\mathrm{d}\boldsymbol{Y}}{\mathrm{d}x}(x) = \boldsymbol{A}\boldsymbol{Y}(x) \quad \text{and} \quad \boldsymbol{Y}(0) = Y_0, \tag{30}$$

where $\boldsymbol{Y}(x)$ is the eigenvector, $\boldsymbol{Y}(0)$ is the vector of unknown integration constants, i.e. generalized displacements and forces at the component's boundary, and $\boldsymbol{A}$ is the constant real 18×18 matrix. The analytical solution of (30) can be given as, see [Perko 1991]

$$\boldsymbol{Y}(x) = \exp^{Ax}\boldsymbol{Y}_0. \tag{31}$$

The vector of unknown integration constants $\boldsymbol{Y}(0)$ can be obtained from the boundary conditions (24)–(29). By inserting (31) into (24)–(29) one obtains a system of 18 homogeneous linear algebraic equations

for the same number of unknown integration constants

$$\boldsymbol{K}\boldsymbol{Y}_0 = \boldsymbol{0}, \tag{32}$$

where $\boldsymbol{K}$ is the tangent stiffness matrix. A non-trivial solution of (32) is obtained from the condition of vanishing determinant of the tangent stiffness matrix $\boldsymbol{K}$. For the known geometric parameters, the only unknown is the applied load P. As a result, the critical buckling load P_{cr} is determined from the characteristic equation

$$|\boldsymbol{K}| = 0, \tag{33}$$

and is equal to the lowest eigenvalue of (31). In this case, the analytical expressions are obtained using Mathematica. However, these analytical expressions are too extensive to be shown in the paper in a closed-form, except for the two limiting cases, namely for perfectly bonded and perfectly debonded case. Thus, for the CFDST column with perfectly bonded interface between the sandwiched concrete core and the steel tubes, the critical buckling load is

$$P_{\text{cr}} = \sum_i P_{\text{cr}}^i = P_{\text{cr}}^a + P_{\text{cr}}^b + P_{\text{cr}}^c = \frac{\pi^2 \sum_i E^i J^i}{(1+\varepsilon)L^2} = \frac{\pi^2 (E^a J^a + E^b J^b + E^c J^c)}{(1+\varepsilon)L^2}, \tag{34}$$

where P_{cr}^a, P_{cr}^b, and P_{cr}^c are the buckling loads of the concrete core, inner and outer steel tubes, respectively. On the other hand, in the limiting case when the interface is fully debonded the critical buckling loads is

$$P_{\text{cr}} = P^a + P_{\text{cr}}^b + P^c = (E^a A^a + E^c A^c)\varepsilon + \frac{\pi^2 E^b J^b}{(1+\varepsilon)L^2}, \tag{35}$$

where P^a and P^c are the corresponding axial loads carried by the concrete core and outer steel tube, respectively.

3. Results and discussion

3.1. ***Validation.*** The principal aim of this section is to check and demonstrate the validity of this mathematical model and its exact solution in comparison to the available experimental and design results in the literature. Therefore, the validation of the critical buckling loads of CFDST slender columns uses the four available specimens in the literature experimentally tested in [Essopjee and Dundu 2015] and whose geometric and material properties are given in Table 1. Further, the exact critical buckling loads are compared to the adjusted (see [Eurocode 2004; SANS 2011]) design predictions obtained in [Essopjee and Dundu 2015] for the same four specimens. The results are given in Table 2 and Figure 2.

Specimen	L[cm]	D_{out}[cm]	t_{out}[mm]	D_{in}[cm]	t_{in}[mm]	E_a[kN/cm^2]	E_b, E_c[kN/cm^2]
S139.2-2.5	250	13.92	3.0	7.6	2.0	2821	20323.3
S152.4-2.5	250	15.24	3.0	7.6	2.0	2821	20622.0
S165.1-2.5	250	16.51	3.0	7.6	2.0	2821	20353.0
S193.7-2.5	250	19.37	3.5	7.6	2.0	2821	20796.2

Table 1. Material and geometric properties of CFDST columns.

Specimen	N_{TEST}[kN]	N_{EC4}[kN]	N_{SANS}[kN]	P^{*}_{cr}[kN]	P^{**}_{cr}[kN]	$C(P_{cr} = N_{TEST})$[kN/cm^2]
S139.2-2.5	732.1	692	679	672.1	1674.2	6.15 10^{-4}
S152.4-2.5	949.0	920	882	792.4	2314.5	2.80 10^{-4}
S165.1-2.5	1036.5	1011	1028	907.7	3044.6	1.86 10^{-4}
S193.7-2.5	1458.7	1272	1467	1270.5	5793.8	2.04 10^{-4}
					Average	3.21 10^{-4}

Table 2. Comparison of exact, test and adjusted EC4 and SANS code predictions. P^{*}_{cr} and P^{**}_{cr} are the buckling loads of, respectively, a fully debonded and a fully bonded CFDST column.

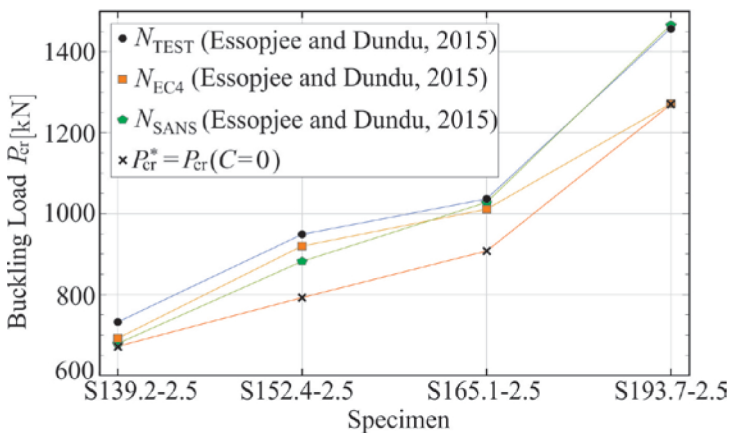

Figure 2. Comparison of exact, test and adjusted code predictions of buckling loads of circular CFDST slender columns.

It can be seen from Table 2 and Figure 2 that the code buckling loads are in general smaller than test results. The test buckling loads of all four specimens are between the results for fully debonded ($P^{*}_{cr} = P_{cr}(C = 0)$) and fully bonded ($P^{**}_{cr} = P_{cr}(C = \infty)$) CFDST slender columns. In fact, in these particular cases, the test results are closer to the exact buckling loads of fully debonded CFDST columns. In addition, with the inverse analysis, one can calculate the corresponding contact stiffness K and C from the equality of test and analytical buckling loads, i.e. $P_{cr} = N_{TEST}$. Nevertheless, it is found out that the critical buckling load of a CFDST slender column is independent of K. Thus, only C that corresponds to the test results obtained in [Essopjee and Dundu 2015] are given in Table 2. The exact buckling loads are in good agreement with the test results if adequate contact stiffness is used in the calculations.

The exact buckling loads are also compared to the numerical results obtained by finite element (FE) analysis in [Hassanein and Kharoob 2014a]. Table 3 shows a summary of the comparison for different columns and various C. The geometric and material data of each column are given in [Hassanein and Kharoob 2014a]. It is clear from Table 3 that P_{cr} is decreasing with increasing the P_{cr} and decreasing C.

For intermediate slender column $C5$, the FE buckling load P_{FE} is always smaller than P_{cr} irrespective to C. In case of other columns, e.i. $C6$–$C17$, the FE buckling load P_{FE} is always between the two limits, i.e. fully debonded ($C = 0$) and perfectly bonded ($C = \infty$) interface between the concrete and steel.

			P_{cr}[kN]				
Column	λ	P_{FE}[kN]	$C=0$	$C=10^{-6}$	$C=10^{-5}$	$C=10^{-4}$	$C=\infty$
C5	51	9440	12711	12733	12926	14775	35992
C6	62	8431	8621	8652	8936	11512	24410
C7	73	7358	6228	6273	6661	9891	17636
C8	84	6591	4709	4768	5273	8910	13335
C9	94	5803	3686	3759	4391	8039	10435
C10	105	5014	2963	3054	3816	7109	8388
C11	116	4393	2433	2544	3433	6186	6889
C12	127	3951	2033	2166	3169	5354	5759
C13	138	3140	1725	1881	2974	4641	4885
C14	149	2827	1482	1661	2812	4043	4197
C15	160	2455	1287	1491	2659	3544	3644
C16	171	2156	1128	1358	2501	3127	3194
C17	182	1971	997	1253	2336	2776	2822

Table 3. Comparison of analytical buckling loads with the FE buckling loads from [Hassanein and Kharoob 2014a].

3.2. ***Parametric study.*** The derived mathematical model and its exact solution are used to analyse the effects of different parameters like column slenderness ratio (λ), hollow ratio (χ), concrete elastic modulus (E_a), and thickness ratio (τ) on buckling loads (P_{cr}) of CFDST slender column, in this case the specimen S139.2-2.5 is used in the analysis. The results are given in Figures 3 and 4.

3.2.1. *Effect of column slenderness ratio.* The column slenderness ratio is generally one of the most important parameters that influence the buckling behaviour of circular CFDST slender columns. Here, the column slenderness ratio is defined as $\lambda = L\sqrt{A}/\sqrt{I}$, where L is the effective buckling length, A is the cross-sectional area and $I$is the moment of inertia of the CFDST column. The effect of λ on P_{cr} is illustrated for different contact stiffness (fully bonded ($C=\infty\,\mathrm{kN/cm^2}$) and fully debonded ($C=0\,\mathrm{kN/cm^2}$), and all in between) in Figure 3, left.

It can be seen that P_{cr} decreases as λ increases. Notice also that the buckling load $\bar{P}_{cr} = P_{cr}(C = 3.21\cdot 10^{-4}\,\mathrm{kN/cm^2})$ that belongs to the average contact stiffness of the selected tested four specimens in [Essopjee and Dundu 2015] is for $\lambda \le 100$ closer to $P^{*}_{cr} = P_{cr}(C=0)$, while for $\lambda > 100$ is closer to $P^{**}_{cr} = P_{cr}(C=\infty)$. Thus, it is seen that for very slender CFDST columns the effect of C on P_{cr} is insignificant and can be neglected.

3.2.2. *Effect of hollow ratio.* The effect of hollow ratio ($\chi = D_{in}/(D_{out}-2t_{out})$) on P_{cr} is shown in Figure 3, middle. This effect is investigated by varying the external tube thickness t_{out}. It can be seen from the graph that increasing χ, which reduces the cross-sectional area of the sandwiched concrete, increases P_{cr}, especially for nearly fully debonded columns, while on the other hand, for fully bonded columns, this effect is negligible. Again, it could be seen that $\bar{P}_{cr}$ is closer to fully debonded CFDST columns.

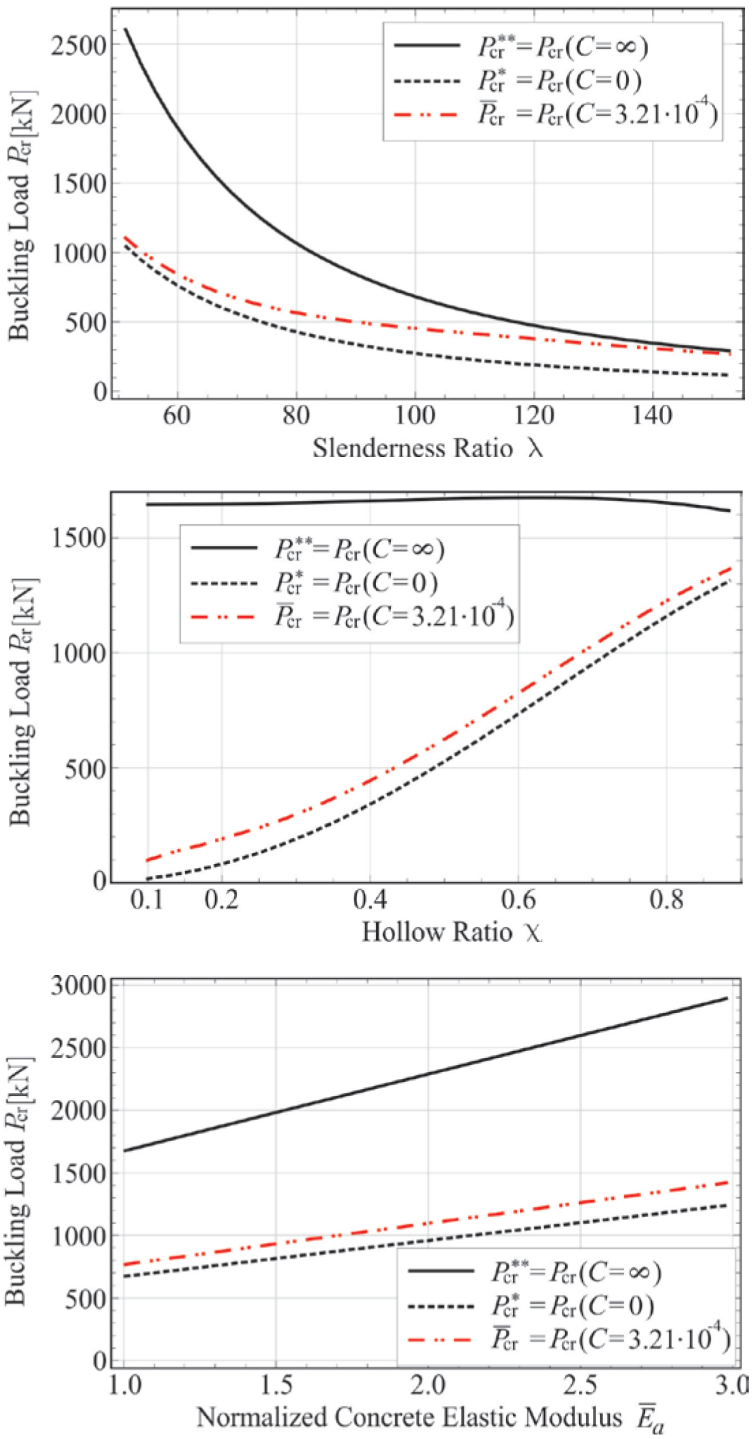

Figure 3. Effect of slenderness ratio λ (top), hollow ratio χ (middle) and elastic modulus (E_a) of sandwiched concrete (bottom) on the buckling load (P_{cr}) of a circular CFDST slender column.

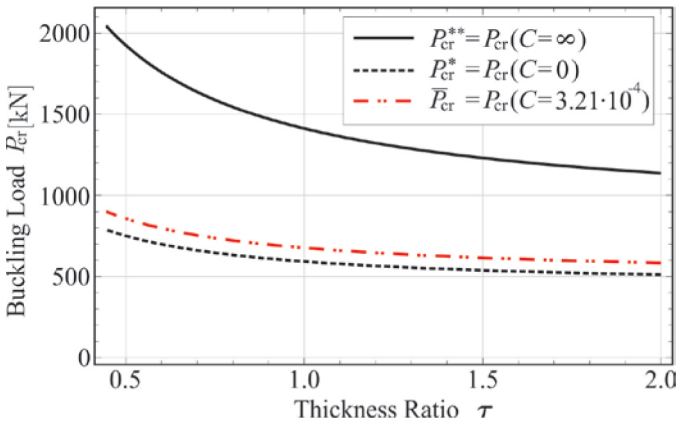

Figure 4. Effect of thickness ratio (τ) on buckling load (P_{cr}) of circular CFDST slender column.

3.2.3. *Effect of concrete elastic modulus.* The effect of concrete elastic modulus on P_{cr} is investigated next. Figure 3, bottom, shows P_{cr} versus normalized concrete elastic modulus, i.e., $\bar{E}_a = E_a/2821$.

As can been seen, the elastic modulus of sandwiched concrete E_a has a considerable effect on P_{cr}. The increasing of E_a increases linearly P_{cr}. This effect in more pronounced for CFDST columns with highly bonded components. Similarly as above, for the circular CFDST slender column whose contact stiffness corresponds to the test results, the buckling capacity is again closer to one with almost fully debonded components.

3.2.4. *Effect of thickness ratio.* The effect of thickness ratio ($\tau = t_{in}/t_{out}$) on P_{cr} of CFDST column is also investigated. This effect is investigated by varying the outer tube thickness (t_{out}). Figure 4. shows P_{cr} versus τ for values of contact stiffness between the one of fully bonded components to the one of fully debonded components. Note that τ increases by decreasing the outer tube thickness. As would be expected, by increasing of τ, the buckling load of CFDST column decreases. This effect is more pronounced for smaller values of τ while for higher is almost negligible. Again, $\bar{P}_{cr}$ is nearly the same as P_{cr}^{*}.

4. Conclusions

The paper presented a new mathematical model and its exact solution for the buckling analysis of circular CFDST columns with compliant interfaces between the steel and sandwiched concrete. After the validation of the results, the exact critical buckling loads were calculated using the proposed exact model and a parametric study was also performed by which the effects of different parameters on buckling behaviour of CFDST columns were investigated. Based on the results obtained, the following conclusions can be made:

1. The present mathematical model and its exact solution are simple, efficient and derived for the first time.
2. The exact results agree well with the experimental results obtained in [Essopjee and Dundu 2015].
3. The results also agree well with the adjusted design predictions [Eurocode 2004; SANS 2011].

4. The exact results can agree completely with the numerical results of [Hassanein and Kharoob 2014a] if calibrated values of C are used in the calculations.
5. The buckling load is independent on axial contact stiffness K.
6. The buckling load of CFDST column decreases with increasing the column slenderness and thickness ratio, while increases with increasing the elastic modulus of sandwiched concrete and hollow ratio.
7. The exact results can be used as a benchmark solution.

Conflict of Interests. The authors declare that they have no conflict of interests regarding the publication of this paper.

Data Availability. No data were used to support this study.

Acknowledgement. The authors acknowledge the financial support from the Slovenian Research Agency (research core funding No. P2-0260).

Notation. The following symbols are used in this paper:

A = cross-sectional area (cm^2)
C = contact modulus in Z direction ($\mathrm{kN/cm}^2$)
D = tube diameter (cm)
E = elastic modulus ($\mathrm{kN/cm}^2$)
J = moment of inertia (cm^4)
K = contact modulus in X direction ($\mathrm{kN/cm}^2$)
L = column length (cm)
M_Y = cross-sectional bending moment (kNcm)
P = centrally applied point load (kN)
P_{cr} = critical bucklig load (kN)
p_X, p_Z = contact tractions in X and Z directions ($\mathrm{kN/cm}^2$)
R_X, R_Z = X and Z components of the cross-sectional equilibrium force (kN)
t = tube thickness (cm)
u = axial displacement (cm)
w = deflection (cm)
Δ = generalized slip (cm)
ε = extensional strain
κ = presudocurvature (rad/cm)
φ = rotation (rad)

Subcripts

in = inner
out = outer

References

[Essopjee and Dundu 2015] Y. Essopjee and M. Dundu, "Performance of concrete-filled double-skin circular tubes in compression", *Compos. Struct.* **133** (2015), 1276–1283.

[Eurocode 2004] European Committee for Standardization, "Design of composite steel and concrete structures, 1-1: General rules and rules for buildings", technical handbook EN 1994-1-1, 2004, Available at https://tinyurl.com/eurcode41.

[Han et al. 2004] L.-H. Han, Z. Tao, H. Huang, and X.-L. Zhao, "Concrete-filled double skin (SHS outer and CHS inner) steel tubular beam-columns", *Thin-Walled Struct.* **42**:9 (2004), 1329–1355.

[Hassanein and Kharoob 2014a] M. F. Hassanein and O. F. Kharoob, "Analysis of circular concrete-filled double skin tubular slender columns with external stainless steel tubes", *Thin-Walled Struct.* **79** (2014), 23–37.

[Hassanein and Kharoob 2014b] M. F. Hassanein and O. F. Kharoob, "Compressive strength of circular concrete-filled double skin tubular short columns", *Thin-Walled Struct.* **77** (2014), 165–173.

[Hassanein et al. 2013] M. F. Hassanein, O. F. Kharoob, and Q. Q. Liang, "Circular concrete-filled double skin tubular short columns with external stainless steel tubes under axial compression", *Thin-Walled Struct.* **73** (2013), 252–263.

[Huang et al. 2010] H. Huang, L.-H. Han, Z. Tao, and X.-L. Zhao, "Analytical behaviour of concrete-filled double skin steel tubular (CFDST) stub columns", *J. Constr. Steel Res.* **66**:4 (2010), 542–555.

[Kryžanowski et al. 2009] A. Kryžanowski, S. Schnabl, G. Turk, and I. Planinc, "Exact slip-buckling analysis of two-layer composite columns", *Int. J. Solids Struct.* **46**:14-15 (2009), 2929–2938.

[Li et al. 2012] W. Li, L.-H. Han, and X.-L. Zhao, "Axial strength of concrete-filled double skin steel tubular (CFDST) columns", *Thin-Walled Struct.* **56** (2012), 9–20.

[Perko 1991] L. Perko, *Differential equations and dynamical systems*, Texts Appl. Math. **7**, Springer, 1991.

[Reissner 1972] E. Reissner, "On one-dimensional finite-strain beam theory: the plane problem", *Z. Angew. Math. Phys.* **23** (1972), 795–804.

[Romero et al. 2015] M. L. Romero, A. Espinos, J. M. Portolés, A. Hospitaler, and C. Ibañez, "Slender double-tube ultra-high strength concrete-filled tubular columns under ambient temperature and fire", *Eng. Struct.* **99** (2015), 536–545.

[Romero et al. 2017] M. L. Romero, C. Ibañez, A. Espinos, J. M. Portolés, and A. Hospitaler, "Influence of ultra-high strength concrete on circular concrete-filled dual steel columns", *Structures* **9** (2017), 13–20.

[SANS 2011] South African Bureau of Standards, "The structural use of steel, I: Limit-state design of hot-rolled steelwork", technical handbook SANS 1062-1, 2011. Version 2.01.

[Schnabl et al. 2007] S. Schnabl, M. Saje, G. Turk, and I. Planinc, "Analytical solution of two-layer beam taking into account interlayer slip and shear deformation", *J. Struct. Eng.* (*ASCE*) **133**:6 (2007), 886–894.

[Schnabl et al. 2015] S. Schnabl, G. Jelenić, and I. Planinc, "Analytical buckling of slender circular concrete-filled steel tubular columns with compliant interfaces", *J. Constr. Steel Res.* **115** (2015), 252–262.

[Tao et al. 2004] Z. Tao, L.-H. Han, and X.-L. Zhao, "Behaviour of concrete-filled double skin (CHS inner and CHS outer) steel tubular stub columns and beam-columns", *J. Constr. Steel Res.* **60**:8 (2004), 1129–1158.

[Yang et al. 2012] Y.-F. Yang, L.-H. Han, and B.-H. Sun, "Experimental behaviour of partially loaded concrete filled double-skin steel tube (CFDST) sections", *J. Constr. Steel Res.* **71** (2012), 63–73.

Received 2 Mar 2020. Revised 15 Jun 2020. Accepted 23 Jul 2020.

SIMON SCHNABL: simon.schnabl@fkkt.uni-lj.si
Faculty of Civil and Geodetic Engineering, University of Ljubljana, 1000 Ljubljana, Slovenia

and

Faculty of Chemistry and Chemical Technology, University of Ljubljana, 1000 Ljubljana, Slovenia

BOJAN ČAS: bcas@fgg.uni-lj.si
Faculty of Civil and Geodetic Engineering, University of Ljubljana, 1000 Ljubljana, Slovenia

JOURNAL OF MECHANICS OF MATERIALS AND STRUCTURES
Vol. 15, No. 4, 2020
https://doi.org/10.2140/jomms.2020.15.511

A SIMPLE SCALAR DIRECTIONAL HARDENING MODEL FOR THE BAUSCHINGER EFFECT COMPARED WITH A TENSORIAL MODEL

MARTIN KROON AND M. B. RUBIN

Modeling the Bauschinger effect is usually accomplished by introducing a second-order back-stress or directional hardening tensor. The objective of this paper is to propose a simpler scalar model of the Bauschinger effect based on a scalar directional hardening parameter that is determined by integration of an evolution equation. The behavior of this scalar model is compared to a tensorial model for a number of load cases. Strongly objective numerical algorithms are developed for integrating the evolution equations for both the tensorial and scalar models. Also, a consistent tangent is developed for both models. Obviously, the numerical implementation of the scalar model is significantly less complicated than for the tensorial model. Examples show that the tensorial and scalar models predict the same results for cyclic proportional triaxial extension and triaxial compression loadings. In contrast, the tensorial model predicts a Bauschinger effect for cyclic proportional pure torsion loading which is not predicted by the scalar model. More complicated examples with nonproportional loading paths and inhomogeneous deformations indicate that, relative to the tensorial model, the scalar model accounts for directional hardening fairly well and the simplicity of the model makes it an attractive option to add to isotropic hardening models.

1. Introduction

The inelastic response of isotropic metals typically exhibits some form of hardening. The simplest model for hardening introduces an isotropic hardening variable κ, which is determined by integrating an evolution equation for its rate. Cyclic loading in uniaxial stress using a model with only isotropic hardening indicates that the magnitude of stress in tension at the onset of unloading is the same as that in compression at the onset of inelastic response during reverse loading. For many metals, however, cyclic loading in uniaxial stress also exhibits a Bauschinger effect [Bauschinger 1881], which is observed as a reduced magnitude of stress and a rounding of the stress-strain curve at the onset of reverse loading. A review of aspects of the Bauschinger effect in metals up until 1979 can be found in [Sowerby et al. 1979]. There the physical reason for the Bauschinger effect is described as long range stresses caused by inhomogeneous deformations of the grains that introduce directionality of the resistance to inelastic flow.

The introduction in [Langer et al. 2010] reviews comments by major researchers of hardening in metals who conclude that phenomenological models of hardening are necessary since a theory of hardening based on first-principles has not been developed. Langer et al. [2010] then proceed to develop a theory that characterizes the thermodynamically irreversible nature of dislocations which successfully predicts the strain hardening of copper over a wide range of temperatures and strain rates. Specifically, they introduce an effective temperature of dislocations and a second-law for externally driven systems within the context

Keywords: Bauschinger effect, finite deformation, isotropic elastic-inelastic response, numerical algorithm, scalar directional hardening.

of homogeneous deformations. However, this theory is not relevant for quasistatic experiments. A recent thermodynamical theory based on nonuniform plastic deformations, which account for excess dislocations due to the incompatibility of plastic distortion, has been developed in [Le and Tran 2018]. This theory explains that the Bauschinger effect is due to movement and annihilation of excess dislocations during load reversal but it does not predict the observed smoothing of the stress-strain curve during load reversal.

Within the context of small deformations, [Prager 1949] used a yield function with the stress replaced by the difference between the stress and a kinematic hardening parameter (sometimes referred to as a back-stress) which he attributed to a conference abstract by Reuss [1935]. This model captures the Bauschinger effect but it exhibits a sharp elastic-inelastic transition. An early model for cyclic loading that captures the Bauschinger effect and smooths the elastic-inelastic transition with a finite number of segments was introduced by Besseling [1958], who used a number of inelastic elements that are activated at different stress levels. More modern phenomenological continuum models typically introduce kinematic hardening, with the yield surface being expressed as a function of the stress $\boldsymbol{T}$ minus back-stress tensor $\boldsymbol{\beta}$. The original report by [Armstrong and Frederick 1966] has been republished with a historical introduction. Another feature of this formulation of kinematic hardening is that the inelastic deformation rate is proportional to the difference between the stress and the kinematic hardening variable. This allows the model to capture more complicated response for nonproportional loadings. A review of plastic and viscoplastic response with kinematic hardening can be found in [Chaboche 2008].

Directional hardening is an alternative to kinematic hardening (e.g., [Bodner 1968]). In this model an effective yield strength is determined by a function of the isotropic hardening variable and the inner product of the stress with a symmetric directional hardening tensor $\boldsymbol{\beta}$ to account for different yielding properties in different directions. Moreover, the inelastic deformation rate remains proportional to the deviatoric stress. Within the context of the directional hardening formulation, the direction of the inelastic deformation rate was modified in [Rubin and Bodner 1995] to include a component normal to the deviatoric stress which produced a reduced modulus for nonproportional loading. For both of these directional hardening models the rate of material dissipation remains nonnegative. In contrast, depending on the formulation of kinematic hardening, the model can produce negative material dissipation for proportional cyclic uniaxial stress loading if inelasticity occurs during unloading before the stress changes sign as the material goes into reverse loading. A more recent alternative formulation to kinematic hardening, which models the Bauschinger effect, can be found in [Barlat et al. 2011].

For large deformations with the back-stress tensor $\boldsymbol{\beta}$ being subtracted from the Cauchy stress $\boldsymbol{T}$ in the yield function it is necessary to propose an evolution equation for $\boldsymbol{\beta}$ which ensures that $\boldsymbol{\beta}$ rotates like $\boldsymbol{T}$ under Superposed Rigid Body Motions (SRBM). This means that the modeling includes an inelastic spin tensor that needs a constitutive equation (e.g., [Bammann 1990]).

To model more complicated multiaxial response, [Armstrong and Frederick 1966] introduced an effective kinematic hardening tensor as the sum of a number of hardening tensors which each were determined by evolution equations. Similarly, motivated by the work in [Hollenstein et al. 2013], which proposed a large deformation model with a smooth elastic-inelastic transition for both rate independent and rate-dependent response, LS-DYNA [Gladman 2018] developed a generalized model (MAT_275) which includes a number of elastic distortional deformation tensors to model more complicated inelastic effects for cyclic and multiaxial loadings with relaxation.

The objective of this paper is to propose a simplified scalar model for the Bauschinger effect which introduces a scalar evolution equation for a directional hardening parameter β. The responses of this scalar model are compared with those of a tensorial model which introduces an evolution equation for a directional hardening tensor $\boldsymbol{\beta}$. The simplified scalar model predicts the same results as the tensorial model for cyclic proportional triaxial extension and triaxial compression loadings. However, in contrast with the tensorial model, the scalar model cannot predict the Bauschinger effect for cyclic proportional pure torsion loading. Robust and strongly objective numerical integration algorithms are developed for both the scalar model and tensorial models. In this regard, it is recalled [Rubin and Papes 2011] that an algorithm will be strongly objective if all of the numerical estimates of tensorial quantities satisfy the same transformation relations under SRBM as the exact tensorial measures. Moreover, it is shown that the scalar model predicts nearly the same effective yield strength contours as the tensorial model for example problems with nonproportional loading and inhomogeneous deformation.

An outline of this paper is as follows: Section 2 provides an outline of the general theoretical framework to be used, whereas Section 3 describes the details of the different hardening models employed. Section 4 summarizes the objectivity properties of relevant entities in the theoretical framework, and Section 5 contains a description of a strongly objective numerical integration procedure for the state variables, including an algorithmic tangent stiffness. A number of numerical examples are provided in Section 6, and a discussion and some concluding remarks are given in Section 7.

2. Basic equations

Let $\boldsymbol{x}$ and $\boldsymbol{v} = \dot{\boldsymbol{x}}$ denote the position and velocity, respectively, of a material point in the current configuration at time t, where $\dot{(\,)}$ denotes the material time derivative. Then, the velocity gradient is given by $\boldsymbol{L} = \partial \boldsymbol{v}/\partial \boldsymbol{x}$, and the rate of deformation $\boldsymbol{D}$ and the spin $\boldsymbol{W}$ are defined by

$$\boldsymbol{L} = \boldsymbol{D} + \boldsymbol{W}, \qquad \boldsymbol{D} = \tfrac{1}{2}(\boldsymbol{L} + \boldsymbol{L}^T), \quad \boldsymbol{W} = \tfrac{1}{2}(\boldsymbol{L} - \boldsymbol{L}^T). \tag{1}$$

The need for an Eulerian formulation of evolution equations for finite deformation elastic-inelastic response has been discussed in a series of papers (e.g., [Rubin and Attia 1996; Rubin 2012]). This Eulerian formulation is insensitive to the choice of reference configuration, an intermediate configuration, a total deformation measure and an inelastic deformation measure. Eckart [1948] seems to be the first to propose an evolution equation directly for elastic deformation that is used to determine stress for finite elastic-inelastic deformations of solids. Leonov [1976] proposed similar equations for polymeric liquids.

Within the context of the Eulerian formulation of isotropic, hyperelastic-inelastic materials, Rubin and Attia [1996] proposed evolution equations for an elastic dilatational deformation J_{e} and a symmetric, positive-definite, unimodular second order elastic distortional deformation tensor $\bar{\boldsymbol{B}}_{\mathrm{e}}$. In the absence of inelastic dilatational deformation, the elastic dilatation is defined by

$$J_{\mathrm{e}} = \rho_{\mathrm{z}}/\rho \tag{2}$$

with ρ being the current mass density and ρ_{z} being its zero-stress value. Furthermore, the evolution equations for these quantities were proposed in the forms

$$\frac{\dot{J}_{\mathrm{e}}}{J_{\mathrm{e}}} = \boldsymbol{D} : \boldsymbol{I}, \quad \overset{\circ}{\bar{\boldsymbol{B}}}_{\mathrm{e}} = \boldsymbol{L}\bar{\boldsymbol{B}}_{\mathrm{e}} + \bar{\boldsymbol{B}}_{\mathrm{e}}\boldsymbol{L}^T - \tfrac{2}{3}(\boldsymbol{D} : \boldsymbol{I})\bar{\boldsymbol{B}}_{\mathrm{e}} - \Gamma \boldsymbol{A}_{\mathrm{p}}, \quad \boldsymbol{A}_{\mathrm{p}} = \bar{\boldsymbol{B}}_{\mathrm{e}} - \left(\frac{3}{\bar{\boldsymbol{B}}_{\mathrm{e}}^{-1} : \boldsymbol{I}}\right)\boldsymbol{I}, \tag{3}$$

where the scalar function $\Gamma \geq 0$ controls the magnitude of inelastic distortional deformation rate, and the tensor $\boldsymbol{A}_{\rm p}$ controls the direction of inelastic distortional deformation rate. This form ensures that inelastic deformation rate causes a tendency for $\bar{\boldsymbol{B}}_{\rm e}$ to approach the identity $\boldsymbol{I}$ and for $\bar{\boldsymbol{B}}_{\rm e}$ to remain a unimodular tensor. The evolution equation for $J_{\rm e}$ is appropriate for nonporous metals with no inelastic dilatation rate and can be determined by the conservation of mass equation. Also, $\boldsymbol{A} : \boldsymbol{B} = \text{tr}(\boldsymbol{A}\boldsymbol{B}^T)$ denotes the inner product of two second order tensors $\boldsymbol{A}$ and $\boldsymbol{B}$ and $\boldsymbol{I}$ is the second order unit tensor.

The formulation in [Rubin and Cardiff 2017] simplifies that in [Simo 1992, 2.19a] and [Simo 1998, §50] and recorded in [Simo and Hughes 1998, Box 9.1], which corrected that proposed in [Simo 1988, Table 1]. Specifically, for a neo-Hookean material, the strain energy function Σ per unit mass can be specified in the form

$$\rho_{\rm z}\Sigma = \tfrac{1}{2}K(J_{\rm e}-1)^2 + \tfrac{1}{2}\mu(\alpha_1 - 3), \tag{4}$$

where K and μ are the zero-stress bulk and shear modulus, respectively, and the first invariant α_1 of the elastic distortional deformation tensor $\bar{\boldsymbol{B}}_{\rm e}$ satisfies the equations

$$\alpha_1 = \bar{\boldsymbol{B}}_{\rm e} : \boldsymbol{I} \geq 3, \quad \dot{\alpha}_1 = 2\bar{\boldsymbol{B}}'_{\rm e} : \boldsymbol{D} - \Gamma \boldsymbol{A}_p : \boldsymbol{I}, \tag{5}$$

where a superscript prime $(\bullet)'$ is added to the symbol of a tensor to denote its deviatoric part. For example, the deviatoric part $\bar{\boldsymbol{B}}'_{\rm e}$ of $\bar{\boldsymbol{B}}_{\rm e}$ is defined by

$$\bar{\boldsymbol{B}}'_{\rm e} = \bar{\boldsymbol{B}}_{\rm e} - \tfrac{1}{3}(\bar{\boldsymbol{B}}_{\rm e} : \boldsymbol{I})\boldsymbol{I}. \tag{6}$$

It follows that the Cauchy stress $\boldsymbol{T}$ associated with this strain energy function is given by

$$\boldsymbol{T} = -p\boldsymbol{I} + \boldsymbol{T}', \quad p = -\rho_{\rm z}\frac{\partial \Sigma}{\partial J_{\rm e}} = K(1-J_{\rm e}), \quad \boldsymbol{T}' = 2J_{\rm e}^{-1}\rho_{\rm z}\frac{\partial \Sigma}{\partial \alpha_1}\bar{\boldsymbol{B}}'_{\rm e} = J_{\rm e}^{-1}\mu\bar{\boldsymbol{B}}'_{\rm e}. \tag{7}$$

Also, the rate of material dissipation $\mathcal{D}$ automatically satisfies the restriction that

$$\mathcal{D} = \boldsymbol{T} : \boldsymbol{D} - \rho\dot{\Sigma} = \tfrac{1}{2}J_{\rm e}^{-1}\mu\Gamma\boldsymbol{A}_{\rm p} : \boldsymbol{I} \geq 0. \tag{8}$$

Next, consider a yield function of the form

$$g = 1 - \frac{H\kappa}{\gamma_e}, \tag{9}$$

with $g < 0$ implying elastic response, and $g = 0$ defining the elastic-inelastic boundary. In this yield function, the effective elastic distortional strain γ_e is defined by

$$\gamma_e = \tfrac{1}{2}\sqrt{\tfrac{3}{2}\bar{\boldsymbol{B}}'_{\rm e} : \bar{\boldsymbol{B}}'_{\rm e}}. \tag{10}$$

In the expression (9) for the yield function g, κ is a positive measure of isotropic hardening that is determined by integrating an evolution equation (16) defined later and H is a scalar measure of directional hardening defined later in (19) for the tensorial model or in (25) for the scalar model.

A simple rate-independent version of the smooth elastic-inelastic transition model proposed in [Hollenstein et al. 2013] is obtained by using the yield function g in (9) and specifying the function Γ in the form

$$\Gamma = b_1\dot{\varepsilon}\langle g\rangle, \quad b_1 > 0, \tag{11}$$

where b_1 is a constant that controls the smoothness of the elastic-inelastic transition, the effective total distortional rate of deformation $\dot{\varepsilon}$ is defined by

$$\dot{\varepsilon} = \sqrt{\tfrac{2}{3}\boldsymbol{D}' : \boldsymbol{D}'}, \tag{12}$$

with the Macaulay brackets $\langle g \rangle$ defined by

$$\langle g \rangle = \max(g, 0). \tag{13}$$

From (3) and (11) it is observed that the material response is elastic when the inelastic deformation rate vanishes ($g \leq 0$) and is inelastic with an overstress when $g > 0$. Moreover, this model does not require loading and unloading conditions. Large values of b_1 reduce the magnitude of the overstress with the response asymptotically approaching that predicted by standard loading and unloading conditions with no overstress ($g \leq 0$) in the limit that $b_1 \to \infty$.

Even though a measure of plastic deformation is not necessary in the present Eulerian formulation, an equivalent plastic deformation may still be introduced to identify regions in a structure which have experienced inelastic deformation. It can be shown that for small deformations, the inelastic distortional deformation rate can be approximated by

$$\dot{\boldsymbol{\varepsilon}}_{\mathrm{p}} \approx \tfrac{1}{2}\Gamma \bar{\boldsymbol{B}}'_{\mathrm{e}}. \tag{14}$$

Then, the equivalent inelastic deformation rate is defined as

$$\dot{\varepsilon}_{\mathrm{p}} = \sqrt{\tfrac{2}{3}\dot{\boldsymbol{\varepsilon}}_{\mathrm{p}} : \dot{\boldsymbol{\varepsilon}}_{\mathrm{p}}} = \tfrac{1}{2}\Gamma\sqrt{\tfrac{2}{3}\bar{\boldsymbol{B}}'_{\mathrm{e}} : \bar{\boldsymbol{B}}'_{\mathrm{e}}} = \tfrac{2}{3}\Gamma\gamma_{\mathrm{e}}. \tag{15}$$

3. Models for hardening

3.1. ***Prerequisites.*** A combination of isotropic and directional hardening is used. The same model for isotropic hardening is used throughout this work, whereas two formulations of directional hardening models are explored:

(a) a formulation using a second-order directional hardening tensor $\boldsymbol{\beta}$, and

(b) a formulation using a single scalar state variable β.

3.2. ***Isotropic hardening.*** For all models discussed in this paper, the isotropic hardening variable κ is determined by the evolution equation [Chan et al. 1988]

$$\dot{\kappa} = m_1\Gamma(\kappa_{\mathrm{s}} - \kappa) - m_2(\kappa - \kappa_{\mathrm{a}}), \quad \Gamma \geq 0, \quad m_1 \geq 0, \quad m_2 \geq 0, \quad \kappa_{\mathrm{a}} \leq \kappa \leq \kappa_{\mathrm{s}} > 0. \tag{16}$$

This evolution equation includes a competition of strain hardening rate and thermal recovery rate. Strain hardening causes a tendency for κ to approach its saturated value κ_{s} with its rate controlled by the constant m_1. Thermal recovery causes a tendency for κ to approach its fully annealed value κ_{a} with its rate controlled by the constant m_2.

3.3. ***A tensor-based model for directional hardening.*** A formulation of directional hardening, using a second-order tensor, is now presented. To distinguish between the different models for directional hardening, the present model is termed "Model T" ("T" for "tensor"). Motivated by the work in [Chan et al. 1988], the evolution equation for the directional hardening tensor $\boldsymbol{\beta}$ is proposed in the form

$$\hat{\boldsymbol{\beta}} = m_3\Gamma(\beta_s \boldsymbol{U} - \boldsymbol{\beta}) - m_4\boldsymbol{\beta}, \quad 0 \le \beta_s < 1, \quad m_3 \ge 0, \quad m_4 \ge 0, \tag{17}$$

where $\hat{\boldsymbol{\beta}}$ denotes the objective Jaumann derivative and is defined by

$$\hat{\boldsymbol{\beta}} \equiv \dot{\boldsymbol{\beta}} - (\boldsymbol{W}\boldsymbol{\beta} + \boldsymbol{\beta}\boldsymbol{W}^T). \tag{18}$$

The function H, which accounts for directional hardening in the yield function (9), is specified by

$$H = H_T = 1 + \boldsymbol{\beta} : \boldsymbol{U}. \tag{19}$$

In these equations, $\boldsymbol{\beta}$ is a symmetric, deviatoric, directional hardening tensor, $\boldsymbol{U}$ is defined by the direction of the deviatoric elastic distortional deformation tensor $\bar{\boldsymbol{B}}'_e$, such that

$$\boldsymbol{\beta}^T = \boldsymbol{\beta}, \quad \boldsymbol{\beta} : \boldsymbol{I} = 0, \quad \boldsymbol{U} = \frac{\bar{\boldsymbol{B}}'_e}{|\bar{\boldsymbol{B}}'_e|}, \quad \boldsymbol{U}^T = \boldsymbol{U}, \quad \boldsymbol{U} : \boldsymbol{I} = 0, \quad \boldsymbol{U} : \boldsymbol{U} = 1. \tag{20}$$

Hence, the value of H_T in (19) depends on the magnitude of $\boldsymbol{\beta}$ and on its direction relative the tensor $\boldsymbol{U}$. In particular, it can be seen that the evolution equation (17) causes a competition of $\boldsymbol{\beta}$ increasing towards the value $\beta_s\boldsymbol{U}$, with the rate controlled by m_3 and thermal recovery with the rate controlled by m_4. This evolution equation causes H_T to satisfy the restriction

$$0 < 1 - \beta_s \le H_T \le 1 + \beta_s, \tag{21}$$

which ensures that the resistance $H\kappa$ to inelastic deformation rate in (9) remains positive for positive κ.

3.4. ***A scalar-based model for directional hardening.*** The scalar-based model for directional hardening is now outlined, and this model is termed "Model S" ("S" for "scalar"). A state variable β is introduced, whose evolution is given by

$$\dot{\beta} = m_3\Gamma(\beta_s U - \beta) - m_4\beta, \quad -\beta_s \le \beta \le \beta_s, \tag{22}$$

where the constants m_3, m_4 and β_s satisfy the restrictions in (17), and the Lode parameter U is defined by

$$U = \begin{cases} 0 & \text{for } \gamma_e = 0, \\ \dfrac{27\det(\boldsymbol{T}')}{2\sigma_e^3} = \dfrac{27\det\bar{\boldsymbol{B}}'_e}{16\gamma_e^3} & \text{for } \gamma_e > 0, \end{cases} \quad -1 \le U \le 1. \tag{23}$$

Next, introducing the Lode angle ϑ by the expressions

$$\sin(3\vartheta) = U, \quad -\tfrac{1}{6}\pi \le \vartheta \le \tfrac{1}{6}\pi\,, \tag{24}$$

and motivated by the simple failure surface developed in [Rubin 1991], the function H in (9) is specified by the form

$$H = H_S = 1 + \beta U. \tag{25}$$

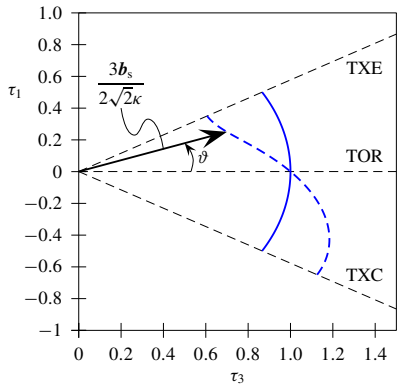

Figure 1. Normalized yield surfaces displayed in the τ_3-τ_1-plane for $\vartheta \in \left[-\frac{1}{6}\pi, \frac{1}{6}\pi\right]$: the von Mises curve (solid blue line) and an example of a curve with accumulated directional hardening (dashed blue line).

This gives the values

$$H_S\left(\vartheta = \tfrac{1}{6}\pi\right) = 1 + \beta, \quad H_S(\vartheta = 0) = 1, \quad H_S\left(\vartheta = -\tfrac{1}{6}\pi\right) = 1 - \beta. \tag{26}$$

3.5. ***Graphical representations of models for directional hardening.*** Following [Rubin 1991], three special load cases are identified:

- triaxial extension (TXE), $U = 1$, $\vartheta = \frac{1}{6}\pi$,
- pure torsion (TOR), $U = 0$, $\vartheta = 0$,
- triaxial compression (TXC), $U = -1$, $\vartheta = -\frac{1}{6}\pi$.

Notice that the sign of ϑ is opposite to that defined in [Rubin 1991].

The loading state is characterized by $\bar{\boldsymbol{B}}'_e$, whose ordered eigenvalues are denoted by $\bar{B}'_{e1}$, $\bar{B}'_{e2}$, and $\bar{B}'_{e3}$, with $\bar{B}'_{e1} \geq \bar{B}'_{e2} \geq \bar{B}'_{e3}$. The three load states introduced above are then characterized by

- TXE: $\bar{B}'_{e1} = \frac{4}{3}\gamma_e, \quad \bar{B}'_{e2} = \bar{B}'_{e3} = -\frac{2}{3}\gamma_e$,
- TOR: $\bar{B}'_{e1} = \frac{2}{\sqrt{3}}\gamma_e, \quad \bar{B}'_{e2} = 0, \quad \bar{B}'_{e3} = -\frac{2}{\sqrt{3}}\gamma_e$,
- TXC: $\bar{B}'_{e1} = \bar{B}'_{e2} = \frac{2}{3}\gamma_e, \quad \bar{B}'_{e3} = -\frac{4}{3}\gamma_e$.

The yield function may be illustrated by its contour in the synoptic (or octahedral) plane, whose unit normal is given by the vector $\frac{1}{\sqrt{3}}(\boldsymbol{p}_1 + \boldsymbol{p}_2 + \boldsymbol{p}_3)$, where $\boldsymbol{p}_i$ are the orthonormal eigenvectors of $\bar{\boldsymbol{B}}'_e$. Again, following [Rubin 1991], two orthogonal unit vectors in the synoptic plane are defined as

$$\bar{\boldsymbol{e}}_3 = \tfrac{1}{\sqrt{2}}(\boldsymbol{p}_1 - \boldsymbol{p}_3), \quad \bar{\boldsymbol{e}}_1 = \tfrac{1}{\sqrt{6}}(-\boldsymbol{p}_1 + 2\boldsymbol{p}_2 - \boldsymbol{p}_3). \tag{27}$$

The yield surface can be described by the vector $\boldsymbol{b}_s$, defined as

$$\boldsymbol{b}_s = \bar{\boldsymbol{B}}'_e\left[\tfrac{1}{\sqrt{3}}(\boldsymbol{p}_1 + \boldsymbol{p}_2 + \boldsymbol{p}_3)\right] = \frac{2\sqrt{2}\,\kappa}{3}(\tau_3\bar{\boldsymbol{e}}_3 + \tau_1\bar{\boldsymbol{e}}_1), \tag{28}$$

where

$$\tau_3 = H(\vartheta)\cos\vartheta, \quad \tau_1 = H(\vartheta)\sin\vartheta. \tag{29}$$

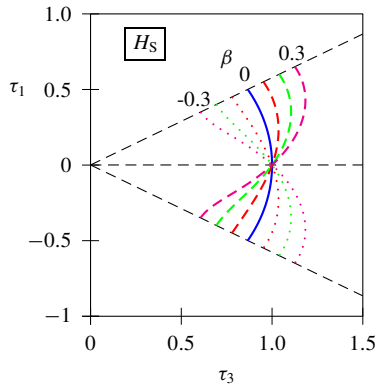

Figure 2. Yield surfaces for directional hardening displayed in the τ_3-τ_1-plane for $\vartheta \in \left[-\frac{1}{6}\pi, \frac{1}{6}\pi\right]$ for different values of β.

(It is noted that $\mu \boldsymbol{b}_s / J_e$ is the shearing component of the traction vector applied to the synoptic plane.) With the specification $\gamma_e = \kappa H(\vartheta)$, the vector $\boldsymbol{b}_s$ in (28) describes the contour of the yield surface in the synoptic plane; see Figure 1.

The state variable κ governs the isotropic expansion (or contraction) of the yield surface in the synoptic plane, whereas evolution of $\boldsymbol{\beta}$ and β cause directional hardening, i.e., different hardening for different loading modes.

The following discussion starts with the scalar-based model for directional hardening. Figure 2 shows contours of the normalized yield surface in the τ_3-τ_1-plane for different values of β. From this figure it can be seen that loading in uniaxial tension (TXE), causes an increase in β and thereby increased hardening for loading modes with $\vartheta > 0$ and softening for $\vartheta < 0$. Loading in uniaxial compression (TXC) causes the opposite tendency. For the model S, the normalized yield surface is pivoting around the yield point at $\vartheta = 0$ (TOR), which remains unaffected by directional hardening.

The yielding contour of the tensor-based model is illustrated by considering two cases of accumulated directional hardening $\boldsymbol{\beta}$: one case where the material has experienced uniaxial tension, such that

$$\beta_{ij}^{\mathrm{TXE}} = \sqrt{\tfrac{2}{3}}\beta \begin{bmatrix} 1 & 0 & 0 \\ 0 & -\frac{1}{2} & 0 \\ 0 & 0 & -\frac{1}{2} \end{bmatrix}, \tag{30}$$

and one case where the material has experienced pure torsion, i.e.,

$$\beta_{ij}^{\mathrm{TOR}} = \tfrac{1}{\sqrt{2}}\beta \begin{bmatrix} 0 & 1 & 0 \\ 1 & 0 & 0 \\ 0 & 0 & 0 \end{bmatrix}. \tag{31}$$

Above, β_{ij} denotes the Cartesian components of $\boldsymbol{\beta}$, and β is a scalar. The yield contour is then described by considering load states characterized by

$$U_{ij} = \begin{bmatrix} \xi & \zeta & 0 \\ \zeta & -\frac{1}{2}\xi & 0 \\ 0 & 0 & -\frac{1}{2}\xi \end{bmatrix}, \quad 3\xi^2 + 4\zeta^2 = 2, \tag{32}$$

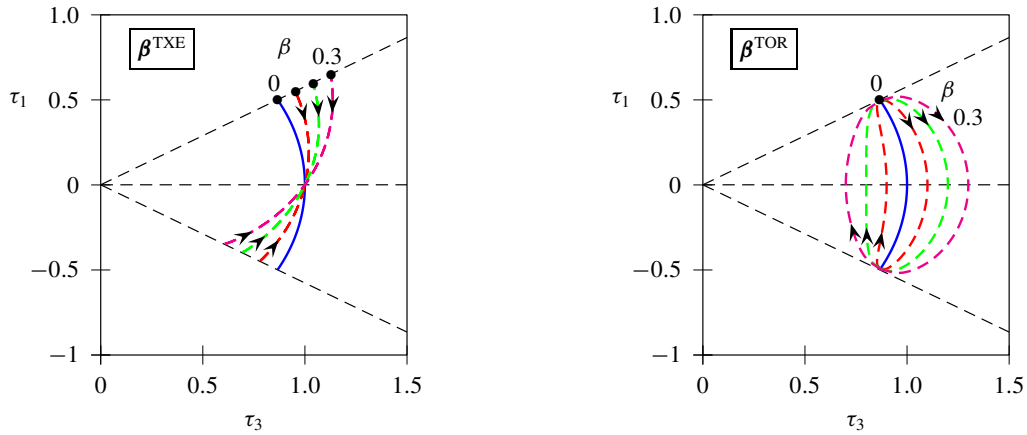

Figure 3. Yield surfaces for directional hardening predicted by the tensorial model T and displayed in the τ_3-τ_1-plane for $\vartheta \in \left[-\frac{1}{6}\pi, \frac{1}{6}\pi\right]$ for different values of β. Left: $\boldsymbol{\beta}^{\mathrm{TXE}}$. Right: $\boldsymbol{\beta}^{\mathrm{TOR}}$.

where U_{ij} are the Cartesian components of $\boldsymbol{U}$. By definition, $\boldsymbol{U} : \boldsymbol{U} = 1$, implying that $(32)_2$ must hold, and that $-\sqrt{\frac{2}{3}} \le \xi \le \sqrt{\frac{2}{3}}$ and $-\frac{1}{\sqrt{2}} \le \zeta \le \frac{1}{\sqrt{2}}$.

A loading path is now considered where the material starts in a state of uniaxial tension, passes through a state of pure torsion, then through a state of biaxial tension, then again through a state of pure torsion but with the opposite sign of the shearing, and finally back to uniaxial tension. The path of $\boldsymbol{U}$ thus passes through the points

$$\begin{aligned}
&\xi = \sqrt{\tfrac{2}{3}}, && \zeta = 0 && \text{(TXE)},\\
&\xi = 0, && \zeta = \tfrac{1}{\sqrt{2}} && \text{(TOR)},\\
&\xi = -\sqrt{\tfrac{2}{3}}, && \zeta = 0 && \text{(TXC)},\\
&\xi = 0, && \zeta = -\tfrac{1}{\sqrt{2}} && \text{(TOR)},\\
&\xi = \sqrt{\tfrac{2}{3}}, && \zeta = 0 && \text{(TXE)}.
\end{aligned} \tag{33}$$

The outcome is shown in Figure 3, where solutions for different values of β are shown. The black dots indicate the starting point (TXE) of the path, and the arrows indicate the direction of the path. For $\boldsymbol{\beta} = \boldsymbol{\beta}^{\mathrm{TXE}}$, the material has experienced directional hardening and softening for loads with $\vartheta > 0$ and $\vartheta < 0$, respectively, whereas the yield point for pure torsion remains unaffected. This behavior is similar to the scalar model S, as seen from Figure 2, even though the functional forms are not identical.

For a material that has experienced pure torsion, i.e., $\boldsymbol{\beta} = \boldsymbol{\beta}^{\mathrm{TOR}}$, yield contours are shown in Figure 3, right. From this figure it can be seen that torsion with a positive shearing component causes hardening in this torsion direction and softening for shearing in the opposite direction (i.e., with a negative shearing component). Yielding in TXE and TXC remains unaffected. This ability to distinguish between positive and negative shearing sets the tensor-based model apart from the scalar-based model, which is not able to make this distinction.

4. Invariance under Superposed Rigid Body Motions (SRBM)

Under Superposed Rigid Body Motions (SRBM) a quantity like the stress tensor $\boldsymbol{T}$ transforms to $\boldsymbol{T}^+$, where a superscript $(^+)$ is added to indicate the value of a quantity in the superposed configuration. In the above equations all scalars are uninfluenced by SRBM and the tensors $\boldsymbol{D}$, $\bar{\boldsymbol{B}}_{\rm e}$, $\boldsymbol{T}$, $\boldsymbol{\beta}$ and the Jaumann rate $\hat{\boldsymbol{\beta}}$ satisfy the transformation relations

$$\boldsymbol{D}^+ = \boldsymbol{Q}\boldsymbol{D}\boldsymbol{Q}^T, \quad \bar{\boldsymbol{B}}_{\rm e}^+ = \boldsymbol{Q}\bar{\boldsymbol{B}}_{\rm e}\boldsymbol{Q}^T, \quad \boldsymbol{T}^+ = \boldsymbol{Q}\boldsymbol{T}\boldsymbol{Q}^T, \quad \boldsymbol{\beta}^+ = \boldsymbol{Q}\boldsymbol{\beta}\boldsymbol{Q}^T, \quad \hat{\boldsymbol{\beta}}^+ = \boldsymbol{Q}\hat{\boldsymbol{\beta}}\boldsymbol{Q}^T, \tag{34}$$

where $\boldsymbol{Q}(t)$ is an arbitrary proper orthogonal tensor function of time t only. It follows that the evolution equation (3) for $\bar{\boldsymbol{B}}_{\rm e}$ and (17) for $\boldsymbol{\beta}$ remain form-invariant under SRBM.

5. Numerical integration algorithms

5.1. ***Preliminaries.*** This section discusses numerical algorithms to integrate the evolution equations (3) for J_e and $\bar{\boldsymbol{B}}_{\rm e}$ as well as the evolution equations (16) for isotropic hardening (κ), (17) for the tensorial measure $\boldsymbol{\beta}$ of directional hardening for the tensor-based model and (22) for the scalar measure β of directional hardening for the scalar-based model. These equations also use the yield function g in (9), the effective elastic distortional strain γ_e in (10), the rate of inelasticity Γ in (11) and the effective total distortional deformation rate $\dot{\varepsilon}$ in (12). Also, the constitutive equation for the Cauchy stress $\boldsymbol{T}$ is given in (7). Specifically, for the integration algorithms it is assumed that the values $J_e(t_n)$, $\bar{\boldsymbol{B}}_{\rm e}(t_n)$, $\kappa(t_n)$ and $\boldsymbol{\beta}(t_n)$ or $\beta(t_n)$ are known at the beginning of the time step $t = t_n$. The numerical algorithms determine the values $J_e(t_{n+1})$, $\bar{\boldsymbol{B}}_{\rm e}(t_{n+1})$, $\kappa(t_{n+1})$ and $\boldsymbol{\beta}(t_{n+1})$ or $\beta(t_{n+1})$ at the end of the time step $t = t_{n+1}$ with increment $\Delta t = t_{n+1} - t_n$.

Motivated by the work in [Simo 1988; Rubin and Papes 2011], recall that the relative deformation gradient $\boldsymbol{F}_{\rm r}$ from the time $t = t_n$, the relative dilatation $J_{\rm r}$ and the unimodular relative deformation gradient $\bar{\boldsymbol{F}}_{\rm r}$, satisfy the equations

$$\begin{aligned} &\dot{\boldsymbol{F}}_{\rm r} = \boldsymbol{L}\boldsymbol{F}_{\rm r}, \quad && \boldsymbol{F}_{\rm r}(t_n) = \boldsymbol{I}, \\ &J_{\rm r} = \det \boldsymbol{F}_{\rm r}, \quad && \dot{J}_{\rm r} = J_{\rm r}(\boldsymbol{D} : \boldsymbol{I}), \quad && J_{\rm r}(t_n) = 1, \\ &\bar{\boldsymbol{F}}_{\rm r} = J_{\rm r}^{-1/3}\boldsymbol{F}_{\rm r}, \quad && \dot{\bar{\boldsymbol{F}}}_{\rm r} = \boldsymbol{L}'\bar{\boldsymbol{F}}_{\rm r}, && \bar{\boldsymbol{F}}_{\rm r}(t_n) = \boldsymbol{I}. \end{aligned} \tag{35}$$

In [Rubin 2020], a strongly objective estimate $\widetilde{\boldsymbol{D}}$ of the average deformation rate over the time step was developed and is given by

$$\widetilde{\boldsymbol{D}} = \frac{1}{3\Delta t}\ln[J_r(t_{n+1})]\boldsymbol{I} + \widetilde{\boldsymbol{D}}', \quad \widetilde{\boldsymbol{D}}' = \frac{1}{2\Delta t}\left[\boldsymbol{I} - \left\{\frac{3}{\bar{\boldsymbol{B}}_{\rm r}^{-1}(t_{n+1}) : \boldsymbol{I}}\right\}\bar{\boldsymbol{B}}_{\rm r}^{-1}(t_{n+1})\right], \tag{36}$$

where $\bar{\boldsymbol{B}}_{\rm r}(t_{n+1}) = \bar{\boldsymbol{F}}_{\rm r}(t_{n+1})\bar{\boldsymbol{F}}_{\rm r}^{\rm T}(t_{n+1})$. Moreover, using this expression the average effective total distortional deformation rate $\dot{\varepsilon}$ during the time step is approximated by

$$\dot{\varepsilon} \approx \dot{\tilde{\varepsilon}} = \sqrt{\tfrac{2}{3}\widetilde{\boldsymbol{D}}' : \widetilde{\boldsymbol{D}}'}. \tag{37}$$

5.2. ***Integration of $J_{\rm e}$, $\bar{\boldsymbol{B}}_{\rm e}$, κ, and $\boldsymbol{\varepsilon}_{\rm p}^{\rm e}$.*** It is recalled from [Rubin and Cardiff 2017] that the exact solution for $J_{\rm e}$ is given by

$$J_{\rm e}(t_{n+1}) = J_{\rm r}(t_{n+1})J_{\rm e}(t_n). \tag{38}$$

Also, using the elastic trial $\bar{\boldsymbol{B}}_{\mathrm{e}}^{*}$

$$\bar{\boldsymbol{B}}_{\mathrm{e}}^{*} = \bar{\boldsymbol{F}}_{\mathrm{r}} \bar{\boldsymbol{B}}_{\mathrm{e}}(t_n) \bar{\boldsymbol{F}}_{\mathrm{r}}^{\mathrm{T}}, \tag{39}$$

it can be shown that its deviatoric part $\bar{\boldsymbol{B}}_{\mathrm{e}}^{\prime *}$ satisfies the evolution equation

$$\dot{\bar{\boldsymbol{B}}}_{\mathrm{e}}^{\prime *} = \boldsymbol{L}^{\prime} \bar{\boldsymbol{B}}_{\mathrm{e}}^{*} + \bar{\boldsymbol{B}}_{\mathrm{e}}^{*} \boldsymbol{L}^{\prime T} - \tfrac{2}{3} (\bar{\boldsymbol{B}}_{\mathrm{e}}^{\prime *} : \boldsymbol{D}^{\prime}) \boldsymbol{I}. \tag{40}$$

Also, taking the deviatoric part of the evolution equation (3) requires $\bar{\boldsymbol{B}}_{\mathrm{e}}^{\prime}$ to satisfy the evolution equation

$$\dot{\bar{\boldsymbol{B}}}_{\mathrm{e}}^{\prime} = \boldsymbol{L}^{\prime} \bar{\boldsymbol{B}}_{\mathrm{e}} + \bar{\boldsymbol{B}}_{\mathrm{e}} \boldsymbol{L}^{\prime T} - \tfrac{2}{3} (\bar{\boldsymbol{B}}_{\mathrm{e}}^{\prime} : \boldsymbol{D}^{\prime}) \boldsymbol{I} - \Gamma \bar{\boldsymbol{B}}_{\mathrm{e}}^{\prime}. \tag{41}$$

Then, approximating this equation by

$$\dot{\bar{\boldsymbol{B}}}_{e}^{\prime} = \dot{\bar{\boldsymbol{B}}}_{\mathrm{e}}^{\prime *} - \Gamma \bar{\boldsymbol{B}}_{\mathrm{e}}^{\prime}, \tag{42}$$

and using a backward Euler approximation of the derivative yields the solution

$$\bar{\boldsymbol{B}}_{\mathrm{e}}^{\prime}(t_{n+1}) = \frac{\bar{\boldsymbol{B}}_{\mathrm{e}}^{\prime *}(t_{n+1})}{1 + \Delta\Gamma} = \lambda \bar{\boldsymbol{B}}_{\mathrm{e}}^{\prime *}(t_{n+1}), \tag{43}$$

where $\Delta\Gamma$ is defined by

$$\Delta\Gamma = \Delta t \Gamma(t_{n+1}), \tag{44}$$

and $\Gamma(t_{n+1})$ is the value of function Γ defined in (11) at the end of the time step. It can be seen that the solution (43) is similar to the radial return algorithm proposed by [Wilkins 1963] with the final value of elastic distortional deformation being a scalar time its elastic trial value. Once $\bar{\boldsymbol{B}}_{\mathrm{e}}^{\prime}(t_{n+1})$ is known, the value $\bar{\boldsymbol{B}}_{\mathrm{e}}(t_{n+1})$ can be determined by solving the cubic equation

$$\det\left[\tfrac{1}{3}\alpha_1 \boldsymbol{I} + \bar{\boldsymbol{B}}_{\mathrm{e}}^{\prime}(t_{n+1})\right] = 1 \tag{45}$$

for α_1, as discussed in [Rubin and Attia 1996; Hollenstein et al. 2013].

The evolution equation (16) for the isotropic hardening variable κ can be integrated using an backward Euler estimate of the derivative to obtain

$$\kappa(t_{n+1}) = \frac{\kappa(t_n) + m_1 \Delta\Gamma \kappa_{\mathrm{s}} + \Delta t m_2 \kappa_{\mathrm{a}}}{1 + m_1 \Delta\Gamma + \Delta t m_2}. \tag{46}$$

Also, the equivalent inelastic strain is determined by integrating the evolution equation

$$\varepsilon_{\mathrm{p}}(t_{n+1}) = \varepsilon_{\mathrm{p}}(t_n) + \tfrac{2}{3} \Delta\Gamma \lambda \gamma_{\mathrm{e}}^{*}. \tag{47}$$

5.3. ***Integration of $\boldsymbol{\beta}$.*** Using the Jaumann derivative (18), the evolution equation for the deviatoric tensor $\boldsymbol{\beta}$ can be written in the form

$$\dot{\boldsymbol{\beta}} = \boldsymbol{W}\boldsymbol{\beta} + \boldsymbol{\beta}\boldsymbol{W}^{T} + m_3 \Gamma(\beta_{\mathrm{s}} \boldsymbol{U} - \boldsymbol{\beta}) - m_4 \boldsymbol{\beta}. \tag{48}$$

Now, following the work in [Rubin 2020], it is convenient to introduce the elastic trial value $\boldsymbol{\beta}^{*}$, which is the solution for $\boldsymbol{\beta}$ in the absence of inelasticity and thermal recovery, i.e.,

$$\dot{\boldsymbol{\beta}}^{*} = \boldsymbol{W}\boldsymbol{\beta}^{*} + \boldsymbol{\beta}^{*}\boldsymbol{W}^{T} = \boldsymbol{L}\boldsymbol{\beta}^{*} + \boldsymbol{\beta}^{*}\boldsymbol{L}^{T} - \tfrac{2}{3}(\boldsymbol{\beta}^{*} : \boldsymbol{D})\boldsymbol{I} - \boldsymbol{R}, \quad \boldsymbol{\beta}^{*}(t_n) = \boldsymbol{\beta}(t_n), \tag{49}$$

with

$$\boldsymbol{R} = \boldsymbol{R}(\boldsymbol{\beta}^*, \boldsymbol{D}) = \boldsymbol{D}\boldsymbol{\beta}^* + \boldsymbol{\beta}^*\boldsymbol{D} - \tfrac{2}{3}(\boldsymbol{\beta}^* : \boldsymbol{D})\boldsymbol{I}. \tag{50}$$

Equation (48) can then be approximated by

$$\dot{\boldsymbol{\beta}} \approx \dot{\boldsymbol{\beta}}^* + m_3\Gamma(\beta_s\boldsymbol{U} - \boldsymbol{\beta}) - m_4\boldsymbol{\beta}\,. \tag{51}$$

To solve (49), it is also convenient to introduce the auxiliary deviatoric tensor $\bar{\boldsymbol{\beta}}'$, which satisfies the equations

$$\bar{\boldsymbol{\beta}} = \boldsymbol{F}_r\boldsymbol{\beta}(t_n)\boldsymbol{F}_r^{\mathrm{T}}, \quad \bar{\boldsymbol{\beta}}'(t_n) = \boldsymbol{\beta}(t_n), \quad \dot{\bar{\boldsymbol{\beta}}}' = \boldsymbol{L}\bar{\boldsymbol{\beta}}' + \bar{\boldsymbol{\beta}}'\boldsymbol{L}^{\mathrm{T}} - \tfrac{2}{3}(\bar{\boldsymbol{\beta}}' : \boldsymbol{D})\boldsymbol{I}, \tag{52}$$

and rewrite (49) in the approximate form

$$\dot{\boldsymbol{\beta}}^* \approx \dot{\bar{\boldsymbol{\beta}}}' - \boldsymbol{R}(\bar{\boldsymbol{\beta}}', \boldsymbol{D}). \tag{53}$$

Using a backward Euler approximation of the derivatives, (53) is integrated to obtain

$$\boldsymbol{\beta}^*(t_{n+1}) \approx \alpha(\bar{\boldsymbol{\beta}}'(t_{n+1}) - \Delta\boldsymbol{R}), \quad \Delta\boldsymbol{R} = \Delta t\,\boldsymbol{R}(\bar{\boldsymbol{\beta}}'(t_{n+1}), \widetilde{\boldsymbol{D}}), \alpha = \frac{|\boldsymbol{\beta}(t_n)|}{|\bar{\boldsymbol{\beta}}'(t_{n+1}) - \Delta\boldsymbol{R}|}, \tag{54}$$

where the scalar α is a correction factor that ensures that the elastic trial $\boldsymbol{\beta}^*(t_{n+1})$ is consistent with a pure rotation, since it has the same magnitude as $\boldsymbol{\beta}(t_n)$.

Also, with the help of (20) and (43) it can be shown that

$$\boldsymbol{U}(t_{n+1}) = \boldsymbol{U}^* = \frac{\bar{\boldsymbol{B}}_e'^*}{|\bar{\boldsymbol{B}}_e'^*|} = \sqrt{\tfrac{3}{8}}\frac{\bar{\boldsymbol{B}}_e'^*}{\gamma_e^*}, \tag{55}$$

with

$$\gamma_e^* = \tfrac{1}{2}\sqrt{\tfrac{3}{2}\bar{\boldsymbol{B}}_e'^* : \bar{\boldsymbol{B}}_e'^*}. \tag{56}$$

Finally, using a backward Euler approximation of the derivative in (51), the value $\boldsymbol{\beta}(t_{n+1})$ is determined by

$$\boldsymbol{\beta}(t_{n+1}) = \frac{\boldsymbol{\beta}^*(t_{n+1}) + m_3\beta_s\Delta\Gamma\boldsymbol{U}(t_{n+1})}{1 + m_3\Delta\Gamma + m_4\Delta t}, \tag{57}$$

where $\Delta\Gamma$ is defined by (44).

5.4. ***Integration of β.*** Using the fact that the Lode parameter U defined in (23) has the same value at the end of the time step as its value based on the elastic trial solution

$$U(\bar{\boldsymbol{B}}_e'(t_{n+1})) = U^*(\bar{\boldsymbol{B}}_e'^*) = \frac{27\det\bar{\boldsymbol{B}}_e'^*}{16\gamma_e^{*3}}, \tag{58}$$

the evolution equation (22) for the directional hardening parameter β can be integrated to obtain

$$\beta(t_{n+1}) = \frac{\beta(t_n) + m_3\beta_s\Delta\Gamma U(t_{n+1})}{1 + m_3\Delta\Gamma + m_4\Delta t}. \tag{59}$$

5.5. ***Determination of*** $\boldsymbol{\Delta\Gamma}$**.** The numerical approximations of the state variables above depend on the increment $\Delta\Gamma$, which has not been specified yet. If $\gamma_{\mathrm{e}}^* \le \kappa^* H^*$, where κ^* and H^* denote the values of $\kappa(t_{n+1})$ and $H(t_{n+1})$ evaluated for $\Delta\Gamma = 0$, then the step is elastic and $\Delta\Gamma = 0$ holds. On the other hand, if $\gamma_{\mathrm{e}}^* > \kappa^* H^*$, then the step is inelastic, and $\Delta\Gamma$ needs to be determined by solving (44), which implicitly defines $\Delta\Gamma$, since the right-hand side of (44) is a function of the updated state variables that in turn depend on $\Delta\Gamma$. In the present work, (44) is solved through a Newton–Raphson scheme.

5.6. ***Strong objectivity.*** These numerical estimates $J_e(t_{n+1})$, $\bar{\boldsymbol{B}}_{\mathrm{e}}(t_{n+1})$, $\kappa(t_{n+1})$, $\boldsymbol{\beta}(t_{n+1})$ and $\beta(t_{n+1})$ are strongly objective in the sense discussed in [Papes 2012] and [Rubin and Papes 2011] since they satisfy the same transformation under SRBM as the exact values

$$J_e^+(t_{n+1}) = J_e(t_{n+1}), \quad \bar{\boldsymbol{B}}_{\mathrm{e}}^+(t_{n+1}) = \boldsymbol{Q}\bar{\boldsymbol{B}}_{\mathrm{e}}(t_{n+1})\boldsymbol{Q}^T, \tag{60}$$

$$\kappa^+(t_{n+1}) = \kappa(t_{n+1}), \quad \boldsymbol{\beta}^+(t_{n+1}) = \boldsymbol{Q}\boldsymbol{\beta}(t_{n+1})\boldsymbol{Q}^T, \quad \beta^+(t_{n+1}) = \beta(t_{n+1}), \tag{61}$$

for arbitrary SRBM.

5.7. ***Algorithmic tangent stiffness.*** In the derivation of the algorithmic (consistent) tangent stiffness below, entities are understood as pertaining to the end of the time step, i.e., $t = t_{n+1}$, unless otherwise specified. To simplify the notation, two tensor operators are introduced:

$$(\boldsymbol{Q} \otimes \boldsymbol{R})_{ijkl} = Q_{ij}R_{kl}, \tag{62}$$

$$(\boldsymbol{Q} \oplus \boldsymbol{R})_{ijkl} = \tfrac{1}{2}(Q_{ik}R_{jl} + R_{il}Q_{jk}). \tag{63}$$

The Kirchhoff stress is given by $\boldsymbol{\tau} = J_{\mathrm{e}}\boldsymbol{T}$ and is a function of $\boldsymbol{F}_{\mathrm{r}}$. The variation of $\boldsymbol{\tau}$ is given by

$$\delta\boldsymbol{\tau} = \frac{\partial\boldsymbol{\tau}}{\partial\boldsymbol{F}_{\mathrm{r}}} : \delta\boldsymbol{F}_{\mathrm{r}} = \left[\left(\frac{\partial\boldsymbol{\tau}}{\partial\boldsymbol{F}_{\mathrm{r}}}\right)\boldsymbol{F}_{\mathrm{r}}^{\mathrm{T}}\right] : (\delta\boldsymbol{F}_{\mathrm{r}}\boldsymbol{F}_{\mathrm{r}}^{-1}). \tag{64}$$

The consistent tangent modulus, $\mathbb{C}$, is then identified as

$$\mathbb{C} = \frac{1}{J_e}\left(\frac{\partial\boldsymbol{\tau}}{\partial\boldsymbol{F}_{\mathrm{r}}}\right)\boldsymbol{F}_{\mathrm{r}}^{\mathrm{T}} = \frac{1}{J_{\mathrm{e}}}\left[K\boldsymbol{I} \otimes \frac{\partial J_{\mathrm{e}}}{\partial\boldsymbol{F}_{\mathrm{r}}} + \mu\left(\frac{\partial\bar{\boldsymbol{B}}'_{\mathrm{e}}}{\partial\boldsymbol{F}_{\mathrm{r}}}\right)\right]\boldsymbol{F}_{\mathrm{r}}^{\mathrm{T}}. \tag{65}$$

A few simplifications are made when deriving the consistent tangent modulus. In practice, the factor α in (54) is close to unity, and the influence of α on the algorithmic stiffness is therefore ignored. Furthermore, the approximation of $\boldsymbol{D}$ is replaced by the simpler expression [Hollenstein et al. 2013]

$$\boldsymbol{D} \approx \frac{1}{2\Delta t}(\boldsymbol{B}_{\mathrm{r}} - \boldsymbol{I}), \tag{66}$$

where $\boldsymbol{B}_{\mathrm{r}} = \boldsymbol{F}_{\mathrm{r}}\boldsymbol{F}_{\mathrm{r}}^{\mathrm{T}}$. However, the forms (36) and (54) are used in evaluating the constitutive equations.

Recalling that the current value of J_{e} is given by $J_{\mathrm{e}} = J_{\mathrm{e}}(t_1)J_{\mathrm{r}}$, it follows that

$$\frac{\partial J_{\mathrm{e}}}{\partial\boldsymbol{F}_{\mathrm{r}}}\boldsymbol{F}_{\mathrm{r}}^{\mathrm{T}} = J_{\mathrm{e}}(t_1)\frac{\partial J_{\mathrm{r}}}{\partial\boldsymbol{F}_{\mathrm{r}}}\boldsymbol{F}_{\mathrm{r}}^{\mathrm{T}} = J_{\mathrm{e}}(t_1)J_{\mathrm{r}}\boldsymbol{F}_{\mathrm{r}}^{-\mathrm{T}}\boldsymbol{F}_{\mathrm{r}}^{\mathrm{T}} = J_{\mathrm{e}}\boldsymbol{I}. \tag{67}$$

The second term in (65) is given by

$$\left(\frac{\partial\bar{\boldsymbol{B}}'_{\mathrm{e}}}{\partial\boldsymbol{F}_{\mathrm{r}}}\right)\boldsymbol{F}_{\mathrm{r}}^{\mathrm{T}} = \partial(\lambda\bar{\boldsymbol{B}}'^{*}_{\mathrm{e}})\partial\boldsymbol{F}_{\mathrm{r}}\boldsymbol{F}_{\mathrm{r}}^{\mathrm{T}} = -\lambda^2\bar{\boldsymbol{B}}'^{*}_{\mathrm{e}} \otimes \left(\frac{\partial(\Delta\Gamma)}{\partial\boldsymbol{F}_{\mathrm{r}}}\boldsymbol{F}_{\mathrm{r}}^{\mathrm{T}}\right) + \lambda\left(\frac{\partial\bar{\boldsymbol{B}}'^{*}_{\mathrm{e}}}{\partial\boldsymbol{F}_{\mathrm{r}}}\right)\boldsymbol{F}_{\mathrm{r}}^{\mathrm{T}}. \tag{68}$$

For the last derivative in the expression above, it is first noted that

$$\left(\frac{\partial \bar{\boldsymbol{B}}_{\mathrm{e}}^{*}}{\partial \boldsymbol{F}_{\mathrm{r}}}\right)=-\tfrac{2}{3}\bar{\boldsymbol{B}}_{\mathrm{e}}^{*}\otimes \boldsymbol{F}_{\mathrm{r}}^{-\mathrm{T}}+\frac{1}{J_{\mathrm{r}}^{2/3}}\frac{\partial[\boldsymbol{F}_{\mathrm{r}}\bar{\boldsymbol{B}}_{\mathrm{e}}(t_1)\boldsymbol{F}_{\mathrm{r}}^{\mathrm{T}}]}{\partial \boldsymbol{F}_{\mathrm{r}}}, \tag{69}$$

and that

$$\frac{\partial[\boldsymbol{F}_{\mathrm{r}}\bar{\boldsymbol{B}}_{\mathrm{e}}(t_1)\boldsymbol{F}_{\mathrm{r}}^{\mathrm{T}}]}{\partial \boldsymbol{F}_{\mathrm{r}}}=2(\boldsymbol{I}\oplus \boldsymbol{F}_{\mathrm{r}})\bar{\boldsymbol{B}}_{\mathrm{e}}(t_1). \tag{70}$$

A fourth-order tensor $\mathbb{D}_1$ is then defined as

$$\mathbb{D}_1=\left(\frac{\partial \bar{\boldsymbol{B}}_{\mathrm{e}}^{\prime *}}{\partial \boldsymbol{F}_{\mathrm{r}}}\right)\boldsymbol{F}_{\mathrm{r}}^{\mathrm{T}}=2\boldsymbol{I}\oplus \bar{\boldsymbol{B}}_{\mathrm{e}}^{*}-\tfrac{2}{3}(\boldsymbol{I}\otimes \bar{\boldsymbol{B}}_{\mathrm{e}}^{*}+\bar{\boldsymbol{B}}_{\mathrm{e}}^{*}\otimes \boldsymbol{I})+\tfrac{2}{9}(\bar{\boldsymbol{B}}_{\mathrm{e}}^{*}:\boldsymbol{I})\boldsymbol{I}\otimes \boldsymbol{I}. \tag{71}$$

Differentiation of $\Delta\Gamma$ in (44) yields

$$\left(1+\lambda\zeta_1+\frac{\zeta_1\zeta_2}{\kappa}\right)\delta(\Delta\Gamma)=\frac{\Delta\Gamma}{\dot{\varepsilon}}\delta\dot{\varepsilon}+\frac{\zeta_1}{\gamma_{\mathrm{e}}^{*}}\delta\gamma_{\mathrm{e}}^{*}-\frac{\zeta_1}{H}\delta H, \tag{72}$$

where

$$\delta\dot{\varepsilon}=\frac{2}{3\dot{\varepsilon}}\boldsymbol{D}^{\prime}:\left(\frac{\partial \boldsymbol{D}^{\prime}}{\partial \boldsymbol{F}_{\mathrm{r}}}\right):\delta \boldsymbol{F}_{\mathrm{r}}, \tag{73}$$

$$\left(\frac{\partial \boldsymbol{D}^{\prime}}{\partial \boldsymbol{F}_{\mathrm{r}}}\right)=\frac{1}{\Delta t}\big(\boldsymbol{I}\oplus \boldsymbol{F}_{\mathrm{r}}-\tfrac{1}{3}\boldsymbol{I}\otimes \boldsymbol{F}_{\mathrm{r}}\big), \tag{74}$$

$$\delta\gamma_{\mathrm{e}}^{*}=\frac{3}{8\gamma_{\mathrm{e}}^{*}}\bar{\boldsymbol{B}}_{\mathrm{e}}^{\prime *}:\left(\frac{\partial \bar{\boldsymbol{B}}_{\mathrm{e}}^{\prime *}}{\partial \boldsymbol{F}_{\mathrm{r}}}\right):\delta \boldsymbol{F}_{\mathrm{r}}, \tag{75}$$

and

$$\zeta_1=\frac{b_1\dot{\varepsilon}\Delta t\kappa H}{\gamma_{\mathrm{e}}},\quad \zeta_2=\frac{\mathrm{d}\kappa}{\mathrm{d}(\Delta\Gamma)}=\frac{m_1(\kappa_{\mathrm{s}}-\kappa)}{1+m_1\Delta\Gamma+m_2\Delta t}. \tag{76}$$

For the scalar model (model S) it follows that

$$\delta H=\delta H_{\mathrm{S}}=U\delta\beta+\beta\delta U=U\zeta_3\delta(\Delta\Gamma)+(\beta+\zeta_4 U)\delta U, \tag{77}$$

where

$$\zeta_3=\frac{\mathrm{d}\beta}{\mathrm{d}(\Delta\Gamma)}=\frac{m_3(\beta_{\mathrm{s}}U-\beta)}{1+m_3\Delta\Gamma+m_4\Delta t},\quad \zeta_4=\frac{m_3\beta_{\mathrm{s}}\Delta\Gamma}{1+m_3\Delta\Gamma+m_4\Delta t}, \tag{78}$$

and

$$\delta U=\boldsymbol{M}_{\mathrm{S}}:\left(\frac{\partial \bar{\boldsymbol{B}}_{\mathrm{e}}^{\prime *}}{\partial \boldsymbol{F}_{\mathrm{r}}}\right):\delta \boldsymbol{F}_{\mathrm{r}}, \tag{79}$$

where

$$\boldsymbol{M}_{\mathrm{S}}=U\left(\bar{\boldsymbol{B}}_{\mathrm{e}}^{\prime *-1}-\frac{9}{8\gamma_{\mathrm{e}}^{*2}}\bar{\boldsymbol{B}}_{\mathrm{e}}^{\prime *}\right). \tag{80}$$

For the tensorial model (model T) it follows that

$$\delta H=\delta H_{\mathrm{T}}=\boldsymbol{U}:\delta\boldsymbol{\beta}+\boldsymbol{\beta}:\delta\boldsymbol{U}=\zeta_5\boldsymbol{U}:\delta\boldsymbol{\beta}^{*}+\boldsymbol{U}:\boldsymbol{M}_{\mathrm{T}}\delta(\Delta\Gamma)+(\boldsymbol{\beta}+\zeta_4\boldsymbol{U}):\delta\boldsymbol{U}, \tag{81}$$

where

$$\zeta_5=\frac{1}{1+m_3\Delta\Gamma+m_4\Delta t},\quad \boldsymbol{M}_{\mathrm{T}}=\frac{m_3(\beta_{\mathrm{s}}\boldsymbol{U}-\boldsymbol{\beta})}{1+m_3\Delta\Gamma+m_4\Delta t}. \tag{82}$$

Moreover, we have

$$\delta\boldsymbol{\beta}^* = \left(\frac{\partial\boldsymbol{\beta}^*}{\partial\boldsymbol{F}_\mathrm{r}}\right) : \delta\boldsymbol{F}_\mathrm{r},$$

$$\left(\frac{\partial\boldsymbol{\beta}^*}{\partial\boldsymbol{F}_\mathrm{r}}\right) = \left(2\boldsymbol{I} - \tfrac{1}{2}\boldsymbol{B}_\mathrm{r}\right)\left(\frac{\partial\bar{\boldsymbol{\beta}}'}{\partial\boldsymbol{F}_\mathrm{r}}\right) + \tfrac{1}{3}\boldsymbol{I}\otimes\left[\boldsymbol{B}_\mathrm{r} : \left(\frac{\partial\bar{\boldsymbol{\beta}}'}{\partial\boldsymbol{F}_\mathrm{r}}\right) + 2\bar{\boldsymbol{\beta}}'\boldsymbol{F}_\mathrm{r}\right] - \boldsymbol{I}\oplus(\bar{\boldsymbol{\beta}}'\boldsymbol{F}_\mathrm{r}) - \bar{\boldsymbol{\beta}}'\oplus\boldsymbol{F}_\mathrm{r}, \tag{83}$$

$$\left(\frac{\partial\bar{\boldsymbol{\beta}}'}{\partial\boldsymbol{F}_\mathrm{r}}\right) = 2\left(\boldsymbol{I}\oplus\boldsymbol{F}_\mathrm{r} - \tfrac{1}{3}\boldsymbol{I}\otimes\boldsymbol{F}_\mathrm{r}\right)\boldsymbol{\beta}(t_n), \tag{84}$$

$$\delta\boldsymbol{U} = \mathbb{M}_\mathrm{T} : \left(\frac{\partial\bar{\boldsymbol{B}}_\mathrm{e}'^*}{\partial\boldsymbol{F}_\mathrm{r}}\right) : \delta\boldsymbol{F}_\mathrm{r}, \tag{85}$$

$$\mathbb{M}_\mathrm{T} = \sqrt{\frac{3}{8}}\frac{1}{\gamma_\mathrm{e}^*}\left(\mathbb{I} - \frac{3}{8\gamma_\mathrm{e}^{*2}}\bar{\boldsymbol{B}}_\mathrm{e}'^*\otimes\bar{\boldsymbol{B}}_\mathrm{e}'^*\right), \tag{86}$$

where $\mathbb{I} = \boldsymbol{I}\oplus\boldsymbol{I}$ is the fourth-order unit tensor. This finally gives

$$\frac{\partial(\Delta\Gamma)}{\partial\boldsymbol{F}_\mathrm{r}}\boldsymbol{F}_\mathrm{r}^\mathrm{T} = \boldsymbol{H} = \frac{\kappa}{\zeta_6}\left\{\frac{2\Delta\Gamma H\gamma_\mathrm{e}^{*2}}{3}\boldsymbol{D}' : \mathbb{D}_2 + \zeta_1\dot{\varepsilon}^2\left[\frac{3H}{8}\bar{\boldsymbol{B}}_\mathrm{e}'^* - \gamma_\mathrm{e}^{*2}\boldsymbol{N}_{1,\mathrm{S/T}}\right] : \mathbb{D}_1 - \boldsymbol{N}_{2,\mathrm{S/T}}\right\}, \tag{87}$$

where

$$\zeta_6 = \dot{\varepsilon}^2\gamma_\mathrm{e}^{*2}(\kappa H + \zeta_1\lambda\kappa H + \zeta_1\zeta_2 H + N_\mathrm{S/T}), \tag{88}$$

$$\mathbb{D}_2 = \left(\frac{\partial\boldsymbol{D}'}{\partial\boldsymbol{F}_\mathrm{r}}\right)\boldsymbol{F}_\mathrm{r}^\mathrm{T} = \frac{1}{\Delta t}\left[\boldsymbol{I}\oplus\boldsymbol{B}_\mathrm{r} - \tfrac{1}{3}\boldsymbol{I}\otimes\boldsymbol{B}_\mathrm{r}\right], \tag{89}$$

$$N_\mathrm{S} = \zeta_1\zeta_3\kappa U, \quad N_\mathrm{T} = \zeta_1\kappa\boldsymbol{U} : \boldsymbol{M}_\mathrm{T}, \tag{90}$$

$$\boldsymbol{N}_{1,\mathrm{S}} = (\beta + \zeta_4 U)\boldsymbol{M}_\mathrm{S}, \quad \boldsymbol{N}_{1,\mathrm{T}} = (\boldsymbol{\beta} + \zeta_4\boldsymbol{U}) : \mathbb{M}_\mathrm{T}, \tag{91}$$

$$\boldsymbol{N}_{2,\mathrm{S}} = \boldsymbol{0}, \quad \boldsymbol{N}_{2,\mathrm{T}} = \zeta_1\zeta_5\dot{\varepsilon}^2\gamma_\mathrm{e}^{*2}\boldsymbol{U} : \mathbb{D}_3, \tag{92}$$

$$\mathbb{D}_3 = \left(\frac{\partial\boldsymbol{\beta}^*}{\partial\boldsymbol{F}_\mathrm{r}}\right)\boldsymbol{F}_\mathrm{r}^\mathrm{T} = 4\left(\boldsymbol{I}\oplus\bar{\boldsymbol{\beta}} - \tfrac{1}{3}\boldsymbol{I}\otimes\bar{\boldsymbol{\beta}}\right) + \boldsymbol{I}\oplus(\bar{\boldsymbol{\beta}}'\boldsymbol{B}_\mathrm{r} + \boldsymbol{B}_\mathrm{r}\bar{\boldsymbol{\beta}}') + \bar{\boldsymbol{\beta}}\oplus\boldsymbol{B}_\mathrm{r} + \boldsymbol{B}_\mathrm{r}\oplus\bar{\boldsymbol{\beta}} - \tfrac{2}{3}\boldsymbol{B}_\mathrm{r}\otimes\bar{\boldsymbol{\beta}} + \tfrac{2}{3}\boldsymbol{I}\otimes(\boldsymbol{B}_\mathrm{r}'\bar{\boldsymbol{\beta}} + \bar{\boldsymbol{\beta}}'\boldsymbol{B}_\mathrm{r}). \tag{93}$$

Above, the entities $(\bullet)_\mathrm{S/T}$ take on the values $(\bullet)_\mathrm{S}$ and $(\bullet)_\mathrm{T}$ for model S and model T, respectively. It then follows that

$$\left(\frac{\partial\bar{\boldsymbol{B}}_\mathrm{e}'}{\partial\boldsymbol{F}_\mathrm{r}}\right)\boldsymbol{F}_\mathrm{r}^\mathrm{T} = \mathbb{H} = \lambda\left(\frac{\partial\bar{\boldsymbol{B}}_\mathrm{e}'^*}{\partial\boldsymbol{F}_\mathrm{r}}\right)\boldsymbol{F}_\mathrm{r}^\mathrm{T} - \lambda^2\bar{\boldsymbol{B}}_\mathrm{e}'^*\otimes\frac{\partial(\Delta\Gamma)}{\partial\boldsymbol{F}_\mathrm{r}}\boldsymbol{F}_\mathrm{r}^\mathrm{T} = \lambda\mathbb{D}_1 - \lambda^2\bar{\boldsymbol{B}}_\mathrm{e}'^*\otimes\boldsymbol{H}. \tag{94}$$

The total mechanical stiffness is then given by

$$\mathbb{C} = K\boldsymbol{I}\otimes\boldsymbol{I} + \frac{\mu}{J_\mathrm{e}}\mathbb{H}. \tag{95}$$

6. Examples

6.1. ***Prerequisites.*** The stress response and evolution of relevant state variables for different loading paths and cases are now considered. The components, T_{ij} of the stress tensor $\boldsymbol{T}$ referred to the fixed

rectangular Cartesian base vectors $\boldsymbol{e}_i$ are defined by

$$T_{ij} = \boldsymbol{T} : \boldsymbol{e}_i \otimes \boldsymbol{e}_j, \tag{96}$$

with $\boldsymbol{a} \otimes \boldsymbol{b}$ denoting the tensor product between the two vectors $\boldsymbol{a}$ and $\boldsymbol{b}$. The following examples consider steel at room temperature with thermal recovery inactive so that

$$m_2 = m_4 = 0. \tag{97}$$

In addition, the material is assumed to be initially in a zero-stress fully annealed state with the initial conditions specified by:

$$J_{\mathrm{e}}(0) = 1, \quad \bar{\boldsymbol{B}}_{\mathrm{e}}(0) = \boldsymbol{I}, \quad \kappa(0) = \kappa_{\mathrm{a}}, \quad \boldsymbol{\beta}(0) = \boldsymbol{0}, \quad \beta(0) = 0. \tag{98}$$

6.2. ***Cyclic uniaxial stress loading — comparison with experiments.*** For cyclic uniaxial stress loading, the deformation gradient $\boldsymbol{F}$ is specified by

$$\boldsymbol{F} = a\boldsymbol{e}_1 \otimes \boldsymbol{e}_1 + b(\boldsymbol{e}_2 \otimes \boldsymbol{e}_2 + \boldsymbol{e}_3 \otimes \boldsymbol{e}_3), \tag{99}$$

where a is the stretch in the loading direction and b is the lateral stretch. The axial stretch a is a specified function of time only and the lateral stretch b is determined by the lateral boundary condition

$$T_{22} = 0, \tag{100}$$

where it is noted that $T_{33} = T_{22}$ for this deformation.

Figure 4 considers uniaxial tension to different extensions $a - 1$ followed by reverse loadings into compression. The experimental data for austenitic stainless steel (316L) at room temperature is taken from [Choteau et al. 2005] and is denoted by symbols. It should be noted that for this case of uniaxial stress, models T and S predict exactly the same response for the same material constants. The following model material constants

$$\begin{aligned} &\mu = 69\,\mathrm{GPa}, \quad K = 167\,\mathrm{GPa}, \quad b_1 = 2.5 \cdot 10^3, \quad m_1 = 0.0017, \\ &\kappa_a = 0.0012, \quad \kappa_s = 0.01, \quad m_3 = 0.15, \quad \beta_s = 0.35, \end{aligned} \tag{101}$$

have been calibrated, and the results in Figure 4 show excellent comparison of model predictions to the experimental data.

6.3. ***Cyclic loading with simple deformation modes.*** For the remaining examples in this paper, the material constants are specified by

$$\begin{aligned} &\mu = 77\,\mathrm{GPa}, \quad K = 167\,\mathrm{GPa}, \quad b_1 = 10^5, \quad m_1 = 0.001, \\ &\kappa_a = 0.002, \quad \kappa_s = 0.012, \quad m_3 = 0.2, \quad \beta_s = 0.3. \end{aligned} \tag{102}$$

Also, in this subsection attention is limited to isochoric deformation with the deformation gradient $\boldsymbol{F}$ specified by

$$\boldsymbol{F} = a\boldsymbol{e}_1 \otimes \boldsymbol{e}_1 + \left(a\gamma\boldsymbol{e}_1 + \frac{1}{\sqrt{a}}\boldsymbol{e}_2\right) \otimes \boldsymbol{e}_2 + \frac{1}{\sqrt{a}}\boldsymbol{e}_3 \otimes \boldsymbol{e}_3, \quad J_{\mathrm{e}} = \det \boldsymbol{F} = 1, \tag{103}$$

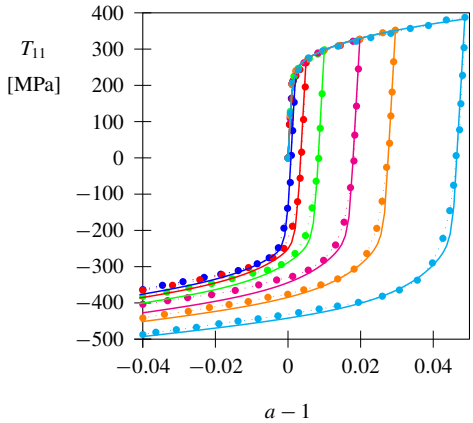

Figure 4. Material response for cyclic uniaxial stress with loading up to different maximum extensions $a-1$ followed by reversed loading; data from [Choteau et al. 2005] (symbols) for austenitic stainless steel (316L) together with the calibrated model responses (solid lines).

where a and γ are functions of time only. Using this expression it can be shown that the rate of deformation tensor $\boldsymbol{D}$ and the spin tensor $\boldsymbol{W}$ can be expressed in the forms

$$\begin{aligned}\boldsymbol{D} &= \frac{\dot{a}}{a}\big[\boldsymbol{e}_1\otimes\boldsymbol{e}_1 - \tfrac{1}{2}(\boldsymbol{e}_2\otimes\boldsymbol{e}_2+\boldsymbol{e}_3\otimes\boldsymbol{e}_3)\big] + \tfrac{1}{2}a^{3/2}\dot{\gamma}(\boldsymbol{e}_1\otimes\boldsymbol{e}_2+\boldsymbol{e}_2\otimes\boldsymbol{e}_1),\\ \boldsymbol{W} &= \tfrac{1}{2}a^{3/2}\dot{\gamma}(\boldsymbol{e}_1\otimes\boldsymbol{e}_2-\boldsymbol{e}_2\otimes\boldsymbol{e}_1).\end{aligned} \tag{104}$$

From these expressions is can be seen that a controls the rates of stretching of material fibers and γ controls shearing.

Two modes of simple deformation are considered:

(1) cyclic isochoric extension and contraction, and

(2) simple shear.

For cyclic isochoric extension and contraction, a and γ are specified by

$$a = 1+0.1\sin(2\pi t), \quad \gamma = 0. \tag{105}$$

In particular, for this loading it can be shown that

$$\begin{aligned}\bar{\boldsymbol{B}}_{\mathrm{e}} &= a_{\mathrm{e}}^2\boldsymbol{e}_1\otimes\boldsymbol{e}_1 + \frac{1}{a_{\mathrm{e}}}(\boldsymbol{e}_2\otimes\boldsymbol{e}_2+\boldsymbol{e}_3\otimes\boldsymbol{e}_3),\\ \boldsymbol{N}' &= \sqrt{\tfrac{2}{3}}\big[\boldsymbol{e}_1\otimes\boldsymbol{e}_1 - \tfrac{1}{2}(\boldsymbol{e}_2\otimes\boldsymbol{e}_2+\boldsymbol{e}_3\otimes\boldsymbol{e}_3)\big],\\ \bar{\boldsymbol{B}}'_{\mathrm{e}} &= B_{\mathrm{e}}\boldsymbol{N}', \quad B_{\mathrm{e}} = \sqrt{\tfrac{2}{3}}\Big(a_{\mathrm{e}}^2 - \frac{1}{a_{\mathrm{e}}}\Big),\\ U &= \operatorname{sign}(B_e), \quad \boldsymbol{U} = U\boldsymbol{N}', \quad \boldsymbol{\beta} = \beta\boldsymbol{N}',\end{aligned} \tag{106}$$

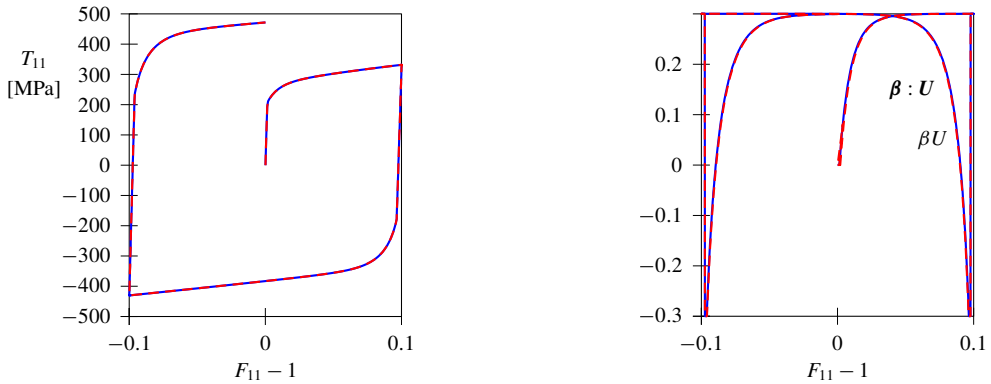

Figure 5. Isochoric extension and contraction: model T (solid blue lines) and S (dashed red lines). Left: stress-strain response. Right: evolution of βU and $\boldsymbol{\beta} : \boldsymbol{U}$ vs. strain.

where the function $\operatorname{sign}(x)$ is defined by

$$\operatorname{sign}(x) = \begin{cases} -1 & \text{for } x < 0, \\ 0 & \text{for } x = 0, \\ 1 & \text{for } x > 0. \end{cases} \tag{107}$$

Using these expressions with U and $\boldsymbol{U}$ being constants, it follows that the tensorial evolution equation (48) for $\boldsymbol{\beta}$ yields the same equation for β as the scalar equation (22). Also, the expressions (19) for the tensorial model and (25) for the scalar model yield the same value of H. Consequently, the two models yield exactly the same results for cyclic isochoric extension and contraction. This is illustrated in Figure 5. The tensorial model and the scalar-based model predict exactly the same stress-strain response in Figure 5, left, and also the same evolution for H in Figure 5, right. Even though it is not evident from Figure 5, right, it should be noted that the evolution of β vanishes during elastic deformation.

The main difference between the scalar model of directional hardening and the tensorial model can be seen for cyclic pure shear (TOR) for which U vanishes. For this loading, the scalar model exhibits no Bauschinger effect, whereas the tensorial model does. Although pure shear and simple shear are not identical, the following example considered cyclic simple shear specified by

$$a = 1, \quad \gamma = 0.1 \sin(2\pi t), \tag{108}$$

to demonstrate the differences between the models.

Figure 6 shows the stress-strain response and the evolution of the relevant state variables for directional hardening for the two models. From Figure 6, left, it is evident that directional hardening is present in the tensorial model, whereas the scalar model only exhibits isotropic hardening for this load case. The reason is that for this load case, the loading variable U is close to zero, implying that directional hardening is not activated in the scalar model. This is further illustrated in Figure 6, right, where $\boldsymbol{\beta} : \boldsymbol{U}$ evolves whereas βU for the scalar model remains close to zero. There is, in fact, some evolution of β due to the fact that for large deformations and nonlinear kinematics, U is not exactly zero, but β remains very small in comparison to $\boldsymbol{\beta}$.

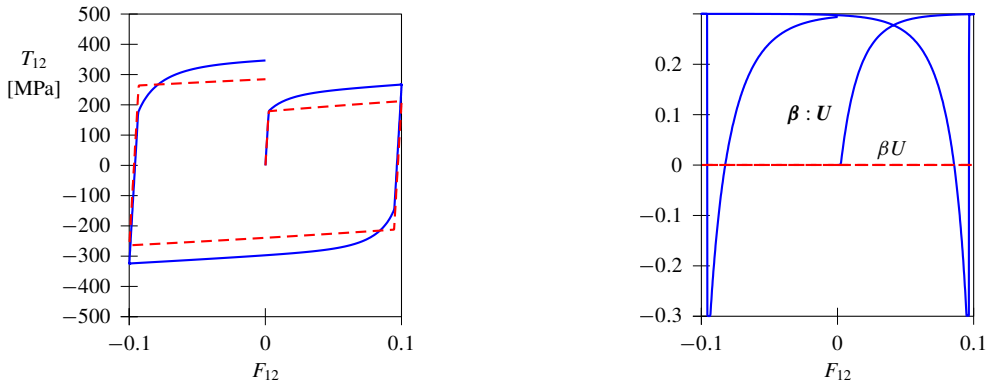

Figure 6. Cyclic loading in simple shear: model T (solid blue lines) and model S (dashed red lines). Left: stress-strain response. Right: evolution of βU and $\boldsymbol{\beta} : \boldsymbol{U}$ vs. strain.

6.4. ***Cyclic extension and contraction followed by simple shear.*** A load case is now considered where the material is first exposed to a cycle of isochoric extension and contraction, in accordance with the paths in Figure 5. After that, the material is exposed to a cycle of simple shear, as discussed in the previous subsection. In Figure 7, the stress-strain response and the evolution of the relevant directional hardening variable during the shearing cycle are shown.

During the preceding extension/contraction cycle the material has accumulated both isotropic and directional hardening. The evolution of the stress components T_{11}, T_{22}, and T_{33} is identical for models T and S, i.e., these components quickly drop to zero (or close to zero) once the extension/contraction loading mode ceases and the shearing mode is initiated. The shear stress curves in Figure 7, bottom-left, show a higher amplitude than the corresponding curves without any preceding deformation shown in Figure 6, left. In the tensorial model, directional hardening is accumulated in the variables β_{11}, β_{22}, and β_{33} during the first isochoric extension/contraction. Hence, when the shear loading starts, the evolution of β_{12} virtually starts from zero. This interaction causes an initial drop in $\boldsymbol{\beta}{:}\boldsymbol{U}$, as seen in Figure 7, bottom-right. However, when β_{12} has accumulated some hardening, $\boldsymbol{\beta}{:}\boldsymbol{U}$ soon starts to increase again. For the scalar-based model, directional hardening is accumulated in β during the isochoric extension/contraction cycle. During the shear loading, the hardening value decreases from 0.3 down to zero, since U is close to zero for this load case.

6.5. ***Cyclic loading with complex a deformation mode.*** A load case is now considered where the material is exposed to a more complex loading mode, i.e., a combination of isochoric extension and shearing. For this case, the velocity gradient is specified in the form

$$\begin{aligned} \boldsymbol{L} = \boldsymbol{D} = \boldsymbol{D}' &= D\sqrt{\tfrac{3}{2}}[\cos 2\pi t\, \boldsymbol{U}_{\mathrm{E}} + \sin 2\pi t\, \boldsymbol{U}_{\mathrm{S}}], \\ \boldsymbol{U}_{\mathrm{E}} &= \sqrt{\tfrac{2}{3}}\big[\boldsymbol{e}_1 \otimes \boldsymbol{e}_1 - \tfrac{1}{2}(\boldsymbol{e}_2 \otimes \boldsymbol{e}_2 + \boldsymbol{e}_3 \otimes \boldsymbol{e}_3)\big], \\ \boldsymbol{U}_{\mathrm{S}} &= \tfrac{1}{\sqrt{2}}[\boldsymbol{e}_1 \otimes \boldsymbol{e}_2 + \boldsymbol{e}_2 \otimes \boldsymbol{e}_1], \\ \boldsymbol{U}_{\mathrm{E}} : \boldsymbol{U}_{\mathrm{E}} &= 1, \quad \boldsymbol{U}_{\mathrm{S}} : \boldsymbol{U}_{\mathrm{S}} = 1, \quad \boldsymbol{U}_{\mathrm{E}} : \boldsymbol{U}_{\mathrm{S}} = 0, \end{aligned} \tag{109}$$

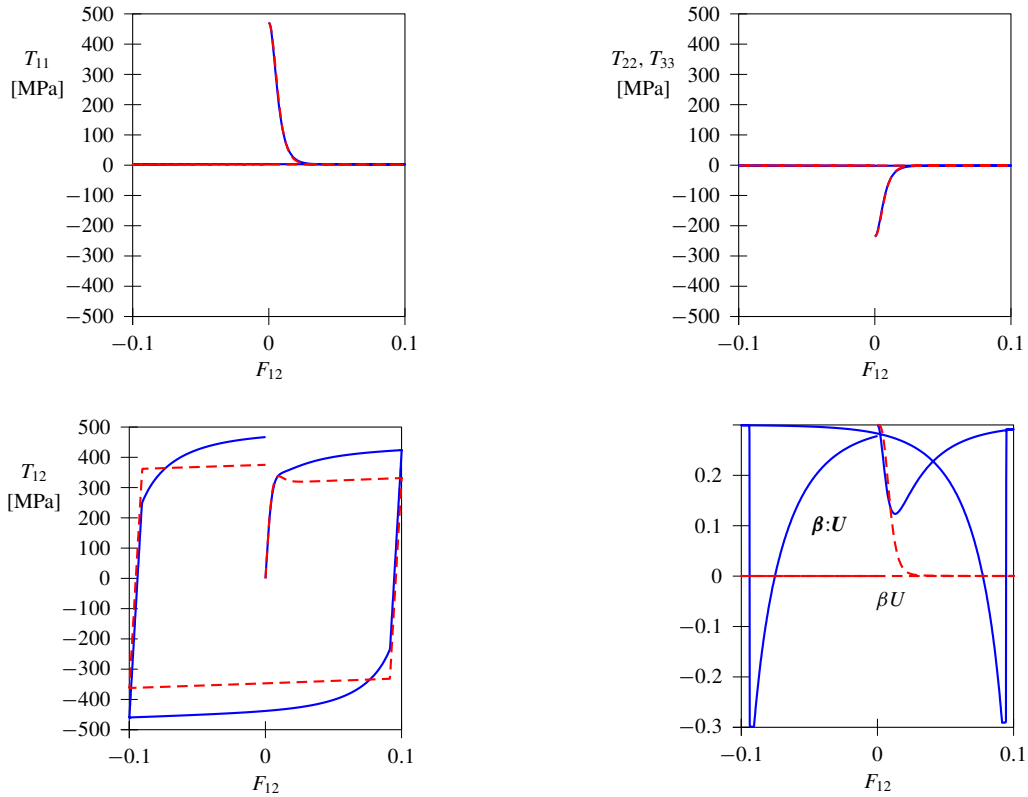

Figure 7. Cyclic loading in simple shear that was preceded by one cycle of isochoric extension and contraction: model T (solid blue lines) and model S (dashed red lines). Top and bottom-left: stress-strain response. Bottom-right: evolution of βU and $\boldsymbol{\beta} : \boldsymbol{U}$ vs. strain.

where $D = 1\text{s}^{-1}$. The deformation gradient is then attained by integrating the evolution equation

$$\dot{\boldsymbol{F}} = \boldsymbol{L}\boldsymbol{F}, \quad \boldsymbol{F}(0) = \boldsymbol{I}. \tag{110}$$

In Figure 8, the outcome from the complex loading path is shown. The responses for T'_{11}, T'_{22}, and T'_{33} in Figure 8, top, for models T and S are virtually identical. The responses for T_{12} for models T and S differ somewhat. Especially the stress peaks differ by about 100 MPa between models T and S. The associated variations in βU and $\boldsymbol{\beta}:\boldsymbol{U}$ are shown in Figure 8, bottom-right. In the beginning of the load path, both $\boldsymbol{\beta}:\boldsymbol{U}$ and βU quickly approach the saturation level $\beta_{\text{s}} = 0.3$. The value of $\boldsymbol{\beta}:\boldsymbol{U}$ then decreases slowly during the rest of the loading cycle, whereas βU oscillates between β_{s} and (approximately) zero.

6.6. ***Cyclic loading of a plate with a circular hole.*** As a last numerical example, cyclic deformation of a plate with a circular hole is considered. In order to study this 3D problem, the material model was implemented in Abaqus as a UMAT user subroutine. The geometry of the plate is shown in Figure 9. The outer dimensions of the plate are given by $H_{\text{p}} = 4\text{cm}$ and $B_{\text{p}} = 2\text{cm}$. The radius of the central hole is $R_{\text{p}} = 1\text{cm}$, and the thickness of the plate is $T_{\text{p}} = 2\text{mm}$.

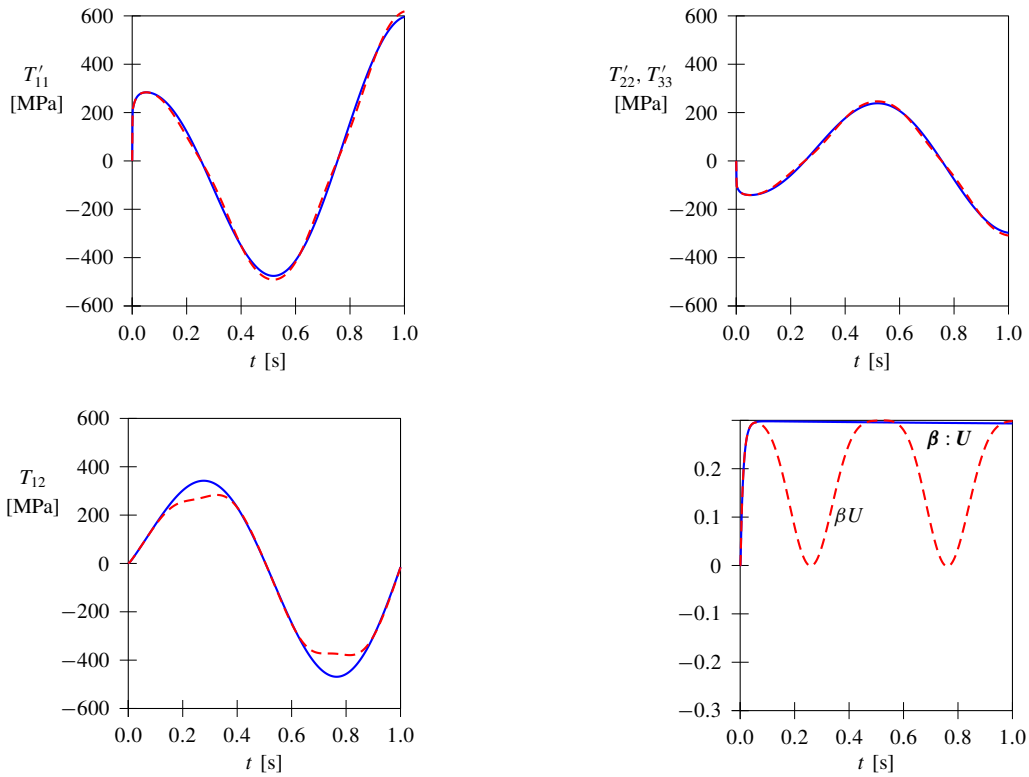

Figure 8. Cyclic loading in combined isochoric extension and contraction and simple shear: model T (solid blue lines) and model S (dashed red lines). Top and bottom-left: stress vs. time response. Bottom-right: evolution of βU and $\boldsymbol{\beta} : \boldsymbol{U}$ vs. time.

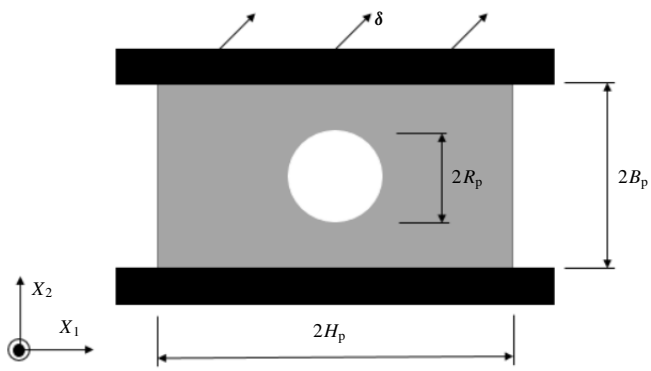

Figure 9. Geometry and loading of plate with a hole.

The plate (gray) is clamped between two rigid blocks (black). The lower block is fixed, whereas the upper block moves with a pure translation, $\boldsymbol{\delta}$, relative to the lower block. The translation is defined by

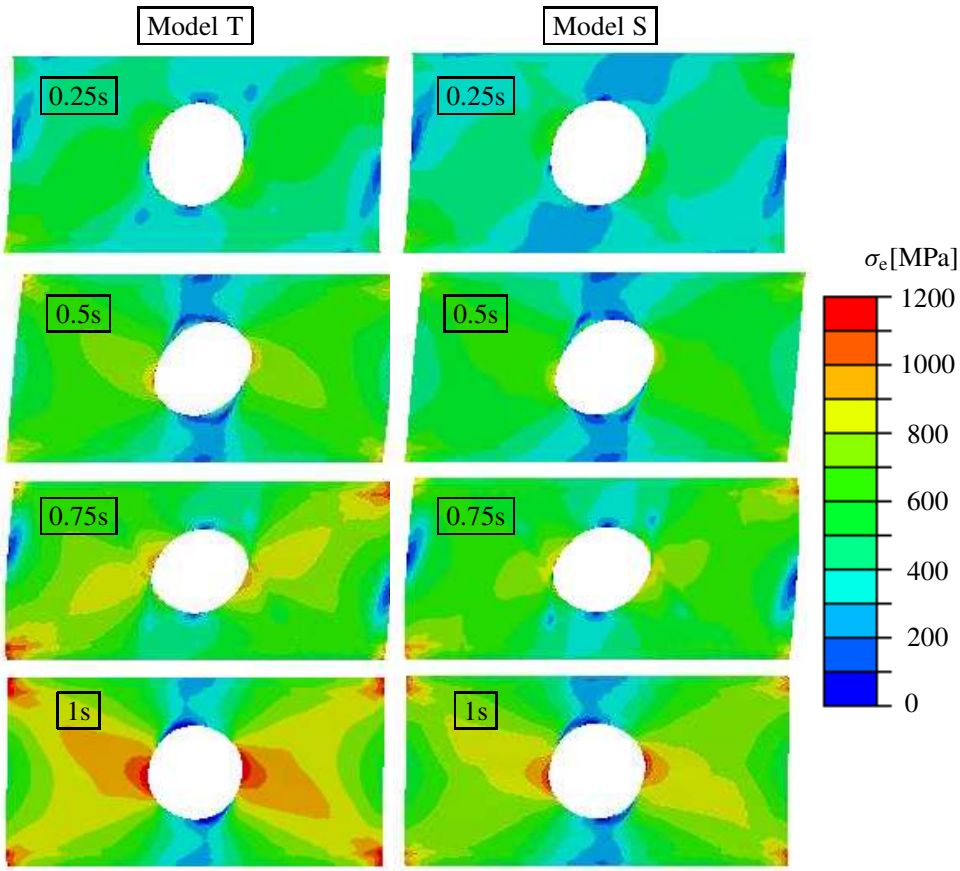

Figure 10. Distributions of σ_e at $t = 0.25$ s, 0.5 s, 0.75 s, and 1 s.

the velocities

$$\dot{\delta}_1 = 4\pi \cos(2\pi t)\ \text{mm/s}, \quad \dot{\delta}_2 = 4\pi \sin(2\pi t)\ \text{mm/s}, \quad t \in [0, 1], \tag{111}$$

implying that the upper block moves in a circle, causing a combination of tension/compression and shearing of the plate.

Wedge elements (i.e., triangular elements with thickness) with quadratic shape functions were used in the finite element analyses, and the characteristic length of the elements close to the hole, where the gradients of stress and strain are strongest, was 1 mm. One layer of elements was used in the thickness (X_3) direction of the plate. Due to symmetry, only half the plate was modeled in the through thickness direction, the material was allowed to slide freely on the symmetry plane $X_3 = 0$ and the surface of the plate was traction free.

Figures 10–13 show results from the plate simulations. In Figure 10, the distribution of the von Mises stress, σ_e, is shown at four different times. In general, the peaks in the stress fields are more pronounced in the solutions for model T than for model S. Besides that, the patterns of the stress fields are very similar for the two models. It can also be noted, that for this type of boundary condition, where the plate is fixed to the rigid blocks, significant stress concentrations appear at the corners of the plate. In the areas

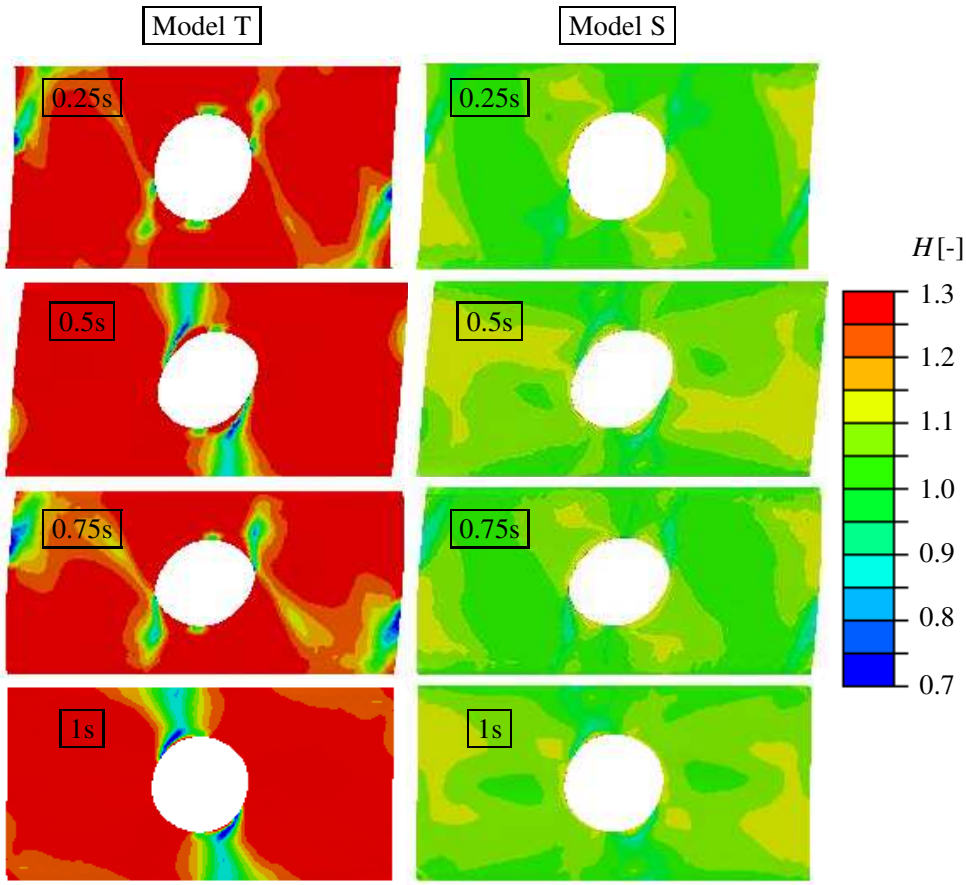

Figure 11. Distributions of (left) H_T and (right) H_S at $t = 0.25$ s, 0.5 s, 0.75 s, and 1 s.

at the hole where the highest stress peaks appear, the peak stress differs by about 100 MPa between the two models.

In Figure 11, distributions of the functions for directional hardening, i.e., H_T and H_S, are shown. The discrepancy between H_T and H_S is significant, where large areas of H_T are more or less saturated with $H_T \approx 1 + \beta_s = 1.3$, whereas the distribution of H_S doesn't deviate much from unity. This observation holds not only at the end of the simulation but also for the earlier stages of the simulation, as seen in the upper images in Figure 11.

Figure 12 shows the distribution of the effective hardening, i.e., κH, for the two models and at the same points in time as before. It can be seen, that the difference in total hardening is not as dramatic as the difference in the H-function. This is also the reason why, in the end, the distributions of effective stress for the two models in Figure 10 agree fairly well.

Finally, Figure 13 shows the distributions of the accumulated equivalent inelastic strain ε_p. By definition, this entity can only increase at a material point. The distribution of this entity is very similar for the two models, not only in the final state of the analysis, but throughout the analysis. Again, the corners of the plate experience stress concentrations with large cyclic shear stresses, which cause large amounts of

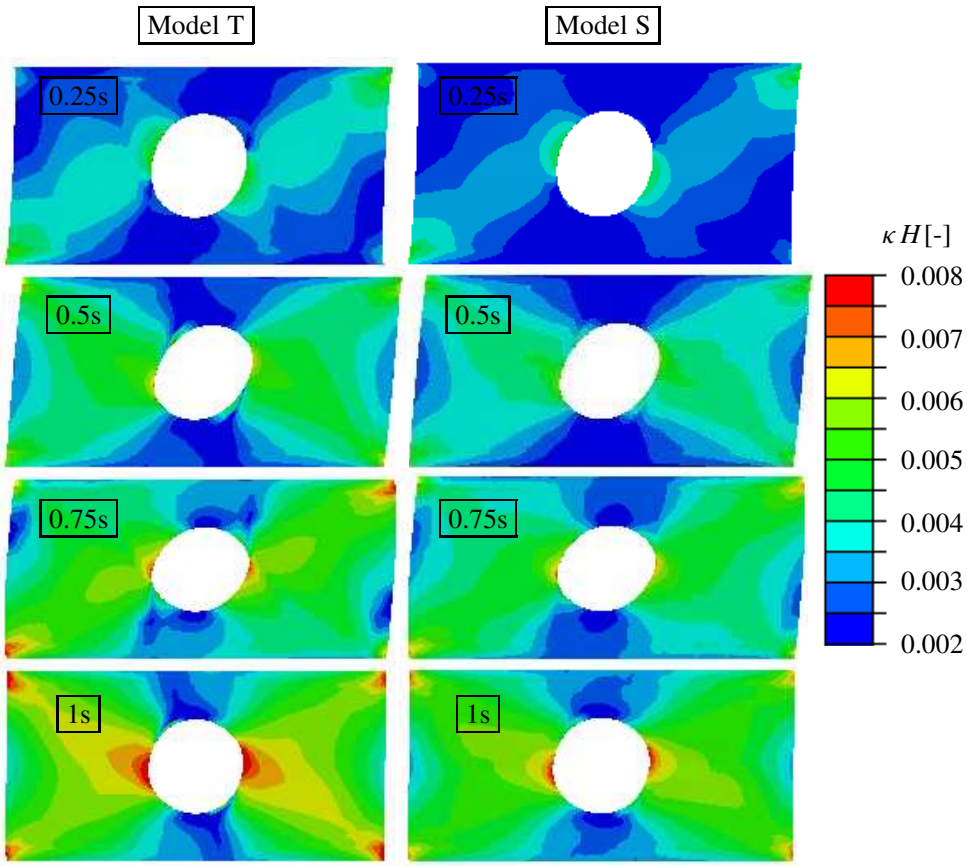

Figure 12. Distributions of (left) κH_{T} and (right) κH_{S} at $t = 0.25$ s, 0.5 s, 0.75 s, and 1 s.

accumulated inelastic strain. Peaks in the equivalent inelastic strain also appear to the left and right of the hole. The magnitude of these peaks is more or less the same for the two models.

7. Discussion and concluding remarks

One approach to modeling the Bauschinger effect is to introduce a history-dependent back-stress tensor with the stress in a yield function replaced by the difference of the stress and the back-stress. Directional hardening is an alternative approach which introduces a history-dependent directional hardening tensor $\boldsymbol{\beta}$ with the effective hardening being a function of isotropic hardening κ and the inner product of $\boldsymbol{\beta}$ with a normalized stress (or elastic deformation) tensor. The main idea of the present work is to propose a simplified version of directional hardening which introduces a history-dependent directional hardening scalar instead of a history-dependent directional hardening tensor. To test this idea, the predictions of scalar model are compared with those of the tensorial model.

Example problems indicate that the two models predict the same response for cyclic proportional triaxial extension and triaxial compression loadings. In contrast, for cyclic proportional pure torsion loading the tensorial model predicts a Bauschinger effect but the scalar model does not. However, in

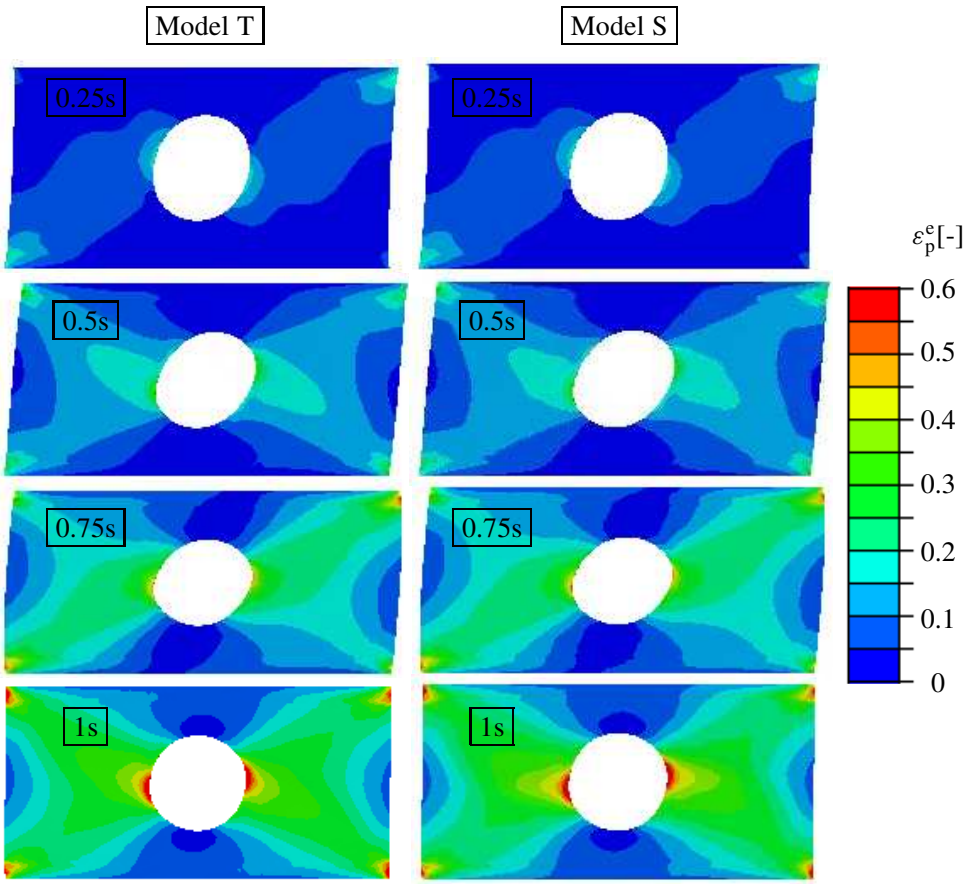

Figure 13. Distributions of equivalent plastic strain ε_p at $t = 0.25$ s, 0.5 s, 0.75 s, and 1 s.

practical problems the stress field is usually inhomogeneous so the material is not in a state of pure torsion. Consequently, additional examples with complex nonproportional loading paths were considered which indicate that the discrepancy between the two models in terms of stress levels is not dramatic. For the 3D analysis of a plate with a hole, the amplitudes of the peak stresses around the hole differed by less than 10% between the two models even though the value of $\beta_s = 0.3$ would indicate a potential effective yield stress κH in the range of $0.7\kappa \leq \kappa H \leq 1.3\kappa$.

Strongly objective numerical algorithms were developed to integrate the evolution equations for both models. Also, a consistent tangent operator was developed for both models. Obviously, the numerical implementation of the scalar model is significantly less complicated than for the tensorial model. Overall, the scalar model accounts for directional hardening fairly well and the simplicity of the model makes it an attractive option to add to isotropic hardening models.

Acknowledgements

The authors would like to thank Prof. P. Steinmann for helpful comments.

References

[Armstrong and Frederick 1966] P. J. Armstrong and C. O. Frederick, "A mathematical representation of the multiaxial Bauschinger effect", technical report 731, Central Elect. Generating Board, 1966. Reprinted with supplemental material in *Mater. High Temp.* **24**:1 (2007), 1–26.

[Bammann 1990] D. J. Bammann, "Modeling temperature and strain rate dependent large deformations of metals", *Appl. Mech. Rev.* (*ASME*) **43**:5S (1990), S312–S319.

[Barlat et al. 2011] F. Barlat, J. J. Gracio, M.-G. Lee, E. F. Rauch, and G. Vincze, "An alternative to kinematic hardening in classical plasticity", *Int. J. Plast.* **27**:9 (2011), 1309–1327.

[Bauschinger 1881] J. Bauschinger, "Über die Veränderung der Elasticitätgenze und des Elasticitätmodulus verschiedener Metalle", *Civilingenjeur* **27** (1881), 289–348.

[Besseling 1958] J. R. Besseling, "A theory of elastic, plastic and creep deformations of an initially isotropic material showing anisotropic strain-hardening, creep recovery, and secondary creep", *J. Appl. Mech.* **25** (1958), 529–536.

[Bodner 1968] S. R. Bodner, "Constitutive equations for dynamic material behavior", pp. 176–190 in *Mechanical behaviour of materials under dynamic loads*, edited by U. S. Lindholm, Springer, 1968.

[Chaboche 2008] J. L. Chaboche, "A review of some plasticity and viscoplasticity constitutive theories", *Int. J. Plast.* **24**:10 (2008), 1642–1693.

[Chan et al. 1988] K. S. Chan, S. R. Bodner, and U. S. Lindholm, "Phenomenological modeling of hardening and thermal recovery in metals", *J. Eng. Mater. Technol.* (*ASME*) **110**:1 (1988), 1–8.

[Choteau et al. 2005] M. Choteau, P. Quaegebeur, and S. Degallaix, "Modelling of Bauschinger effect by various constitutive relations derived from thermodynamical formulation", *Mech. Mater.* **37**:11 (2005), 1143–1152.

[Eckart 1948] C. Eckart, "The thermodynamics of irreversible processes, IV: The theory of elasticity and anelasticity", *Phys. Rev.* **73**:4 (1948), 373–382.

[Gladman 2018] B. Gladman, "LS-DYNA keyword user's manual, II: Material models", software manual, 2018, Available at https://tinyurl.com/lsdynar902. Version R11.

[Hollenstein et al. 2013] M. Hollenstein, M. Jabareen, and M. B. Rubin, "Modeling a smooth elastic-inelastic transition with a strongly objective numerical integrator needing no iteration", *Comput. Mech.* **52**:3 (2013), 649–667. Corrected in **55**:2 (2015), 453.

[Langer et al. 2010] J. S. Langer, E. Bouchbinder, and T. Lookman, "Thermodynamic theory of dislocation-mediated plasticity", *Acta Mater.* **58**:10 (2010), 3718–3732.

[Le and Tran 2018] K. C. Le and T. M. Tran, "Thermodynamic dislocation theory: Bauschinger effect", *Phys. Rev. E* **97**:4 (2018), art. id. 043002.

[Leonov 1976] A. I. Leonov, "Nonequilibrium thermodynamics and rheology of viscoelastic polymer media", *Rheol. Acta* **15** (1976), 85–98.

[Papes 2012] O. Papes, *Nonlinear continuum mechanics in modern engineering applications*, Ph.D. thesis, ETH Zürich, 2012, Available at https://doi.org/10.3929/ethz-a-007139775.

[Prager 1949] W. Prager, "Recent developments in the mathematical theory of plasticity", *J. Appl. Phys.* **20** (1949), 235–241.

[Rubin 1991] M. B. Rubin, "Simple, convenient isotropic failure surface", *J. Eng. Mech.* (*ASCE*) **117**:2 (1991), 348–369.

[Rubin 2012] M. B. Rubin, "Removal of unphysical arbitrariness in constitutive equations for elastically anisotropic nonlinear elastic-viscoplastic solids", *Int. J. Eng. Sci.* **53** (2012), 38–45.

[Rubin 2020] M. B. Rubin, "A strongly objective expression for the average deformation rate with application to numerical integration algorithms", *Finite Elem. Anal. Des.* **175** (2020), art. id. 103409.

[Rubin and Attia 1996] M. B. Rubin and A. Attia, "Calculation of hyperelastic response of finitely deformed elastic-viscoplastic materials", *Int. J. Numer. Methods Eng.* **39**:2 (1996), 309–320.

[Rubin and Bodner 1995] M. B. Rubin and S. R. Bodner, "An incremental elastic-viscoplastic theory indicating a reduced modulus for non-proportional buckling", *Int. J. Solids Struct.* **32**:20 (1995), 2967–2987.

[Rubin and Cardiff 2017] M. B. Rubin and P. Cardiff, "Advantages of formulating an evolution equation directly for elastic distortional deformation in finite deformation plasticity", *Comput. Mech.* **60**:5 (2017), 703–707.

[Rubin and Papes 2011] M. B. Rubin and O. Papes, "Advantages of formulating evolution equations for elastic-viscoplastic materials in terms of the velocity gradient instead of the spin tensor", *J. Mech. Mater. Struct.* **6**:1-4 (2011), 529–543.

[Ruess 1935] E. Ruess, "Abstract", pp. 91 in *Proc. Fourth Int. Cong. Appl. Mech.* (Cambridge, England, 1934), Cambridge University Press, 1935.

[Simo 1988] J. C. Simo, "A framework for finite strain elastoplasticity based on maximum plastic dissipation and the multiplicative decomposition, II: Computational aspects", *Comput. Methods Appl. Mech. Eng.* **68**:1 (1988), 1–31.

[Simo 1992] J. C. Simo, "Algorithms for static and dynamic multiplicative plasticity that preserve the classical return mapping schemes of the infinitesimal theory", *Comput. Methods Appl. Mech. Eng.* **99**:1 (1992), 61–112.

[Simo 1998] J. C. Simo, "Numerical analysis and simulation of plasticity", pp. 183–499 in *Handbook of numerical analysis, VI*, edited by P. G. Ciarlet and J. L. Lions, North-Holland, Amsterdam, 1998.

[Simo and Hughes 1998] J. C. Simo and T. J. R. Hughes, *Computational inelasticity*, Interdisc. Appl. Math. **7**, Springer, 1998.

[Sowerby et al. 1979] R. Sowerby, D. K. Uko, and Y. Tomita, "A review of certain aspects of the Bauschinger effect in metals", *Mater. Sci. Eng.* **41**:1 (1979), 43–58.

[Wilkins 1963] M. L. Wilkins, "Calculation of elastic-plastic flow", technical report 7322, Lawrence Radiation Lab., 1963, Available at https://tinyurl.com/radiatlab.

Received 9 Mar 2020. Revised 1 Jun 2020. Accepted 7 Jun 2020.

MARTIN KROON: martin.kroon@lnu.se
Department of Mechanical Engineering, Linnaeus University, Växjö, Sweden

M. B. RUBIN: mbrubin@tx.technion.ac.il
Faculty of Mechanical Engineering, Technion - Israel Institute of Technology, Haifa, Israel

JOURNAL OF MECHANICS OF MATERIALS AND STRUCTURES
Vol. 15, No. 4, 2020
https://doi.org/10.2140/jomms.2020.15.539

CLOSED-FORM SOLUTIONS FOR AN EDGE DISLOCATION INTERACTING WITH A PARABOLIC OR ELLIPTICAL ELASTIC INHOMOGENEITY HAVING THE SAME SHEAR MODULUS AS THE MATRIX

XU WANG AND PETER SCHIAVONE

We use complex variable methods to derive closed-form solutions to the problems of an edge dislocation interacting with a parabolic or elliptical elastic inhomogeneity embedded inside an infinite elastic matrix. The inhomogeneity and the matrix have the same shear modulus but distinct Poisson's ratios. The edge dislocation can be located in the matrix, in the elastic inhomogeneity or precisely on the parabolic or elliptical interface. Explicit expressions of the image force acting on the edge dislocation as a result of its interaction with the parabolic or elliptical elastic inhomogeneity are presented. Our analyses indicate that the image force on an edge dislocation inside a parabolic or an elliptical elastic inhomogeneity is invariant with the direction of the Burgers vector of the edge dislocation.

1. Introduction

Green's functions for composites subjected to a line dislocation and/or a line force have been studied extensively by many investigators (see, for example, [Dundurs 1969; Stagni 1982; 1993; 1999; Warren 1983; Stagni and Lizzio 1983; Suo 1989; 1990; Tsuchida et al. 1991; Gong and Meguid 1994; Qaissaunee and Santare 1995; Yen et al. 1995; Ting 1996; Chen 1996; Wang and Sudak 2006; Wang 2015; Shi and Li 2006]). It appears that exact and closed-form representations of Green's functions exist only in cases involving two bonded isotropic or anisotropic elastic half-planes and for problems involving circular isotropic elastic inhomogeneities [Dundurs 1969; Ting 1996; Wang 2015]. Series-form representations of Green's functions are available for elliptical and nonelliptical elastic inhomogeneities [Stagni 1982; 1993; 1999; Warren 1983; Stagni and Lizzio 1983; Tsuchida et al. 1991; Gong and Meguid 1994; Qaissaunee and Santare 1995; Yen et al. 1995; Ting 1996; Chen 1996; Wang and Sudak 2006].

In this paper, we study the plane problems associated with an edge dislocation interacting with a parabolic or elliptical elastic inhomogeneity. The edge dislocation can be located in the matrix, in the elastic inhomogeneity or even on the parabolic or elliptical interface. Using Kolosov–Muskhelishvili's complex variable formulation [Muskhelishvili 1953], we demonstrate that elementary closed-form solutions can still be obtained when the elastic inhomogeneity and the matrix have equal shear moduli but distinct Poisson's ratios. Using the Peach–Koehler formula [Dundurs 1969], explicit expressions of the image force acting on the edge dislocation are presented. Some interesting features of the image force are observed, especially when the edge dislocation lies inside the elastic inhomogeneity. The paper is structured as follows. Kolosov–Muskhelishvili's complex variable formulation is briefly reviewed in Section 2. Closed-form solutions are derived in Section 3 for an edge dislocation interacting with a

Keywords: parabolic elastic inhomogeneity, elliptical elastic inhomogeneity, edge dislocation, image force, closed-form solution.

parabolic elastic inhomogeneity. Closed-form solutions are derived in Section 4 for an edge dislocation interacting with an elliptical elastic inhomogeneity. In Section 5, we present a closed-form expression of the image force on an edge dislocation inside an elastic inhomogeneity of arbitrary shape having the same shear modulus as that of the matrix. In Section 6, we obtain a closed-from expression of the image force on an edge dislocation in an infinite matrix reinforced by an elastic inhomogeneity of arbitrary shape having the same shear modulus as that of the matrix. We summarize our findings and conclusions in Section 7. We remark that since an edge dislocation is a defect in a crystalline solid, its mobility and stability resulting from its interaction with an elastic inhomogeneity of parabolic, elliptical or nonelliptical shape is of fundamental importance in understanding the mechanical properties of the corresponding composite structure. In our case, this can be clearly observed from the obtained closed-form expressions for the image force acting on the edge dislocation.

2. Kolosov–Muskhelishvili's complex variable formulation

A Cartesian coordinate system $\{x_i\}$ $(i = 1, 2, 3)$ is established. For the in-plane deformations of an isotropic elastic material, the three in-plane stresses $(\sigma_{11}, \sigma_{22}, \sigma_{12})$, two in-plane displacements (u_1, u_2) and two stress functions (ϕ_1, ϕ_2) are given in terms of two analytic functions $\varphi(z)$ and $\psi(z)$ of the complex variable $z = x_1 + \mathrm{i}x_2$ as [Muskhelishvili 1953]

$$\begin{aligned} &\sigma_{11} + \sigma_{22} = 2[\varphi'(z) + \overline{\varphi'(z)}], \\ &\sigma_{22} - \sigma_{11} + 2\mathrm{i}\sigma_{12} = 2[\bar{z}\varphi''(z) + \psi'(z)], \end{aligned} \tag{1}$$

$$\begin{aligned} &2\mu(u_1 + \mathrm{i}u_2) = \kappa\varphi(z) - z\overline{\varphi'(z)} - \overline{\psi(z)}, \\ &\phi_1 + \mathrm{i}\phi_2 = \mathrm{i}[\varphi(z) + z\overline{\varphi'(z)} + \overline{\psi(z)}], \end{aligned} \tag{2}$$

where $\kappa = 3 - 4\nu$ for plane strain and $\kappa = (3 - \nu)/(1 + \nu)$ for plane stress, μ and ν $(0 \le \nu \le 1/2)$ are the shear modulus and Poisson's ratio, respectively. In fact, energy considerations dictate that the range of Poisson's ratio can be relaxed to $-1 \le \nu \le 1/2$: materials with a negative Poisson's ratio are referred to as 'auxetic materials' [Lakes 1987; Argatov et al. 2012]. In addition, the in-plane stresses are related to the two stress functions through [Ting 1996]

$$\sigma_{11} = -\phi_{1,2}, \quad \sigma_{12} = \phi_{1,1}, \quad \sigma_{21} = -\phi_{2,2}, \quad \sigma_{22} = \phi_{2,1}. \tag{3}$$

In fact, the stress expressions in (1) can be obtained after differentiation of the stress functions in $(2)_2$. Thus, Equation (2) is fundamental to the formulation.

3. An edge dislocation interacting with a parabolic elastic inhomogeneity

3.1. ***Problem description.*** As shown in Figure 1, a parabolic elastic inhomogeneity, denoted by S_1, is perfectly bonded to the surrounding matrix, denoted by S_2, through a parabolic interface L described by

$$L : x_1 = H - \frac{x_2^2}{4H}, \quad H > 0. \tag{4}$$

In addition, an edge dislocation with Burgers vector (b_1, b_2) is located at $z = z_0 = x_0 + \mathrm{i}y_0 = r\mathrm{e}^{\mathrm{i}\theta}$ with x_0 and y_0 being the Cartesian coordinates of z_0 whilst r and θ represent the polar coordinates of z_0.

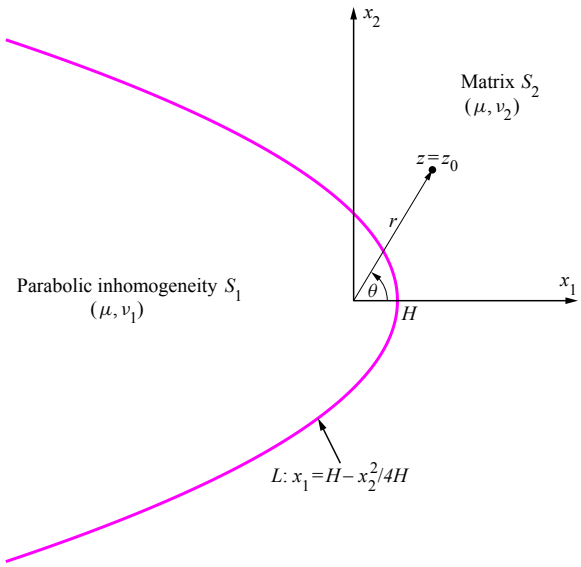

Figure 1. An edge dislocation interacting with a parabolic elastic inhomogeneity. The edge dislocation located at $z = z_0$ can be in the matrix, in the inhomogeneity or just on the parabolic interface.

Throughout the paper, subscript 1 and 2 are used to identify the respective quantities in S_1 and S_2 (we remark that this notation clearly does not apply to the two components of the Burgers vector.) In order to arrive at closed-form solutions, we assume that the parabolic inhomogeneity and the matrix have the same shear modulus but distinct Poisson's ratios (i.e., $\mu_1 = \mu_2 = \mu$ and $\nu_1 \neq \nu_2$).

It follows from (2) that the conditions representing continuity of tractions and displacements across the perfect parabolic interface L can be expressed in terms of the two pairs of analytic functions $\varphi_i(z)$, $\psi_i(z)$ $(i = 1, 2)$ as follows:

$$\begin{aligned} &\varphi_1(z) + z\overline{\varphi_1'(z)} + \overline{\psi_1(z)} = \varphi_2(z) + z\overline{\varphi_2'(z)} + \overline{\psi_2(z)}, \\ &\kappa_1\varphi_1(z) - z\overline{\varphi_1'(z)} - \overline{\psi_1(z)} = \kappa_2\varphi_2(z) - z\overline{\varphi_2'(z)} - \overline{\psi_2(z)}, \quad z \in L. \end{aligned} \tag{5}$$

Equation (5) can be conveniently rewritten in the form

$$\varphi_1(z) = \frac{\kappa_2 + 1}{\kappa_1 + 1}\varphi_2(z) = -\frac{\mathrm{i}\mu(b_1 + \mathrm{i}b_2)}{\pi(\kappa_1 + 1)}\ln(z - z_0), \quad z \in S_1 \cup S_2; \tag{6}$$

$$\psi_1(z) + \frac{\kappa_2 - \kappa_1}{\kappa_1 + 1}\overline{\varphi_2(z)} + \frac{\kappa_2 - \kappa_1}{\kappa_1 + 1}(z^{1/2} - 2H^{1/2})^2\varphi_2'(z) = \psi_2(z), \quad z \in L. \tag{7}$$

Equation (6) serves as an analytic continuation of the two analytic functions $\varphi_1(z)$ and $\varphi_2(z)$. In writing (7), we have adopted the identity that $\bar{z}^{1/2} = 2H^{1/2} - z^{1/2}$ for $z \in L$. This identity will also be used in the following derivations. It remains to determine the two analytic functions $\psi_1(z)$ and $\psi_2(z)$ through satisfaction of (7). In the ensuing three sections, $\psi_1(z)$ and $\psi_2(z)$ will be derived separately for the three cases in which an edge dislocation is located in the matrix, in the parabolic inhomogeneity and on the interface.

3.2. ***An edge dislocation in the matrix.*** When the edge dislocation is located in the matrix, it follows from (7) and the identity: $\ln(\bar{z}-\bar{z}_0)=\ln(z^{1/2}-\bar{z}_0^{1/2}-2H^{1/2})+\ln(z^{1/2}+\bar{z}_0^{1/2}-2H^{1/2})$, $z\in L$ that the two analytic functions $\psi_1(z)$ and $\psi_2(z)$ can be determined explicitly as

$$\psi_1(z)=\frac{\mathrm{i}\mu(\kappa_1-\kappa_2)(b_1-\mathrm{i}b_2)}{\pi(\kappa_1+1)(\kappa_2+1)}\ln[z-(\bar{z}_0^{1/2}+2H^{1/2})^2]$$
$$+\frac{\mathrm{i}\mu(b_1-\mathrm{i}b_2)}{\pi(\kappa_2+1)}\ln(z-z_0)+\frac{\mathrm{i}\mu(b_1+\mathrm{i}b_2)}{\pi(\kappa_2+1)}\frac{\bar{z}_0}{z-z_0}+\frac{\mathrm{i}\mu(\kappa_2-\kappa_1)(b_1+\mathrm{i}b_2)}{\pi(\kappa_1+1)(\kappa_2+1)}\frac{(2H^{1/2}-z_0^{1/2})^2}{z-z_0},$$
$$z\in S_1; \tag{8}$$

$$\psi_2(z)=\frac{\mathrm{i}\mu(b_1-\mathrm{i}b_2)}{\pi(\kappa_2+1)}\ln(z-z_0)+\frac{\mathrm{i}\mu(b_1+\mathrm{i}b_2)}{\pi(\kappa_2+1)}\frac{\bar{z}_0}{z-z_0}+\frac{\mathrm{i}\mu(\kappa_2-\kappa_1)(b_1+\mathrm{i}b_2)}{\pi(\kappa_1+1)(\kappa_2+1)}\frac{4H^{1/2}}{z^{1/2}+z_0^{1/2}}$$
$$+\frac{\mathrm{i}\mu(\kappa_2-\kappa_1)(b_1-\mathrm{i}b_2)}{\pi(\kappa_1+1)(\kappa_2+1)}\ln(z^{1/2}+\bar{z}_0^{1/2}-2H^{1/2})+\frac{\mathrm{i}\mu(\kappa_1-\kappa_2)(b_1-\mathrm{i}b_2)}{\pi(\kappa_1+1)(\kappa_2+1)}\ln(z^{1/2}+\bar{z}_0^{1/2}+2H^{1/2}),$$
$$z\in S_2, \tag{9}$$

where the branch cut for $z^{1/2}$ is chosen as the negative x_1-axis. In obtaining (8) and (9), one must ensure that $\psi_1(z)$ defined in the parabolic inhomogeneity is indeed an analytic function of z. The stresses in the composite induced by the edge dislocation in the matrix can be arrived at by substituting (6), (8) and (9) into (1). Using the Peach–Koehler formula [Dundurs 1969], the image force acting on the edge dislocation can be explicitly determined as follows:

$$\begin{aligned}F_1&=\frac{H^{1/2}\mu(\kappa_2-\kappa_1)}{2\pi r^{3/2}(\kappa_1+1)(\kappa_2+1)}\left[(b_2^2-b_1^2)\cos\frac{3\theta}{2}-2b_1b_2\sin\frac{3\theta}{2}+\frac{2r(b_1^2+b_2^2)}{r(1+\cos\theta)-2H}\cos\frac{\theta}{2}\right],\\ F_2&=\frac{H^{1/2}\mu(\kappa_2-\kappa_1)}{2\pi r^{3/2}(\kappa_1+1)(\kappa_2+1)}\left[(b_2^2-b_1^2)\sin\frac{3\theta}{2}+2b_1b_2\cos\frac{3\theta}{2}+\frac{2r(b_1^2+b_2^2)}{r(1+\cos\theta)-2H}\sin\frac{\theta}{2}\right],\end{aligned} \tag{10}$$

where F_1 and F_2 are, respectively, the force components along the x_1 and x_2 directions. We see that the image force in (10) varies with the direction of the vector (b_1, b_2).

When the edge dislocation lies on the x_1-axis, Equation (10) becomes

$$F_1=\frac{H^{1/2}\mu(\kappa_2-\kappa_1)}{2\pi r^{3/2}(\kappa_1+1)(\kappa_2+1)}\left[b_2^2-b_1^2+\frac{r(b_1^2+b_2^2)}{r-H}\right],\quad F_2=\frac{H^{1/2}\mu(\kappa_2-\kappa_1)b_1b_2}{\pi r^{3/2}(\kappa_1+1)(\kappa_2+1)}. \tag{11}$$

When the edge dislocation approaches the vertex of the parabola L, Equation (11) reduces to

$$F_1=\frac{\mu(\kappa_2-\kappa_1)(b_1^2+b_2^2)}{2\pi(\kappa_1+1)(\kappa_2+1)(r-H)},\quad F_2=\frac{\mu(\kappa_2-\kappa_1)b_1b_2}{\pi H(\kappa_1+1)(\kappa_2+1)},\quad \text{as } r\to H. \tag{12}$$

The expression for F_1 in (12) is simply the classical result for an edge dislocation interacting with a planar bimaterial interface [Dundurs 1969]. On the other hand, when the edge dislocation lying on the x_1-axis is further from the parabola L, Equation (11) reduces to

$$F_1\cong\frac{H^{1/2}\mu(\kappa_2-\kappa_1)b_2^2}{\pi r^{3/2}(\kappa_1+1)(\kappa_2+1)}+O(r^{-\frac{5}{2}}),\quad F_2=\frac{H^{1/2}\mu(\kappa_2-\kappa_1)b_1b_2}{\pi r^{3/2}(\kappa_1+1)(\kappa_2+1)},\quad \text{as } r\to\infty, \tag{13}$$

which implies that the far-field asymptotic behavior of F_1 is dominated by the b_2 component of the Burgers vector.

3.3. ***An edge dislocation in the parabolic inhomogeneity.*** When the edge dislocation is located in the parabolic inhomogeneity, it follows from (7) that the two analytic functions $\psi_1(z)$ and $\psi_2(z)$ can be explicitly determined as

$$\psi_1(z) = \frac{i\mu(b_1 - ib_2)}{\pi(\kappa_1+1)}\ln(z-z_0) + \frac{i\mu(b_1+ib_2)}{\pi(\kappa_1+1)}\frac{\bar{z}_0}{z-z_0} + \frac{i\mu(\kappa_1-\kappa_2)(b_1-ib_2)}{\pi(\kappa_1+1)(\kappa_2+1)}\{\ln[z-(\bar{z}_0^{1/2}-2H^{1/2})^2] + \ln[z-(\bar{z}_0^{1/2}+2H^{1/2})^2]\}, \quad z \in S_1; \tag{14}$$

$$\psi_2(z) = \frac{i\mu(b_1 - ib_2)}{\pi(\kappa_1+1)}\ln(z-z_0) + \frac{i\mu(b_1+ib_2)}{\pi(\kappa_1+1)}\frac{\bar{z}_0}{z-z_0} + \frac{i\mu(\kappa_1-\kappa_2)(b_1+ib_2)}{\pi(\kappa_1+1)(\kappa_2+1)}\frac{(z^{1/2}-2H^{1/2})^2}{z-z_0} + \frac{i\mu(\kappa_1-\kappa_2)(b_1-ib_2)}{\pi(\kappa_1+1)(\kappa_2+1)}[\ln(z^{1/2}-\bar{z}_0^{1/2}+2H^{1/2}) + \ln(z^{1/2}+\bar{z}_0^{1/2}+2H^{1/2})], \quad z \in S_2. \tag{15}$$

The stresses in the composite induced by the edge dislocation in the inhomogeneity can be arrived at by substituting (6), (14) and (15) into (1). Using the Peach–Koehler formula, the image force acting on the edge dislocation can be explicitly determined as follows

$$\begin{aligned} F_1 &= \frac{2\mu(\kappa_1-\kappa_2)(b_1^2+b_2^2)}{\pi(\kappa_1+1)(\kappa_2+1)}\frac{H}{r^2\sin^2\theta + 4Hr\cos\theta - 4H^2}, \\ F_2 &= \frac{\mu(\kappa_1-\kappa_2)(b_1^2+b_2^2)}{\pi(\kappa_1+1)(\kappa_2+1)}\frac{r\sin\theta}{r^2\sin^2\theta + 4Hr\cos\theta - 4H^2}, \end{aligned} \tag{16}$$

which implies that the image force is invariant with the direction of the vector (b_1, b_2).

When the edge dislocation lies on the x_1-axis, (16) becomes

$$F_1 = \frac{\mu(\kappa_2-\kappa_1)(b_1^2+b_2^2)}{2\pi(\kappa_1+1)(\kappa_2+1)(H-x_0)}, \quad F_2 = 0, \quad -\infty < x_0 \le H. \tag{17}$$

Interestingly, Equation (17) is always identical in form to the result for an edge dislocation near a planar interface [Dundurs 1969]. We interpret from (17) that as far as the force on the edge dislocation is concerned, an edge dislocation lying on the axis of symmetry of the parabola L can be treated as equivalent to the same edge dislocation near a planar bimaterial interface at $\{x_1 = H, -\infty < x_2 < +\infty\}$. We illustrate in Figure 2 the variation of F_1 with an edge dislocation on the x_1-axis. It is seen from Figure 2 and from our previous analysis that as the edge dislocation is further away from the vertex of the parabola L, the image force decays faster in the matrix than in the parabolic inhomogeneity, especially when $b_2 = 0$.

3.4. ***An edge dislocation on the parabolic interface.*** When the edge dislocation is located precisely on the parabolic interface with $z_0^{1/2} + \bar{z}_0^{1/2} = 2H^{1/2}$, the two analytic functions $\psi_1(z)$ and $\psi_2(z)$ can be obtained either from (8) and (9) or from (14) and (15) as

$$\psi_1(z) = \frac{i\mu(b_1 - ib_2)}{\pi(\kappa_2+1)}\ln(z-z_0) + \frac{i\mu(b_1+ib_2)}{\pi(\kappa_1+1)}\frac{\bar{z}_0}{z-z_0} + \frac{i\mu(\kappa_1-\kappa_2)(b_1-ib_2)}{\pi(\kappa_1+1)(\kappa_2+1)}\ln[z-(\bar{z}_0^{1/2}+2H^{1/2})^2], \quad z \in S_1; \tag{18}$$

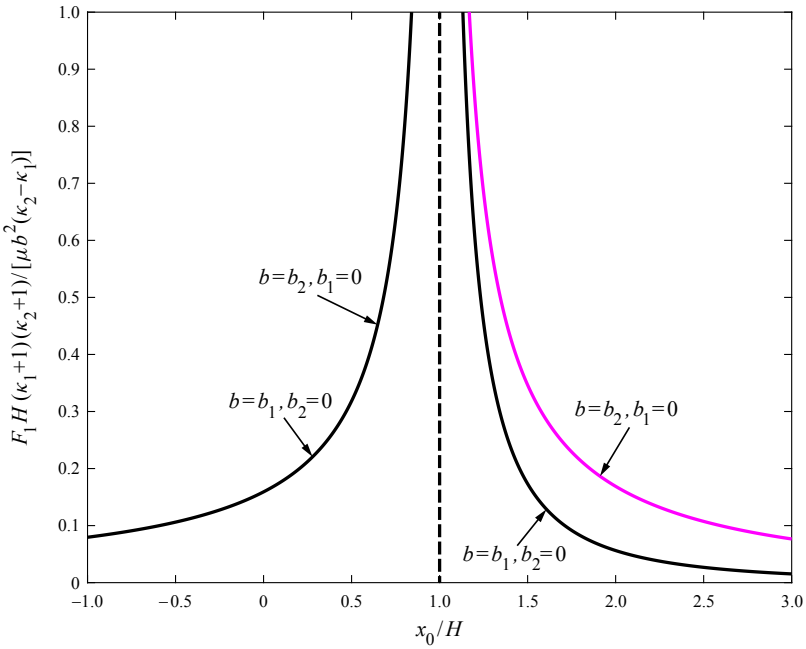

Figure 2. Variation of the image force F_1 on an edge dislocation on the x_1-axis in the matrix and in the parabolic inhomogeneity.

$$\psi_2(z)=\frac{\mathrm{i}\mu(b_1-\mathrm{i}b_2)}{\pi(\kappa_1+1)}\ln(z-z_0)+\frac{\mathrm{i}\mu(b_1+\mathrm{i}b_2)}{\pi(\kappa_2+1)}\frac{\bar{z}_0}{z-z_0}+\frac{\mathrm{i}\mu(\kappa_2-\kappa_1)(b_1+\mathrm{i}b_2)}{\pi(\kappa_1+1)(\kappa_2+1)}\frac{4H^{1/2}}{z^{1/2}+z_0^{1/2}}$$
$$+\frac{\mathrm{i}\mu(\kappa_1-\kappa_2)(b_1-\mathrm{i}b_2)}{\pi(\kappa_1+1)(\kappa_2+1)}[\ln(z^{1/2}+z_0^{1/2})+\ln(z^{1/2}+\bar{z}_0^{1/2}+2H^{1/2})],\quad z\in S_2. \tag{19}$$

The development of the (identical) expressions for the two analytic functions $\psi_1(z)$ and $\psi_2(z)$ in (18) and (19) whether obtained from (8) and (9) (when the edge dislocation is located in the matrix) or from (14) and (15) (when the edge dislocation lies inside the inhomogeneity) not only suggests the rationale for the solutions derived in the following Secs. 4 and 5 but also confirms their correctness. The stresses in the composite induced by the edge dislocation located precisely on the parabolic interface can be obtained by substituting (6), (18) and (19) into (1).

4. An edge dislocation interacting with an elliptical elastic inhomogeneity

As shown in Figure 3, an elliptical elastic inhomogeneity, denoted by S_1, is perfectly bonded to the surrounding matrix, denoted by S_2, through an elliptical interface L described by

$$L:\frac{x_1^2}{a^2}+\frac{x_2^2}{b^2}=1, \tag{20}$$

with a and b being the semi-major and semi-minor axes of the ellipse L, respectively. In addition, an edge dislocation with Burgers vector (b_1, b_2) is located at $z=z_0=x_0+\mathrm{i}y_0$ with x_0 and y_0 being the Cartesian coordinates of z_0. As before, subscript 1 and 2 are used to identify the respective quantities

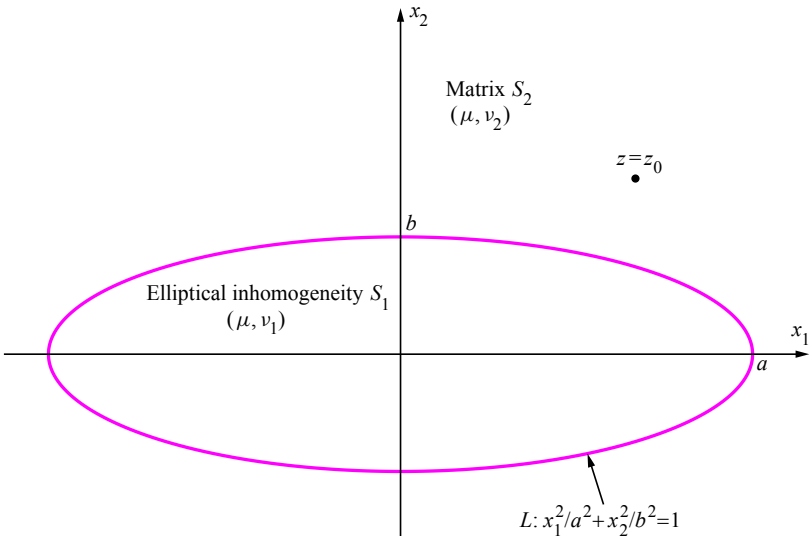

Figure 3. An edge dislocation interacting with an elliptical elastic inhomogeneity. The edge dislocation located at $z = z_0$ can be in the matrix, in the inhomogeneity or just on the elliptical interface.

in S_1 and S_2. The elliptical inhomogeneity and the matrix have the same shear modulus but different Poisson's ratios (i.e., $\mu_1 = \mu_2 = \mu$ and $\nu_1 \neq \nu_2$).

After some algebraic operations, the continuity conditions of tractions and displacements across the perfect elliptical interface L in (5) can be rewritten as

$$\varphi_1(z) = \frac{\kappa_2 + 1}{\kappa_1 + 1}\varphi_2(z) = -\frac{\mathrm{i}\mu(b_1 + \mathrm{i}b_2)}{\pi(\kappa_1 + 1)} \ln(z - z_0), \quad z \in S_1 \cup S_2; \tag{21}$$

$$\psi_1(z) + \frac{\kappa_2 - \kappa_1}{\kappa_1 + 1}\overline{\varphi_2(z)} + \frac{\kappa_2 - \kappa_1}{\kappa_1 + 1} D(z)\varphi_2'(z) = \psi_2(z), \quad z \in L, \tag{22}$$

where

$$\bar{z} = D(z) = \frac{m + m^{-1}}{2} z + \frac{m - m^{-1}}{2}\sqrt{z^2 - 4mR^2}, \quad z \in L, \tag{23}$$

with

$$R = \frac{a + b}{2}, m = \frac{a - b}{a + b}. \tag{24}$$

When the edge dislocation is located in the matrix, it follows from (22) and the identity: $\ln(\bar{z} - \bar{z}_0) = \ln[R(\xi^{-1} - \bar{\xi}_0)(1 - m\bar{\xi}_0^{-1}\xi)]$, $z \in L$ with

$$\xi = \omega^{-1}(z) = \frac{1}{2R}\left(z + \sqrt{z^2 - 4mR^2}\right) \quad \text{and} \quad \xi_0 = \omega^{-1}(z_0) = \frac{1}{2R}\left(z_0 + \sqrt{z_0^2 - 4mR^2}\right)$$

that the two analytic functions $\psi_1(z)$ and $\psi_2(z)$ can be explicitly determined as

$$\psi_1(z) = \frac{\mathrm{i}\mu(\kappa_1-\kappa_2)(b_1-\mathrm{i}b_2)}{\pi(\kappa_1+1)(\kappa_2+1)}\ln(z-z_1) + \frac{\mathrm{i}\mu(b_1-\mathrm{i}b_2)}{\pi(\kappa_2+1)}\ln(z-z_0) + \frac{\mathrm{i}\mu(b_1+\mathrm{i}b_2)}{\pi(\kappa_2+1)}\frac{\bar{z}_0}{z-z_0} + \frac{\mathrm{i}\mu(\kappa_2-\kappa_1)(b_1+\mathrm{i}b_2)}{\pi(\kappa_1+1)(\kappa_2+1)}\frac{D(z_0)}{z-z_0}, \quad z \in S_1; \tag{25}$$

$$\psi_2(z) = \frac{\mathrm{i}\mu(b_1-\mathrm{i}b_2)}{\pi(\kappa_2+1)}\ln(z-z_0) + \frac{\mathrm{i}\mu(b_1+\mathrm{i}b_2)}{\pi(\kappa_2+1)}\frac{\bar{z}_0}{z-z_0} + \frac{\mathrm{i}\mu(\kappa_1-\kappa_2)(m-m^{-1})(b_1+\mathrm{i}b_2)}{2\pi(\kappa_1+1)(\kappa_2+1)}\frac{z+z_0}{\sqrt{z^2-4mR^2}+\sqrt{z_0^2-4mR^2}} + \frac{\mathrm{i}\mu(\kappa_2-\kappa_1)(b_1-\mathrm{i}b_2)}{\pi(\kappa_1+1)(\kappa_2+1)}\ln\left[1-\frac{\bar{\xi}_0^{-1}}{\omega^{-1}(z)}\right] + \frac{\mathrm{i}\mu(\kappa_1-\kappa_2)(b_1-\mathrm{i}b_2)}{\pi(\kappa_1+1)(\kappa_2+1)}\ln\left[1-\frac{m^2\bar{\xi}_0^{-1}}{\omega^{-1}(z)}\right], \quad z \in S_2, \tag{26}$$

where

$$z_1 = R(m^{-1}\bar{\xi}_0 + m^2\bar{\xi}_0^{-1}). \tag{27}$$

By using the Peach–Koehler formula, the image force acting on the edge dislocation can be finally derived as follows:

$$F_1 - \mathrm{i}F_2 = \frac{R^2\mu(\kappa_2-\kappa_1)(1-m^2)}{\pi(\kappa_1+1)(\kappa_2+1)(z_0^2-4mR^2)^{3/2}} \times \left[b_2^2 - b_1^2 - 2\mathrm{i}b_1b_2 + \frac{4(b_1^2+b_2^2)(z_0^2-4mR^2)|z_0+\sqrt{z_0^2-4mR^2}|^2}{(|z_0+\sqrt{z_0^2-4mR^2}|^2-4m^2R^2)(|z_0+\sqrt{z_0^2-4mR^2}|^2-4R^2)}\right], \tag{28}$$

where F_1 and F_2 are respectively the force components along the x_1 and x_2 directions.

When an edge dislocation lying on the positive x_1-axis approaches the elliptical interface, (28) becomes

$$F_1 = \frac{\mu(\kappa_2-\kappa_1)(b_1^2+b_2^2)}{2\pi(\kappa_1+1)(\kappa_2+1)(x_0-a)}, \; F_2 = \frac{2\mu(\kappa_2-\kappa_1)b_1b_2}{\pi(\kappa_1+1)(\kappa_2+1)b^2/a}, \quad x_0 \to a. \tag{29}$$

The expression for F_1 in (29) is just the result for an edge dislocation near a planar bimaterial interface [Dundurs 1969], whilst the expression of F_2 in (29) is consistent with that in (12) by considering the fact that b^2/a is the curvature radius of the ellipse at $z = a$ and $2H$ is the curvature radius of the parabola at the vertex.

On the other hand, when the edge dislocation is far from the interface, (28) reduces to

$$F_1 - \mathrm{i}F_2 = \frac{R^2\mu(\kappa_2-\kappa_1)(1-m^2)}{\pi(\kappa_1+1)(\kappa_2+1)z_0^3}\left[b_2^2\left(1+\frac{z_0}{\bar{z}_0}\right) - b_1^2\left(1-\frac{z_0}{\bar{z}_0}\right) - 2\mathrm{i}b_1b_2\right], \quad |z_0| \to \infty. \tag{30}$$

When $m = 0$ for a circular inhomogeneity, (28) simply reduces to the classical result in Equations (7.8) and (7.9) by [Dundurs 1969].

When the edge dislocation is located inside the elliptical inhomogeneity, it follows from (22) that the two analytic functions $\psi_1(z)$ and $\psi_2(z)$ can be explicitly determined as

$$\psi_1(z) = \frac{\mathrm{i}\mu(b_1-\mathrm{i}b_2)}{\pi(\kappa_1+1)}\ln(z-z_0) + \frac{\mathrm{i}\mu(b_1+\mathrm{i}b_2)}{\pi(\kappa_1+1)}\frac{\bar{z}_0}{z-z_0} + \frac{\mathrm{i}\mu(\kappa_1-\kappa_2)(b_1-\mathrm{i}b_2)}{\pi(\kappa_1+1)(\kappa_2+1)}\ln[(z-z_1)(z-z_2)], \quad z \in S_1; \tag{31}$$

$$\psi_2(z) = \frac{\mathrm{i}\mu(b_1 - \mathrm{i}b_2)}{\pi(\kappa_1+1)}\ln(z-z_0) + \frac{\mathrm{i}\mu(b_1+\mathrm{i}b_2)}{\pi(\kappa_1+1)}\frac{\bar{z}_0}{z-z_0} + \frac{\mathrm{i}\mu(\kappa_1-\kappa_2)(b_1+\mathrm{i}b_2)}{\pi(\kappa_1+1)(\kappa_2+1)}\frac{D(z)}{z-z_0} + \frac{\mathrm{i}\mu(\kappa_1-\kappa_2)(b_1-\mathrm{i}b_2)}{\pi(\kappa_1+1)(\kappa_2+1)}\left[\ln\left[1-\frac{m^2\bar{\xi}_0^{-1}}{\omega^{-1}(z)}\right] + \ln[\omega^{-1}(z) - m\bar{\xi}_0]\right], \quad z \in S_2, \tag{32}$$

where

$$\begin{aligned} \xi = \omega^{-1}(z) &= \frac{1}{2R}\left(z + \sqrt{z^2 - 4mR^2}\right), \quad z_1 = R(m^{-1}\bar{\xi}_0 + m^2\bar{\xi}_0^{-1}), \\ \xi_0 = \omega^{-1}(z_0) &= \frac{1}{2R}\left(z_0 + \sqrt{z_0^2 - 4mR^2}\right), \quad z_2 = R(m\bar{\xi}_0 + \bar{\xi}_0^{-1}). \end{aligned} \tag{33}$$

By using the Peach–Koehler formula, the image force acting on the edge dislocation can be finally derived as follows

$$F_1 - \mathrm{i}F_2 = \frac{\mu(\kappa_1-\kappa_2)(b_1^2+b_2^2)}{\pi(\kappa_1+1)(\kappa_2+1)}\left(\frac{1}{z_0-z_1} + \frac{1}{z_0-z_2}\right), \tag{34}$$

which implies that the image force is invariant with the direction of the vector (b_1, b_2). It will be seen in the next section that the invariance of the image force with the direction of the Burger vector is invalid for an edge dislocation inside an elastic inhomogeneity of *nonelliptical shape* having the same shear modulus as that of the matrix.

When the edge dislocation lies on the x_1-axis, (34) becomes

$$F_1 = \frac{\mu(\kappa_2-\kappa_1)(b_1^2+b_2^2)}{\pi(\kappa_1+1)(\kappa_2+1)}\frac{x_0}{a^2-x_0^2}, \quad F_2 = 0, \tag{35}$$

which is identical to that for an edge dislocation inside a circular elastic inhomogeneity of radius a [Dundurs 1969]. Equation (35) implies that the semi-minor axis b exerts no influence on the image force on an edge dislocation lying on the x_1-axis inside the elliptical inhomogeneity.

When the edge dislocation lies on the x_2-axis, (34) becomes

$$F_2 = \frac{\mu(\kappa_2-\kappa_1)(b_1^2+b_2^2)}{\pi(\kappa_1+1)(\kappa_2+1)}\frac{y_0}{b^2-y_0^2}, \quad F_1 = 0, \tag{36}$$

which is identical to that for an edge dislocation inside a circular elastic inhomogeneity of radius b [Dundurs 1969]. Equation (36) implies that the semi-major axis a exerts no influence on the image force on an edge dislocation lying on the x_2-axis inside the elliptical inhomogeneity.

Through a limiting process, the two analytic functions $\psi_1(z)$ and $\psi_2(z)$ can be obtained for the case when the edge dislocation just lies on the elliptical interface. The specific expressions are suppressed here.

5. An edge dislocation inside an elastic inhomogeneity of arbitrary shape

In this section, we consider an edge dislocation with Burgers vector (b_1, b_2) located at $z = z_0$ inside an elastic inhomogeneity of arbitrary shape (denoted as S_1) perfectly bonded to the surrounding infinite matrix (denoted as S_2) through a sharp interface L. Here, we use the term "sharp interface" to mean an interface with vanishing thickness between two dissimilar adjacent phases. As before, subscript 1 and 2 are used to identify the respective quantities in S_1 and S_2. The elastic inhomogeneity and the matrix have the same shear modulus but different Poisson's ratios.

We consider the following conformal mapping function [England 1971]:

$$z=\omega(\xi)=R\left(\xi+\sum_{n=1}^{N}a_n\xi^{-n}\right),\ \xi=\omega^{-1}(z),\quad |\xi|\geq 1, \tag{37}$$

where R is a real scaling constant, and $a_n, n=1,2,\ldots,N$ are N complex constants.

By using the mapping function in (37), the exterior of the inhomogeneity is mapped onto the exterior of the unit circle in the ξ-plane.

On the interface L, we have

$$\bar{z}-\bar{z}_0=R\xi^{-1}\left(\sum_{n=1}^{N}\bar{a}_n\xi^{n+1}-\bar{z}_0R^{-1}\xi+1\right)=R\bar{a}_N\xi^{-1}\prod_{n=1}^{N+1}(\xi-\xi_n),\quad z\in L, \tag{38}$$

where $\xi_n, n=1,2,\ldots,N+1$, all of which are located outside the unit circle, are the $N+1$ roots of the following $(N+1)$-order algebraic equation in ξ

$$\sum_{n=1}^{N}\bar{a}_n\xi^{n+1}-\bar{z}_0R^{-1}\xi+1=0. \tag{39}$$

Furthermore, the following relationship is also valid on the interface L

$$\frac{\bar{z}}{z-z_0}=G(z),\ z\in L, \tag{40}$$

where $G(z)$ is analytic in the exterior of the inhomogeneity except infinity where it has a pole of finite degree determined by its asymptotic behavior

$$G(z)\cong Q(z)+O(1),\quad |z|\to\infty, \tag{41}$$

where $Q(z)$ is a polynomial in z of $(N-1)$-degree. Apparently, the polynomial $Q(z)$ is non-constant for a nonelliptical inhomogeneity with $N\geq 2$ and is constant for an elliptical inhomogeneity with $N=1$.

The analytic function $\phi_1(z)$ defined in the inhomogeneity is still given by (21). Consequently, the analytic function $\psi_1(z)$ defined in the inhomogeneity can be finally determined as

$$\begin{aligned}\psi_1(z)=&\frac{\mathrm{i}\mu(b_1-\mathrm{i}b_2)}{\pi(\kappa_1+1)}\ln(z-z_0)+\frac{\mathrm{i}\mu(b_1+\mathrm{i}b_2)}{\pi(\kappa_1+1)}\frac{\bar{z}_0}{z-z_0}\\&+\frac{\mathrm{i}\mu(\kappa_1-\kappa_2)(b_1-\mathrm{i}b_2)}{\pi(\kappa_1+1)(\kappa_2+1)}\sum_{n=1}^{N+1}\ln(z-z_n)+\frac{\mathrm{i}\mu(\kappa_2-\kappa_1)(b_1+\mathrm{i}b_2)}{\pi(\kappa_1+1)(\kappa_2+1)}Q(z),\quad z\in S_1,\end{aligned} \tag{42}$$

where

$$z_n=\omega(\xi_n),\ n=1,2,\ldots,N+1. \tag{43}$$

By using the Peach–Koehler formula, the image force acting on the edge dislocation is

$$F_1-\mathrm{i}F_2=\frac{\mu(\kappa_1-\kappa_2)}{\pi(\kappa_1+1)(\kappa_2+1)}\left[(b_1^2+b_2^2)\sum_{n=1}^{N+1}\frac{1}{z_0-z_n}-(b_1^2-b_2^2+2\mathrm{i}b_1b_2)Q'(z_0)\right], \tag{44}$$

so that the image force varies with the direction of the vector (b_1,b_2) for an inhomogeneity of nonellip-

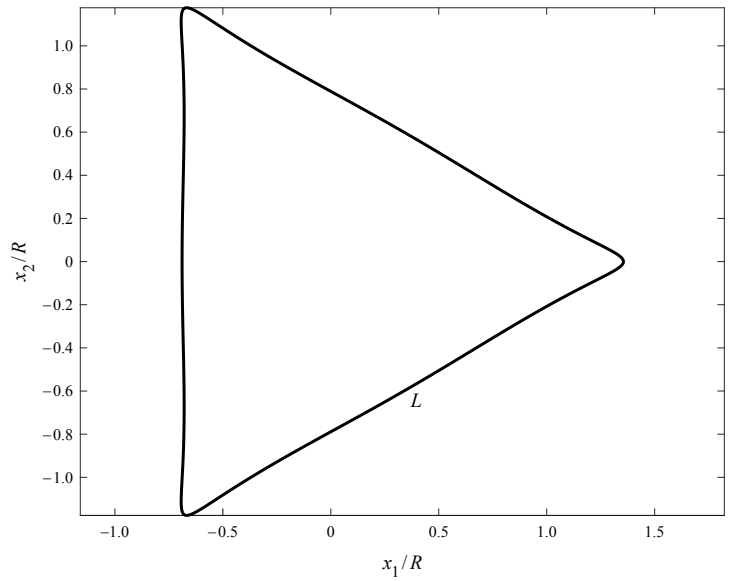

Figure 4. A rounded triangular interface L described by Equation (45).

tical shape. The image force is known once $z_n, n = 1, 2, \ldots, N+1$ and $Q'(z_0)$ have been determined.

For example, we consider a rounded triangular interface in Figure 4 described by

$$z = \omega(\xi) = R\left(\xi + \frac{1}{3\xi^2} + \frac{1}{45\xi^5}\right), \quad |\xi| = 1. \tag{45}$$

In this example, $N = 5$. The polynomial $Q(z)$ is explicitly determined by

$$Q(z) = \frac{z^4 + z_0 z^3 + z_0^2 z^2}{45R^4} + z\left(\frac{z_0^3}{45R^4} + \frac{8}{27R}\right). \tag{46}$$

Thus, the term $Q'(z_0)$ can be easily determined by

$$Q'(z_0) = \frac{2z_0^3}{9R^4} + \frac{8}{27R}. \tag{47}$$

The image force on an edge dislocation on the x_1-axis inside the rounded triangular inhomogeneity is illustrated in Figure 5. It is seen from Figure 5 that: $z_0 = -0.1647R$ is an equilibrium position for an edge dislocation with $b_2 = 0$; whilst $z_0 = 0.2240R$ is an equilibrium position for an edge dislocation with $b_1 = 0$. The variance of the image force with the direction of the Burgers vector is also clearly reflected in Figure 5.

6. An edge dislocation outside an elastic inhomogeneity of arbitrary shape

We now consider an edge dislocation with Burgers vector (b_1, b_2) located at $z = z_0$ in an infinite matrix (denoted as S_2) perfectly bonded to an elastic inhomogeneity of arbitrary shape (denoted as S_1) through a sharp interface L. As before, subscript 1 and 2 are used to identify the respective quantities in S_1 and S_2. The elastic inhomogeneity and the matrix have the same shear modulus but different Poisson's ratios.

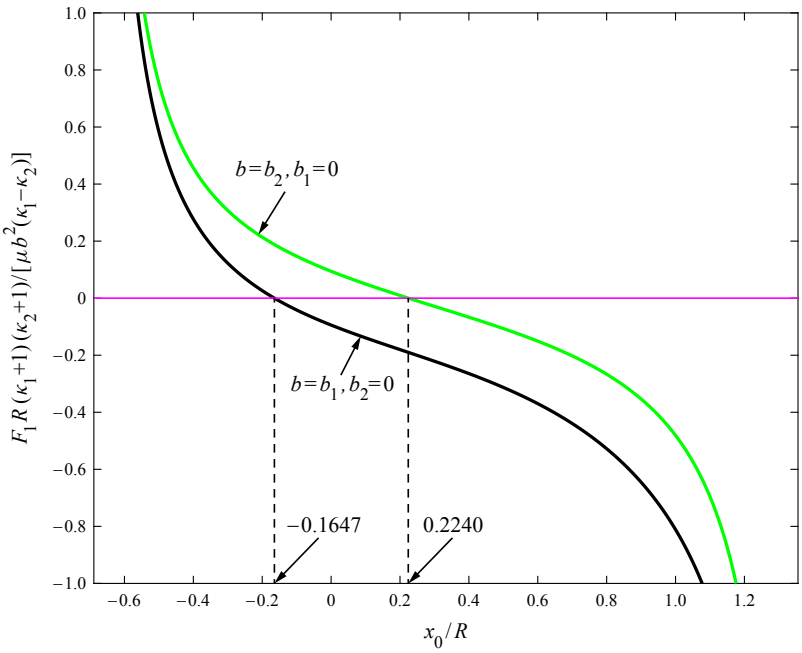

Figure 5. The image force on an edge dislocation on the x_1-axis inside the rounded triangular inhomogeneity. $F_2 \equiv 0$.

We consider the conformal mapping function [Muskhelishvili 1953; Jarczyk and Mityushev 2012]

$$z = \omega(\xi) = R\sum_{n=1}^{M} c_n \xi^n, \xi = \omega^{-1}(z), \quad |\xi| \le 1, \tag{48}$$

where R is a real scaling constant, and $c_n, n = 1, 2, \ldots, M$ are M complex constants. Without losing generality, one can set $c_1 = 1$.

By using the mapping function in (48), the interior of the inhomogeneity is mapped onto the interior of the unit circle in the ξ-plane.

On the interface L, the following relationship is valid

$$\bar{z} - \bar{z}_0 = -\xi^{-M}\left(\bar{z}_0\xi^M - R\sum_{n=1}^{M}\bar{c}_n\xi^{M-n}\right) = -\bar{z}_0\xi^{-M}\prod_{n=1}^{M}(\xi-\xi_n), \quad z \in L, \tag{49}$$

where $\xi_n, n = 1, 2, \ldots, M$, all of which are located inside the unit circle, are the M roots of the following M-order algebraic equation in ξ

$$\bar{z}_0\xi^M - R\sum_{n=1}^{M}\bar{c}_n\xi^{M-n} = 0. \tag{50}$$

The following relationship is also valid on the interface L:

$$\frac{\bar{z}}{z - z_0} = H(z), \ z \in L, \tag{51}$$

where $H(z)$ is analytic in the interior of the inhomogeneity except the point at $z=0$ where it has a pole of finite degree determined by its asymptotic behavior

$$H(z) \cong P(z) + O(1), \quad z \to 0, \tag{52}$$

where $P(z)$ is a polynomial in z^{-1} of degree M.

The analytic function $\phi_2(z)$ defined in the matrix is still given by (21). Consequently, the analytic function $\psi_2(z)$ defined in the matrix can be finally determined as

$$\begin{aligned}\psi_2(z) = {} & \frac{\mathrm{i}\mu(b_1 - \mathrm{i}b_2)}{\pi(\kappa_2+1)} \ln(z - z_0) + \frac{\mathrm{i}\mu(b_1 + \mathrm{i}b_2)}{\pi(\kappa_2+1)} \frac{\bar{z}_0}{z - z_0} \\ & + \frac{\mathrm{i}\mu(\kappa_2 - \kappa_1)(b_1 - \mathrm{i}b_2)}{\pi(\kappa_1+1)(\kappa_2+1)} \sum_{n=1}^{M} \ln \frac{z - z_n}{z} + \frac{\mathrm{i}\mu(\kappa_1 - \kappa_2)(b_1 + \mathrm{i}b_2)}{\pi(\kappa_1+1)(\kappa_2+1)} P(z), \quad z \in S_2, \end{aligned} \tag{53}$$

where

$$z_n = \omega(\xi_n), \quad n = 1, 2, \ldots, M. \tag{54}$$

By using the Peach–Koehler formula, the image force acting on the edge dislocation is

$$F_1 - \mathrm{i}F_2 = \frac{\mu(\kappa_2 - \kappa_1)}{\pi(\kappa_1+1)(\kappa_2+1)} \left[(b_1^2 + b_2^2) \sum_{n=1}^{M} \frac{z_n}{z_0(z_0 - z_n)} - (b_1^2 - b_2^2 + 2\mathrm{i}b_1 b_2) P'(z_0) \right], \tag{55}$$

which also implies that the image force varies with the direction of the vector (b_1, b_2) when $P'(z_0) \neq 0$. When $M = 1$ for a circular inhomogeneity, we have $z_1 = R^2/\bar{z}_0$ and $P'(z_0) = R^2/z_0^3$. In this special case, (55) simply recovers the classical result in Equations (7.8) and (7.9) by [Dundurs 1969].

For example, as illustrated in Figure 6, we consider an interface described by

$$z = \omega(\xi) = R(\xi + c\xi^2), \quad -\tfrac{1}{2} \le c \le \tfrac{1}{2}, \quad |\xi| = 1. \tag{56}$$

In this example, $M = 2$. The two roots of Equation (50) can be explicitly given by

$$\xi_{1,2} = \frac{R \pm \sqrt{R^2 + 4Rc\bar{z}_0}}{2\bar{z}_0}, \quad |\xi_{1,2}| < 1, \tag{57}$$

and thus,

$$\begin{aligned} z_1 &= \frac{cR^3 + R^2\bar{z}_0(2c^2+1) + R(\bar{z}_0 + Rc)\sqrt{R^2 + 4Rc\bar{z}_0}}{2\bar{z}_0^2}, \\ z_2 &= \frac{cR^3 + R^2\bar{z}_0(2c^2+1) - R(\bar{z}_0 + Rc)\sqrt{R^2 + 4Rc\bar{z}_0}}{2\bar{z}_0^2}. \end{aligned} \tag{58}$$

In addition, the polynomial $P(z)$ is determined by

$$P(z) = -\frac{R^2(1 + 2c^2 + Rz_0^{-1}c)}{z_0 z} - \frac{R^3 c}{z_0 z^2}. \tag{59}$$

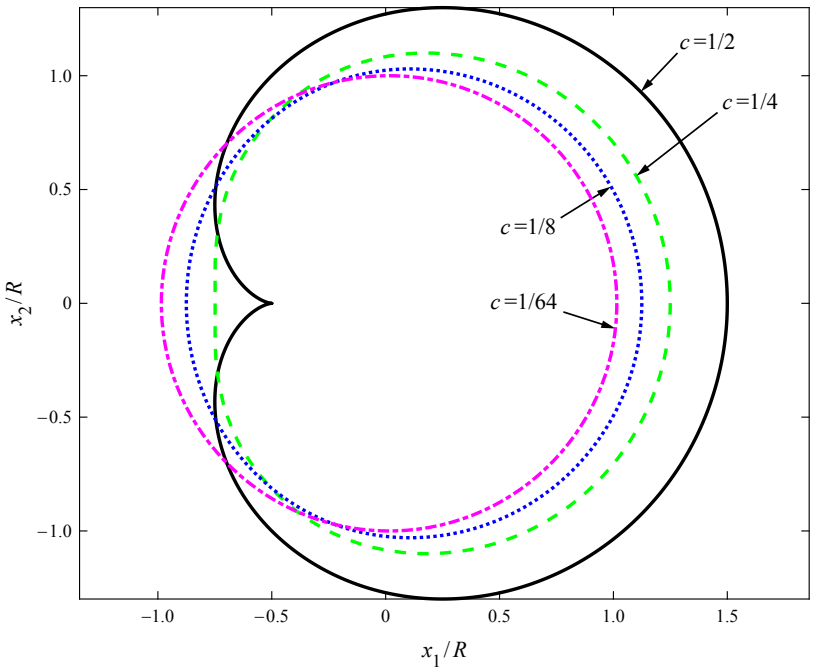

Figure 6. Shapes of the interface described by (56) for different values of c.

Thus, the term $P'(z_0)$ can be easily determined by

$$P'(z_0) = \frac{R^2 z_0(1+2c^2)+3R^3 c}{z_0^4}. \tag{60}$$

Consequently, the image force can be given explicitly by

$$\begin{aligned} &F_1 - \mathrm{i}F_2 \\ &= \frac{\mu(\kappa_2-\kappa_1)}{\pi(\kappa_1+1)(\kappa_2+1)} \\ &\times \left(\frac{2R^2 z_0^{-1}(b_1^2+b_2^2)[[cR+\bar{z}_0(2c^2+1)][2z_0\bar{z}_0^2 - cR^3 - R^2\bar{z}_0(2c^2+1)] + R(\bar{z}_0+Rc)^2(R+4c\bar{z}_0)]}{[2z_0\bar{z}_0^2 - cR^3 - R^2\bar{z}_0(2c^2+1)]^2 - R^3(\bar{z}_0+Rc)^2(R+4c\bar{z}_0)} \right. \\ &\qquad \left. -R^2 z_0^{-4}(b_1^2-b_2^2+2\mathrm{i}b_1b_2)[z_0(1+2c^2)+3Rc] \right) \end{aligned} \tag{61}$$

In particular, if we set $c = 1/2$ and $z_0 = R(2+\mathrm{i})$, the image force on the edge dislocation can be determined from (61) as follows:

$$\begin{aligned} F_1 &= \frac{\mu(\kappa_2-\kappa_1)(0.2704b_1^2+0.2848b_2^2-0.3792b_1b_2)}{\pi R(\kappa_1+1)(\kappa_2+1)}, \\ F_2 &= \frac{\mu(\kappa_2-\kappa_1)(-0.0345b_1^2+0.3447b_2^2+0.0144b_1b_2)}{\pi R(\kappa_1+1)(\kappa_2+1)}. \end{aligned} \tag{62}$$

It can be seen from (60) and (61) that when the dislocation is located at the following particular point

$$z_0 = -\frac{3Rc}{1+2c^2}, \quad 0.2779 \le |c| \le 0.5, \tag{63}$$

the image force remains invariant with the direction of the Burgers vector and is given by

$$F_1 = \frac{\mu(\kappa_2-\kappa_1)(b_1^2+b_2^2)(2c^2+1)^5}{6\pi R(\kappa_1+1)(\kappa_2+1)c(c^2-1)(4c^6+12c^4+12c^2-1)}, \quad F_2 = 0. \tag{64}$$

The component F_1 in (64) becomes infinite as $c \to \pm 0.2779$ since now the edge dislocation just approaches the interface L in view of (56) and (63).

7. Conclusions

We have obtained simple and closed-form Green's function solutions for an edge dislocation interacting with a parabolic or elliptical elastic inhomogeneity under the assumption that the inhomogeneity and the matrix have equal shear moduli. For the interaction between an edge dislocation and a parabolic elastic inhomogeneity, the two analytic functions $\psi_1(z)$ and $\psi_2(z)$ are obtained in (8) and (9) for an edge dislocation in the matrix, in (14) and (15) for an edge dislocation in the parabolic inhomogeneity and in (18) and (19) for an edge dislocation located on the parabolic interface; the image force is given by (10) when the dislocation lies in the matrix and by (16) when the dislocation lies in the parabolic inhomogeneity. For the interaction between an edge dislocation and an elliptical elastic inhomogeneity, the two analytic functions $\psi_1(z)$ and $\psi_2(z)$ are obtained in (25) and (26) for an edge dislocation in the matrix, in (31) and (32) for an edge dislocation in the elliptical inhomogeneity; the image force is given by (28) when the dislocation lies in the matrix and by (34) when the dislocation lies in the elliptical inhomogeneity.

We have also obtained closed-form expressions in (44) and (55) for the image force on an edge dislocation in the interior and exterior of an elastic inhomogeneity of arbitrary shape. It is stressed that the mapping function in (37) that maps the exterior of an inhomogeneity onto the exterior of the unit circle in the image plane is distinct from the one in (48) that maps the interior of an inhomogeneity onto the interior of a unit circle in the image plane.

Acknowledgements

This work is supported by the National Natural Science Foundation of China (Grant No. 11272121) and through a Discovery Grant from the Natural Sciences and Engineering Research Council of Canada (Grant No. RGPIN-2017-03716115112).

References

[Argatov et al. 2012] I. I. Argatov, R. Guinovart-Díaz, and F. J. Sabina, "On local indentation and impact compliance of isotropic auxetic materials from the continuum mechanics viewpoint", *Int. J. Eng. Science* **54** (2012), 42–57.

[Chen 1996] D. H. Chen, "Green's functions for a point force and dislocation outside an elliptic inclusion in plane elasticity", *Z. angew. Math. Phys.* **47** (1996), 894–905.

[Dundurs 1969] J. Dundurs, "Elastic interaction of dislocations with inhomogeneities", pp. 70–115 in *Mathematical theory of dislocations*, edited by T. Mura, American Society of Mechanical Engineers, New York, 1969.

[England 1971] A. H. England, *Complex variable method in elasticity*, John Wiley and Sons, New York, 1971.

[Gong and Meguid 1994] S. X. Gong and S. A. Meguid, "A screw dislocation interacting with an elastic elliptical inhomogeneity", *Int. J. Eng. Sci.* **32** (1994), 1221–1228.

[Jarczyk and Mityushev 2012] P. Jarczyk and V. Mityushev, "Neutral coated inclusions of finite conductivity", *Proc. R. Soc. A* **468**:2140 (2012), 954–970.

[Lakes 1987] R. S. Lakes, "Foam structures with a negative Poisson's ratio", *Science* **235**:4792 (1987), 1038–1040.

[Muskhelishvili 1953] N. I. Muskhelishvili, *Some basic problems of the mathematical theory of elasticity*, Noordhoff, Groningen, 1953.

[Qaissaunee and Santare 1995] M. T. Qaissaunee and M. H. Santare, "Edge dislocation interacting with an elliptical inclusion surrounded by an interfacial zone", *Quart. J. Mech. Appl. Math.* **48**:3 (1995), 465–482.

[Shi and Li 2006] J. Shi and Z. Li, "An approximate solution of the interaction between an edge dislocation and an inclusion of arbitrary shape", *Mech. Res. Commun.* **33** (2006), 804–810.

[Stagni 1982] L. Stagni, "On the elastic field perturbation by inhomogeneities in plane elasticity", *Z. Angew. Math. Phys.* **33** (1982), 315–325.

[Stagni 1993] L. Stagni, "Edge dislocation near an elliptic inhomogeneity with either an adhering or a slipping interface: A comparative study", *Phil. Mag.* **68** (1993), 49–57.

[Stagni 1999] L. Stagni, "The effect of the interface on the interaction of an interior edge dislocation with an elliptical inhomogeneity", *Z. angew. Math. Phys.* **50** (1999), 327–337.

[Stagni and Lizzio 1983] L. Stagni and R. Lizzio, "Shape effects in the interaction between an edge dislocation and elliptical inhomogeneity", *J. Appl. Phys. A* **30** (1983), 217–221.

[Suo 1989] Z. G. Suo, "Singularities interacting with interfaces and cracks", *Int. J. Solids Struct.* **25** (1989), 1133–1142.

[Suo 1990] Z. G. Suo, "Singularities, interfaces and cracks in dissimilar anisotropic media", *Proc. Roy. Soc. London Ser. A* **427**:1873 (1990), 331–358.

[Ting 1996] T. C. T. Ting, *Anisotropic elasticity: theory and applications*, Oxford University Press, New York, 1996.

[Tsuchida et al. 1991] E. Tsuchida, M. Ohno, and D. A. Kouris, "Effects of an inhomogeneous elliptic insert on the elastic field of an edge dislocation", *Solids Mater.* **53** (1991), 285–291.

[Wang 2015] X. Wang, "Eshelby's inclusion and dislocation problems for an isotropic circular domain bonded to an anisotropic medium", *Acta Mech.* **226** (2015), 103–121.

[Wang and Sudak 2006] X. Wang and L. J. Sudak, "Interaction of a screw dislocation with an arbitrary shaped elastic inhomogeneity", *ASME J. Appl. Mech.* **73** (2006), 206–211.

[Warren 1983] W. E. Warren, "The edge dislocation inside an elliptical inclusion", *Mech. Mater.* **2**:4 (1983), 319–330.

[Yen et al. 1995] W. J. Yen, C. Hwu, and Y. K. Liang, "Dislocation inside, outside, or on the interface of an anisotropic elliptical inclusion", *ASME J. Appl. Mech.* **62** (1995), 306–311.

Received 8 May 2020. Revised 21 Jul 2020. Accepted 1 Aug 2020.

XU WANG: xuwang@ecust.edu.cn
School of Mechanical and Power Engineering, East China University of Science and Technology, 130 Meilong Road, Shanghai, 200237, China

PETER SCHIAVONE: p.schiavone@ualberta.ca
Department of Mechanical Engineering, University of Alberta, 10-203 Donadeo Innovation Center for Engineering, Edmonton AB 6G 1H9, Canada

SUBMISSION GUIDELINES

ORIGINALITY

Authors may submit manuscripts in PDF format online at the Submissions page. Submission of a manuscript acknowledges that the manuscript is original and has neither previously, nor simultaneously, in whole or in part, been submitted elsewhere. Information regarding the preparation of manuscripts is provided below. Correspondence by email is requested for convenience and speed. For further information, write to contact@msp.org.

LANGUAGE

Manuscripts must be in English. A brief abstract of about 150 words or less must be included. The abstract should be self-contained and not make any reference to the bibliography. Also required are keywords and subject classification for the article, and, for each author, postal address, affiliation (if appropriate), and email address if available. A home-page URL is optional.

FORMAT

Authors can use their preferred manuscript-preparation software, including for example Microsoft Word or any variant of TEX. The journal itself is produced in LATEX, so accepted articles prepared using other software will be converted to LATEX at production time. Authors wishing to prepare their document in LATEX can follow the example file at www.jomms.net (but the use of other class files is acceptable). At submission time only a PDF file is required. After acceptance, authors must submit all source material (see especially Figures below).

REFERENCES

Bibliographical references should be complete, including article titles and page ranges. All references in the bibliography should be cited in the text. The use of BibTEX is preferred but not required. Tags will be converted to the house format (see a current issue for examples); however, for submission you may use the format of your choice. Links will be provided to all literature with known web locations; authors can supply their own links in addition to those provided by the editorial process.

FIGURES

Figures must be of publication quality. After acceptance, you will need to submit the original source files in vector format for all diagrams and graphs in your manuscript: vector EPS or vector PDF files are the most useful. (EPS stands for Encapsulated PostScript.)

Most drawing and graphing packages—Mathematica, Adobe Illustrator, Corel Draw, MATLAB, etc.—allow the user to save files in one of these formats. Make sure that what you're saving is vector graphics and not a bitmap. If you need help, please write to graphics@msp.org with as many details as you can about how your graphics were generated.

Please also include the original data for any plots. This is particularly important if you are unable to save Excel-generated plots in vector format. Saving them as bitmaps is not useful; please send the Excel (.xls) spreadsheets instead. Bundle your figure files into a single archive (using zip, tar, rar or other format of your choice) and upload on the link you been given at acceptance time.

Each figure should be captioned and numbered so that it can float. Small figures occupying no more than three lines of vertical space can be kept in the text ("the curve looks like this:"). It is acceptable to submit a manuscript with all figures at the end, if their placement is specified in the text by means of comments such as "Place Figure 1 here". The same considerations apply to tables.

WHITE SPACE

Forced line breaks or page breaks should not be inserted in the document. There is no point in your trying to optimize line and page breaks in the original manuscript. The manuscript will be reformatted to use the journal's preferred fonts and layout.

PROOFS

Page proofs will be made available to authors (or to the designated corresponding author) at a Web site in PDF format. Failure to acknowledge the receipt of proofs or to return corrections within the requested deadline may cause publication to be postponed.

Journal of Mechanics of Materials and Structures
Volume 15, No. 4 July 2020